

Copyright
By
Xianhui Kong
2014

**The Dissertation Committee for Xianhui Kong Certifies that this is the approved
version of following dissertation:**

**Petrophysical Modeling and Simulation Study of Geological
CO₂ Sequestration**

Committee:

Mojdeh Delshad, Supervisor

Mary F. Wheeler, Co-Supervisor

Todd J. Arbogast

Kamy Sepehrnoori

Ian Duncan

**Petrophysical Modeling and Simulation Study of
Geological CO₂ Sequestration**

By

Xianhui Kong, B.S.; M.E.

Dissertation

Presented to the Faculty of the Graduate School of
The University of Texas at Austin
in Partial Fulfillment
of the Requirements
for the Degree of
DOCTOR OF PHILOSOPHY

THE UNIVERSITY OF TEXAS AT AUSTIN

May 2014

Dedicating to my family

ACKNOWLEDGEMENT

I would like to express my sincere gratitude to my supervisor, Dr. Mojdeh Delshad, for her continuous guidance, support, and encouragement throughout my PhD study. I am grateful for the efforts she devoted to my PhD training in all aspects. Her diligence and enthusiasm in research inspired me to learn from her. What she provided was far beyond supervising and I am grateful for that. I am grateful to Dr. Mary F. Wheeler, my co-supervisor, for teaching me detail-oriented work. Without her persistent help and profound knowledge, this work would not have been possible. I also extend my gratitude to my committee members, Dr. Todd Arbogast, Dr. Kamy Sepehrnoori, and Dr. Ian Duncan, for their valuable advices and comments on my work.

This PhD research wouldn't have completed without the help from others. Thanks everyone that contributed in developing IPARS. Thanks to Sunil Thomas, Rick Dean and other developers for the compositional IPARS. I would like to thank many members in CSM and PGE department for their continued help and friendship. I am also grateful to the financial support of the Center for Frontiers of Subsurface Energy Security (CFSES) of the DOE's Energy Frontier Research Centers (EFRC).

I would like to thank these people that helped me in my life. Thanks to USTC alumni that have been helping me from the moment I landed in the US. Thanks to Brownstone group for the memorable time. Thanks to the Far West tennis club for the practices all seasons that refreshing my body and mind.

I am truly indebt and grateful to my family for their love, support, and patience over the unusual long separation and hardship. Their hope supported me in making this achievement. I would like to thank my beloved fiancée for her endless love and support.

ABSTRACT

Petrophysical Modeling and Simulation Study of Geological CO₂ Sequestration

Publication No. _____

Xianhui Kong, Ph.D.

The University of Texas at Austin, 2014

Supervisors: Mojdeh Delshad, Mary F. Wheeler

Global warming and greenhouse gas (GHG) emissions have recently become the significant focus of engineering research. The geological sequestration of greenhouse gases such as carbon dioxide (CO₂) is one approach that has been proposed to reduce the greenhouse gas emissions and slow down global warming. Geological sequestration involves the injection of produced CO₂ into subsurface formations and trapping the gas through many geological mechanisms, such as structural trapping, capillary trapping, dissolution, and mineralization. While some progress in our understanding of fluid flow in porous media has been made, many petrophysical phenomena, such as multi-phase flow, capillarity, geochemical reactions, geomechanical effect, *etc.*, that occur during geological CO₂ sequestration remain inadequately studied and pose a challenge for continued study. It is critical to continue to research on these important issues.

Numerical simulators are essential tools to develop a better understanding of the geologic characteristics of brine reservoirs and to build support for future CO₂ storage projects. Modeling CO₂ injection requires the implementation of multiphase flow model and an Equation of State (EOS) module to compute the dissolution of CO₂ in brine and

vice versa. In this study, we used the Integrated Parallel Accurate Reservoir Simulator (IPARS) developed at the Center for Subsurface Modeling at The University of Texas at Austin to model the injection process and storage of CO₂ in saline aquifers. We developed and implemented new petrophysical models in IPARS, and applied these models to study the process of CO₂ sequestration.

The research presented in this dissertation is divided into three parts.

The first part of the dissertation discusses petrophysical and computational models for the mechanical, geological, petrophysical phenomena occurring during CO₂ injection and sequestration. The effectiveness of CO₂ storage in saline aquifers is governed by the interplay of capillary, viscous, and buoyancy forces. Recent experimental data reveals the impact of pressure, temperature, and salinity on interfacial tension (IFT) between CO₂ and brine. The dependence of CO₂-brine relative permeability and capillary pressure on IFT is also clearly evident in published experimental results. Improved understanding of the mechanisms that control the migration and trapping of CO₂ in the subsurface is crucial to design future storage projects for long-term, safe containment. We have developed numerical models for CO₂ trapping and migration in aquifers, including a compositional flow model, a relative permeability model, a capillary model, an interfacial tension model, and others. The heterogeneities in porosity and permeability are also coupled to the petrophysical models. We have developed and implemented a general relative permeability model that combines the effects of pressure gradient, buoyancy, and capillary pressure in a compositional and parallel simulator. The significance of IFT variations on CO₂ migration and trapping is assessed. The variation of residual saturation is modeled based on interfacial tension and trapping number, and a hysteretic trapping model is also presented.

The second part of this dissertation is a model validation and sensitivity study using coreflood simulation data derived from laboratory study. The motivation of this study is to gain confidence in the results of the numerical simulator by validating the models and the numerical accuracies using laboratory and field pilot scale results. Published steady state, core-scale CO₂/brine displacement results were selected as a reference basis for our numerical study. High-resolution compositional simulations of brine displacement with supercritical CO₂ are presented using IPARS. A three-dimensional (3D) numerical model of the Berea sandstone core was constructed using heterogeneous permeability and porosity distributions based on geostatistical data. The measured capillary pressure curve was scaled using the Leverett J-function to include local heterogeneity in the sub-core scale. Simulation results indicate that accurate representation of capillary pressure at sub-core scales is critical. Water drying and the shift in relative permeability had a significant impact on the final CO₂ distribution along the core. This study provided insights into the role of heterogeneity in the final CO₂ distribution, where a slight variation in porosity gives rise to a large variation in the CO₂ saturation distribution.

The third part of this study is a simulation study using IPARS for Cranfield pilot CO₂ sequestration field test, conducted by the Bureau of Economic Geology (BEG) at The University of Texas at Austin. In this CO₂ sequestration project, a total of approximately 2.5 million tons supercritical CO₂ was injected into a deep saline aquifer about ~10000 ft deep over 2 years, beginning December 1st 2009. In this chapter, we use the simulation capabilities of IPARS to numerically model the CO₂ injection process in Cranfield. We conducted a corresponding history-matching study and got good agreement with field observation. Extensive sensitivity studies were also conducted for

CO₂ trapping, fluid phase behavior, relative permeability, wettability, gravity and buoyancy, and capillary effects on sequestration. Simulation results are consistent with the observed CO₂ breakthrough time at the first observation well. Numerical results are also consistent with bottomhole injection flowing pressure for the first 350 days before the rate increase. The abnormal pressure response with rate increase on day 350 indicates possible geomechanical issues, which can be represented in simulation using an induced fracture near the injection well. The recorded injection well bottomhole pressure data were successfully matched after modeling the fracture in the simulation model. Results also illustrate the importance of using accurate trapping models to predict CO₂ immobilization behavior. The impact of CO₂/brine relative permeability curves and trapping model on bottom-hole injection pressure is also demonstrated.

Table of Contents

Acknowledgement	v
Abstract	vi
List of Tables	xv
List of Figures	xvii
Chapter 1: Introduction	1
1.1 Motivation	1
1.2 Literature Review.....	8
1.3 Dissertation Layout	19
Chapter 2: IPARS Review	21
2.1 IPARS Overview.....	21
2.1.1 Fluid Modeling.....	22
2.1.2 Gridding and Discretization	22
2.1.3 Solvers.....	23
2.1.4 Post-Processing and Visualization.....	24
2.2 IPARS Compositional Model	24
2.2.1 Equations for Compositional Fluid Flow.....	25
2.2.2 Equations for Molar Volumes and Saturations.....	26
2.2.3 Well Model	28
2.2.4 Viscosity Model.....	31
2.3 CO ₂ Module in IPARS	33

Chapter 3: Phase Behavior and Physical Property Enhancements..... 36

3.1	CO ₂ Phase Behavior.....	36
3.2	Interfacial Tension Correlations	40
3.2.1	IFT as a Function of Pressure, Temperature, Salinity	40
3.2.2	IFT Correlation Based on CO ₂ Concentration in Brine	42
3.2.3	MacLeod-Sugden Correlation.....	43
3.2.4	IFT Model Based on Phase Density Difference	44
3.2.5	Summary of Interfacial Tension Models	45
3.3	Trapping Model.....	46
3.3.1	Trapping Number.....	46
3.3.2	Capillary Desaturation Curves.....	47
3.3.3	Relative Permeability Model as Function of Trapping Number.....	49
3.3.4	Model Validation to Laboratory Data.....	53
3.4	Hysteresis Model.....	58
3.4.1	Land’s Hysteresis Trapping Model.....	61
3.4.2	Hysteretic Relative Permeability	63
3.4.3	Hysteretic Capillary Pressure.....	65
3.5	Leverett J-function for Capillary Pressure.....	66

Chapter 4: Model Validation with Coreflood Simulation 69

4.1	Review of Published Experimental and Numerical Results	70
4.2	Coreflood Simulation with IPARS	73
4.2.1	Core Model Based on Heterogeneous Permeability and Porosity	73
4.2.2	Porosity-Permeability Correlation	75
4.2.3	Capillary Pressure Model.....	79
4.3	IPARS Coreflood Simulation Results.....	81

4.3.1	Case 1: History Match Simulation	81
4.3.2	Case 2: Sensitivity to Capillary Pressure Scaling	84
4.3.3	Case 3: Sensitivity to Residual Brine Saturation	85
4.4	Summary	88
Chapter 5: CO₂ Sequestration Simulation with IPARS		91
5.1	Stacked Geological Model	91
5.2	Effect of Interfacial Tension and Capillary Pressure	96
5.2.1	Impact of Capillary Pressure Scaling Based on J-Function	96
5.2.2	Impact of Contact Angle, IFT, and Wettability on CO ₂ Migration	99
5.3	Simulations with the Trapping Model	108
5.3.1	Case 1 to Study Relative Permeability as a Function of Trapping Number	108
5.3.2	Comparison of Cases with and without Trapping Model	110
5.4	Test Study for Hysteresis Model in IPARS	117
5.4.1	1D Hysteresis Model	117
5.4.2	3D Hysteresis TEST	121
5.5	Summary	131
Chapter 6: Cranfield CO₂ Sequestration Pilot Test		133
6.1	Cranfield Pilot CO ₂ Sequestration Project	133
6.2	Cranfield Simulation Model	136
6.2.1	Grid Upscaling	141
6.2.2	Isothermal Sensitivity Simulations	145
6.2.3	History Matching with Near Wellbore Fracture Modeling	156
6.2.4	Thermal Simulation	159
6.3	Summary	163

Chapter 7: Summary and Future Works	164
7.1 Summary and Conclusions	164
7.2 Future Works.....	171
Appendix A: Compositional Model.....	173
A.1 Phase Equilibrium	173
A.2 Rachford-Rice Equations for Vapor Fraction	174
A.3 Peng-Robinson Equation of State.....	175
Appendix B: IPARS Compositional Input	178
B.1 IPARS Compositional Input.....	178
B.2 New Keywords for New Models in IPARS	186
Appendix C: SAMG and HYPRE Solvers for UTCHEM	188
C.1 UTCHEM Review	188
C.1.1 UTCHEM Formulations.....	188
C.1.2 UTCHEM Discretization.....	190
C.2 Implementation of SAMG and HYPRE Solvers	191
C.2.1 Compressed Row Storage (CRS)	191
C.2.2 SAMG	192
C.2.3 HYPRE.....	193
C.3 Speed-up Tests.....	195
Appendix D: IPARS and CMG Isothermal Benchmark	198
D.1 Governing Equations for Energy Balance.....	198
D.2 Analytical Solution for Buckley-Leverett Flow.....	199

D.3 IPARS and CMG Isothermal Benchmark	203
D.3.3 Non-Isothermal Test with IPARS and CMG	204
Nomenclature	208
References.....	214
Vita	226

LIST OF TABLES

Table 3.1 General properties for carbon dioxide and water (Ozah <i>et al.</i> , 2005)	38
Table 3.2 Fitting parameters for Bennion's IFT correlation based on CO ₂ mole fraction.	43
Table 3.3 Fitting parameters for Chalbaud's correlation (Chalbaud, 2006).....	44
Table 3.4 Core data used for relative permeability and capillary pressure measurements (Bennion and Bachu, 2006b).	54
Table 3.5 Parameters for Corey-type model match to the measured relative permeability data at different pressure and IFT condition by Bennion and Bachu (2006b).....	55
Table 4.1 Core properties and coreflood conditions (Krause <i>et al.</i> , 2011).....	70
Table 4.2 Drainage relative permeability and capillary pressure model parameters	75
Table 4.3 FFTSIM input parameters.....	76
Table 4.4 Coreflood simulation cases	81
Table 5.1 Model parameters for the stacked aquifer simulation.....	92
Table 5.2 Rock properties for aquifer and seal are from (Bennion and Bachu, 2006a) ...	93
Table 5.3 Input parameters for the J-function test case	98
Table 5.4 Reservoir model for wettability test case simulation.....	102
Table 5.5 Sensitivity test cases for contact angle	103
Table 5.6 Relative permeability model parameters as a function of trapping number ...	112
Table 5.7 Model parameters for hysteresis model test case.....	121
Table 5.8 Model-fitting parameters for drainage relative permeability of Cardium sandstone (Bennion and Bachu, 2006).....	123
Table 5.9 Test cases for hysteresis study.	124
Table 6.1 Reservoir properties for the Cranfield test.....	137
Table 6.2 PVT data for compositional simulation of the Cranfield case.....	138
Table 6.3 Number of grid cells and grid sizes for upscaled cases	142
Table 6.4 Rock-fluid thermal properties.....	161
Table D.1 Reservoir model for benchmark case in IPARS and CMG-GEM	201

Table D.2 Non-isothermal benchmark case thermal properties..... 205

LIST OF FIGURES

Figure 1.1 Observed changes in (a) global average surface temperature; (b) global average sea level from tide gauge (blue) and satellite (red) data and (c) Northern Hemisphere snow cover for March-April. (IPCC Fourth Assessment Report: Climate Change 2007)	2
Figure 1.2 Sources of global CO ₂ emissions, 1970–2004 (only direct emissions by sector). Source: Adapted from Olivier <i>et al.</i> , 2005	3
Figure 1.3 CO ₂ emissions from year 1750 to year 2000 (Marland <i>et al.</i> , 2003).....	3
Figure 1.4 Global anthropogenic greenhouse gas emissions in 2004. Source: Adapted from Olivier <i>et al.</i> , 2005	4
Figure 1.5 Predicted mutual solubility of CO ₂ and H ₂ O (Spycher and Pruess 2005).....	11
Figure 1.6 Evolution of the density of carbon dioxide with pressure at 307 K (▲), 309 K (○), 313 K (×) and 323 K (◆). The critical point (CP) is presented (ρ^*), ρ^* is 467.6 kg/m ⁻³ . (Cabaço <i>et al.</i> , 2010).....	12
Figure 1.7 Density of carbon dioxide with temperature (Bahadori, 2009).....	12
Figure 1.8 Density of carbon dioxide with temperature at different pressures (Bachu, 2003; 2008).....	13
Figure 1.9 Density of carbon dioxide vs. depth with different geothermal gradient temperatures (Bachu, 2003; 2008).....	13
Figure 1.10 Viscosity of carbon dioxide with density at different temperatures. (Vesovic <i>et al.</i> , 1990).....	18
Figure 2.1 A schematic of IPARS models	22
Figure 2.2 IPARS gridding and reservoir modeling	23
Figure 2.3 Compositional modules in IPARSv3.1.....	25
Figure 2.4 CO ₂ petrophysical modules in compositional IPARSv3.1	34
Figure 3.1 Carbon dioxide phase diagram (Bachu, 2008)	37

Figure 3.2 IFT vs. Pressure, model fit of Bennion's correlation for different temperatures.	41
Figure 3.3 Interfacial tension vs. pressure; Bennion's model fit for different salinities and $T = 60^{\circ}C$	42
Figure 3.4 Measured IFT vs. CO ₂ solubility in fresh water (Bennion and Bachu, 2008). 43	
Figure 3.5 Model fit of interfacial tension of water-CO ₂ with density difference (Chalbaud, 2006).....	45
Figure 3.6 Schematic capillary desaturation curves, residual saturation vs. capillary number (Lake, 1989).....	48
Figure 3.7 Example capillary desaturation curves for CO ₂ -brine, residual saturations vs. trapping number	49
Figure 3.8 Prototype relative permeability curves for low and high trapping numbers (Green: water; Red: CO ₂).....	50
Figure 3.9 Endpoint relative permeability vs. trapping number.	51
Figure 3.10 Relative permeability exponent vs. trapping number.....	52
Figure 3.11 Relative permeability curves at low trapping number of 10^{-8}	53
Figure 3.12 Relative permeability curves at high trapping number 10^{-2}	53
Figure 3.13 Relative permeability curves at different pressures (data from Bennion and Bachu, 2006b).	56
Figure 3.14 Curve-fit of relative permeability at low and high trapping number conditions (points are data from Bennion and Bachu, 2006b and lines are calculated).....	57
Figure 3.15 Comparison of model calculation (dash line) and laboratory data (points) of relative permeability curves at intermediate trapping number, solid lines are input relative permeability curves at high and low trapping number.....	58
Figure 3.16 Non-wetting phase gas trapping (S_{gt}) in pore space during imbibition process.	59
Figure 3.17 Sketch of hysteresis capillary pressure path.....	60

Figure 3.18 Maximum trapped non-wetting phase saturation vs. initial non-wetting phase saturation (Land's model).....	62
Figure 3.19 Trapped non-wetting phase saturation vs. wetting phase saturation during imbibition process starting at $Sw_{min} = 0$, based on Lenhard's interpolation.....	63
Figure 3.20 Drainage and imbibition relative permeability curves for CO ₂ -brine	64
Figure 3.21 Hysteretic capillary pressure for drainage and imbibition process	65
Figure 3.22 Capillary scaling based on heterogeneous rock with different permeability	67
Figure 3.23 Measured capillary pressure curves at different IFT (i.e.trapping number condition) (Bennion and Bachu, 2006b).....	68
Figure 4.1 Measured porosity (grid size of $0.254\text{ mm} \times 0.254\text{ mm} \times 1.5\text{ mm}$) (Krause <i>et al.</i> , 2011).....	71
Figure 4.2 Measured CO ₂ saturation (grid size of $0.254\text{ mm} \times 0.254\text{ mm} \times 1.5\text{ mm}$) (Krause <i>et al.</i> , 2011).....	71
Figure 4.3 Measured CO ₂ saturation in the middle slice (Krause <i>et al.</i> 2011).....	71
Figure 4.4 Measured CO ₂ saturation histogram (Krause <i>et al.</i> 2011).....	71
Figure 4.5 Measured relative permeability curves (Krause <i>et al.</i> 2011) and curve fit using Eq. 4.1 and 4.2	72
Figure 4.6 Measured capillary pressure curve (Krause <i>et al.</i> 2011) and curve fit using Eq. 4.3.....	72
Figure 4.7 Simulated CO ₂ saturation in middle slice (Krause <i>et al.</i> 2011).....	73
Figure 4.8 Simulated CO ₂ saturation histogram (Krause <i>et al.</i> 2011)	73
Figure 4.9 IPARS simulation grid using $32 \times 32 \times 32$ cells.....	74
Figure 4.10 Generated porosity with normal distribution.....	77
Figure 4.11 Log normal distribution of permeability ($Ln(k)$)	77
Figure 4.12 Porosity distribution in the core model	78
Figure 4.13 Porosity in middle slice (#16).....	78
Figure 4.14 Permeability in middle slice (#16)	78
Figure 4.15 Correlated permeability and porosity along the core	79

Figure 4.16 Capillary pressure curves for different permeability values with J-function	80
Figure 4.17 Final CO ₂ saturation simulated using IPARS (grid size of 1.27 mm × 1.27 mm × 6.35 mm)	82
Figure 4.18 CT-scan measured final CO ₂ saturation (Krause <i>et al.</i> 2011)	82
Figure 4.19 IPARS simulation results of CO ₂ saturation in middle slice (#16)	82
Figure 4.20 CT-scan measured CO ₂ saturation in middle slice (Krause <i>et al.</i> , 2011)	82
Figure 4.21 IPARS simulation result of CO ₂ saturation histogram for Case 1	83
Figure 4.22 Experimental histogram of CO ₂ saturation (Krause <i>et al.</i> , 2011)	83
Figure 4.23 Simulation results of slice-averaged CO ₂ saturation and porosity along the core for Case 1	83
Figure 4.24 Measured slice-averaged saturation along the core (Perrin and Benson, 2010)	83
Figure 4.25 Final CO ₂ saturation for simulation Case 2	84
Figure 4.26 Measured CO ₂ saturation (Krause <i>et al.</i> , 2011)	84
Figure 4.27 CO ₂ saturation histogram from simulation Case 2	85
Figure 4.28 Experimental histogram of CO ₂ saturation (Krause <i>et al.</i> , 2011)	85
Figure 4.29 Relative permeability curves for $S_{wr} = 0.0, 0.1, 0.2$	86
Figure 4.30 Capillary pressure curves for $S_{wr} = 0.0, 0.1, 0.2$	86
Figure 4.31 CO ₂ saturation results using IPARS for Case 3 with $S_{wr} = 0.2$	86
Figure 4.32 CT-scan measured CO ₂ saturation (Krause <i>et al.</i> 2011)	86
Figure 4.33 CO ₂ saturation profile for Case 3 with $S_{wr} = 0.0$	87
Figure 4.34 CO ₂ saturation profile for Case 3 with $S_{wr} = 0.1$	87
Figure 4.35 CO ₂ saturation profile in the middle slice for Case 3 with $S_{wr} = 0.2$	87
Figure 4.36 Experimental CO ₂ saturation profile in middle slice (Krause <i>et al.</i> , 2011)	87
Figure 4.37 Case 3 CO ₂ saturation histogram using $S_{wr} = 0.0$	88
Figure 4.38 Case 3 CO ₂ saturation histogram using $S_{wr} = 0.1$	88
Figure 4.39 Simulation histogram of CO ₂ saturation for Case 3 with $S_{wr} = 0.2$	88
Figure 4.40 Experimental histogram of CO ₂ saturation (Krause <i>et al.</i> , 2011)	88

Figure 5.1 Reservoir model configured for the stack aquifer CO ₂ sequestration simulation, the four injection wells are completed only in aquifer layer 1	91
Figure 5.2 Relative permeability curves for shale and sandstone aquifer (Bennion and Bachu, 2006a,b)	93
Figure 5.3 Capillary pressure curves for shale and sandstone aquifer (Bennion and Bachu, 2006a,b)	93
Figure 5.4 Horizontal permeability (md) for the stacked model	94
Figure 5.5 Permeability (md) distribution in the injection layer	94
Figure 5.6 Reservoir permeability (md) at vertical slice for all layers	95
Figure 5.7 CO ₂ saturation at the end of 5 years injection for the stacked reservoir case.	95
Figure 5.8 CO ₂ saturation at the end of 10 years for a stacked reservoir case.....	96
Figure 5.9 Reservoir model for the Leverett J-function test case (red: injector; green: boundary well)	97
Figure 5.10 Heterogeneous porosity for J-function test case.....	97
Figure 5.11 Heterogeneous permeability for J-function test case.....	97
Figure 5.12 CO ₂ saturation at 1 year without the Leverett J-function	98
Figure 5.13 CO ₂ saturation at 1 year with the Leverett J-function	98
Figure 5.14 CO ₂ saturation at 3 years without Leverett J-function	99
Figure 5.15 CO ₂ saturation at 3 years with the Leverett J-function.....	99
Figure 5.16 Gas saturation in cross-section after 1 year of injection with J-function.	99
Figure 5.17 Gas saturation in cross-section after 3 years of injection with J-function.....	99
Figure 5.18 Variation in contact angle change at different pressure and temperature (Zhu <i>et al.</i> , 2011)	100
Figure 5.19 Impact of contact angle (Red: $\theta = 0^\circ$, Purple: $\theta = 55^\circ$) on capillary pressure curve (Chalbaud <i>et al.</i> , 2007)	100
Figure 5.20 Model grid for contact angle tests	101
Figure 5.21 Drainage capillary pressure and relative permeability for wettability simulation case.....	102

Figure 5.22 Capillary pressure with different contact angles	103
Figure 5.23 CO ₂ saturation at 50 days in cross-section of injection well, contact angle a) 0 b) 30 c) 60 d) 90 degrees.....	104
Figure 5.24 CO ₂ saturation at 100 days in cross-section of injection well, contact angle a) 0 b) 30 c) 60 d) 90 degrees.....	105
Figure 5.25 Capillary pressure for water and CO ₂ system with contact angle of 0 and 180 degree.....	105
Figure 5.26 Capillary pressure for contact angle of 120 and 180 degrees.....	106
Figure 5.27 CO ₂ saturation at 50 days for contact angle a) 120 ⁰ b) 180 ⁰	106
Figure 5.28 Capillary pressure (in psi) for contact angle a) 120 ⁰ ; b) 180 ⁰ at the end of injection period	107
Figure 5.29 CO ₂ saturation at 100 days contact angle a) 120 ⁰ ; b) 180 ⁰	107
Figure 5.30 Reservoir model for one-year CO ₂ injection test	109
Figure 5.31 Gas saturation in well cross-section during the injection period at 1 year ..	109
Figure 5.32 Pressure profile (in psi) at 1 year in well cross-section.....	109
Figure 5.33 Calculated IFT (in <i>mN/m</i>) distribution at 1 year in well cross-section	110
Figure 5.34 Calculated trapping number at 1 year.....	110
Figure 5.35 Reservoir model (red: injector, green: producer)	111
Figure 5.36 Relative permeability curves for trapping numbers of (red: 1×10^{-7} , blue: 1×10^{-8} , green: 1×10^{-9}).....	112
Figure 5.37 Gas saturation at the end of 50 day injection without trapping model and <i>Sgr</i> = 0 (Case 1).....	113
Figure 5.38 Gas saturation at the end of 50 day injection without trapping model and <i>Sgr</i> = 0.102 (Case 2).....	113
Figure 5.39 Gas saturation at the end of 50 day injection with trapping model and maximum <i>Sgr</i> = 0.102 (Case 3)	114
Figure 5.40 Gas saturation at the end of 50 day injection without trapping model and <i>Sgr</i> = 0 (Case 1).....	114

Figure 5.41 Gas saturation at the end of 50 days injection without trapping model and $S_{gr} = 0.102$ (Case 2).....	115
Figure 5.42 Gas saturation at the end of 50 days injection with trapping model and maximum $S_{gr} = 0.102$ (Case 3)	115
Figure 5.43 Gas saturation at 500 days without a trapping model and with $S_{gr} = 0.0$ (Case 1).....	116
Figure 5.44 Gas saturation at 500 days without a trapping model and with $S_{gr} = 0.102$ (Case 2).....	116
Figure 5.45 Gas saturation at 500 days with a trapping model and with maximum $S_{gr} = 0.102$ (Case 3).....	116
Figure 5.46 Schematic of hysteresis behavior in capillary pressure curve.	118
Figure 5.47 Water saturation in grid cell #10 during drainage and imbibition process..	119
Figure 5.48 Normalized water saturation in gridblock #10 and minimum water saturation at the reversal point.	119
Figure 5.49 Trapped CO_2 saturation in injection well gridblock #10 with the hysteresis model vs. time.	120
Figure 5.50 Hysteretic relative permeability for wetting phase (K_{rw}) and non-wetting phase (K_{rg}) in grid #10.	120
Figure 5.51 Hysteretic capillary pressure during drainage and imbibition in injection well grid #10.	120
Figure 5.52 Reservoir model for the hysteresis model test case.....	122
Figure 5.53 Drainage and imbibition relative permeability curves for the hysteresis test model.....	122
Figure 5.54 Drainage and imbibition capillary pressure curves for the test of hysteresis model.....	123
Figure 5.55 Case 1 without hysteresis: gas saturation in a vertical cross-section at 50 days, end of injection.	125

Figure 5.56 Case 2 with hysteresis: gas saturation in a vertical cross-section at 50 days, end of injection.	125
Figure 5.57 Case 1 without hysteresis: gas saturation in a vertical cross-section at 500 days (zero P_c).	125
Figure 5.58 Case 2 with hysteresis: gas saturation in a vertical cross-section at 500 days (zero P_c).	125
Figure 5.59 Case 3 CO ₂ saturation in cross section at the end of 50 days of injection ..	126
Figure 5.60 Case 3 CO ₂ saturation in cross section at the end of 500 days	127
Figure 5.61 Case 3 capillary pressure at the end 50 day injection.	127
Figure 5.62 Case 3 capillary pressure at the end of 500 day simulation	127
Figure 5.63 CO ₂ inventory for free gas, trapped gas, and dissolved gas for Case 3 using $S_{gr} = 0$ without the hysteresis model.	128
Figure 5.64 Hysteretic relative permeability in Case 4.	129
Figure 5.65 Case 4 with hysteresis, CO ₂ saturation at the end of 50 day injection	130
Figure 5.66 Case 3 without hysteresis, CO ₂ saturation at the end of 50 day injection ...	130
Figure 5.67 Case 4 with hysteresis, CO ₂ saturation at the end of 500 days.	130
Figure 5.68 Case 3 without hysteresis, CO ₂ saturation at the end of 500 days	130
Figure 5.69 CO ₂ fractional inventory as free, trapped, and dissolved gas for Case 4 with hysteresis, and with $S_{gt,max} = 0.102$	131
Figure 6.1 Contour map (10 ft elevation interval) of the top of the Lower Tuscaloosa formation (Lu <i>et al.</i> 2012a).	134
Figure 6.2 Three wells in vertical cross-section of the DAS area (Bryant, 2010)	135
Figure 6.3 Injection well CFU 31-F1 BHP and injection rate with time (start at day 193, Dec. 1, 2009).	136
Figure 6.4 CO ₂ -brine relative permeability and capillary-pressure curves for sandstone aquifer (Hosseini <i>et al.</i> , 2012). Blue curve: brine relative permeability; red curve: CO ₂ relative permeability; green curve: capillary pressure.	139

Figure 6.5 CO ₂ -brine relative permeability and capillary-pressure curves for over- and underlying shale rocks (Hosseini <i>et al.</i> , 2012). Very low relative permeabilities (blue: CO ₂ ; red: brine) used for shale. Capillary pressure (green curve) is high for shale rock.	139
Figure 6.6 Aquifer depth and well locations	140
Figure 6.7 Depth from top view.....	140
Figure 6.8 CO ₂ injection rate schedule for well CFU 31F1.....	141
Figure 6.9 Upscaled Cranfield permeability field in Y direction, a) 200 ft; b) 100 ft; c) 50 ft.	142
Figure 6.10 Upscaled Cranfield porosity field in Y direction, a) 200 ft; b) 100 ft; c) 50 ft.	143
Figure 6.11 CO ₂ saturation at the end of 3 years of injection with a grid size of 200 ft.	144
Figure 6.12 CO ₂ saturation at the end of 3 years of injection with a grid size of 100 ft.	144
Figure 6.13 CO ₂ saturation at the end of 3 years of injection with a grid size of 50 ft. .	144
Figure 6.14 CO ₂ saturation at the end of 3 years of injection with a grid size of 25 ft. .	144
Figure 6.15 CO ₂ saturation after 10 years with grid size, a) 200 ft; b) 100 ft; c) 50 ft; d) 25 ft.	145
Figure 6.16 Base case CO ₂ saturation at 3 years.	146
Figure 6.17 Base case CO ₂ saturation at 10 years.	146
Figure 6.18 Base case CO ₂ saturation in injection well cross-section at 3 years.....	147
Figure 6.19 Base case CO ₂ saturation in injection well cross-section at 10 years.....	147
Figure 6.20 CO ₂ inventory as fraction of total injection, without hysteresis model.....	147
Figure 6.21 Drainage and imbibition relative permeability curves for CO ₂ -brine.	148
Figure 6.22 CO ₂ saturation at 3 years, with hysteresis.	149
Figure 6.23 CO ₂ saturation at 10 years, with hysteresis.	149
Figure 6.24 A cross section of CO ₂ saturation at 3 years, with hysteresis.	149
Figure 6.25 A cross section of CO ₂ saturation slice at 10 years, with hysteresis.	149

Figure 6.26 CO ₂ inventory as fraction of total injection with hysteresis model ($S_{gr, mx} = 0.2$).....	150
Figure 6.27 Simulated mobile CO ₂ as a fraction of total injection for different residual CO ₂ saturations	151
Figure 6.28 Brine/CO ₂ drainage relative permeability curves for low (1×10^{-8}), intermediate (1×10^{-7}), and high (1×10^{-6}) trapping numbers.....	152
Figure 6.29 CO ₂ saturation at 3 years, with the trapping model.....	152
Figure 6.30 CO ₂ saturation at 10 years, with the trapping model.....	152
Figure 6.31 CO ₂ saturation in the injection well cross-section at 3 years with the trapping model.....	153
Figure 6.32 CO ₂ saturation in the injection well cross-section at 10 years, with the trapping model.	153
Figure 6.33 Trapped amount of CO ₂ with trapping model and hysteresis model.....	154
Figure 6.34 Relative permeability of Cardium #1 sandstone from Bennion and Bachu (2006a).....	155
Figure 6.35 Capillary pressure of Cardium #1 sandstone from Bennion and Bachu (2006a).....	155
Figure 6.36 CO ₂ saturation at 3 years with no hysteresis.	155
Figure 6.37 CO ₂ saturation at 10 years with no hysteresis.	155
Figure 6.38 A cross section of CO ₂ saturation at 3 years with no hysteresis.	156
Figure 6.39 A cross section of CO ₂ saturation at 10 years without hysteresis.	156
Figure 6.40 IPARS simulation results of CFU 31-F1 well BHP and field data.	157
Figure 6.41 Simulation results with and without fracture throughout the whole simulation period compared to the field data.....	158
Figure 6.42 CO ₂ saturation in the first observation well, CFU 31-F2.....	159
Figure 6.43 CO ₂ saturation in the cross- section of injection well F1 at the end of injection at 600 days	161

Figure 6.44 Reservoir temperature profile in the cross -section of injection well F1 at the end of injection at 600 days	161
Figure 6.45 CO ₂ saturation in the cross- section of injection well F1 at simulation end at 1200 days	162
Figure 6.46 Reservoir temperature profile in the cross-section of injection well F1 at simulation end at 1200 days.....	162
Figure 6.47 Calculated temperature variation in injection and observation wells.....	162
Figure D.1 CO ₂ thermal conductivity vs. density at different temperature (Vescovic <i>et al.</i> , 1989)	199
Figure D.2 Fractional flow and saturation speed vs. saturation.....	202
Figure D.3 Saturation profile against dimensionless distance for Buckley-Leverett flow at different injected pore volume	202
Figure D.4 Simulation pressure drop in IPARS and CMG at 200 days	203
Figure D.5 Comparison of analytical solution and IPARS simulation results of saturation at 200 days with different level of grid refinement.....	204
Figure D.6 Non-isothermal simulation results of saturation in IPARS and CMG at 200 days	205
Figure D.7 Non-isothermal simulation results of pressure in IPARS and CMG at 200 days	206
Figure D.8 Non-isothermal simulation results of temperature in IPARS and CMG at 200 days	206

CHAPTER 1: INTRODUCTION

1.1 Motivation

Global warming is posing a severe threat to the global climate and is being addressed by more and more researchers all over the world (Allen 2009; Jones, 1999). Increases in average global air and sea temperatures, rising sea levels, and widespread snow and ice melting are observed as evidences of global warming (Figure 1.1). Reports show that the global warming was being caused by increasing greenhouse gas (GHG) concentration in atmosphere due to increasing greenhouse gas emission from human activities (IPCC Fourth Assessment Report: Climate Change 2007). Greenhouse gas emissions have increased significantly in recent years (Figure 1.2), along with an increase of energy consumption. CO₂ emissions from year 1750 to 2000 are shown in Figure 1.3, which shows CO₂ emission from different sources, including fossil-fuels, cement production, etc. Among the many kinds of greenhouse gas, such as methane, water vapor, nitrous oxide, etc., carbon dioxide contributes the most to GHG emissions, accounting for up to 77% of all GHG emissions (Figure 1.4). Carbon dioxide (CO₂) has been identified as the largest driver of increasing greenhouse gas emission. Reducing GHG emissions and sequestration of produced CO₂ have become an urgent global issue that is currently being addressed by increasingly numerous governments and research institutes around the globe (United Nations Framework Convention on Climate Change (UNFCCC); Kyoto Protocol).

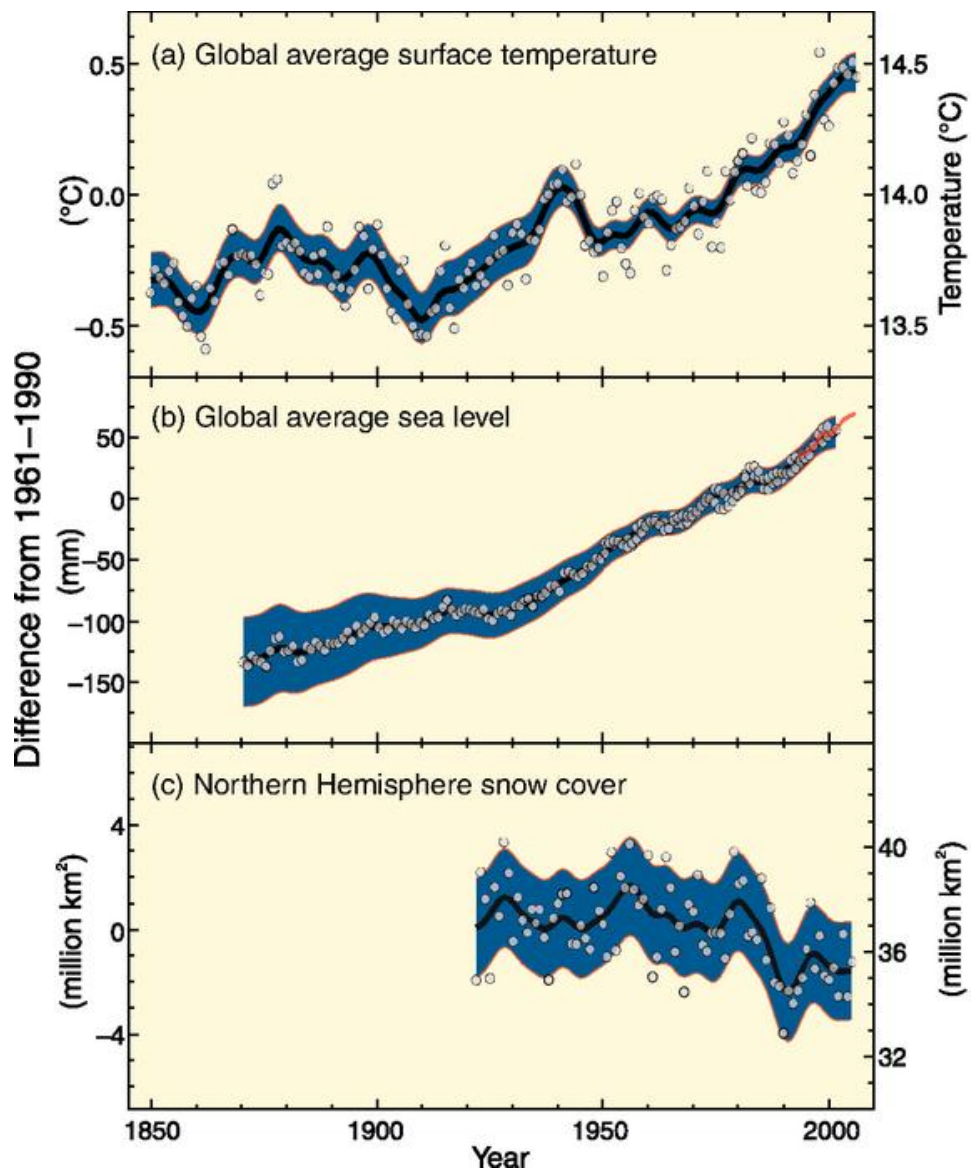


Figure 1.1 Observed changes in (a) global average surface temperature; (b) global average sea level from tide gauge (blue) and satellite (red) data and (c) Northern Hemisphere snow cover for March-April. (IPCC Fourth Assessment Report: Climate Change 2007)

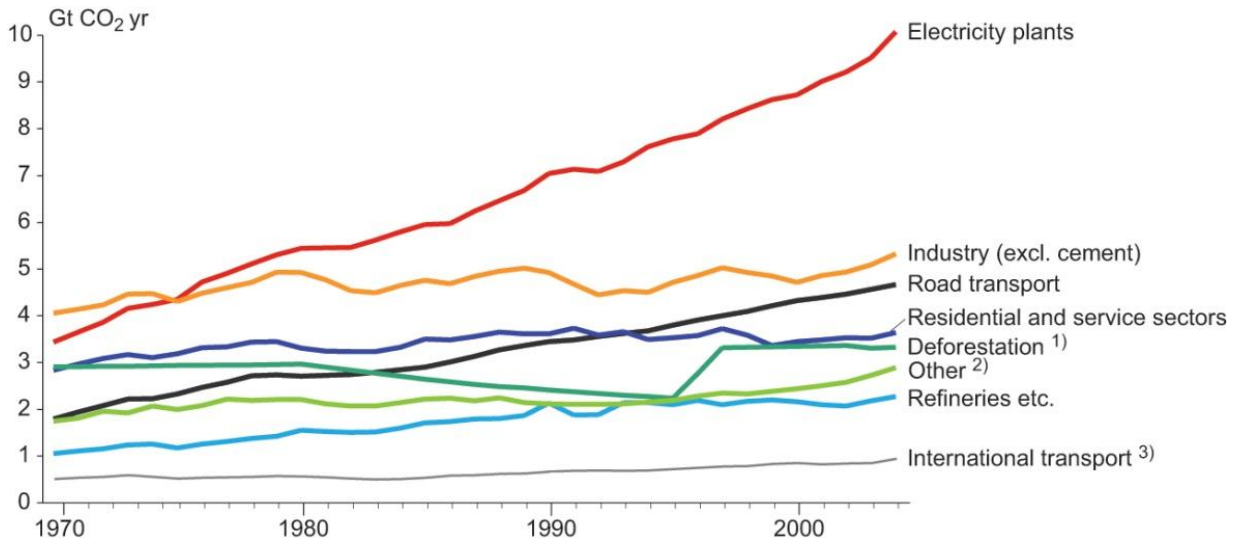


Figure 1.2 Sources of global CO₂ emissions, 1970–2004 (only direct emissions by sector). Source: Adapted from Olivier *et al.*, 2005

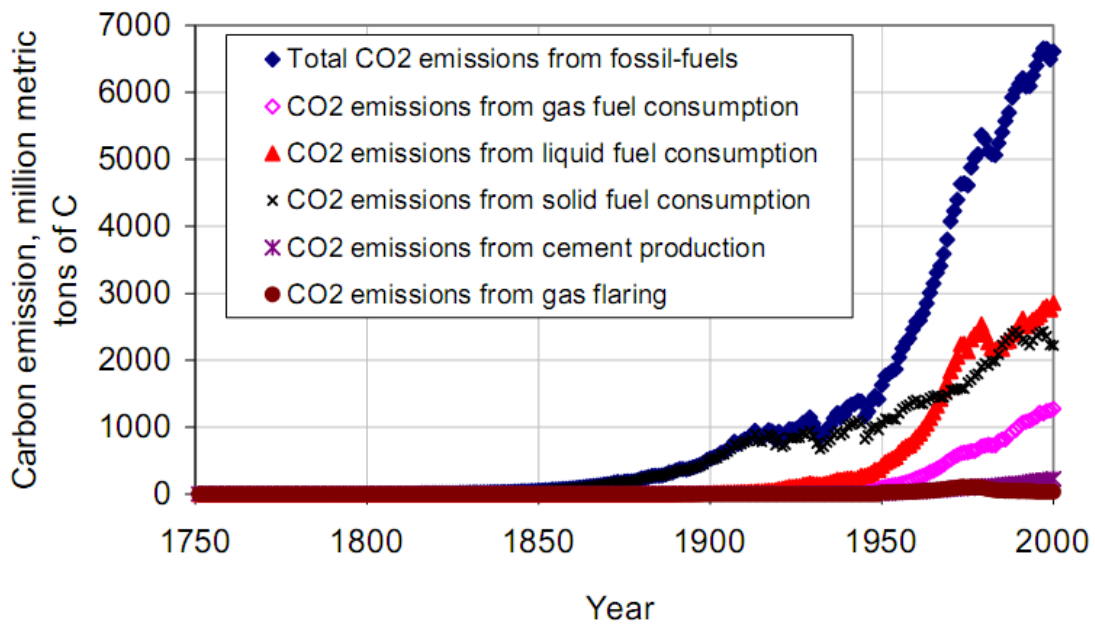


Figure 1.3 CO₂ emissions from year 1750 to year 2000 (Marland *et al.*, 2003)

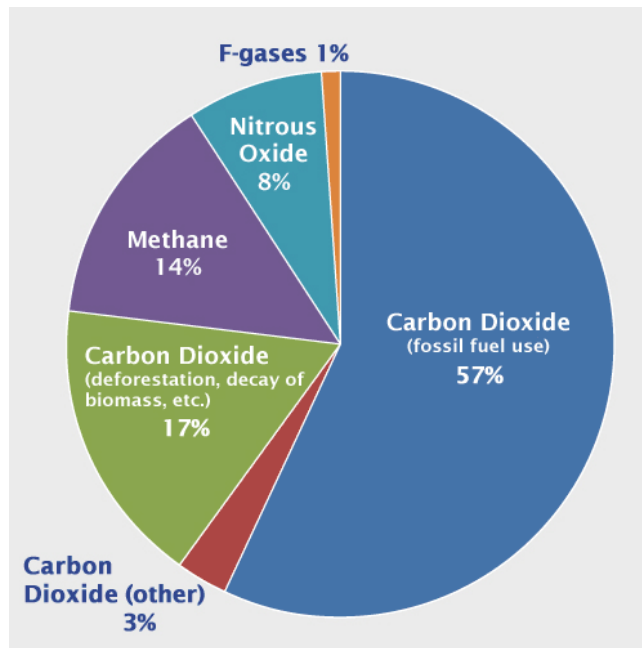


Figure 1.4 Global anthropogenic greenhouse gas emissions in 2004. Source: Adapted from Olivier *et al.*, 2005

Many methods proposed to reduce GHG emissions are currently under research and in development, including geological sequestration, agricultural carbon removal, bio-energy with carbon storage (BECS), mineral carbonation, deep ocean basalt storage, etc. For geological sequestration, produced CO₂ is injected into an underground reservoir or aquifer, and trapped through geological difference mechanisms. Agricultural carbon removal uses the carbon cycle as employed by existing crops to permanently sequester carbon within the soil. BECS includes biomass in power stations and boilers that use carbon capture and storage. The mineral carbonation process involves reacting carbon dioxide with abundantly available metal oxides. Carbon dioxide sequestration in basalt involves the injection of CO₂ into deep-sea formations. When CO₂ is sequestered in basalt, it first mixes with seawater, and then reacts with the basalt, forming stable

carbonate minerals. The effectiveness of these sequestration methods needs to be further evaluated and tested.

Geological CO₂ sequestration by injecting produced CO₂ to underground reservoir or aquifer formations is an effective method for reducing CO₂ emission. Several kinds of formation can serve as the sequestration candidates for CO₂ geological sequestration, such as the deep saline aquifer, oil/gas reservoir. CO₂ can be injected into oil-/gas-producing reservoirs to enhance oil/gas recovery or sequestered in depleted reservoirs (Godec *et al.*, 2011). CO₂ can also be used for coal-bed methane production, serving as storage and enhancing production. Depleted oil/gas reservoirs can also be a good candidate for geological CO₂ storage with a large volume of storage space. These fields usually have good geological seals to prevent gas leakage through the formation cap and many existing infrastructures for CO₂ injection. CO₂ sequestration in deep saline aquifers is another option for sequestration (Benson and Cole, 2008). It is considered the most plausible method. Deep saline aquifers are attractive for long-term CO₂ storage because of the large volume and the widespread availability of those saline aquifers. Large bodies of water would provide great capacity for CO₂ sequestration because injected CO₂ can dissolve into the brine and be trapped in the pore spaces. Saline aquifers are also widely distributed that makes transportation and site selection more flexible.

CO₂ sequestration in deep saline aquifer remains a challenging research topic, due to many reservoir conditions, such as high pressure, high temperature, high salinity, etc. Saline aquifers usually have large volume, and the sequestration process is long term, which also adds to the complexity of this study. CO₂ would be in a supercritical state (31.0 °C 7.38 MPa, 87.7 F and 1070.7 psi) for deep formations at a depth of approximately 800 m or greater. Supercritical CO₂ phase behavior has not been fully

studied. The CO₂-brine two-phase flow model coupling with the geochemical and petrophysical processes poses a research challenge.

Numerical simulation is an increasingly popular way to investigate physical processes, and numerical simulators coupled with accurate physical models are tools for carbon sequestration studies. Several simulators for CO₂ sequestration, including TOUGH+CO₂, CMG-GEM, CHEARS, etc. have been developed by researchers in several institutes. An in-house simulator named the Integrated Parallel Accurate Reservoir Simulator (IPARS) has been developed by the Center for Subsurface Modeling at The University of Texas at Austin. The simulator IPARS is capable of performing multiphase, multi-physics, parallel reservoir simulation. There are many simulation modules in the simulator IPARS, such as black oil, hydro, TrChem, and compositional models. In addition, the IPARS simulator has been further developed to model the CO₂ sequestration process, by the addition of relevant petrophysical modules.

Understanding injected CO₂ redistribution behavior is critical for project success and long-term storage safety. Detailed studies are required to achieve these goals. CO₂ migration and potential leakage are important issues that we need to investigate before the project actually starts. After injection into the saline aquifer, CO₂ will migrate under the mechanism of capillary forces and buoyancy forces. Buoyancy forces will drive the CO₂ upward, due to the density difference between CO₂ and water. If there is a fracture or a high permeability channel in the seal, CO₂ might escape from the injection site and travel to other places through these paths. In some conditions, CO₂ could eventually reach the surface atmosphere. For CO₂ sequestration in oil and gas reservoirs with abandoned wells, CO₂ could leak out of a poorly sealed well. Leakage could happen quickly in a case with small well spacing, leading to project failure and wasted time and

money. During the CO₂ migration, pressure and temperature may change significantly, resulting in large changes in CO₂ properties, including density, viscosity, wettability, etc. In order to accurately predict storage potential and reduce the risk of the failure of CO₂ sequestration, it is necessary to research the behavior and movement of the injected CO₂ during injection and post-injection periods, including the moving front of the plume and the distribution of CO₂ in different forms, referred to as CO₂ inventory.

Rock-fluid properties modeling are critical for simulation studies of geological CO₂ sequestration. Rock-fluid property modeling includes most factors that affect flow, such as relative permeability, capillary pressure, wettability, interfacial tension (IFT), etc. These factors influence the behavior of the CO₂ plume in different ways during different regimes. During the CO₂ injection period, the viscous force is dominant for CO₂ migration. The trapping number and capillary desaturation curve will play a role for the evaluation of CO₂/water residual saturation, which in turn will affect the flow behavior. After CO₂ injection, CO₂ will migrate or be trapped by the interplay of capillary and buoyancy forces. If the buoyancy force is not large enough to overcome the capillary force, CO₂ will be trapped in its original place. This is secured sequestration. Otherwise, CO₂ will migrate upward and reach the top seal of the aquifer. During this process, a fraction of CO₂ will dissolve into brine and the rest will be left behind and trapped in the pore space by the brine. Hysteresis effects will come into play when imbibing water displaces injected CO₂. Hysteresis effects refer to the phenomena that both relative permeability curves and capillary pressure curves follow different paths during drainage and imbibition processes. Hysteresis effects can impact the flow in many aspects, especially in trapping CO₂, thus it is critical to model this phenomenon with the proper hysteresis model for simulation.

Due to challenges posed by the large-scale reservoir model and the difficulties of making accurate long-term prediction for the sequestration process, as well as the complexities of the process, such as phase behavior, hysteresis, heterogeneity, the potential geological leakage, etc., it is important to carry out critical research studies in this area. Because it is impossible to use the analytical solution to describe the real field problem of sequestration process, numerical simulations and pilot tests are effective ways to study CO₂ sequestration. By appropriate petrophysical modeling of the CO₂ sequestration process and incorporating accurate rock-fluid properties and fluid phase behavior models, reservoir simulation studies can provide insight into the sequestration process. This understanding is the ultimate goal of this research.

1.2 Literature Review

Many research works have been conducted on geological CO₂ sequestration. Simulation studies were carried out to determine the potential volume of CO₂ that can be stored in reservoir formations. Bachu (2000, 2002) described the steps that should be followed when selecting a potential sequestration site. Formation capacity, leakage and safety issues are discussed in the paper (Bachu, 2002; Bachu and Adams, 2003). Formation evaluations are also carried out by many studies (Hovorka *et al.* 2001; Bachu, 2000; House *et al.*, 2003), including Frio formation in the Texas Gulf Coast, a North Sea formation, the Sleipner project in the North Sea (Bickle *et al.* 2007), and the Weyburn field in Canada (Wilson *et al.*, 2004). Studies were conducted to estimate the impact of the sequestration project. Zhou *et al.* (2008) put forward a method for quick assessment of CO₂ storage capacity for closed and semi-closed formations. The reservoir pressure building up and storage efficiency factors are closely studied to estimate the formation

capacity. Doughty and Pruess (2003, 2004) did simulation studies for CO₂ sequestration in saline aquifers with the TOUGH2 simulator (Pruess *et al.* 1999; Doughty and Pruess, 2003), including the phase behavior modeling of water, NaCl, and CO₂. A simulation study of the pilot sequestration test was performed using the reservoir model of the Umbrella Point field and a Middle Frio well log (Doughty and Pruess, 2003). These research efforts deepened our understanding of sequestration.

One important issue related to geological CO₂ sequestration is the risk of leakage, such as leakage through faults and fractures, abandoned wells and open boundaries. The injected carbon dioxide has a density less than that of the aquifer brine, so it will migrate upward due to gravity-driven flow. Two ways CO₂ leakage can happen: 1) leakage may occur if there is a fault or open boundary in the formation. Especially if the cap rock has a dip angle, the free carbon dioxide phase will likely travel along the cap rock and; 2) if enough CO₂ is accumulated below the cap rock that overcomes the entry capillary pressure, CO₂ could penetrate the cap rock and get to upper layers (Saripalli and McGrail, 2002). Saripalli and McGrail (2002) found ~20 m thickness of CO₂ will cause leakage into caprock with 2 μm crevices. Pruess (2008) studied the leakage rate and found CO₂ leakage rate is significant only for shallow burial, where three phases (aquifer, liquid CO₂, and gaseous CO₂) are present. The deeper CO₂ is injected, the more barriers are presented for stopping leakage. Birkholzer (2008) did a sensitivity study on the large-scale impact of CO₂ storage in stratified systems. They devised an aquifer model from surface to a deep aquifer at 1000 m depth, and studied CO₂ injection and migration from the bottom layer. Their study shows the pressure response could be observed at a distance of more than 100 km away from the injection zone. The important discovery about this study is that CO₂ leakage to surface through multiple sequences of shale layers is

extremely unlikely. Hence, it is important to pick a favorable sequestration site with multiple shale layers.

During the CO₂ injection and storage process, many petrophysical and chemical phenomena may occur, such as multiphase flow, dissolution, and mineralization. The three major forms of CO₂ existing in geological formation are dissolved in formation water, trapped in pore space, and free/mobile phase. The mechanisms preventing CO₂ migration back to the surface include: 1) solubility trapping, where CO₂ is dissolved into the formation brine; 2) hydrodynamic trapping, where the carbon dioxide remains as a mobile phase but is prevented from moving upward by the impermeable formation cap rock; 3) capillary trapping, where CO₂ is trapped by the pore structure and exists as a residual gas phase; and 4) mineral trapping, where mineral precipitation results from reactions among rock minerals and CO₂. Each mechanism plays an important role in different periods of the sequestration. Bachu *et al.* (1994) studied hydrodynamic and mineral trapping of CO₂ in aquifers. Their study indicates that mineral trapping through the precipitation of carbonates could be one mechanism for long-term CO₂ sequestration. The research results show that mineral trapping is a very slow process, and a relatively small amount of CO₂ is trapped by this mechanism over short periods of time.

There are several methods for calculating CO₂ solubility in brine, including equations of state (EOS), Henry's law, and the activity coefficient model. Thermodynamic phase behavior of CO₂-H₂O systems has been extensively studied (Gallagher *et al.* 1992), because of its importance for many areas. Spycher and Pruess (2005) studied CO₂ solubility in brine at 12-100 °C and up to 600 bar, which extended the correlation presented by Spycher and Pruess (2003) to include the effect of salts in brine. They used the activity coefficient model from Duan and Sun (2003) for solubility

calculations. The activity formulation by Duan and Sun (2003) and Duan *et al.* (2006) is favorable because it was fitted over a wide P-T range, with temperatures ranging from 273 K to 533 K, pressures from 0 to 2000 bar, and iron strengths from 0 to 4.3 m. Their model matches experimental measurements well (Takenouchi and Kennedy, 1965). The Peng-Robinson equation of state (PREOS) (Peng and Robinson, 1976) is an effective way to model CO₂ solubility in brine. Ziabakhsh-Ganji and Kooi (2012) improved PREOS to calculate thermodynamic equilibrium of CO₂-brine mixtures containing impurities. PREOS gives an accurate estimation of the solubility (Valtz *et al.*, 2004; Ziabakhsh-Ganji and Kooi 2012). For our study, PREOS is used for CO₂-brine phase behavior modeling in compositional IPARS. Many other methods are proposed for modeling CO₂ solubility (Portier and Rochelle, 2005; Diamond and Akinfiev, 2003), which are mostly modified empirical correlations based on Henry's law. However, Henry's law has the limitation of application only to gas low solubility case (<0.03 mole fraction). Supercritical CO₂ densities were measured and recorded by Span and Wagner (1996) and also reported by Cabaço *et al.* (2010) and Bahadori *et al.* (2009). Ouyang (2011) put forward a new model for CO₂ density, which matched experimental results well (Bahadori *et al.* 2009).

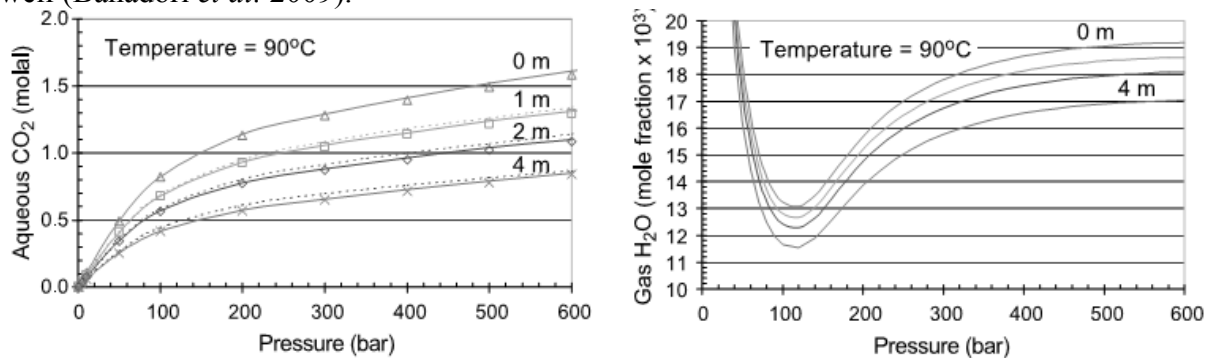


Figure 1.5 Predicted mutual solubility of CO₂ and H₂O (Spycher and Pruess 2005)

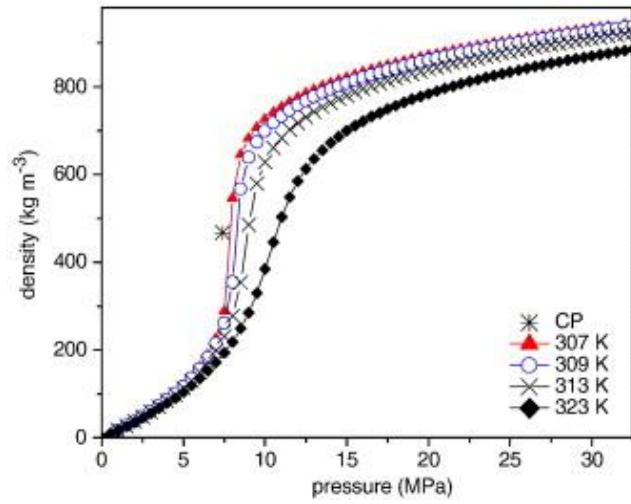


Figure 1.6 Evolution of the density of carbon dioxide with pressure at 307 K (▲), 309 K (○), 313 K (×) and 323 K (◆). The critical point (CP) is presented (ρ^*), ρ^* is 467.6 kg/m^{-3} . (Cabaço *et al.*, 2010)

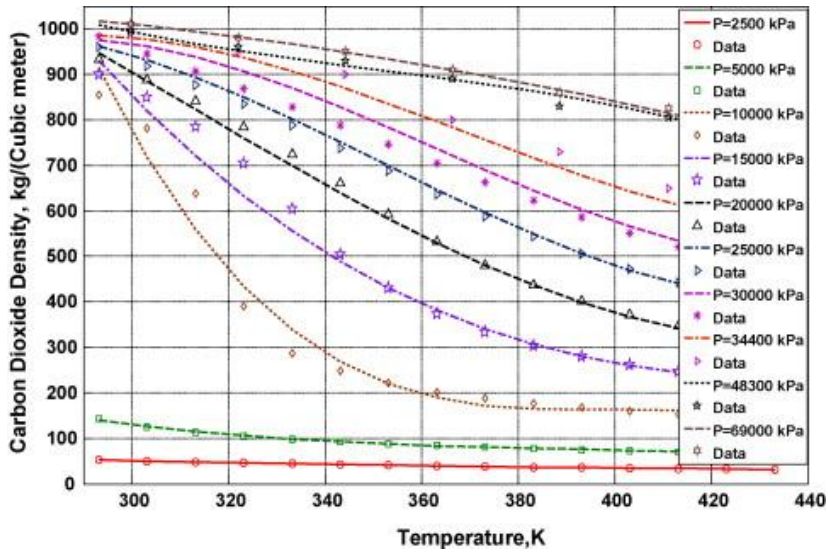


Figure 1.7 Density of carbon dioxide with temperature (Bahadori, 2009)

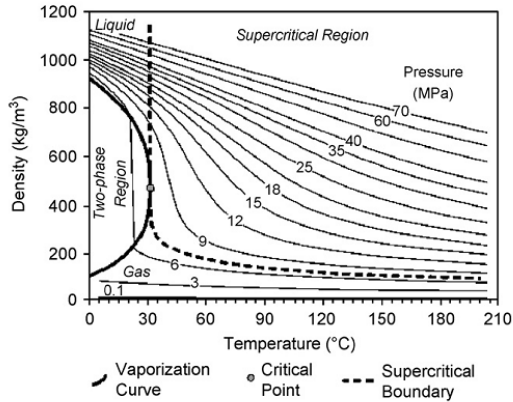


Figure 1.8 Density of carbon dioxide with temperature at different pressures (Bachu, 2003; 2008)

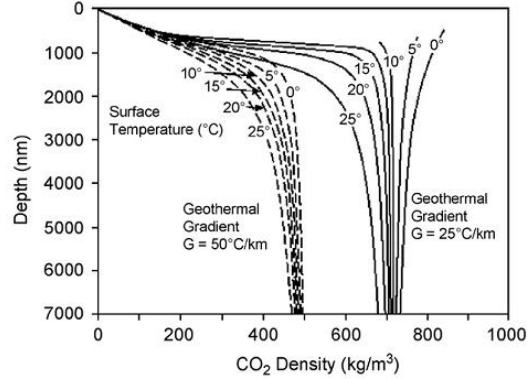


Figure 1.9 Density of carbon dioxide vs. depth with different geothermal gradient temperatures (Bachu, 2003; 2008)

The relative permeability model is critical for simulation studies of CO₂ injection and migration. Laboratory special core analysis (SCAL) could provide the relative permeability and capillary pressure curves for the reservoir rock. However, literature review shows limited experimental data are available for CO₂-brine systems (Bennion and Bachu, 2005, 2006a,b, 2007, 2008, 2010; Perrin *et al.* 2009). Bennion and Bachu (2005, 2006a,b) measured drainage and imbibition relative permeability curves and capillary pressure curves for different rock types, including sandstone and carbonate. Perrin *et al.* (2009) did experimental study on the impact of core-scale relative permeability on CO₂-brine displacements, using steady state measurement. The impact of heterogeneity was shown in the study. Their study found different flow rates will result in different fluid saturation distributions in the core. This might be due to different trapping and relative permeabilities at different Bond and capillary numbers.

Hysteresis is widely observed in laboratory coreflood studies (Bennion and Bachu, 2006b, 2010), which refers to the dependence of relative permeability and

capillary pressure curves on saturation and saturation history. Many studies have been conducted on hysteresis modeling (Altundas *et al.* 2011; Carlson 1981; Delshad *et al.* 2003; Doughty, 2007; Flett *et al.* 2004; Jerauld, 1990, 1997; Juanes *et al.* 2006; Land, 1968, 1971; Spiteri *et al.* 2008). Land (1968, 1971) pioneered the hysteresis modeling research by putting forward a method to calculate the trapping of non-wetting phase from initial saturation and Land's coefficient, which was the basis of many empirical models (Carlson, 1981; Killough 1976). Jerauld and Salter (1990) put forward a hysteresis model for character curves model based on pore-level modeling (Jerauld, 1990) and later Jerauld (1997) put forward a general three-phase hysteresis model. Lenhard and Parker (1987) developed a k-S model in two-phase and three-phase flow in porous media. The trapped amount of non-wetting phase is determined by interpolating the current non-wetting phase to maximum non-wetting phase residual saturation. Delshad *et al.* (2003) developed a hysteresis model for the mixed-wet reservoirs, which was validated by both simulation and experimentally in coreflood and sandpack experiments. Flett *et al.* (2004) used Land's model for calculating trapping and modeled the impact of trapping on relative permeability and capillary pressure curves using a modified Brooks-Corey equation and modified free gas saturation. Doughty (2007) developed a hysteresis model for multiple scanning curves and multiple turning points in TOUGH2. The simulation work showed hysteresis modeling is required for correct modeling of CO₂ sequestration processes (Doughty 2007). Spiteri *et al.* (2008) developed a new trapping model by curve-fitting using a quadratic relationship between the trapped non-wetting phase saturation and initial non-wetting phase saturation. Their model has two fitting parameters, and fits well for different contact angle scenarios after tuning for the proper parameters. Altundas *et al.* (2011) developed a self-consistent hysteresis relative

permeability and capillary pressure model, which is also based on Land's model for trapped non-wetting phase saturation. Their model is principally similar to that of Flett *et al.* (2004), except for the treatment of capillary pressure. A scaling factor was used for the capillary hysteresis, in which imbibition scanning curves are scaled from drainage capillary pressure curves (Altundas *et al.*, 2011).

Many studies have shown the interplay of viscous, capillary, and gravitational forces on CO₂ migration and trapping. Cinar *et al.* (2009) performed a quasi-2D experimental study of CO₂ injection to saline formations and verified the potential pore-scale instability of flow with unfavorable viscous and buoyancy condition (Bond number $\sim 10^{-3}$ and capillary number $\sim 10^{-4}$). Løvoll *et al.* (2004) conducted a pore scale study of the three forces competition in a random, heterogeneous 2D case, which showed a transition from capillary fingering behavior to a viscous fingering behavior. The thresholds of instability from experimental observation, simulation study, and analytical prediction using percolation theory agree well with each other (Løvoll *et al.*, 2004). Alkan *et al.* (2010) studied the combined effects of capillary pressure, salinity, and *in situ* thermodynamic conditions on CO₂-brine-rock interactions with 2D simulations in TOUGH2/ECO2N. Their study suggests CO₂ solubility will help CO₂ injectivity, and high capillary force will give a more uniform CO₂ plume, which enhances CO₂ dissolution and salting out (salt precipitation) (Alkan *et al.*, 2010). Ide *et al.* (2007) did a simulation study of the impact of viscous, capillary and gravitational forces on CO₂ trapping. Their study shows a great decrease in trapped CO₂ when Bond number increases and an increase in trapping when capillary pressure is high and aquifer is inclined. A scheme alternating water and gas is tested, which could enhance trapping (Ide *et al.*, 2007).

Published laboratory results show the impact of IFT on relative permeability and capillary pressure (Bennion and Bachu, 2006). Many studies (Bachu and Bennion, 2009a,b; Hebach *et al.*, 2002; Bennion and Bachu, 2008; Yang and Gu, 2004) have shown that IFT varies at different *in situ* reservoir conditions, such as pressure, temperature, and salinity. Reducing residual saturation by reducing IFT is a proposed method widely used in chemical enhanced oil recovery (EOR). Reducing IFT will decrease the capillary forces, which will in turn reduce the trapped amount of phase saturation. Hence it is critical to model the impact of IFT variation on trapping during sequestration projects. Pope *et al.* (2000) developed a comprehensive trapping model for gas condensate reservoirs, which defined the trapping number as the sum of the capillary number and the Bond number. The trapping model correlated IFT to residual saturation through capillary desaturation curves, with varied residuals at different trapping numbers. The characteristic curves are modeled based on the trapping model (Pope *et al.*, 2000). For capillary number and Bond number calculations, IFT modeling is important, while there are limited data available for supercritical CO₂ and brine. Several IFT correlations for supercritical CO₂-brine systems have been developed. The Macleod-Sugden correlation (Macleod, 1923; Sugden, 1924) is one of most widely used IFT models for reservoir fluids, which includes the density and mole fraction of each component in the IFT model. The advantage of the Macleod-Sugden correlation is that it considers more petrophysical properties than other models. Chalbaud developed an IFT model based on the CO₂-brine phase density difference (Chalbaud *et al.*, 2006). The IFT curve will have a plateau when the density difference between the gas and water phases is less than 0.6 *g/ml*, while the IFT will increase with a slope greater than 4 *mN/m per g/ml*, when the density difference is greater than 0.6 *g/ml* (Chalbaud *et al.*, 2006, 2010). Bennion

and Bachu (2008) modeled IFT as a function of pressure, temperature, salinity, and CO₂ mole fractions. The IFT will increase with increasing temperature and salinity, and decrease with increasing pressure (Bennion and Bachu, 2008; Bachu and Bennion, 2009a,b). Because capillary trapping is critical for long-term CO₂ sequestration, it is necessary to model the IFT effect carefully. Four IFT models were implemented in IPARS based on the above publications.

The wettability of reservoir rock may be affected with CO₂ injection, which will impact fluid contact angle and displacement characteristics. Wettability will also affect relative permeability and capillary pressure (Heiba, 1983). Blunt (1997) has developed a pore-scale model for wettability alternation. Chiquet *et al.* (2005) measured the change of advancing and receding contact angles during CO₂ injection for shale. In the study, the contact angle could vary from ~60 to ~160 degrees depending on salinity and displacing direction. For seals with entry capillary pressures that are not high enough, the change in entry capillary pressure from contact angle could result in CO₂ leakage. Cinar *et al.* (2007) studied the effect of IFT and wettability variation on three-phase relative permeability using experiments, which showed that oil-/gas-phase relative permeability increased with decreased IFT, while the water phase was less affected. Chalbaud *et al.* (2007) measured drainage K_r and P_c for a carbonate core under different wettability conditions. The capillary pressure decreases from strong water wet (WW) to intermediate wet (IW). The relative permeability of the wetting phase of strongly water wet is lower than the intermediate case (Chalbaud *et al.*, 2007). Zhu *et al.* (2011) investigated reservoir rock wettability alternation by the CO₂-brine-rock interactions, which show contact angle varied with temperature and pressure.

Accurate prediction of CO₂ migration is impossible without accurate viscosity calculation for CO₂. Over the years, numerous viscosity models have been developed for reservoir fluids at different pressure/temperature conditions (Jossi *et al.*, 1961; Lohrenz, *et al.*, 1964; Oakes and White, 1987; Lansangan *et al.*, 1993; Yener *et al.*, 1997; Tuan *et al.*, 1999). Many measurements were made for supercritical CO₂ and water (Vesovic *et al.*, 1990; Fenghour *et al.*, 1998; Kestin *et al.*, 1984). Several viscosity models were developed for reservoir fluids including CO₂. The Lohrenz-Bray-Clark (LBC) method is the most widely used viscosity model for reservoir fluids over a wide range of pressure and temperatures (Lohrenz *et al.*, 1964). The method correlates viscosity to the reduced phase density, using a method developed by Jossi *et al.* (1961) for pure components. The LBC correlation accounts for physical factors when modeling viscosity and it has proven its effectiveness as an industry-wide standard. Lansangan *et al.* (1993) completed a comprehensive literature review and put forward an improved viscosity model based on the LBC method. LBC correlation is also implemented in IPARS and used in this study.

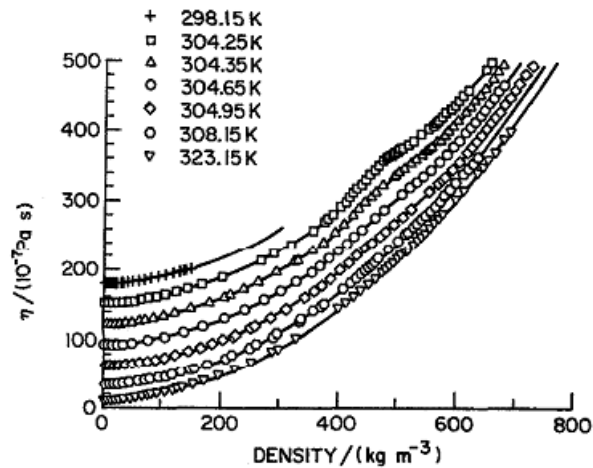


Figure 1.10 Viscosity of carbon dioxide with density at different temperatures. (Vesovic *et al.*, 1990)

Sequestration of CO₂ in aquifers is impacted by many factors, such as phase behavior, dissolution, fluid viscosity, relative permeability, wettability, and geochemical reactions, among others. The injected CO₂ can be trapped through many different mechanisms. However, these phenomena are not fully understood, and they require further study. The long-term impact of CO₂ sequestration in underground reservoirs is another issue that deserves full consideration.

1.3 Dissertation Layout

The chapters of this dissertation are presented as follows. Chapter 2 gives an overview and description of the IPARS simulator, including its current implementations and capabilities. The black oil and compositional models in IPARS are also addressed. Chapter 3 describes the phase behavior and petrophysical modeling enhancements for the CO₂ module in IPARS. Most enhancements were implemented in compositional IPARSv3.1, focusing on modeling relative permeability, capillary pressure, IFT, etc. The implementation and motivation behind these models are discussed in detail, providing a comprehensively detailed picture of the CO₂ module in IPARS.

Chapters 4 and 5 provide validations and tests of the newly implemented models. In Chapter 4, validation tests are presented with a newly developed coreflood model. A coreflood simulation history-matching experimental result is discussed, including a new method for generating heterogeneous core data. Chapter 5 describes large-scale, parallel simulation and sensitivity simulation studies for CO₂ sequestration. Large reservoir models are created and studied, including a stacked geological model. Extensive sensitivity tests are presented for testing the newly implemented petrophysical models.

Chapter 6 discusses the Cranfield CO₂ sequestration pilot test, a field CO₂ sequestration case simulation with IPARS. A simulation model based on the Cranfield pilot test is configured in IPARS, by importing the field geological, petrophysical, and well data. History matching studies were done and reasonable accuracies were achieved for the early period of injection. Sensitivity tests were conducted to study the impact of different petrophysical model for CO₂ injection and migration in the field case.

Chapter 7 provides a summary and conclusions for this research, and points out several potential research areas. Appendices describe additional works that were conducted, including the implementation of different solvers in the UTCHEM simulator, compositional phase behavior, new keywords for the IPARS simulator, examples of input files for CO₂ sequestration models on IPARS, and some benchmark tests for IPARS.

CHAPTER 2: IPARS Review

This chapter gives an overview of the functionalities and different modules in IPARS. In this chapter, the compositional module in IPARSv3.1 for three-phase water, oil, and gas flow is discussed in detail. Formulations and computational modeling are presented.

2.1 IPARS Overview

The Integrated Parallel Accurate Reservoir Simulator (IPARS) is an in-house parallel reservoir simulator developed by the Center for Subsurface Modeling at The University of Texas at Austin. IPARS provides an expandable framework and a growing number of physical models suitable for research studies and practical applications (Lu, *et al.*, 2002) in multiphase and multiphysics reservoir simulation. The simulator is based on Linux and is developed using FORTRAN and C programming language. It can run on both single processor computer and parallel clusters, with parallelization accomplished with the Message Passing Interface (MPI) and OpenMP. It can solve numerical problems on the order of millions of elements using up to thousands of processors. IPARS can also model fluid flow in porous media on both core and field scales (Delshad *et al.*, 2010, 2011, 2013; Kong *et al.*, 2013a,b; Lu *et al.*, 2007; Tavakoli *et al.*, 2012; Thomas *et al.*, 2008).



Figure 2.1 A schematic of IPARS models

2.1.1 FLUID MODELING

There are numerous physical models in IPARS (Gai *et al.*, 2003; Yuan *et al.*, 2010), including a black oil model, a hydro model, a compositional model, a thermal model, transport chemistry, geomechanics, etc. Some models may be coupled in multiple ways (in some cases more than 50) to better study the targeted problem, such as compositional and thermal, etc.

2.1.2 GRIDGING AND DISCRETIZATION

The simulator employs advanced techniques for discretization and gridding, including mixed finite element, discontinuous Galerkin method, finite volume method, non-matching grid, and local grid refinement with enhanced velocity method (Pencheva *et al.*, 2003, 2008; Wheeler *et al.*, 1999, 2002). Iterative coupling numerical schemes and implicit/explicit time-stepping are also available in IPARS.

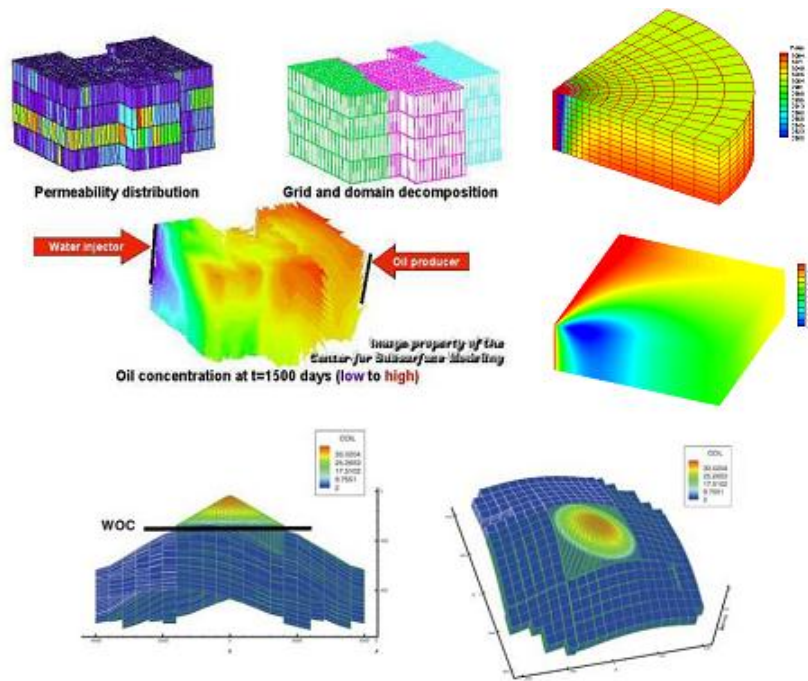


Figure 2.2 IPARS gridding and reservoir modeling

Discretization techniques available are

- Cell-centered finite difference (black oil, oil/water, air/water models)
- Discontinuous Galerkin (two-phase IMPES model)
- Galerkin FEM (poroelastic model)
- Multipoint flux MFE (single phase implicit model/two phase iterative coupled with fractures)
- Mortar finite element

2.1.3 SOLVERS

Solving the Jacobian matrix equation of the discretized governing equations is the most costly part of reservoir simulation, in terms of CPU usage, and it is critical to have efficient solvers for this task. There are multiple preconditioners and non-linear solvers

implemented in IPARS, such as BCGS, AMG, and GMRES. IPARS has a growing number of solvers for different problems (Stueben *et al.*, 2007), and it allows for user input to optimize preconditioner and solver selection according to the specific conditions of a given problem.

2.1.4 POST-PROCESSING AND VISUALIZATION

One important issue with reservoir simulation is the analysis of simulation results both during and after model execution. During simulation, IPARS will output data both visually on screen and on a hard drive. Users can process data with appropriate formatting to plot history curves and 3D map visualizations. IPARS provides many software packages for post-processing and results visualization, as well. IPARS currently supports visualization software packages Tecplot and Paraview by outputting simulation results in the appropriate format onto a computer hard drive. Visualization with these software packages is easily accomplished.

2.2 IPARS Compositional Model

The compositional model in IPARSv3.1 can handle three-phase (aqueous, non-aqueous liquid and non-aqueous vapor) fluid flow problems using compositional formulations with both aqueous and non-aqueous components (Thomas *et al.*, 2012; Wang *et al.*, 1999). The aqueous component is only in the water phase and is not included in the two phase flash calculation. Only the non-aqueous components from user input are included in the two-phase flash calculation, which forms the non-aqueous phases. The Peng-Robinson equation of state (PREOS) (Peng and Robinson, 1976) with volumetric shift parameters and binary interaction parameters (BIP) is used to calculate

fluid densities and phase composition x_{ic}^α . Phase viscosities are calculated using the Lohrenz-Bray-Clark correlation, which will be discussed in detail in section 2.2.4.

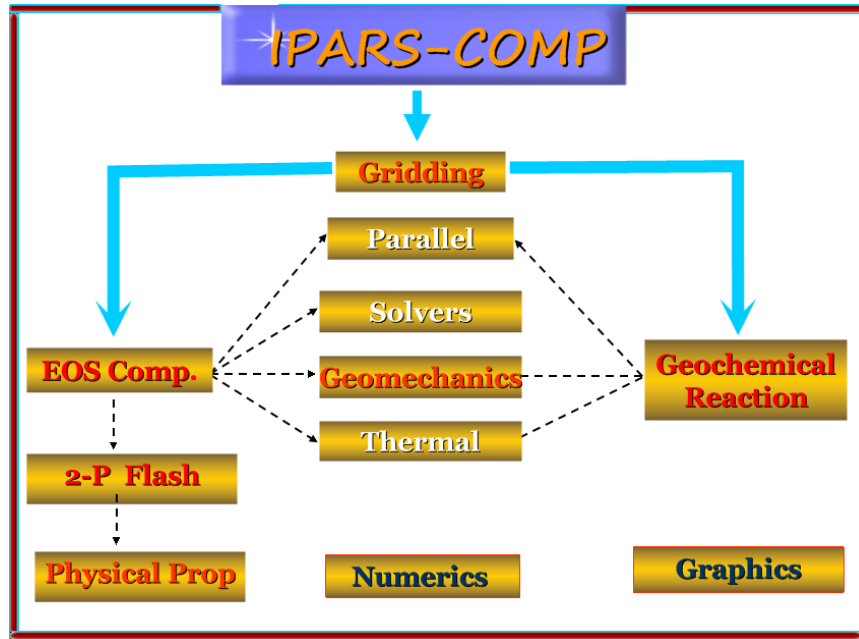


Figure 2.3 Compositional modules in IPARSv3.1

2.2.1 EQUATIONS FOR COMPOSITIONAL FLUID FLOW

For compositional flow, the primary unknown is the component mass in each location. Conservation of mass is the governing law for compositional flow. For a flow system, there can be N_p phases and N_c components. For each component ic , a partial differential equation can be constructed based on continuum and mass conservation.

Partial differential equations representing component mass balances are:

$$\frac{\partial}{\partial t} [\phi N_{ic}] = - \sum_{\alpha} \nabla \cdot x_{ic}^{\alpha} \rho_{\alpha} \vec{U}_{\alpha} + q_{ic}, i c = 1, 2, \dots, N_c. \quad (2.1)$$

The velocity of phase a is given by

$$\vec{U}_\alpha = -\frac{\vec{k}k_{r\alpha}}{\mu_\alpha}(\vec{\nabla}P_\alpha - \gamma_\alpha\vec{\nabla}D), \alpha = 1, 2, \dots, N_p. \quad (2.2)$$

Phase pressures are defined by

$$P_\alpha = P + P_{c\alpha}. \quad (2.3)$$

in which, $P_{c\alpha}$ is the capillary pressure and P is the reference phase pressure (α is phase label). The same reference phase pressure is used for flow, well, and flash calculations. In IPARS CO₂ sequestration simulation, the default reference phase is the water phase, so we choose water phase pressure as reference pressure for this study.

The saturation constraint is applied as:

$$\sum_\alpha S_\alpha = 1. \quad (2.4)$$

Porosity is a function of rock compressibility c_r and pressure and is calculated by

$$\phi = \phi_0[1 + c_r(P - P_{ref})], \quad (2.5)$$

in which ϕ_0 and c_r are measured parameters that vary with rock type and location. P_{ref} is the reference pressure at measurement condition. In each time step, it is updated immediately after the pressure matrix equation is solved.

2.2.2 EQUATIONS FOR MOLAR VOLUMES AND SATURATIONS

The molar volume and saturation of each phase is a function of pressure and temperature. The molar volume for the aqueous phase has the form

$$v_w = v_w^{ref} B_w^0 / [1 + c_w(P - P^0)], \quad (2.6)$$

where v_w^{ref} is the water molar volume at the surface and B_w^0 is the formation volume factor at pressure P^0 and reservoir temperature. Here c_w is water compressibility constant. The parameters P^0 , c_w , and B_w^0 are constants.

The molar volumes ($v_\alpha = 1/\rho_\alpha$) of the non-aqueous phases ($\alpha = 2, 3$) are given by

$$v_\alpha = RTZ_\alpha/P, \quad (2.7)$$

where Z_α is the Z-factor for phase α , R is idea gas constant, T is temperature, P is pressure.

The molar volume of each hydrocarbon phase is determined from flash calculation and phase equilibrium. Fugacity of each phase can be calculated from Z-factors. The fugacity of each component in vapor phase is equal to liquid phase fugacity,

$$f_{ic}^v = f_{ic}^l \quad (2.8)$$

Phase equilibrium at constant temperature and pressure also requires that the Gibbs free energy be a minimum. A detailed description of the flash calculation and phase behavior modeling can be found in Appendix A.

The saturations are then calculated from the mass and molar volume, as follows:

$$S_w = v_w N_w \quad (2.9)$$

$$S_l = (1 - v)v_l \sum_{ic=2}^{n_c} N_{ic} \quad (2.10)$$

$$S_v = vv_v \sum_{ic=2}^{n_c} N_{ic}, \quad (2.11)$$

where v is the vapor fraction, v_w is water molar density, v_l is molar density of non-aqueous liquid phase l , v_v is molar density of non-aqueous vapor phase, S_l is

saturation of non-aqueous liquid phase, S_v is saturation of non-aqueous vapor, N_w is water concentration per unit pore volume, N_{ic} is concentration of component ic per unit pore volume.

We solve the mass conservation equation for the compositional concentration of each component. Then saturation is calculated from the mass and phase molar volumes. The saturations calculated above may not exactly sum to one due to the numerical volume convergence error. To minimize the error, a saturation constraint of the summation equal to one is employed

$$\sum_{\alpha} S_{\alpha} = 1. \quad (2.12)$$

2.2.3 WELL MODEL

Accuracy in well modeling is crucial in reservoir simulations. In engineering projects, wells are the only means of producing an oil field and otherwise influencing reservoir performance. In reservoir simulation, well/reservoir interaction relates bottom-hole conditions in the wellbore to conditions in grid elements that the wellbore penetrates. A proper well model should be adapted to accurately represent the interactions between the well and the reservoir. IPARS uses the well-known Peaceman well model (Peaceman, 1983) for coupling the well and the reservoir in simulation.

If we assume radial flow around the well, and the pressure is P_e at radius r_e , and P_{wf} at wellbore r_w , the radial flow around the well can be described by

$$Q = -\frac{2\pi kh r_w}{\mu} \left. \frac{\partial p}{\partial r} \right|_{r=r_w}. \quad (2.13)$$

The well rate can be calculated using integration by parts, as follows:

$$Q = -\frac{2\pi Kh}{\mu \ln\left(\frac{r_e}{r_w}\right)}(P_e - P_{wf}). \quad (2.14)$$

Here Q is the well rate at the reservoir condition, K is permeability, h is the length of the well that is open to flow, r_w is the well radius, r_e is an equivalent well radius, μ is fluid viscosity, P_{wf} is the well flowing bottomhole pressure, and P_e is the pressure in a well grid element.

The well index can be defined as

$$WI = \frac{2\pi Kh}{\mu \ln\left(\frac{r_e}{r_w}\right)} \quad (2.15)$$

The well rate is calculated readily as

$$Q = WI(P_e - P_{wf}). \quad (2.16)$$

The Peaceman model is defined as

$$r_e = 0.28 \frac{\{(K_y/K_x)^{1/2}(\Delta x)^2 + (K_x/K_y)^{1/2}(\Delta y)^2\}^{1/2}}{(K_y/K_x)^{1/4} + (K_x/K_y)^{1/4}} \quad (2.17)$$

for anisotropic permeability K_x and K_y .

For the special case with homogeneous isotropic permeability in x, y directions ($K_x = K_y$), the equivalent well radius is

$$r_e = 0.14[(\Delta x)^2 + (\Delta y)^2]^{1/2}. \quad (2.18)$$

In the IPARS formulation, the well rate of each fluid phase in each perforated well element is calculated using the pressure condition in each location. Production rates are defined to be negative in the simulator.

The basic flow equation for a given fluid phase f in a well grid element i is given by

$$Q_{f,i} = \frac{G_i L_i K_i k_{f,i}}{\mu_{f,i}} (P_{WB,i} - P_{f,i}) . \quad (2.19)$$

where L_i is length of the open wellbore penetrating element i , K_i is permeability, $k_{f,i}$ is relative permeability of phase f in element i , $\mu_{f,i}$ is viscosity of phase f in element i , and $P_{WB,i}$ is corresponding wellbore fluid pressure in element i . The dimensionless geometry factor G_i is calculated as

$$G_i = 2\pi / \left[\ln \left(\frac{r_{e,i}}{r_{w,i}} \right) + S_i \right] . \quad (2.20)$$

where S_i is skin factor in element i (IPARS allows skin input for each element).

Total well rate is given by the summation of the flow rate in each perforation, as follows:

$$Q_f = \sum_i Q_{f,i} . \quad (2.21)$$

The formulations above define the complete well-reservoir coupling method in IPARS. Given a proper well constraint, these well equations together with the reservoir flow equations can be solved simultaneously by Newtonian iteration using either implicit or semi-implicit methods. The well rate or well bottomhole pressure could be specified for each well as its constraint. For production wells, there is one degree of freedom that the user can specify. For injection wells, the number of degrees of freedom is equal to the number of phases injected. For example, the user can specify production/injection well bottomhole pressure, total rate, or phase rates in IPARS.

2.2.4 VISCOSITY MODEL

IPARS uses the Lohrenz-Bray-Clark correlation to calculate viscosities of each phase based on its composition (Lohrenz *et al.*, 1964). Critical pressure P_c , critical temperature T_c , molecule weight M , and critical Z factor Z_c of each component are needed for calculation.

For the pure component phase, viscosity μ^* is calculated as

$$\mu^* = 34.0 \times 10^{-5} T_R^{0.94} / \xi \quad \text{for } T_r \leq 1.50, \quad (2.22)$$

$$\mu^* = 17.78 \times 10^{-5} [4.58 T_R - 1.67]^{5/8} / \xi \quad \text{for } T_r > 1.50, \quad (2.23)$$

in which, the viscosity parameter ξ of pure phase is

$$\xi = 5.44 \times T_c^{1/6} / (M \times P_c^{2/3}), \quad (2.24)$$

and T_r is the reduced temperature as

$$T_r = \frac{T}{T_c} \quad (2.25)$$

The SI units are used in the above equations.

For low pressure mixture, mixture viscosity μ_{mix}^* is calculated as

$$\mu_{mix}^* = \frac{\sum_{j=1}^n x_j \mu_j^*}{\sum_{j=1}^n x_j M_j^{1/2}}, \quad (2.26)$$

in which, x_j is the mole fraction of component j . M_j is the molecular weight and μ_j is the viscosity of component j .

For high pressure mixture, mixture viscosity parameter is calculated from pseudo properties,

$$\xi_{mix} = 5.44 \times T_{c,mix}^{1/6} / (M_{mix}^{1/2} \times P_{c,mix}^{2/3}), \quad (2.27)$$

in which

$$T_{c,mix} = \sum_{j=1}^n x_j T_{cj} \quad (2.28)$$

$$M_{mix} = \sum_{j=1}^n x_j M_j \quad (2.29)$$

$$P_{c,mix} = \sum_{j=1}^n x_j P_{cj} \quad (2.30)$$

Here, $T_{c,j}, P_{c,j}$ are critical properties of component, $T_{c,mix}, M_{mix}, P_{c,mix}$ are pseudo properties of mixture.

The mixture reduced molar density (ρ_r) is calculated from mixture density ρ , as follow

$$\rho_r = \frac{\rho}{\rho_{c,mix}} \quad (2.31)$$

$$\rho_{c,mix} = \frac{1}{\sum_{j=1}^n x_j V_{cj}} \quad (2.32)$$

here $V_{cj} = 1/\rho_{cj}$ is the critical molar volume of component j .

The high pressure fluid viscosity μ is calculated by applying the Jossi-Stiel-Thodos correlation as (Jossi *et al.*, 1962),

$$\left[(\mu - \mu_{mix}^*) \xi_{mix} + 10^{-4} \right]^{1/4} = 0.1023 + 0.023364 \rho_r \quad \text{for } \rho_r > 0.18 \quad (2.33)$$

$$+ 0.058533 \rho_r^2 - 0.40758 \rho_r^3 + 0.0093324 \rho_r^4$$

$$(\mu - \mu_{mix}^*) \xi_{mix} = 2.05 \times 10^{-4} \rho_r \quad \text{for } \rho_r > 0.18 \quad (2.34)$$

2.3 CO₂ Module in IPARS

Simulator IPARS is capable to perform reservoir simulation study for CO₂ sequestration in saline aquifers (Class *et al.*, 2009). The simulation results were successfully benchmarked to other simulators (Class *et al.*, 2009). Further developments were conducted based on benchmarked model of the simulator IPARS. Recently, a module for CO₂ sequestration was implemented (Delshad *et al.*, 2009, 2010, 2011, 2013; Kong *et al.*, 2013a,b) that includes petrophysical modeling for CO₂-brine systems. Integrated modeling of capillary, viscous, and gravitational forces on CO₂ sequestration is studied. The hysteresis effect on relative permeability and capillary pressure is also modeled using Land's equation (Land, 1968). The CO₂-water mutual dissolution is calculated using the Peng-Robinson equation of state (Peng and Robinson, 1976).

The CO₂ module in IPARSv3.1 is based on non-isothermal compositional EOS coupled with geochemical reactions (Thomas, 2009; Delshad *et al.*, 2009). An iteratively coupled, implicit-pressure, explicit-concentrations scheme is applied to solve the flow and concentration equations, which is then sequentially coupled to a time-split method for solving both the temperature energy balance and the explicit ODE numerical integration method for chemical reactions. The Peng-Robinson cubic equation of state

(PREOS) is used for phase equilibrium calculation of the binary system of CO₂ and water. The phase equilibrium varies as a function of pressure and temperature and a flash algorithm is used to determine the mole fractions of CO₂ and water in two equilibrium phases.

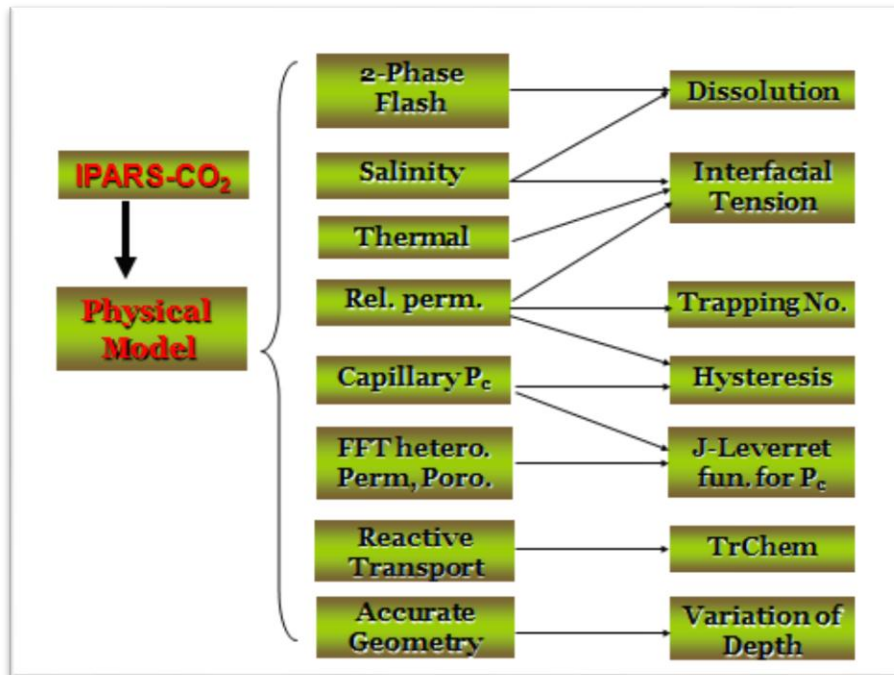


Figure 2.4 CO₂ petrophysical modules in compositional IPARSv3.1

We made numerous improvements to IPARSv3.1 for fluid property calculations of CO₂ and brine flow. We first implemented a new aqueous phase component to model the brine salinity expressed as total dissolved solids (TDS). The EOS variables of binary interaction coefficients and volume shift parameters were then modified according to the salt concentration in the water phase and temperature using published correlations

(Kumar, 2004; Kumar *et al.*, 2005). These correlations proved to give more accurate CO₂ solubility in brine and phase density.

Several correlations for interfacial tension between water and supercritical CO₂ were then implemented that account for pressure, temperature, and brine salinity. Once the interfacial tension is calculated, the next step is to determine the dimensionless trapping number. The residual saturations of CO₂ and water are then calculated, based on the trapping number. The endpoints are scaled, as well, with the change in the residual saturations. Relative permeability and capillary pressure curves are subsequently scaled as a function of trapping number because of the reduction in the residual phase saturations.

The CO₂ module in IPARSv3.1 handles the switch of flow direction between drainage (reduction in water saturation) and imbibition (increase in water saturation) by modeling the hysteresis effect for capillary pressure and relative permeability. We define CO₂ displacing brine as the drainage process, and water invading the pore space as the imbibition process. With the hysteresis model, the saturation path is different for drainage and for imbibition. There will be trapping of CO₂ in the pore space as a non-wetting phase during the imbibition process. The hysteresis trapping model is using Land's equation (Land, 1968) as a basis, which calculates the trapped amount of non-wetting phase as a function of saturation and saturation history.

Other functionalities of the CO₂ module include coupling with the other existing modules, such as the thermal module, Trchem module, and improved gridding for reservoir geometry. This newly developed CO₂ module is an effective tool for CO₂ sequestration studies.

CHAPTER 3: Phase Behavior and Physical Property Enhancements

This chapter discusses petrophysical model enhancements to IPARS. In section 3.1, CO₂-water phase behavior is discussed. In section 3.2, the interfacial tension (IFT) modeling of CO₂-water is presented, including four IFT models. In Section 3.3, the concept of trapping number is introduced and explained in detail. In addition, a trapping model is developed based on trapping number. In Section 3.4, the impact of trapping number on relative permeability and capillary pressure is discussed. In Section 3.5, the hysteresis model is discussed. Hysteresis modeling is very important, because it is impossible to accurately predict CO₂ trapping without properly modeling the effect of saturation direction and history.

3.1 CO₂ Phase Behavior

For CO₂ sequestration in saline aquifers, CO₂ and water will undergo complex petrophysical and geochemical processes. Thermodynamic phase behavior will affect the CO₂ trapping in different ways, including dissolution, capillary trapping, mineralization, etc. Accurate modeling of fluid phase behavior is essential for planning sequestration projects and making predictions. The phase behavior model is necessary to describe the CO₂-brine interactions, mutual solubility, and other fluid properties.

Carbon dioxide is in a gaseous phase under atmospheric and surface conditions. The CO₂ density is ~1.98 Kg/m³, which is about 1.5 times heavier than that of air under standard conditions. However, for CO₂ sequestration, as CO₂ being injected to underground formations under high pressure, it could be in a liquid phase, or supercritical fluid. Phase P-T diagram is used to describe the phase behavior of CO₂ with pressure and temperature. There are also triple and critical points for pure CO₂ on the P-T diagram.

The triple point of a substance refers to the specific temperature and pressure at which all three phases can exist together at equilibrium. The critical point on a P-T diagram is used to describe the point of pressure and temperature above which fluid will be a supercritical fluid. For a supercritical fluid, there is not a clear distinction between liquid and vapor phases, which means that the phase difference disappears at this P-T point. A supercritical fluid will have density properties like liquid and viscosity properties like gas. For supercritical CO₂ in deep aquifers, CO₂ will exist as a phase separated from water. Hence there are two fluid phases for the system of interest.

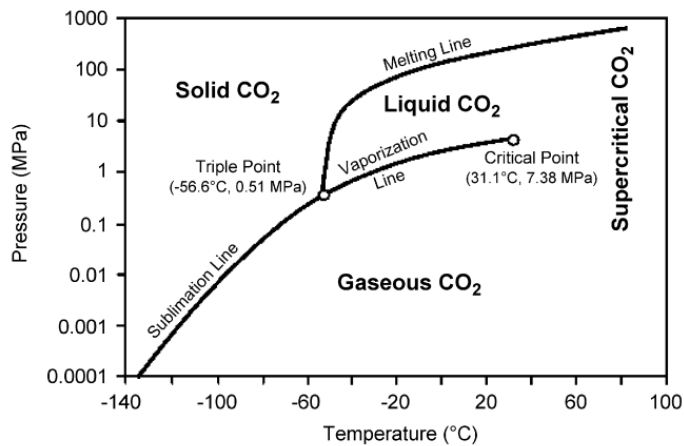


Figure 3.1 Carbon dioxide phase diagram (Bachu, 2008)

During the CO₂ migration after injection, it is possible for CO₂ to undergo a large pressure variation, which will greatly affect its phase behavior. If CO₂ migrates to a depth with a pressure/temperature condition lower than the critical point (Figure 3.1), CO₂ can change from a supercritical fluid to either a liquid phase or a gaseous phase, which will impact the fluid properties. Equation of State (EOS) and flash calculation are used to model the phase equilibrium for all kinds of fluid mixtures at given pressures and

temperatures. For EOS, such as Peng-Robinson EOS in IPARS, several inputs are needed for each component, including critical pressure, critical temperature, etc. The general properties for carbon dioxide and water are listed in Table 3.1. Some of the input parameters, such as critical pressure and temperature are measured values for each component, while some parameters are tuning parameters, such as volume shift parameters and binary interaction parameters. For compositional simulation with EOS, these tuning parameters need to be finely tuned to match the measured fluid properties, such as observed mixture composition and density, for the *in situ* pressure and temperature conditions. The input values of parachor are needed for the IFT calculation with the MacLeod-Sugden correlation.

Table 3.1 General properties for carbon dioxide and water (Ozah *et al.*, 2005)

	Carbon dioxide	Water
Critical Pressure (atm)	72.809	217.755
Critical Temperature (K)	304.128	647.094
Critical Vol. (m ³ /k-mole)	0.094	0.056
Molecular Wt. (g/g-mole)	44.010	18.015
Acentric Factor	0.224	0.344
Parachor	78	52

In the IPARS compositional simulator, there are a maximum of three fluid phases (water, oil, and gas). The phase equilibrium and flash calculations are only performed for the oil and gas phases. The water phase is excluded from the flash calculation. In order to allow CO₂ to interact and dissolve into the water phase, we need to modify the simulator to model the oil phase in the simulator as a fluid phase with water properties. By making

this replacement, the H₂O/CO₂ system is treated as ‘hydrocarbon’ components in the oil phase. The properties of the 'oil' phase containing H₂O and CO₂ are given by a flash calculation using the equation of state (EOS). The volume shift parameters (VSP) are used to obtain an accurate phase density by correcting the molar volumes of each component in the mixture. Binary interaction coefficients (BIC) are used in the flash calculations to obtain the composition of both the liquid and vapor phases. These parameters will be used as finely tuned inputs for the simulation to account for the reservoir condition. Kumar (2004) developed correlations of VSP and BIC to account for the effect of temperature and salinity. The parameter T is the temperature in Fahrenheit and S is the salinity in ppm of NaCl in the reservoir.

The volume shift of CO₂ is a constant value: 0.024668. However, for H₂O,

$$VSP_{H_2O} = 0.179 + (2.2222 \times 10^{-4} \times (T - 113)) + 4.9867 \times 10^{-7} \times S, \quad (3.1)$$

A correlation was developed by Kumar (2004) for the H₂O-CO₂ binary interaction coefficient as a function of temperature and salinity:

$$BIC_{H_2O-CO_2} = -0.093625 + (4.861 \times 10^{-4} \times (T - 113)) + (2.29 \times 10^{-7} \times S), \quad (3.2)$$

where $BIC_{H_2O-CO_2}$ is the binary interaction coefficient for the H₂O-CO₂ pair.

The solubility of CO₂ in brine decreases as salinity increase, and it increases as pressure increases. After phase equilibrium calculation, the CO₂ phase viscosity is then calculated using the Lohrenz-Bray-Clark method (Lohrenz *et al.*, 1964) in IPARS, as discussed in Chapter 2.

3.2 Interfacial Tension Correlations

The interfacial tension (IFT) is critical for CO₂ trapping in pore space of reservoir rocks, because it will affect the capillary forces, which will in turn determine the capillary trapping and efficiency of phase displacement. The capillary pressure is reduced by lowering IFT between wetting and non-wetting phases, which will reduce trapping of CO₂ as the residual gas saturation in pore spaces. Many studies (Hebach, *et al.*, 2002; Yang and Gu, 2004; Bennion and Bachu, 2008a) have shown that IFT for a CO₂-brine system is a function of reservoir conditions, such as pressure, temperature, water salinity, and dissolved amount of CO₂ in brine. Reducing the residual oil saturation by reducing the IFT is one primary mechanism of chemical EOR and miscible CO₂ EOR in practice. For CO₂ sequestration processes, IFT will vary with *in situ* conditions and the injection process. The IFT will increase with increasing temperature and salinity, and decrease with increasing pressure. This IFT variation will affect the capillary forces and in turn affect trapping of CO₂ as residual saturation. Because the capillary trapping is critical for long-term CO₂ storage, it is necessary to model the IFT effect properly. We implemented a total of four IFT models in IPARS based on previous publications and correlations developed by Bennion, Macleod-Sugden, and Chalbaud.

3.2.1 IFT AS A FUNCTION OF PRESSURE, TEMPERATURE, SALINITY

Extensive measurements of CO₂-water interfacial tension under supercritical conditions have been conducted (Bennion and Bachu, 2008a; Bachu and Bennion, 2009a). Based on their findings, an IFT correlation based on pressure, temperature, and salinity was developed:

$$\sigma = 71.69243P^{-0.432639} + 0.210058T^{0.900261} + 0.075859S^{1.457937}, \quad (3.3)$$

where σ is the interfacial tension between CO₂ and brine in mN/m, P is pressure in kPa – abs, T is temperature in °C, and S is brine salinity in wt% in aqueous solution.

The comparison of the measured data with the correlation is given in Figure 3.2.

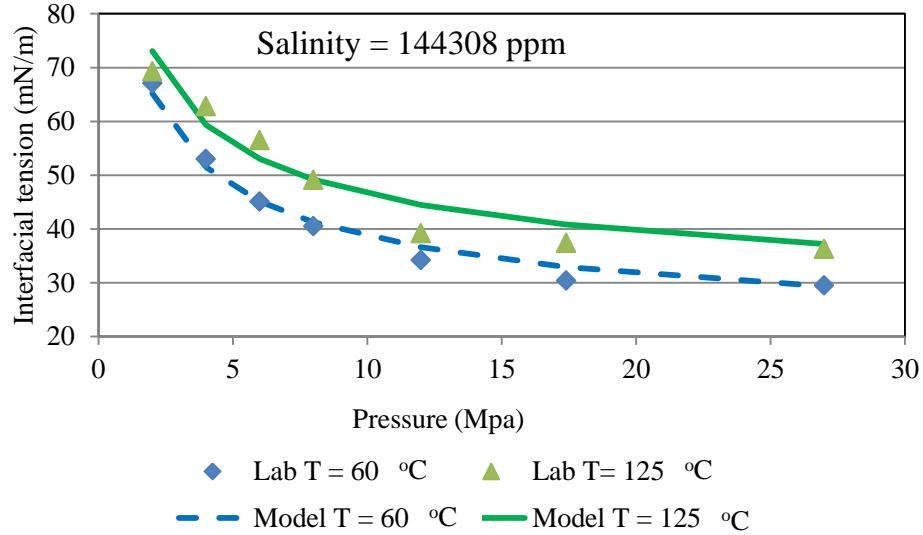


Figure 3.2 IFT vs. Pressure, model fit of Bennion's correlation for different temperatures.

Salinity has a major effect on CO₂-water properties, and it can be measured in the laboratory:

$$S = \frac{\text{mass NaCl}}{\text{mass NaCl} + \text{mass H}_2\text{O}} \times 100\% . \quad (3.4)$$

High salinity not only reduces CO₂ dissolution in brine, but also reduces the interfacial tension. For most deep saline aquifers, the salinity is above 100,000 ppm, so it is quite necessary to model the impact of salinity on IFT. The interfacial tension of CO₂-H₂O will decrease with pressure and increase with temperature and salinity, as shown in Figure 3.2 and Figure 3.3. There is significant increase in IFT when salinity is increased from 0 to 334,008 ppm at the temperature of 60 °C.

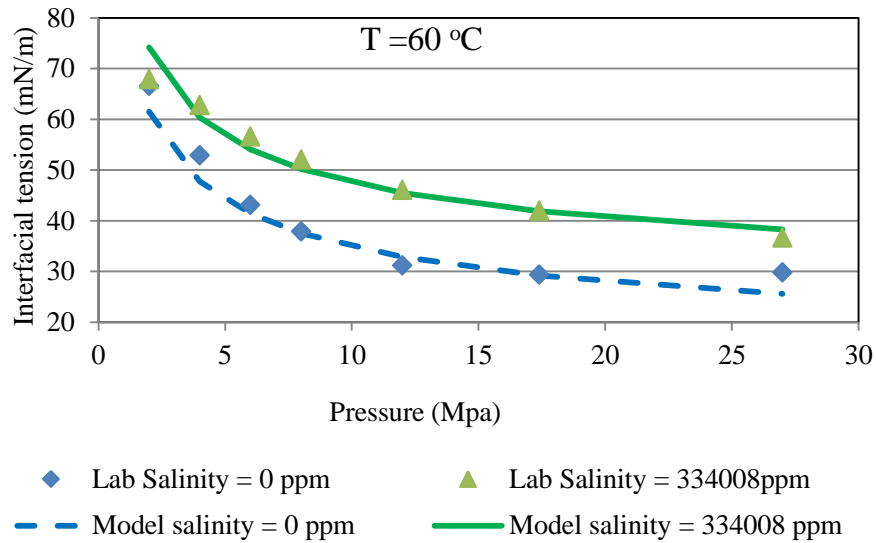


Figure 3.3 Interfacial tension vs. pressure; Bennion's model fit for different salinities and $T = 60^{\circ}C$

3.2.2 IFT CORRELATION BASED ON CO₂ CONCENTRATION IN BRINE

An IFT correlation developed (Bennion and Bachu, 2008a; Bachu and Bennion, 2009a) based on CO₂ concentration (X_{CO_2}) in brine was also implemented in IPARS:

$$\sigma = a_0 + a_1(X_{CO_2}) + a_2(X_{CO_2})^2 + a_3(X_{CO_2})^3, \quad (3.5)$$

where X_{CO_2} is the mole fraction of CO₂ in brine at standard condition, m³ CO₂ per m³ aqueous phase.

The model parameters for Bennion's correlation are listed in Table 3.2, under different salinity conditions. IFT is inversely proportional to the CO₂ concentration in brine (Figure 3.4).

Table 3.2 Fitting parameters for Bennion's IFT correlation based on CO₂ mole fraction.

Salinity (ppm)	a ₀	a ₁	a ₂	a ₃
Fresh water	85.243	-4.172	0.1295	-0.002
144,308	80.417	-3.9456	0.0484	0.0008
334,008	70.532	0.3524	-0.4591	0.0165

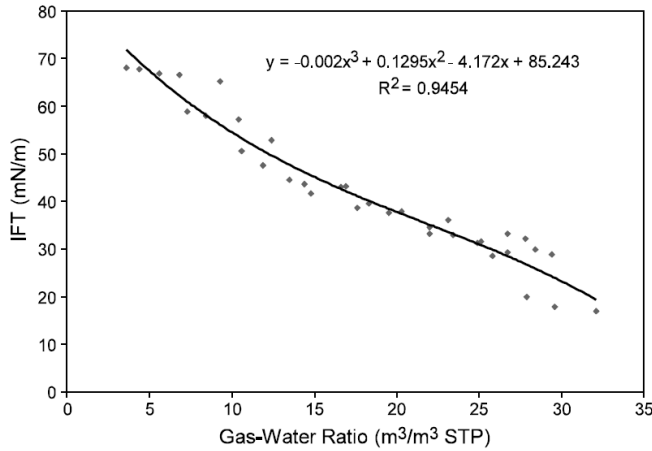


Figure 3.4 Measured IFT vs. CO₂ solubility in fresh water (Bennion and Bachu, 2008)

3.2.3 MACLEOD-SUGDEN CORRELATION

The MacLeod-Sugden correlation (MacLeod, 1923; Sugden, 1924) is the most widely used correlation in the petroleum industry because of its wide compatibility and a full set of parachor tables for different fluids:

$$\sigma = \left[\sum_{i=1}^{Nc} \psi_i \left(x_i \frac{\rho_l}{M_l} - y_i \frac{\rho_v}{M_v} \right) \right]^4, \quad (3.6)$$

where

σ = interfacial tension (dyne/cm),

ψ_i = parachor of component i ,

x_i = mole fraction of component i in liquid phase,

y_i = mole fraction of component i in vapor phase,

ρ_l = liquid phase density,

ρ_v = vapor phase density,

M_l = molecule weight of the liquid phase,

M_v = molecule weight of the vapor phase.

This correlation takes into account the phase compositions, as well as density and molecular weight. Hence it is closely related to *in situ* conditions and petrophysical properties. The parachor for CO₂ is 82, and for water it is 52 (Schechter and Guo, 1998).

3.2.4 IFT MODEL BASED ON PHASE DENSITY DIFFERENCE

We implemented an IFT model based on the phase density difference between CO₂ and water (Chalbaud, 2006):

$$\sigma = \sigma_{plateau} + \lambda x_{NaCl} + \left[\frac{\gamma}{M_w} (\Delta\rho) \right]^\eta T_r^\beta, \quad (3.7)$$

where x_{NaCl} is the concentration of salt in brine (mol/L), γ is constant parachor number for CO₂, M_w is molecular weight of CO₂, $\Delta\rho$ is the density difference ($\rho_w - \rho_g$), T_r is the dimensionless reduced temperature of CO₂ ($T_r = T/T_c$). Other fitting parameters (λ, η, β) are listed in Table 3.3.

Table 3.3 Fitting parameters for Chalbaud's correlation (Chalbaud, 2006).

λ	1.2550	γ	82
η	4.7180	M_w (g/mol)	44.01
β	1.0243	$\sigma_{plateau}$ (mN/m)	26

This model is directly based on fluid density and not directly related to the *in situ* pressure, temperature, and dissolution (Figure 3.6). The IFT curve will have a plateau

when the density difference between the gas and water phases is less than 0.6 g/ml. The IFT will increase with a slope greater than $4 \frac{\text{mN/m}}{\text{g/ml}}$ when the density difference is greater than 0.6 g/ml.

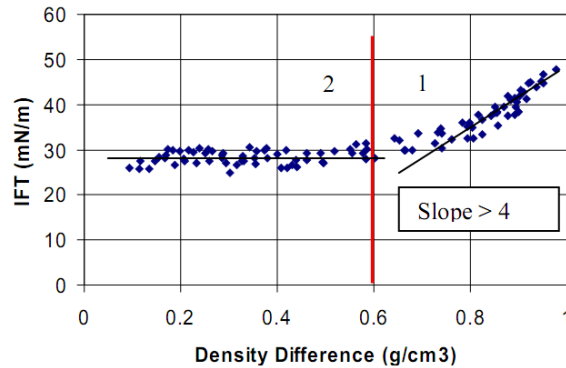


Figure 3.5 Model fit of interfacial tension of water-CO₂ with density difference (Chalbaud, 2006).

3.2.5 SUMMARY OF INTERFACIAL TENSION MODELS

The interfacial tension models discussed above are based on different physics and perform well at their respective applicable range. After comparison of the four IFT models, this study found that the Bennion’s IFT correlation based on pressure, temperature, and salinity gives the best prediction of IFT over a wide range of reservoir conditions. The other three correlations have limitations of relying on accuracy of the phase behavior and flash calculations, and do not account for the direct impact of pressure, temperature, and salinity. The Bennion’s IFT correlation based on CO₂ mole fraction in water requires an accurate calculation of CO₂ dissolution in water. The model only applies to a limited number of salinity conditions with different sets of fitting parameters. The MacLeod-Sugden correlation relies on phase composition, and also does not account for the impact of salinity on IFT. Chalbaud’s correlation includes the impact

of salinity and density on interfacial tension. However it requires an accurate calculation of phase density calculation from EOS model and flash calculation.

3.3 Trapping Model

3.3.1 TRAPPING NUMBER

Brownell and Katz (1947) recognized that the residual phase saturations should be a function of the ratio of viscous forces to capillary forces, and they defined this ratio as capillary number. The residual saturations of each phase can be determined as a function of the capillary number and can be calculated using capillary desaturation curve from laboratory measurements. Many definitions of the capillary number have been published. One of the common definitions of capillary number which is convenient for coreflood study is as follows:

$$N_c = \frac{\mu u}{\sigma} . \quad (3.8)$$

where μ is the viscosity, u is volumetric Darcy velocity, σ is the IFT.

Based on Darcy's law of flow without gravity in porous media,

$$q = -\frac{KA}{\mu} \frac{(\Delta P)}{L} , \quad (3.9)$$

where A is flow area, K is permeability, and $\Delta P/L$ is the pressure gradient.

The capillary number can also be calculated as

$$N_c = \frac{\vec{K}\vec{\nabla}\Phi}{\sigma} . \quad (3.10)$$

where $\Phi = (P + \rho gD)$ is the potential, $\vec{\nabla}\Phi$ is the potential gradient, \vec{K} is permeability tensor.

After CO₂ injection, the buoyancy force from the density difference will cause CO₂ migration. In this process, gravitational force plays a larger role than viscous force. In order to quantify the significance of gravitational forces, a dimensionless Bond

number is used, which refers to the ratio between gravitational force and capillary force in the form of interfacial tension. (Here subscript 1 stands for water phase, 2 for CO₂ phase). Bond number is defined as

$$N_B = \frac{\bar{K}(\rho_2 - \rho_1)g\bar{V}D}{\sigma} . \quad (3.11)$$

Jin (1995) and Pope *et al.* (2000) generalized the capillary number by including the effect of gravity and derived a trapping number (N_{TI}). The trapping number is the sum of capillary number and Bond number. The trapping number for phase 1 displaced by phase 2 is defined as follows:

$$N_{T1} = \frac{\left| \bar{K} \cdot \left[\bar{\nabla}\Phi_2 + g(\rho_2 - \rho_1)\bar{\nabla}D \right] \right|}{\sigma}, \quad (3.12)$$

where $\Phi = (P + \rho gD)$ is the pressure potential, $\bar{\nabla}\Phi$ is the potential gradient, ρ is the density, g is gravity constant, D is the depth.

3.3.2 CAPILLARY DESATURATION CURVES

The capillary desaturation curve is used to describe the trend of residual saturation with capillary number (Figure 3.6). The capillary number represents how hard the displacing phase is being pushed into the pore which is initially occupied by *in situ* phases. For the CO₂ injection process, the viscosity force is much higher than the capillary forces that will push CO₂ into the small pore spaces. The amount of residual saturation for each phase will be reduced at high viscous forces, which implies that the higher the capillary number is, the lower residual saturation will be reached.

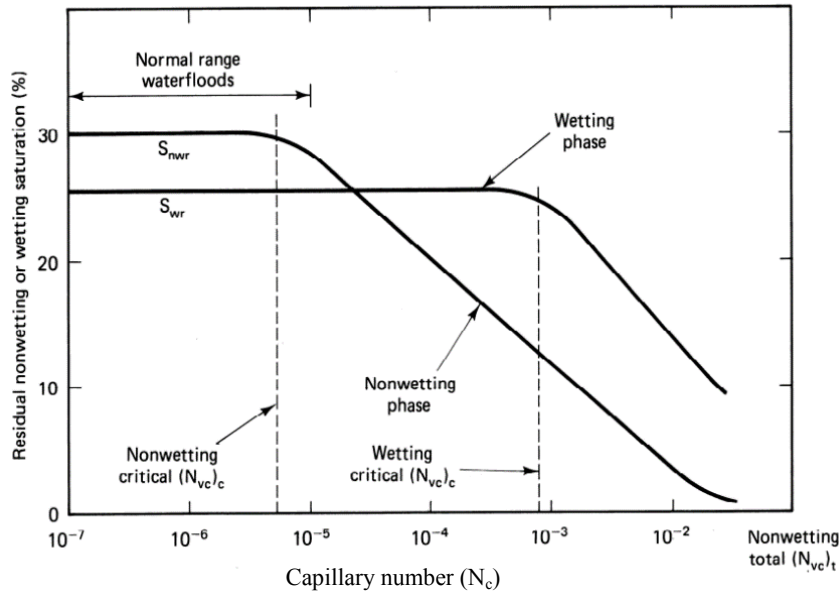


Figure 3.6 Schematic capillary desaturation curves, residual saturation vs. capillary number (Lake, 1989)

The shape of the desaturation curve is determined by several factors, including wettability, heterogeneity, and pore size distribution. While the residual saturation of the non-wetting phase typically starts to decrease at a low capillary number, the wetting phase saturation usually does not start to decline until a capillary number much higher than that for the non-wetting phase is reached. For rock types with less heterogeneity and relatively uniform pore throat radius, the slope of decline will be sharper than heterogeneous rock. Sandstone is a relatively homogeneous rock that has a sharp slope of saturation drop when the capillary number exceeds the critical value. Carbonate rock is normally quite heterogeneous and has a wide pore size distribution, so its desaturation curve will show a slope that spans quite a wide range of capillary numbers.

The trapping number is a sum of the capillary number and the gravitational Bond number. The residual saturation is modeled as a function of trapping number as follow:

$$S_{lr} = \min \left(S_l, S_{lr}^{high} + \frac{S_{lr}^{low} - S_{lr}^{high}}{1 + T_l (N_{Tl})^{\tau_l}} \right) \quad (3.13)$$

where l is the phase label, subscript 1 is liquid, and subscript 2 is CO₂. The parameters T_l and τ_l are trapping model parameters obtained by fitting the residual saturation data for phase l . S_{lr}^{high} and S_{lr}^{low} correspond to the residual saturation at high trapping number (typically zero residual saturation) and low trapping number, respectively. Figure 3.7 shows an example calculation for residual saturations versus trapping number.

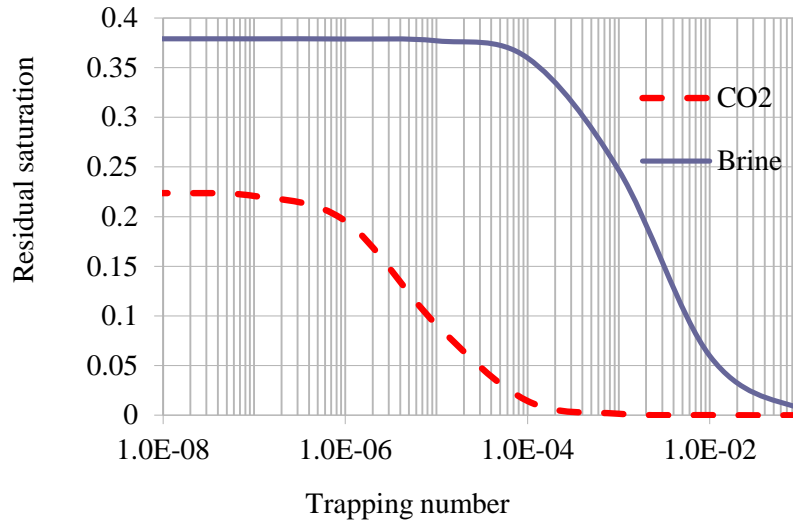


Figure 3.7 Example capillary desaturation curves for CO₂-brine, residual saturations vs. trapping number

3.3.3 RELATIVE PERMEABILITY MODEL AS FUNCTION OF TRAPPING NUMBER

Since the residual saturation for CO₂-brine is modeled with trapping number, the trapping number will have a big impact on the relative permeability and capillary pressure curves (Figure 3.8). The relative permeability curve can be characterized by the endpoint relative permeability k_{rl}^0 , residual saturation S_{lr} , and relative permeability exponent λ_l :

$$k_{rl} = k_{rl}^0 \left(\frac{S_l - S_{lr}}{1 - \sum_l S_{lr}} \right)^{\lambda_l} \quad (3.14)$$

The relative permeability of each phase can be correlated to trapping number in a very predictable way. When trapping number increases (or interfacial tension decreases), the residual saturation will decrease, and the relative permeability will increase for the same saturation. If the relative permeability curves at high and low trapping numbers are defined, the relative permeability curves at other trapping numbers can be interpolated from the given two. The same idea can be applied to calculate the relative permeability endpoint and exponent based on the trapping number and shifted residual saturation.

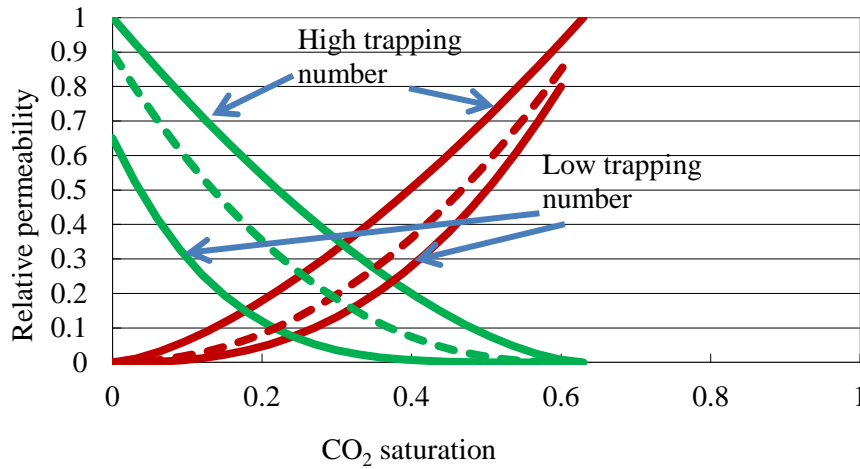


Figure 3.8 Prototype relative permeability curves for low and high trapping numbers (Green: water; Red: CO₂).

The following correlation is used to shift the endpoint relative permeability k_{rl}^0 for water (w) and CO₂ (g) as a function of the residual saturation of the conjugate phase:

$$k_{rg}^0 = k_{rg}^{0low} + \frac{S_{wr}^{low} - S_{wr}}{S_{wr}^{low} - S_{wr}^{high}} (k_{rg}^{0high} - k_{rg}^{0low}) \quad (3.15)$$

$$k_{rw}^0 = k_{rw}^{0low} + \frac{S_{gr}^{low} - S_{gr}}{S_{gr}^{low} - S_{gr}^{high}} (k_{rw}^{0high} - k_{rw}^{0low}) \quad (3.16)$$

where the superscript *low* stands for low trapping number (high residual saturation), and the superscript *high* stands for high trapping number (low residual saturation).

The exponent of relative permeability curves λ_l is also modified to reflect the change in the residual saturation:

$$\lambda_g = \lambda_g^{low} + \frac{S_{wr}^{low} - S_{wr}}{S_{wr}^{low} - S_{wr}^{high}} (\lambda_g^{low} - \lambda_g^{high}) \quad (3.17)$$

$$\lambda_w = \lambda_w^{low} + \frac{S_{gr}^{low} - S_{gr}}{S_{gr}^{low} - S_{gr}^{high}} (\lambda_w^{low} - \lambda_w^{high}) \quad (3.18)$$

Figure 3.9 and Figure 3.10 show the example calculations for relative permeability endpoints and exponents as functions of trapping numbers.

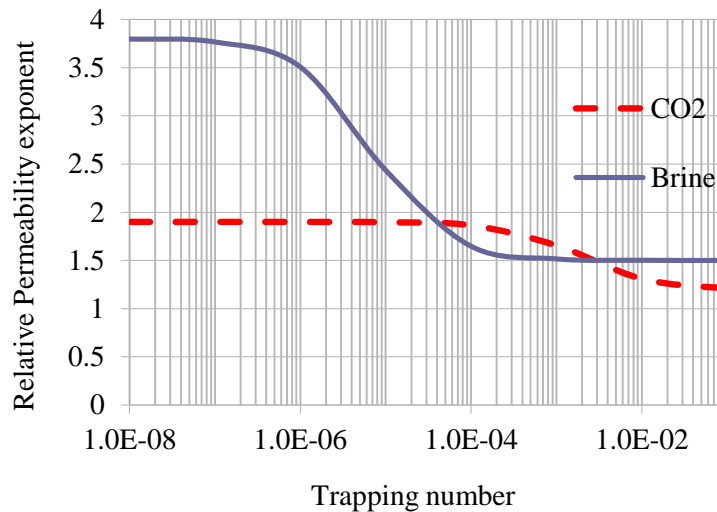


Figure 3.9 Endpoint relative permeability vs. trapping number.

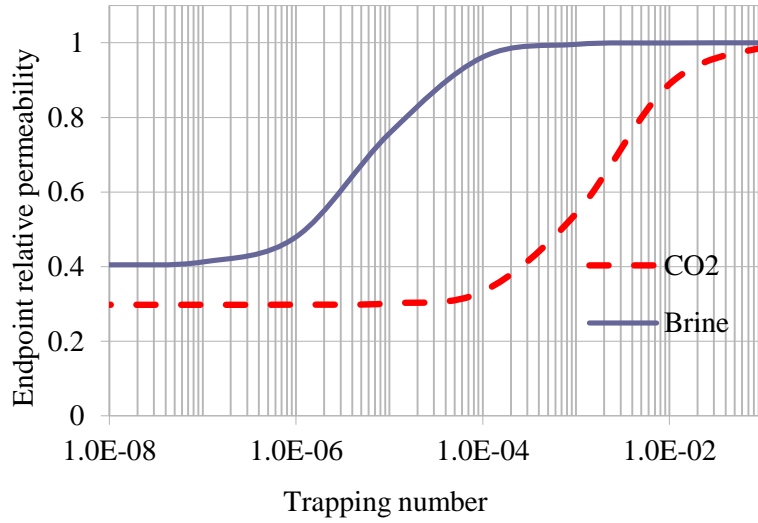


Figure 3.10 Relative permeability exponent vs. trapping number.

The next step is to calculate the relative permeability of each phase as a function of saturation. We assumed a Corey-type relative permeability function where endpoint, exponent, and residual saturations are functions of trapping number.

$$k_{rw} = k_{rw}^0 \left(\frac{S_w - S_{wr}}{1 - S_{wr} - S_{gr}} \right)^{\lambda_w}, \quad (3.19)$$

$$k_{rg} = k_{rg}^0 (1 - \bar{S}_w)^{\lambda_g}, \quad (3.20)$$

where S_w is the water saturation, $\bar{S}_w = \frac{S_w - S_{wr}}{1 - S_{wr} - S_{gr}}$ is the normalized water saturation, and S_{wr} is residual water saturation, S_{gr} is residual gas phase saturation.

Examples showing results of CO₂-brine relative permeability at low and high trapping numbers are given in Figure 3.11 and Figure 3.12, which show the impact of the trapping number on relative permeability. The residual saturation of both phases will be reduced, and the relative permeability curves will shift upward when the trapping number increases.

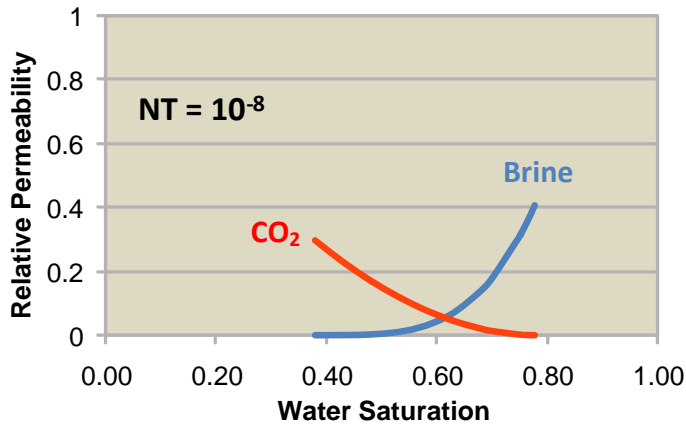


Figure 3.11 Relative permeability curves at low trapping number of 10^{-8} .

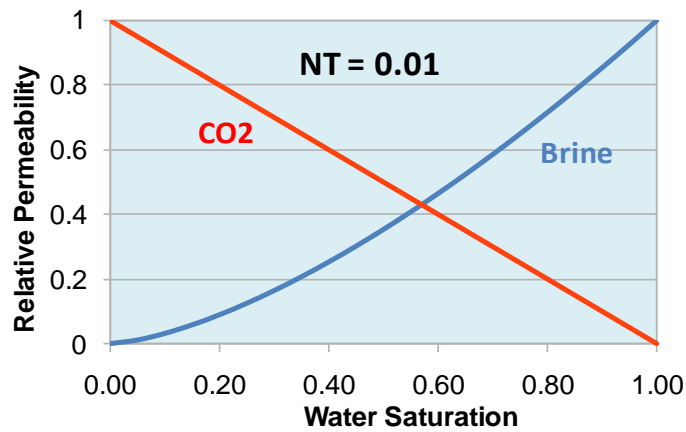


Figure 3.12 Relative permeability curves at high trapping number 10^{-2} .

3.3.4 MODEL VALIDATION TO LABORATORY DATA

We compared the model with three relative permeability data sets provided by Bennion and Bachu (2006b). Bennion and Bachu (2006b) measured relative permeability and capillary pressure of CO_2 and brine in coreflood under different pressure conditions. The relative permeability curves were measured for a sample of sandstone rock at a

temperature of 43 °C and *in situ* salinity of 27,096 ppm. The core length was 3.73 cm with a diameter of 3.77 cm (Table 3.4).

Table 3.4 Core data used for relative permeability and capillary pressure measurements (Bennion and Bachu, 2006b).

Core sample lithology	Sandstone
Sample depth, m	1626
Overburden pressure, kPa	11,000
<i>In situ</i> temperature, °C	43
<i>In situ</i> salinity, ppm	27,096
Core length, cm	3.73
Core diameter, cm	3.77
Cross sectional area, cm ²	11.16
Injection rate, cm ³ /hr	10
Porosity, fraction	0.153

Three sets of relative permeability curves are measured by Bennion and Bachu (2006b), with each case standing for low, medium-ranged, and high trapping number conditions. The three test cases outlined below correspond to different trapping numbers for the CO₂-Brine system. Measured relative permeability curves are presented in Figure 3.13.

- 1) IFT = 56.2 mN/m, $P = 1378$ kPa (200 psig), low trapping number
- 2) IFT = 33.2 mN/m, $P = 6890$ kPa (1000 psig), medium trapping number
- 3) IFT = 19.8 mN/m, $P = 20,000$ kPa (2900 psig), high trapping number

We curve-fitted the measured relative permeability curves with a Corey function

as

$$k_{rl} = k_{rl}^0 (\bar{S}_\ell)^{2n_l}, \quad l = w, g \quad (3.21)$$

where $\bar{S}_l = \frac{S_l - S_{lr}}{1 - S_{wr} - S_{gr}}$ is the normalized saturation.

The fitting parameters to measurement are listed in Table 3.5.

Table 3.5 Parameters for Corey-type model match to the measured relative permeability data at different pressure and IFT condition by Bennion and Bachu (2006b).

P (kPa)	IFT (mN/m)	S_{gr}	S_{wr}	k_g^o	k_w^o	λ_g	λ_w
1378	56.2	0.225	0.379	0.298	0.405	1.90	3.80
6,890	33.2	0.107	0.271	0.456	0.861	1.50	1.30
20,000	19.8	0.102	0.197	0.527	0.905	1.10	1.10

We applied our new trapping number model to curve-fit the experimental results. The endpoint values corresponding to the high and low pressure values were chosen for the high and low model parameters in Equations 3.13-3.16. The experimental data (Figure 3.13) demonstrate a shift in relative permeability curves with different pressure or trapping number.

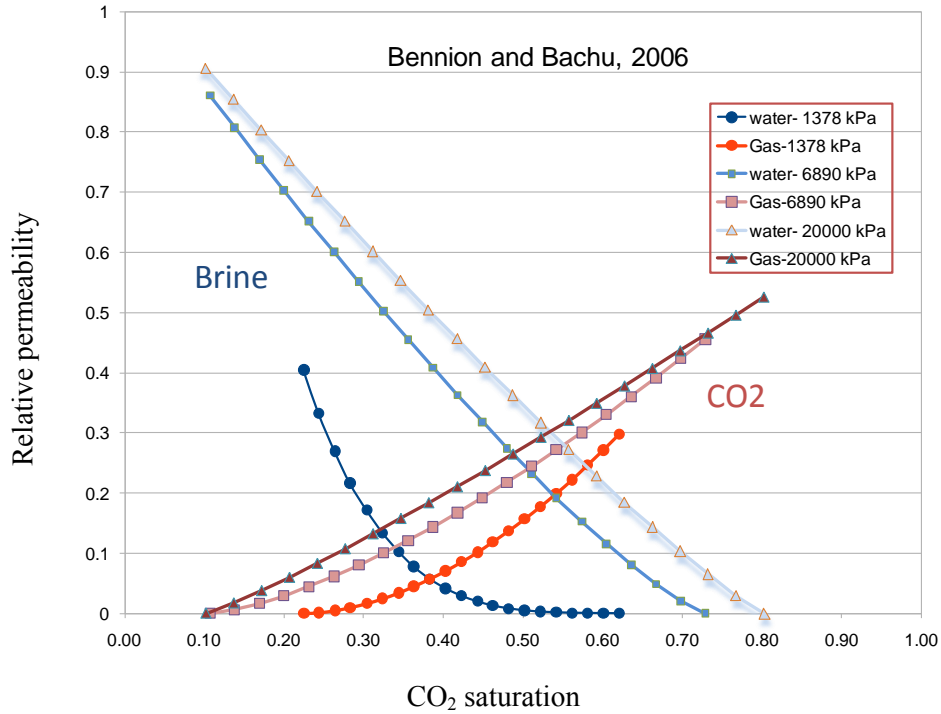


Figure 3.13 Relative permeability curves at different pressures (data from Bennion and Bachu, 2006b).

In order to validate our model using laboratory data, we assumed the relative permeability curves at high and low pressure represented the high and low trapping numbers.

First we curve fit the two sets of relative permeability curves using parameters in Table 3.5. These two sets of curves were used as our model inputs for high and low trapping numbers. Results are shown in Figure 3.14.

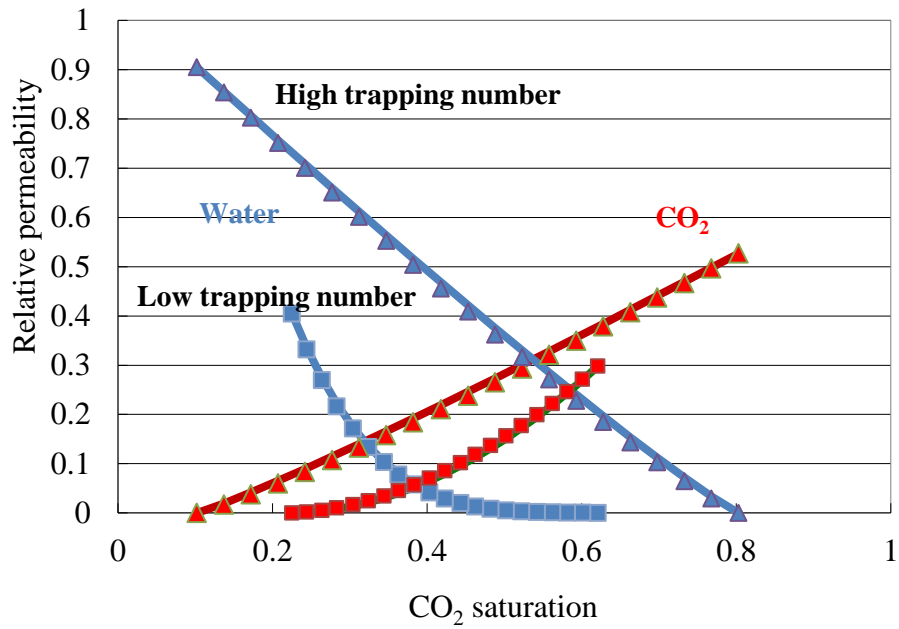


Figure 3.14 Curve-fit of relative permeability at low and high trapping number conditions (points are data from Bennion and Bachu, 2006b and lines are calculated).

The relative permeability curves at intermediate range trapping number were calculated using the trapping model (Figure 3.15). Results show good agreement between calculated relative permeability and lab measurements (Table 3.5).

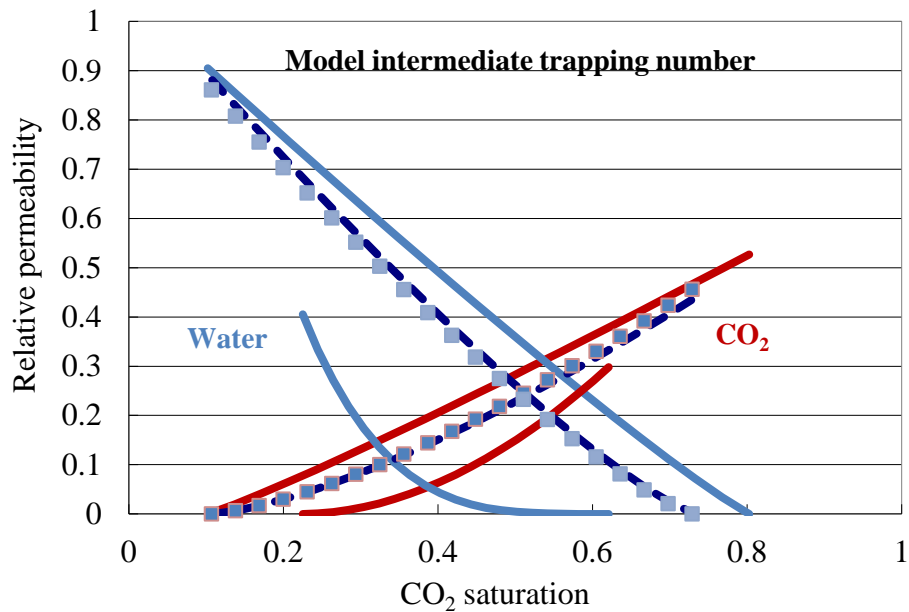


Figure 3.15 Comparison of model calculation (dash line) and laboratory data (points) of relative permeability curves at intermediate trapping number, solid lines are input relative permeability curves at high and low trapping number

3.4 Hysteresis Model

Unlike previous relative permeability models which model the relative permeability as a function of phase saturation only, the hysteresis model relates the relative permeability to the saturation and its history. Hysteresis refers to the phenomenon that capillary pressure and relative permeability take different paths during drainage and imbibition process. Drainage is the process of the non-wetting phase CO₂ displacing the wetting phase water, while imbibition is the process of the wetting phase water displacing non-wetting phase CO₂ in pore spaces. The hysteresis effect is critical for CO₂ sequestration, because it is the main mechanism for capillary trapping. The capillary trapping phenomenon in an imaginary pore space during drainage and

imbibition is shown in Figure 3.16. During the injection period, CO₂ and water undergo the drainage process. CO₂ is a continuous phase and physically there is no trapping of CO₂ ($S_{gt} = 0$). The trapped gas saturation (S_{gt}) is zero in Figure 3.16. After CO₂ injection, CO₂ phase will become discontinuous in certain pore spaces. Part of CO₂ (S_{gt}) will be trapped by capillary forces during the imbibition process (Figure 3.16).

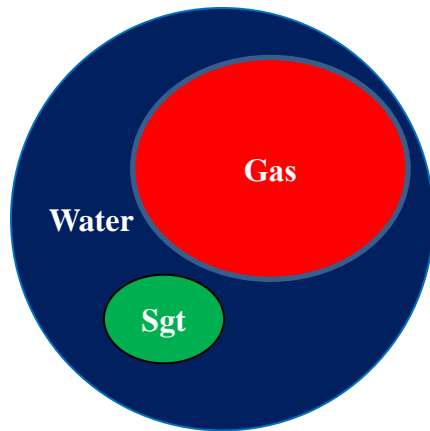


Figure 3.16 Non-wetting phase gas trapping (S_{gt}) in pore space during imbibition process.

Figure 3.17 provides the schematic of capillary pressure for several water saturation directions. For CO₂ injection into an aquifer with 100% water saturation, the capillary pressure curve will initially follow the main drainage curve. During the drainage process, there is no trapping of non-wetting phase CO₂. Water saturation will decrease until it reaches the reversal point A, which is when the imbibition process begins. In the imbibition process, the capillary pressure will follow the dashed line from point A. The spontaneous imbibition process will stop at zero capillary pressure because there is not capillary pressure to imbibe the brine into the pore. If water imbibition reaches zero capillary pressure, the maximum trapped CO₂ (S_{gtrap}), corresponding to the reversal

point A, will be achieved. If point A is on the main imbibition curve and imbibition reaches to zero P_c , the maximum CO₂ residual saturation ($S_{gt,max}$) can be achieved. For an imbibition process started at point A and saturation at point B, the trapped amount of CO₂ (S_{gt}) needs to be calculated by interpolation between zero trapping and $S_{gtrap,A}$. We will discuss the procedures in following sections.

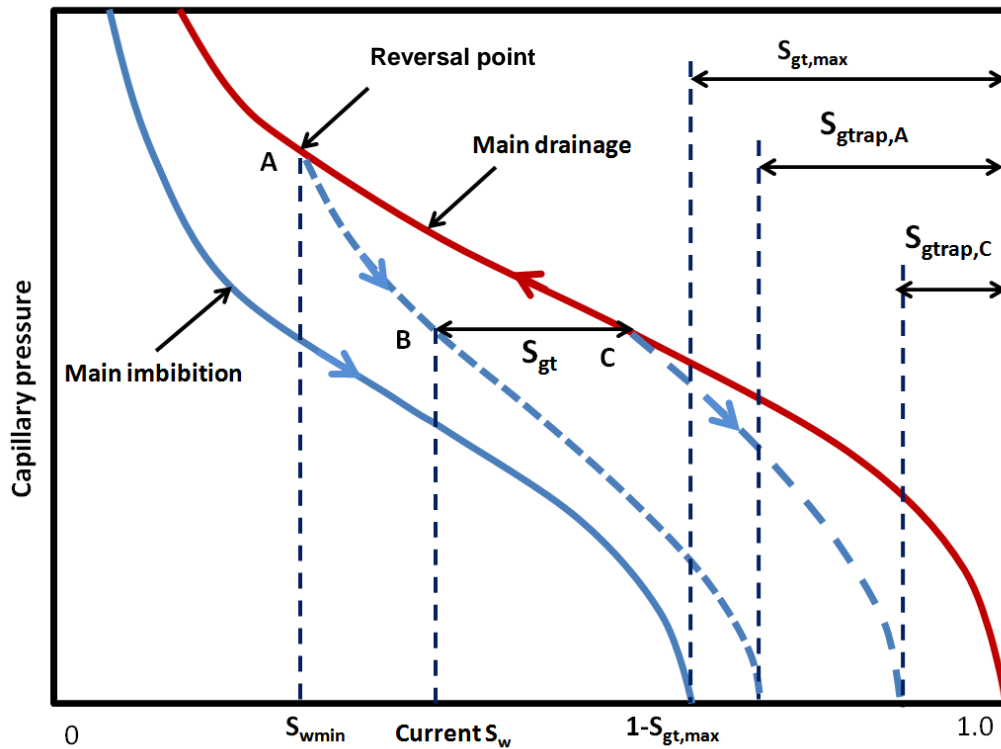


Figure 3.17 Sketch of hysteresis capillary pressure path.

The definitions of variables in Figure 3.17 are given as below:

S_{wr} : Residual water saturation;

S_{gr} : Residual gas saturation;

$S_{w,inv}$: Water saturation at reversal point

S_{wmin} : Normalized water saturation at reversal point A;

$S_{gt,max}$: Maximum trapping gas saturation in hysteresis, equal to S_{gr} ;

S_{gtrap} : Trapped gas saturation at zero P_c , corresponds to reversal point (A or C in Figure 3.17).

\bar{S}_{gt} : Trapped amount gas at current imbibition \bar{S}_w (not normalized)

$S_{g,max}$: Maximum gas saturation for main drainage ($1-S_{wr}$)

3.4.1 LAND'S HYSTERESIS TRAPPING MODEL

Land's model (Land, 1968) is implemented for hysteresis modeling in IPARS. This model correlates the maximum trapped non-wetting phase saturation as a function of initial non-wetting phase saturation. Based on this model, when flow changes from drainage to imbibition direction, the maximum residual gas saturation corresponding to the reversal point is

$$S_{gtrap} = \frac{1 - S_{wmin}}{1 + C(1 - S_{wmin})}, \quad (3.22)$$

where S_{gtrap} is the trapped non-wetting phase saturation (normalized) at $P_c = 0$, corresponding to water saturation at reversal point, S_{wmin} . S_{wmin} is the normalized (or effective) wetting phase saturation at the reversal point (point A in Figure 3.17),

$$\bar{S}_{w,min} = \frac{S_{w,inv} - S_{wr}}{1 - S_{wr}}. \quad (3.23)$$

C is the Land's coefficient, calculated as follows

$$C = \frac{1}{S_{gt,max}} - \frac{1}{S_{g,max}}. \quad (3.24)$$

For example, if $S_{gt,max} = 0.203$, $S_{g,max} = 0.803$, then C equals to 3.68. The maximum trapped non-wetting phase saturation could then be calculated using Land's model as a function of initial non-wetting phase saturation (Figure 3.18).

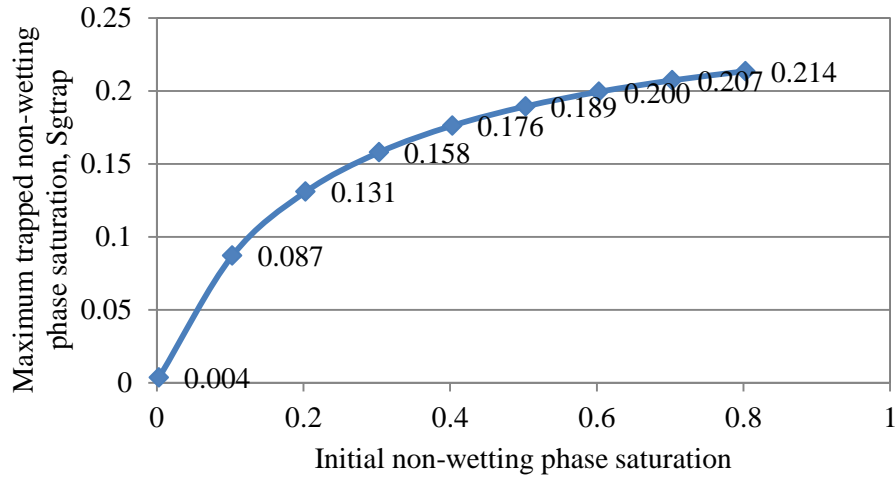


Figure 3.18 Maximum trapped non-wetting phase saturation vs. initial non-wetting phase saturation (Land's model)

The normalized water saturation \bar{S}_w is used to determine the saturation direction,

$$\bar{S}_w = \frac{S_w - S_{wr}}{1 - S_{wr}} \quad (3.25)$$

For each time step, if \bar{S}_w in each gridblock (Point B in Figure 3.17) is increasing (greater than S_{wmin}), it is an imbibition process and $S_{w,min}$ remain the same as reversal point. Otherwise, if \bar{S}_w is decreasing, S_{wmin} will be set to be current \bar{S}_w . For an imbibition process, the trapped gas saturation (S_{gt}) can be calculated (Lenhard and Oostrom, 1998):

$$S_{gt} = S_{gtrap} \frac{\bar{S}_w - S_{wmin}}{1 - S_{gtrap} - S_{wmin}} \quad (3.26)$$

For the example with $S_{gr} = 0.203$, $S_{wr} = 0.197$, if reversal point locates at the residual water saturation, $S_{w,inv} = S_{wr}$, and $S_{wmin} = 0$, the trapped gas saturation during water imbibition would be as indicated in Figure 3.19.

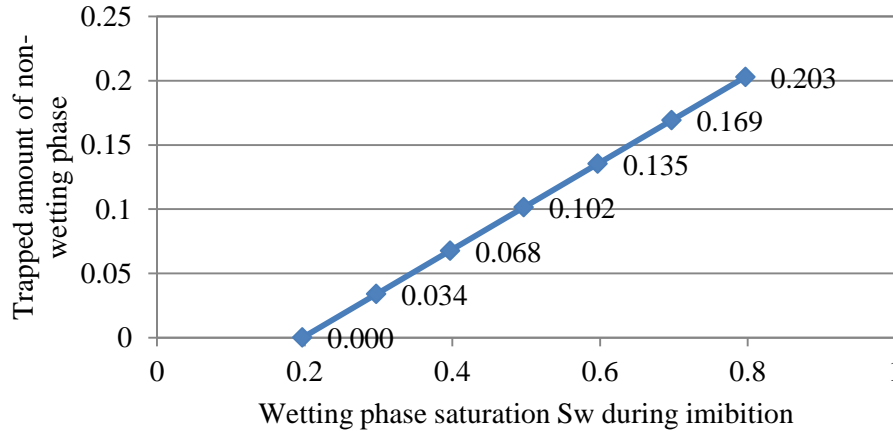


Figure 3.19 Trapped non-wetting phase saturation vs. wetting phase saturation during imbibition process starting at $S_{wmin} = 0$, based on Lenhard's interpolation

We can see from Figure 3.19 that the trapped amount of non-wetting phase saturation will increase linearly with increase of the wetting phase saturation based on a Lenhard's interpolation. The calculated S_{gt} is the trapped amount of non-wetting phase saturation.

3.4.2 HYSTERETIC RELATIVE PERMEABILITY

Once we calculate the trapped non-wetting phase saturation in the pore space, the next step is to calculate the relative permeability and capillary pressure with the consideration of saturation direction using the apparent wetting phase saturation. The apparent wetting phase saturation is calculated as ($\bar{\bar{S}}_w$ less than or equal to 1):

$$\bar{\bar{S}}_w = \bar{S}_w + S_{gt}. \quad (3.27)$$

The apparent water saturation represents a water saturation that contains a discontinuous gas 'bubble' in it. The relative permeability and capillary pressure can be calculated based on $\bar{\bar{S}}_w$ and S_{gt} . The current model uses a Brooks-Corey relative permeability model (Brooks and Corey, 1964).

For the drainage direction S_{gt} equals to zero and $\bar{\bar{S}}_w$ equals \bar{S}_w . The endpoint relative permeability for water is 1:

$$k_{rw} = \bar{S}_w^{\lambda_w} \quad (3.28)$$

$$k_{rg} = k_{rg}^0 (1 - \bar{S}_w)^{\lambda_g} \quad (3.29)$$

For an imbibition direction, the apparent water saturation is used for relative permeability:

$$k_{rw} = k_{rw}^0 \bar{\bar{S}}_w^{\lambda_w} \quad (3.30)$$

$$k_{rg} = k_{rg}^0 (1 - \bar{\bar{S}}_w)^{\lambda_g} \quad (3.31)$$

Examples of hysteretic relative permeability curves are shown in Figure 3.20. During the drainage, trapped gas saturation is 0, and water residual saturation, $S_{wr} = 0.197$. During the imbibition process, gas residual saturation is $S_{gr} = 0.203$.

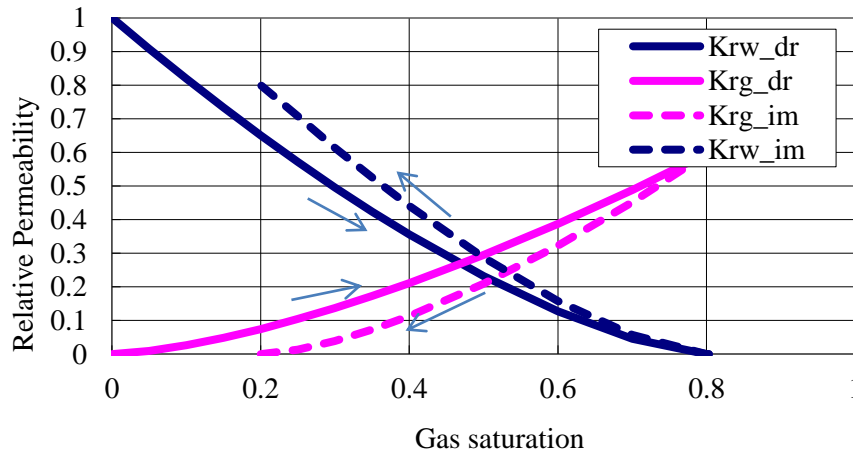


Figure 3.20 Drainage and imbibition relative permeability curves for CO₂-brine

3.4.3 HYSTERETIC CAPILLARY PRESSURE

Capillary pressure hysteresis, referring to the different paths the capillary pressure curve takes during drainage and imbibition processes, is critical for CO₂ trapping. For two-phase flow, the capillary pressure path is depicted in Figure 3.17. An example hysteresis capillary path from drainage to imbibition processes is shown in Figure 3.21.

During the drainage process, capillary pressure is

$$P_{c,Corey} = P_c^{entry} \bar{S}_w^{-1/\lambda_{drainage}} \quad (3.32)$$

For the imbibition process, capillary pressure is modeled as,

$$P_{c,imb} = P_c^{inv} \left(\frac{1 - \bar{S}_w}{1 - S_{wmin}} \right)^{-1/\lambda_{imb}}, \quad (3.33)$$

where P_c^{inv} is the capillary pressure at the saturation reversal point.

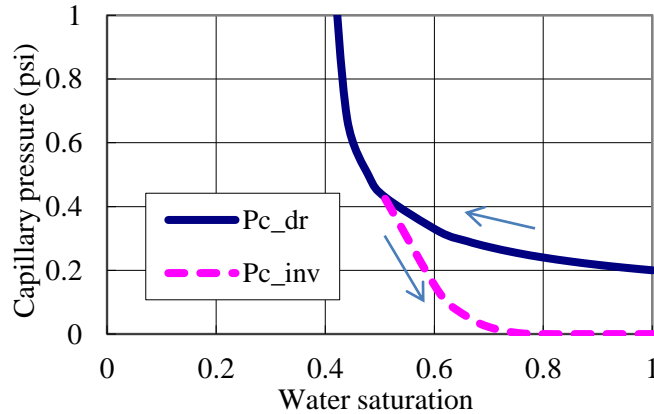


Figure 3.21 Hysteretic capillary pressure for drainage and imbibition process

We can see from example in Figure 3.21 that the imbibition capillary curve starts from reversal point $S_w = 0.5$, and then decreases to zero capillary pressure at $S_w = 0.797$. Hence $(1 - S_w) = 0.203$ is the maximum trapped amount of CO₂ saturation corresponding to the reversal point of $S_w = 0.5$.

3.5 Leverett J-function for Capillary Pressure

The capillary pressure in reservoir rock is affected by many factors, including the interfacial tension (IFT), the contact angle, and the heterogeneous permeability and porosity in the reservoir. The capillary pressure curve for the same kind of rock with similar pore structure could be modeled with a dimensionless function as the Leverett J-function (Leverett 1941):

$$J(S_w) = \frac{P_c}{\sigma \cos \theta} \left(\frac{K}{\phi} \right)^{0.5}, \quad (3.34)$$

Here P_c is the capillary pressure, K is the permeability, ϕ is porosity, σ is the interfacial tension, and θ is the phase contact angle, J is a dimensionless curve for a given rock with similar pore structure.

We scale capillary pressure P_c based on Leverett J-function to include heterogeneity and fluid/rock properties. Reference values including interfacial tension, contact angle, permeability and porosity are needed as input parameters. The capillary pressure can then be calculated as:

$$P_c = P_{c,ref} \left(\frac{\sigma \cos \theta}{\sigma_{ref} \cos \theta_{ref}} \right) \left(\frac{\phi}{K} \right)^{0.5} \left(\frac{K}{\phi} \right)_{ref}^{0.5}, \quad (3.35)$$

where subscript *ref* stands for the capillary pressure curve and other petrophysical properties measured for the reference rock.

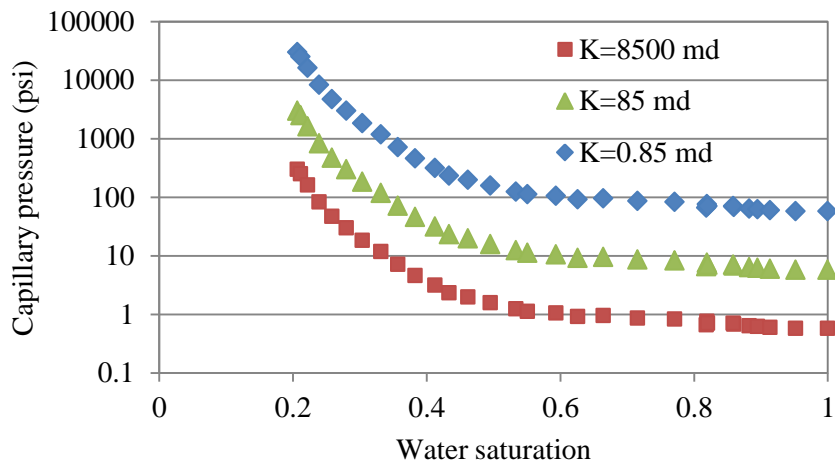


Figure 3.22 Capillary scaling based on heterogeneous rock with different permeability

By scaling capillary pressure based on the Leverett J-function, we can see from Figure 3.22 that the capillary pressure curve is shifted upward or downward for low and high permeability values in each gridblock. When the permeability is low in a gridblock, the capillary pressure curve will be high.

The effect of interfacial tension was accounted for by scaling the capillary pressure such that the capillary pressure is reduced as the interfacial tension decreases.

Bennion and Bachu (2006b) measured capillary pressure for different CO₂-water IFT conditions, which shows downward shifting of capillary pressure curves with decreasing IFT (Figure 3.23).

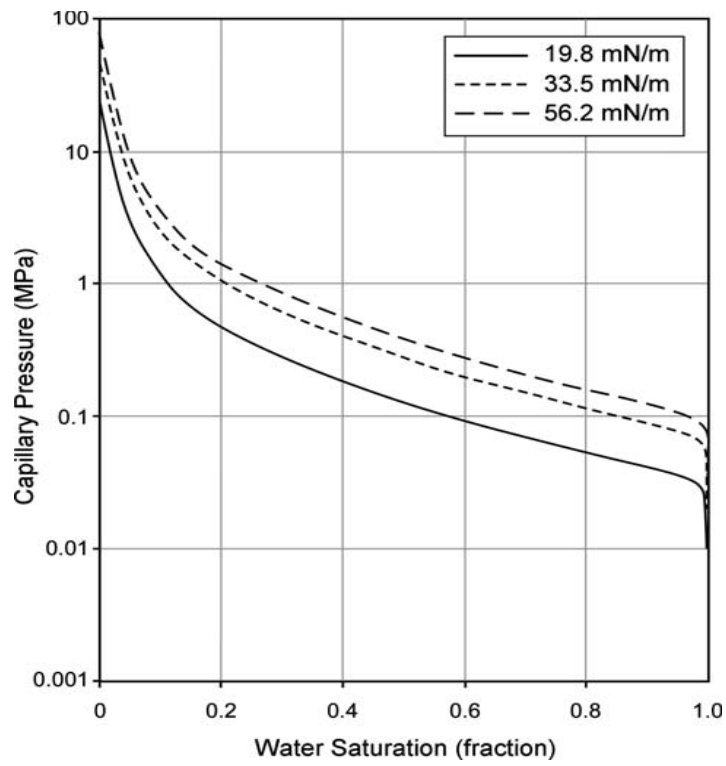


Figure 3.23 Measured capillary pressure curves at different IFT (i.e.trapping number condition) (Bennion and Bachu, 2006b).

CHAPTER 4: Model Validation with Coreflood Simulation

Numerical simulation and laboratory corefloods are effective methods for fluid displacement study in porous media. Numerical simulation of laboratory experiments of CO₂ injection into brine saturated cores with high resolution CT images of porosity and CO₂ saturation provide a deepened understanding of the impact of small-scale heterogeneity on flow and transport of CO₂. Validation of numerical simulators with controlled laboratory experiments and pilot-scale field projects provides confidence in the prediction capability of numerical models for future storage projects. Numerical simulators must include accurate physical property models in order to capture small-scale effects.

The coreflood simulation case presented in this study is based on the published paper by Krause *et al.*, 2011. The goal of this study was to test the rock-fluid model enhancement in IPARS, validate the core permeability and porosity relationship, and history-match the coreflood results. We set up a simulation case in IPARS using a core model similar to the experiment, with the same initial pressure and temperature conditions as in the original experiment. Since we do not have the actual permeability and porosity data, we had to generate the permeability and porosity distributions using the geostatistical program FFTSIM (Jennings *et al.*, 2000) in the absence of measured porosity and permeability data. We honored reported average permeability and porosity by Krause *et al.* (2011), but the distributions of permeability and porosity are different from the coreflood experiment. The IPARS simulation results are compared favorably with experimental results.

4.1 Review of Published Experimental and Numerical Results

Krause *et al.* (2011) conducted a study of CO₂-brine coreflood at elevated pressure and temperature using a Berea sandstone core. Supercritical CO₂ was injected at a constant rate into a 100% brine saturated core until no more water was produced. The final CO₂ saturation distributions as well as porosity were measured with an X-ray CT scanner with a resolution of 0.254 mm × 0.254 mm × 1.5 mm. The average porosity and permeability of the core were 0.185 and 84.7 md. The laboratory and simulation parameters are listed in Table 4.1.

Table 4.1 Core properties and coreflood conditions (Krause *et al.*, 2011).

T (°C)	50	CO ₂ dissolution (mass fraction)	0.04873
P (MPa)	12.41	CO ₂ density (Kg/m ³)	608.38
X _{NaCl} (ppm)	6500	CO ₂ viscosity (cp)	0.06
Average porosity, fraction	0.185	Brine density (Kg/m ³)	993.33
Average permeability (md)	84.7	Interfacial tension (N/m)	0.0285
Core length (cm)	20.32	Injection rate (ml/min)	3
Core diameter (cm)*	5.08	Total injection pore volume	13
Residual water saturation	0.2	Final average gas saturation	0.5026

*: We believe the core diameter should be about 4.38 cm based on the image size and data in Krause *et al.* (2011) paper.

The porosity based on an X-ray CT scan is shown in Figure 4.1. The saturation distribution is shown in Figure 4.2. A high saturation contrast and non-uniform distribution of the CO₂ saturation is clearly shown in the middle slice of the core (Figure 4.3). The measured histogram of CO₂ saturation shows a normal distribution with CO₂ saturation spanning the whole range from 0 to 1 (Figure 4.4). This indicates that the water saturation is reduced to almost zero in certain locations of the core.

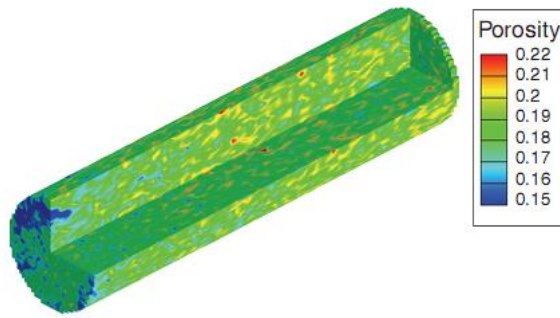


Figure 4.1 Measured porosity (grid size of $0.254\text{ mm} \times 0.254\text{ mm} \times 1.5\text{ mm}$) (Krause *et al.*, 2011)

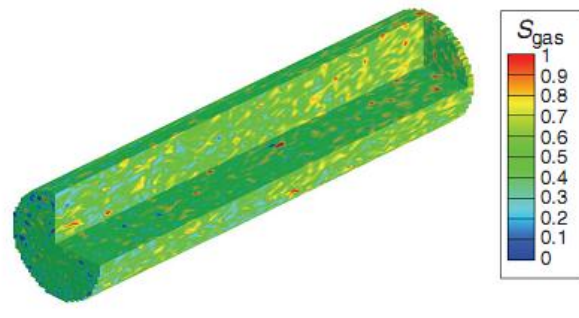


Figure 4.2 Measured CO₂ saturation (grid size of $0.254\text{ mm} \times 0.254\text{ mm} \times 1.5\text{ mm}$) (Krause *et al.*, 2011)

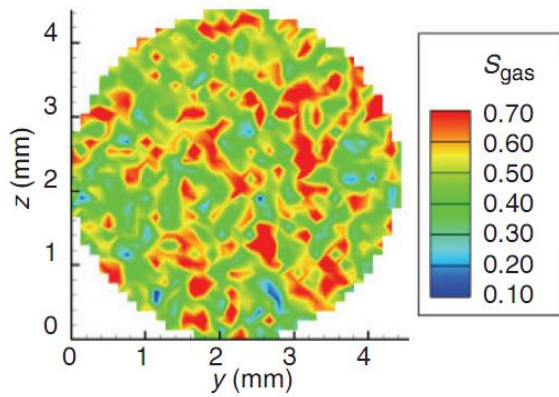


Figure 4.3 Measured CO₂ saturation in the middle slice (Krause *et al.* 2011)

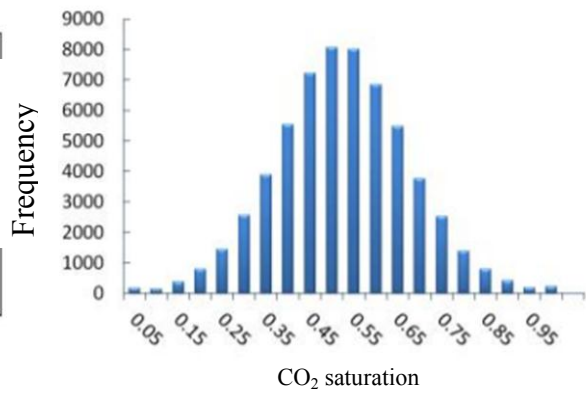


Figure 4.4 Measured CO₂ saturation histogram (Krause *et al.* 2011)

Krause *et al.* (2011) used TOUGH2-MP simulator with the ECO2N module (Pruess, 2005) to history-match the coreflood experiment. Permeability was calculated using several permeability-porosity correlations. The measured relative permeability and capillary pressure curves used in their simulations are shown in Figure 4.5 and Figure 4.6. There were a total of 67 slices along the core length with 936 cells in each slice. The grid size used in the simulations by Krause *et al.* (2011) was $1.27\text{ mm} \times 1.27\text{ mm} \times$

3 mm. The core inlet was maintained at a constant CO₂ injection rate (3 ml/min) and the outlet was at a constant pressure (12.41 MPa). About 13.2 pore volumes (PVs) of CO₂ were injected until there was 100% CO₂ in the effluent.

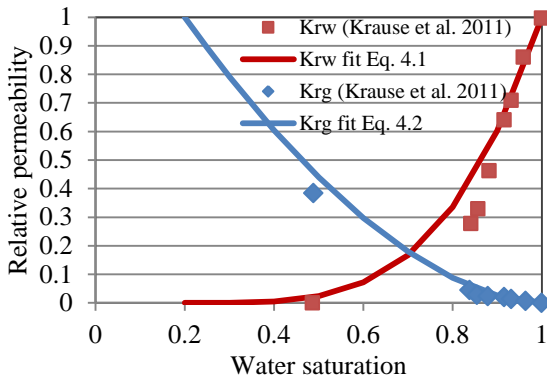


Figure 4.5 Measured relative permeability curves (Krause *et al.* 2011) and curve fit using Eq. 4.1 and 4.2

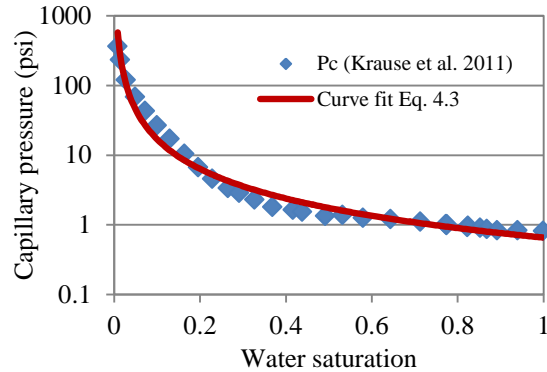


Figure 4.6 Measured capillary pressure curve (Krause *et al.* 2011) and curve fit using Eq. 4.3

Krause *et al.* (2011) compared their simulation results with experimental observations. A comparison of the experimental and simulation saturation distributions in the middle slice (Figure 4.3 vs. Figure 4.7) shows that the saturation profile is similar though the simulated saturation lacks the large contrast as that shown in the measured saturation. The CO₂ saturation histogram in Figure 4.4 compared to Figure 4.8 shows large differences between the experiment and the best simulation model. The saturation histogram of the simulation results (Figure 4.8) is much narrower compared to that measured and lacks high CO₂ saturation values greater than 0.75.

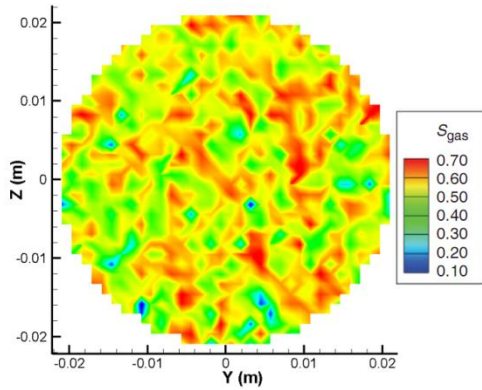


Figure 4.7 Simulated CO₂ saturation in middle slice (Krause *et al.* 2011)

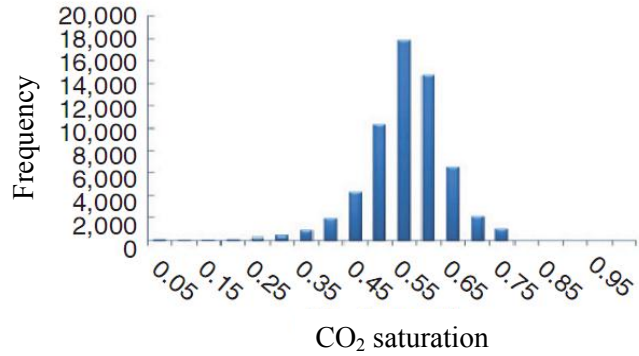


Figure 4.8 Simulated CO₂ saturation histogram (Krause *et al.* 2011)

4.2 Coreflood Simulation with IPARS

4.2.1 CORE MODEL BASED ON HETEROGENEOUS PERMEABILITY AND POROSITY

We constructed a 3D simulation model using the same core properties used by Krause *et al.* (2011). We modeled the core using Cartesian grid, because IPARS does not currently support the cylindrical grid system. The number of grids is $32 \times 32 \times 32$ in x, y, and z directions with a total of 32768 gridblocks (Figure 4.9). The grid sizes in our model is about $1.27 \text{ mm} \times 1.27 \text{ mm} \times 6.35 \text{ mm}$ in x, y, and z directions, compared to the CT scan resolution of $0.254 \text{ mm} \times 0.254 \text{ mm} \times 1.5 \text{ mm}$. The numerical grid resolution was selected to ensure accurate results and fast CPU times for many simulations required to history match lab results and perform sensitivity studies.

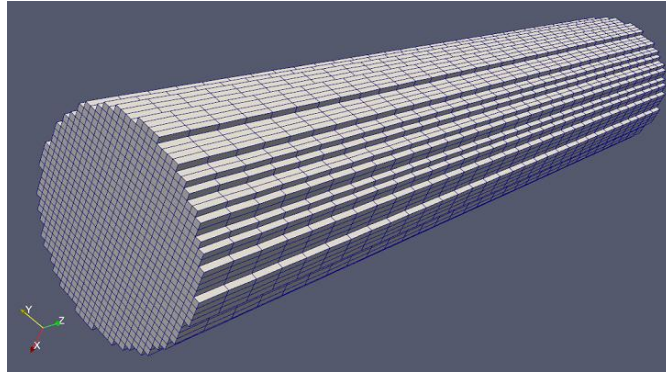


Figure 4.9 IPARS simulation grid using $32 \times 32 \times 32$ cells

The simulated fluid properties of density, viscosity, and CO_2 dissolution were similar to the measured data (Table 4.1) after the EOS parameters were tuned. The pressure and temperature in the simulation model are the same as the experimental condition with an initial pressure of 12.41 MPa and an initial temperature of 50 °C. The calculated solubility of CO_2 in brine was about 0.013 mole fraction, which is consistent with the measured value. Wells are used to model the inflow and outlet boundary conditions of constant injection rate and constant pressure, respectively. The inlet well injects supercritical CO_2 (saturated with brine) at a constant rate of 3 ml/min with a constant producer at 12.41 MPa at the other end of the core. The injection continues until 100% CO_2 is produced at the outlet.

Relative permeability and capillary pressure curves presented by Krause *et al.* (2011) were used. The process of CO_2 injection into a brine-saturated core is a drainage process for which drainage relative permeability and capillary pressure curves should be used. We matched the relative permeability and capillary pressure curves using the Brooks-Corey function (Brooks and Corey, 1964), as follows:

$$k_{rw} = k_{rw}^0 (\bar{S}_w)^{\lambda_w} \quad (4.1)$$

$$k_{rg} = k_{rg}^0 (1 - \bar{S}_w)^{\lambda_g} \quad (4.2)$$

$$P_c = P_{c,entry} (\bar{S}_w)^{-\frac{1}{\lambda_{pc}}}, \quad (4.3)$$

where $\bar{S}_w = \frac{S_w - S_{wr}}{1 - S_{wr} - S_{gr}}$ is the normalized water saturation, S_{wr} is the residual water saturation, S_{gr} is the residual CO₂ saturation. Table 4.2 gives the model parameters. Figure 4.5 and Figure 4.6 show the fitted curves to laboratory data.

Table 4.2 Drainage relative permeability and capillary pressure model parameters

Brine endpoint relative permeability, k_{rw}^0	1
CO ₂ endpoint relative permeability, k_{rg}^0	0.60
Brine relative permeability exponent, λ_w	3.8
CO ₂ relative permeability exponent, λ_g	1.75
Entry capillary pressure, $P_{c,entry}$ (kPa)	5.63
Capillary pressure exponent, λ_{pc}	0.7

4.2.2 POROSITY-PERMEABILITY CORRELATION

Several porosity-permeability correlations, such as Carman-Kozeny, have been developed to compute permeability based on measured porosity (Kozeny, 1927; Carman, 1937). Several published data (Collins and Jordan, 1961; Jensen *et al.*, 1987) show that the porosity follows a normal distribution, whereas permeability follows a log-normal distribution. The distributions of the porosity and permeability could be described by the mean and standard deviation (σ_{std}) of a normal distribution. The standard deviation can be described by the Dykstra-Parsons variation coefficient (V_{DP}) (Dykstra and Parsons 1950) as

$$\sigma_{std} = \ln(1/(1 - V_{DP})). \quad (4.4)$$

The Dykstra-Parsons coefficient of permeability variation is commonly used to describe the reservoir heterogeneity. A homogeneous reservoir has a permeability variation that approaches zero while an extremely heterogeneous reservoir would have a permeability variation approaching one. The same concept is adopted to describe heterogeneity of the core.

$$V_{DP} = (k_{50} - k_{84.1})/k_{50}, \quad (4.5)$$

where K_{50} is permeability with >50% of cumulative probability and $K_{84.1}$ is permeability with >84.1% of cumulative probability, which is one standard deviation from the mean.

The 3D model was constructed with permeability and porosity generated using FFTSIM software based on geostatistics (Jennings *et al.*, 2000). The model input parameters are the correlation length, natural log of mean permeability, and Dykstra-Parsons coefficient (V_{DP}). The output is a set of normally distributed values for each grid. Table 4.3 gives the input parameters.

Table 4.3 FFTSIM input parameters

N_x, N_y, N_z	$32 \times 32 \times 32$	ϕ_{avg}	0.185
Seed number	9	$\sigma_{std,\phi}$	0.1
V_{DP}	0.8	$\ln(k_{avg})$ (md)	4.4
σ_{std}	1.61	$\sigma_{std,K}$	1.7
Dimensionless correlation length in x, y, z directions	$0.41 \times 0.41 \times 1.0$		

The porosity is first generated using the average porosity reported from the laboratory, standard deviation, and a normal distribution of $Z_{i,j,k}$. Figure 4.10 gives the histogram of porosity distribution.

$$\phi_{i,j,k} = \phi_{avg} + \sigma_{std,\phi} Z_{i,j,k} \quad (4.6)$$

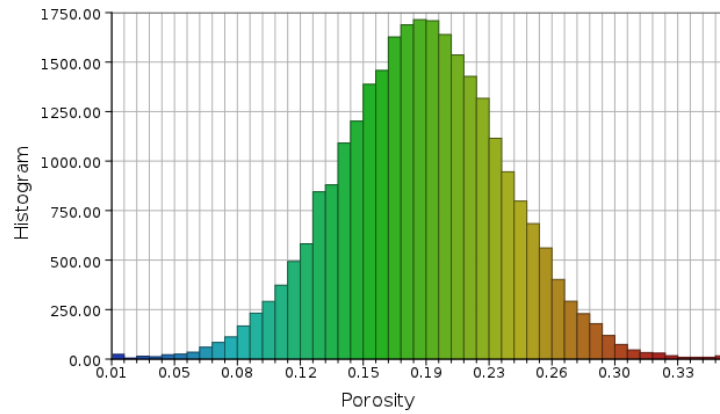


Figure 4.10 Generated porosity with normal distribution

The permeability distribution is then generated using the measured average permeability and the standard deviation as

$$\ln(k_{i,j,k}) = \ln(k_{avg}) + \sigma_{std,K} Z_{i,j,k} \quad (4.7)$$

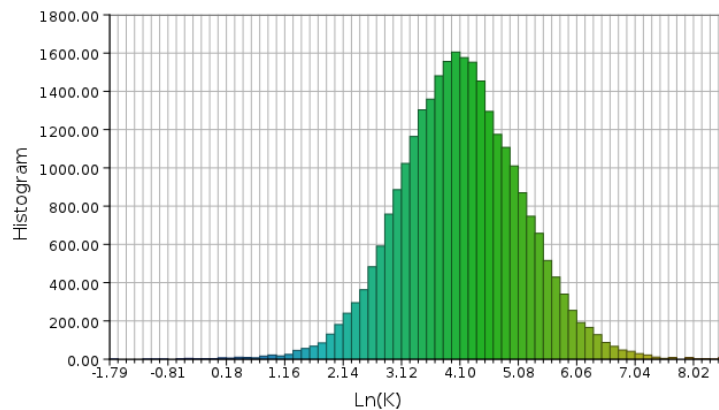


Figure 4.11 Log normal distribution of permeability ($Ln(k)$)

The permeability histogram follows a log-normal distribution (Figure 4.11). The input mean porosity and permeability and standard deviations were adjusted until measured values reported by Krause *et al.* (2011) were obtained. Figure 4.12 gives the porosity distribution with an average of 0.185. The average permeability is 84.7 md.

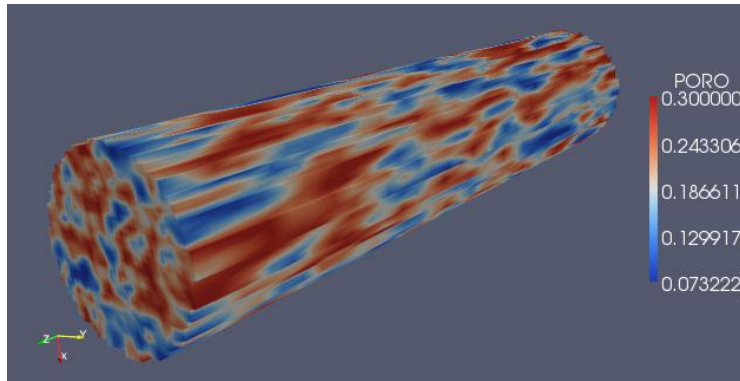


Figure 4.12 Porosity distribution in the core model

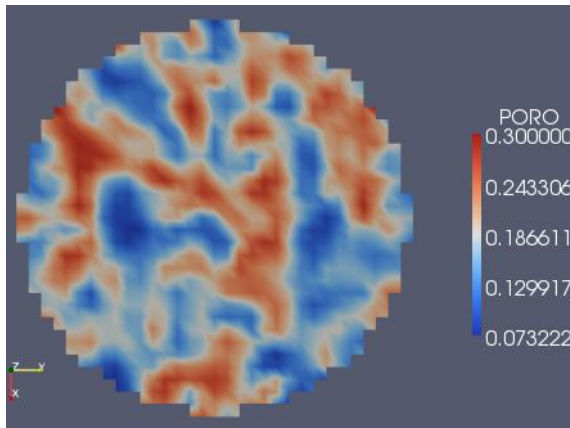


Figure 4.13 Porosity in middle slice (#16)

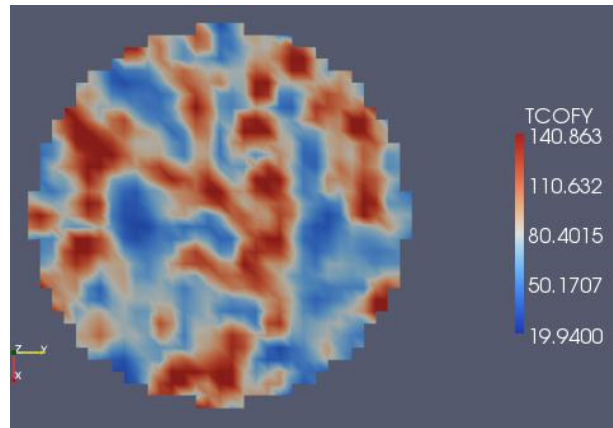


Figure 4.14 Permeability in middle slice (#16)

The porosity and permeability were correlated as shown in the middle slice (#16) of the core (Figure 4.13 and Figure 4.14). The slice-averaged porosity and permeability along the core length have a strong correlation, as shown in Figure 4.15. Slice #16 was

chosen in order to be consistent with the plotting location used by the original experiment (Krause *et al.*, 2011).

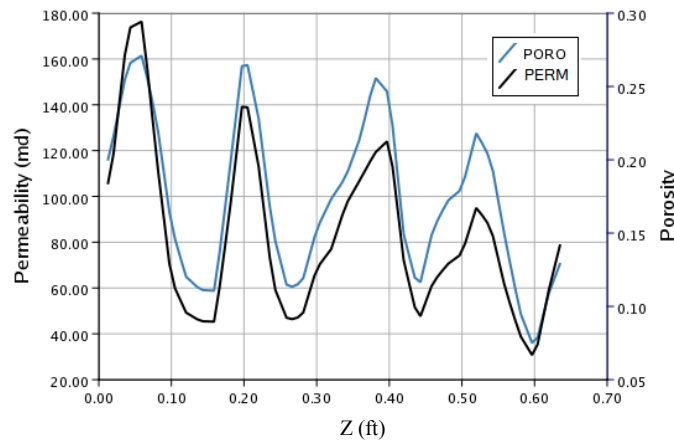


Figure 4.15 Correlated permeability and porosity along the core

Different approaches were studied for the mean values of porosity and permeability when generating the geostatistical distribution. The arithmetic mean for porosity and geometric mean for core permeability gave closer results of average saturation and pressure drop when compared to the measurements.

4.2.3 CAPILLARY PRESSURE MODEL

Capillary forces play a critical role in CO₂ trapping and migration. For CO₂-brine systems, the brine phase is the wetting phase and CO₂ is the non-wetting phase that could be trapped in the pore spaces. For a core initially saturated with brine, enough pressure differentials are needed to push CO₂ into the core and displace the water using CO₂ (*i.e.* entry capillary pressure). The capillary pressure is affected by many factors, such as the interfacial tension (IFT), the contact angle, and the permeability and porosity. A dimensionless J-function for rocks with similar pore structure was developed to model

the capillary pressure based on the fluid interfacial tension and rock properties (Leverett 1941), as follows,

$$J(S_w) = \frac{P_c(S_w)}{\sigma \cos \theta} \sqrt{\frac{k}{\phi}} \quad (4.8)$$

The capillary pressure model in IPARS includes the use of Leverett J-function scaling where the capillary pressure in each grid is adjusted based on the permeability, porosity, and interfacial tension, as follows:

$$P_c = J(S_w) \sigma \cos \theta \sqrt{\frac{\phi}{K}} = P_{c,ref} \frac{\sigma \cos \theta}{\sigma_{ref} \cos \theta_{ref}} \left(\frac{\phi}{k}\right)^{0.5} \left(\frac{k}{\phi}\right)_{ref}^{0.5}, \quad (4.9)$$

here the subscript *ref* represents a measured porosity of 0.185 and a permeability of 84.7 md. Figure 4.16 gives an example of capillary pressure curves for different permeability values.

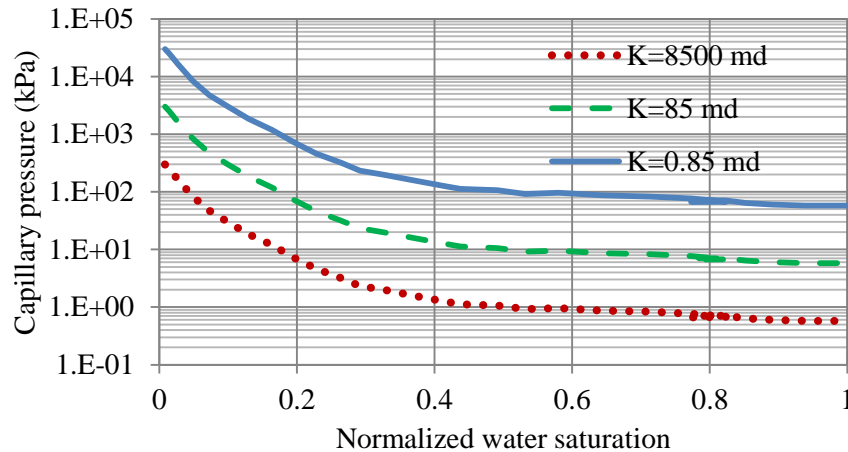


Figure 4.16 Capillary pressure curves for different permeability values with J-function

4.3 IPARS Coreflood Simulation Results

We performed simulations using different permeability and porosity distributions. We studied the effect of capillary pressure, permeability/porosity heterogeneities, and residual water saturation on CO₂ distributions. Case studies were designed to study the impact of different petrophysical models on simulation results (Table 4.4). The core with the same porosity and permeability distributions is used for all these simulation cases.

Table 4.4 Coreflood simulation cases.

<i>Case #</i>	<i>Description</i>	<i>Residual water sat. (S_{wr})</i>	<i>P_c scaling</i>
1	History match simulation	0.0	Yes
2	Sensitivity to S_{wr} and P_c scaling	0.2	No
3	Sensitivity to K_r and P_c with different S_{wr}	0.0, 0.1, 0.2	Yes

Case 1 represents a history match simulation with the Leverett J-function capillary pressure scaling using Eq. 4.9 and a zero residual brine saturation (S_{wr}). In Case 2 the impact of capillary pressure scaling on CO₂ saturation distribution was investigated. Here no scaling for capillary pressure was used and $S_{wr} = 0.2$ was assumed. In Case 3 the sensitivity to residual brine saturation was studied. The final CO₂ saturation distributions and histograms, and average saturations are compared and discussed below.

4.3.1 CASE 1: HISTORY MATCH SIMULATION

We studied the range of CO₂ saturations from the experimental results (Figure 4.4) and found the presence of CO₂ saturations higher than 0.95. This is inconsistent with the measured residual water saturation of 0.2 from the drainage capillary pressure and relative permeability curves. Therefore, we assumed a residual water saturation of zero

and included the J-function for capillary pressure scaling. The simulated CO₂ saturation profile is given in Figure 4.17.

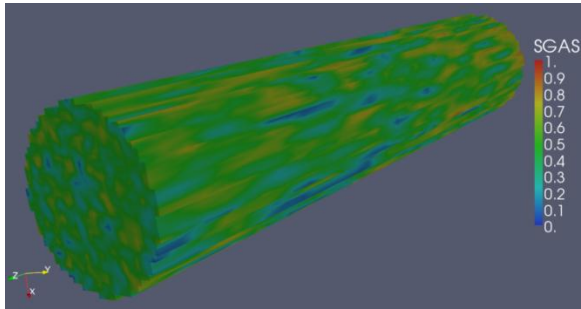


Figure 4.17 Final CO₂ saturation simulated using IPARS (grid size of 1.27 mm × 1.27 mm × 6.35 mm)

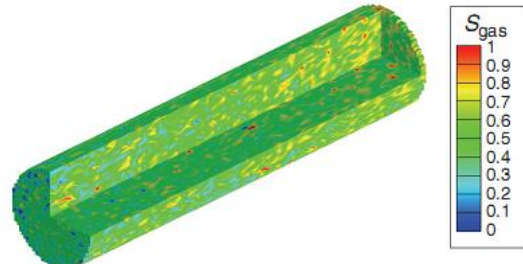


Figure 4.18 CT-scan measured final CO₂ saturation (Krause *et al.* 2011)

The simulated CO₂ saturation corresponding to the middle slice of the core in Figure 4.19 shows the impact of heterogeneity on the saturation profile. Simulation results are quite similar to those measured (Figure 4.20), with features of locally high and low CO₂ saturation contrast.

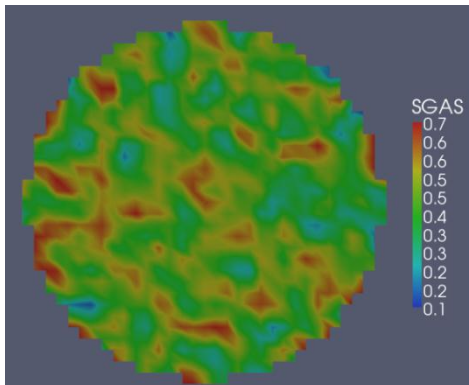


Figure 4.19 IPARS simulation results of CO₂ saturation in middle slice (#16)

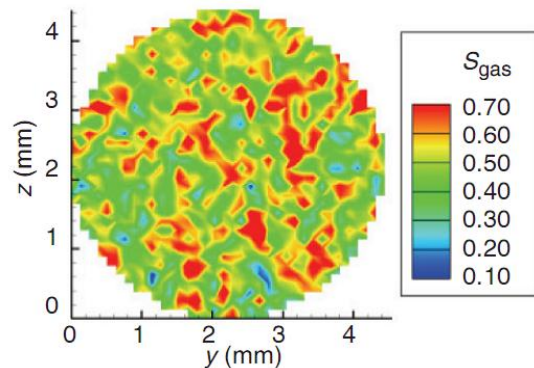


Figure 4.20 CT-scan measured CO₂ saturation in middle slice (Krause *et al.*, 2011)

The final CO₂ saturation histogram calculated based on grid values is plotted in Figure 4.21 with a distribution similar to the normal distribution exhibited by

experimental data (Figure 4.22). There are very low and very high CO₂ saturations consistent with laboratory observations. The final average CO₂ saturation is about 0.52, and this is also consistent with the reported value.

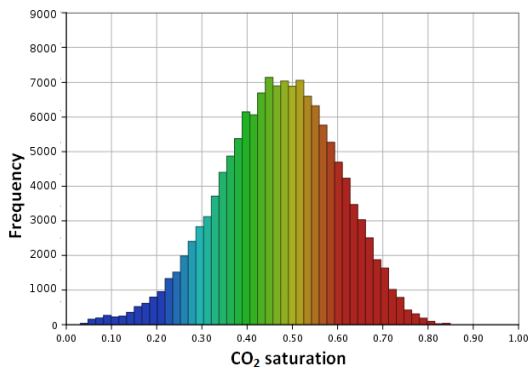


Figure 4.21 IPARS simulation result of CO₂ saturation histogram for Case 1

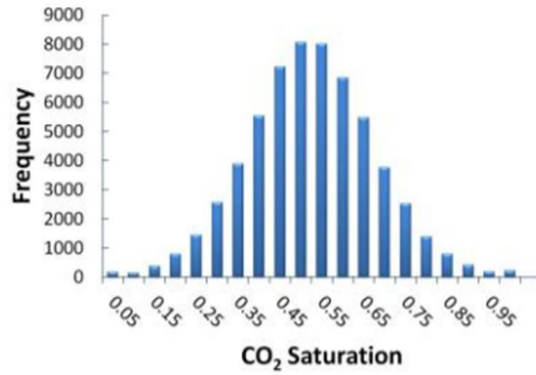


Figure 4.22 Experimental histogram of CO₂ saturation (Krause *et al.*, 2011)

The slice-averaged calculated saturation and porosity along the core is shown in Figure 4.23, where a clear correlation between saturation and porosity is observed for Case 1. A similar trend was observed in another coreflood experiment by Perrin and Benson (2010), shown in Figure 4.24.

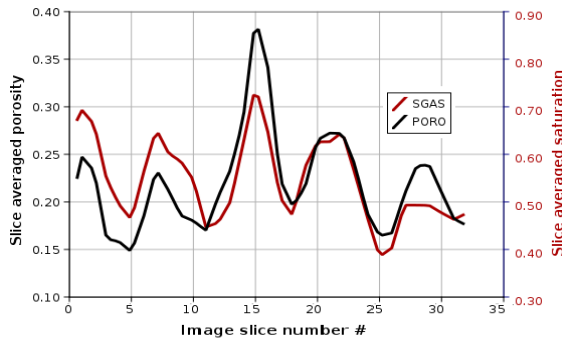


Figure 4.23 Simulation results of slice-averaged CO₂ saturation and porosity along the core for Case 1

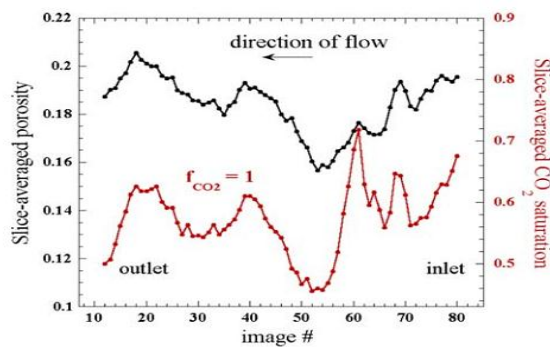


Figure 4.24 Measured slice-averaged saturation along the core (Perrin and Benson, 2010)

4.3.2 CASE 2: SENSITIVITY TO CAPILLARY PRESSURE SCALING

For simulation Case 2, we excluded the J-function scaling for the capillary pressure and assumed a constant residual water saturation of 0.2. The same porosity and permeability distributions as the Case 1 are used. The simulation result of the CO₂ saturation profile is quite uniform (Figure 4.25) and lacks the saturation contrast characteristics observed in the experiment (Figure 4.26).

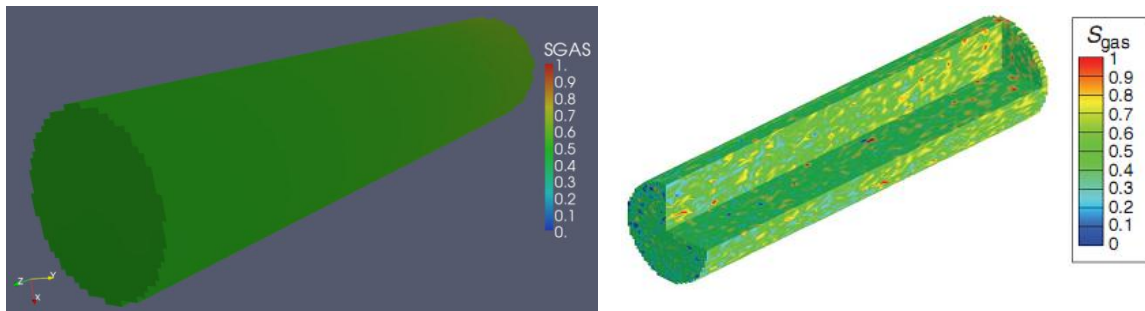


Figure 4.25 Final CO₂ saturation simulation Case 2

Figure 4.26 Measured CO₂ saturation (Krause *et al.*, 2011)

The CO₂ saturation histograms are compared in Figure 4.27 and Figure 4.28, which shows a large difference in CO₂ saturation distribution between the two. The saturation distribution is not correlated to the heterogeneity when only one capillary pressure curve is used, and it is not scaled according to permeability and porosity variations.

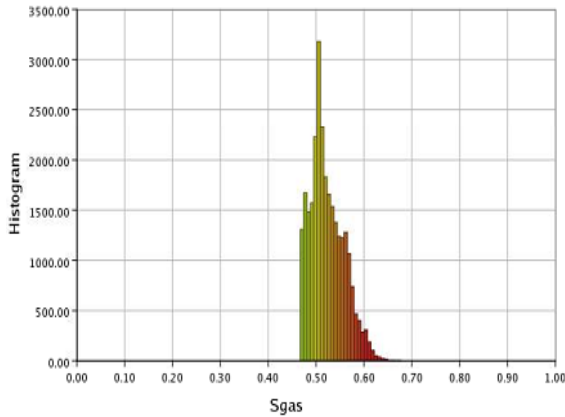


Figure 4.27 CO₂ saturation histogram from simulation Case 2

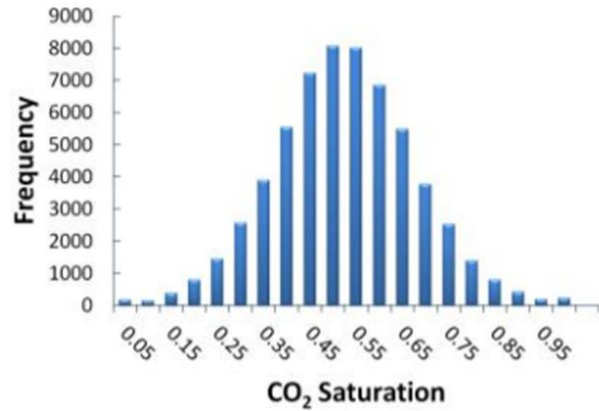


Figure 4.28 Experimental histogram of CO₂ saturation (Krause *et al.*, 2011)

4.3.3 CASE 3: SENSITIVITY TO RESIDUAL BRINE SATURATION

There are some uncertainties associated with residual water saturation after many pore volumes of CO₂ injection. The measured drainage capillary pressure and relative permeability curves indicated a residual water saturation of 0.2 (Figure 4.5), which seems to be inconsistent with the results presented in the measured CO₂ saturation histogram (Figure 4.4).

In order to relax the assumption we made in Case 1 that the residual water saturation was below the value measured during the drainage relative permeability experiment due to drying or other pore scale effects, we conducted sensitivity simulations using different values of S_{wr} . We repeated the simulations with $S_{wr} = 0.0, 0.1, 0.2$. We also scaled relative permeability and capillary pressure curves in accordance with changes in residual water saturation (Figure 4.29 and Figure 4.30). The capillary pressure scaling based on the J-function was also included.

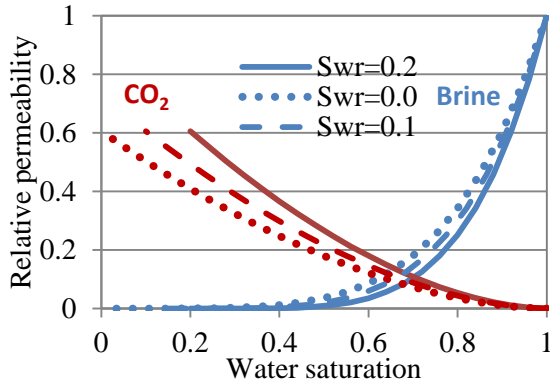


Figure 4.29 Relative permeability curves for $S_{wr} = 0.0, 0.1, 0.2$.

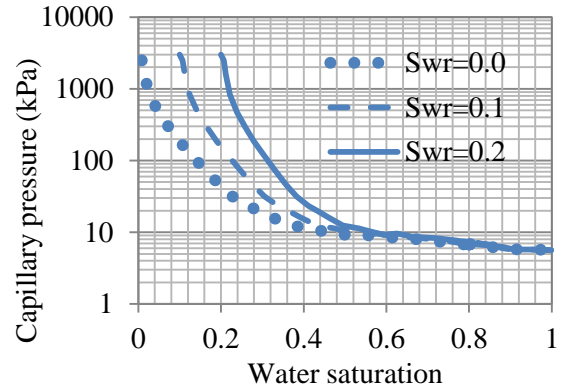


Figure 4.30 Capillary pressure curves for $S_{wr} = 0.0, 0.1, 0.2$.

The simulated CO_2 saturation distribution is shown in Figure 4.31, where less variation is observed as compared to the laboratory results (Figure 4.32).

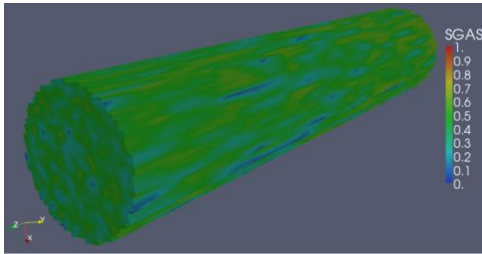


Figure 4.31 CO_2 saturation results using IPARS for Case 3 with $S_{wr} = 0.2$.

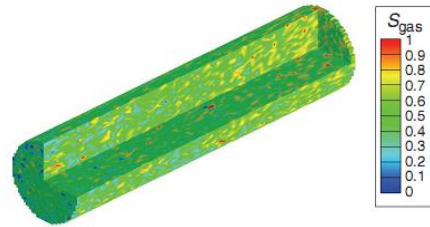


Figure 4.32 CT-scan measured CO_2 saturation (Krause *et al.* 2011)

The simulated CO_2 saturation in the middle slice is shown in Figure 4.33, Figure 4.34, and Figure 4.35 for Case 3, and it is compared to the laboratory observations in Figure 4.36. The CO_2 saturation is lower than experimental values (Figure 4.36) when the residual water saturation is non-zero. The average CO_2 saturation for the whole core is also less than the measured value of 0.5026.

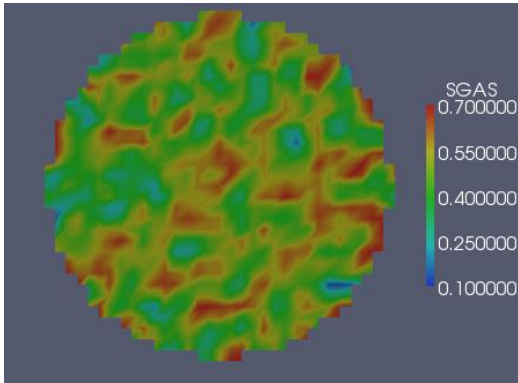


Figure 4.33 CO₂ saturation profile for Case 3 with $S_{wr} = 0.0$.

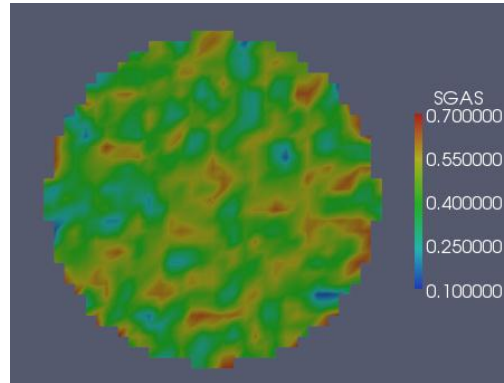


Figure 4.34 CO₂ saturation profile for Case 3 with $S_{wr} = 0.1$.

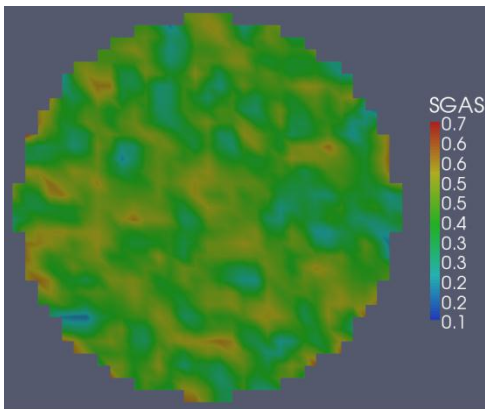


Figure 4.35 CO₂ saturation profile in the middle slice for Case 3 with $S_{wr} = 0.2$

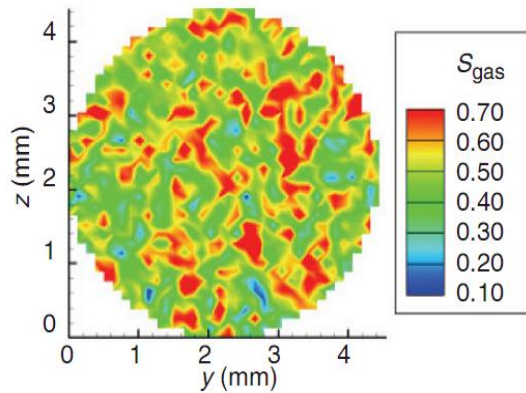


Figure 4.36 Experimental CO₂ saturation profile in middle slice (Krause *et al.*, 2011)

The histograms are compared in Figure 4.37, Figure 4.38, and Figure 4.39, where the distribution for the lower half of the saturation is similar to experimental results (Figure 4.40), but saturation values higher than 0.7 are missing. This demonstrates the significance of residual water saturation modeling for coreflood simulation results. The

lack of high CO₂ saturation in the coreflood simulation with high S_{wr} implies that it S_{wr} may have a non-uniform distribution in the core.

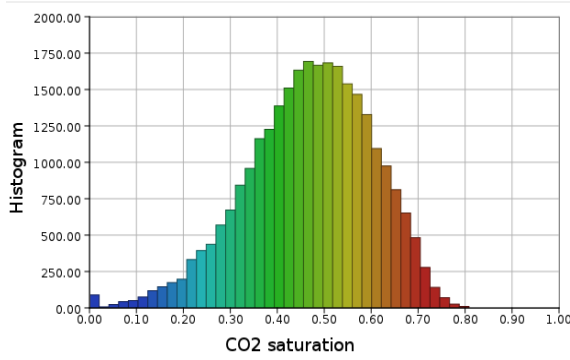


Figure 4.37 Case 3 CO₂ saturation histogram using $S_{wr} = 0.0$

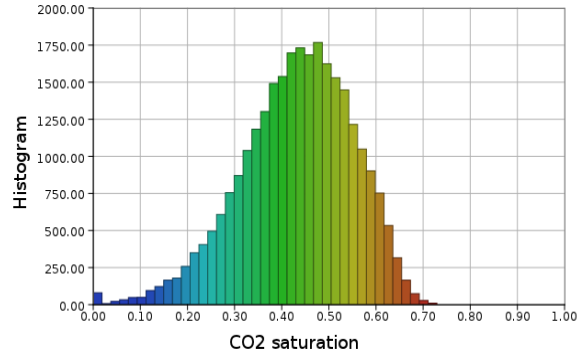


Figure 4.38 Case 3 CO₂ saturation histogram using $S_{wr} = 0.1$

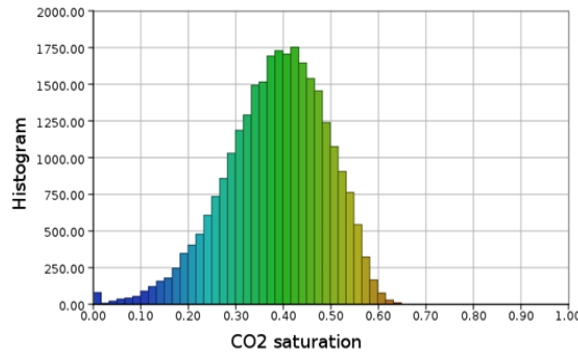


Figure 4.39 Simulation histogram of CO₂ saturation for Case 3 with $S_{wr} = 0.2$

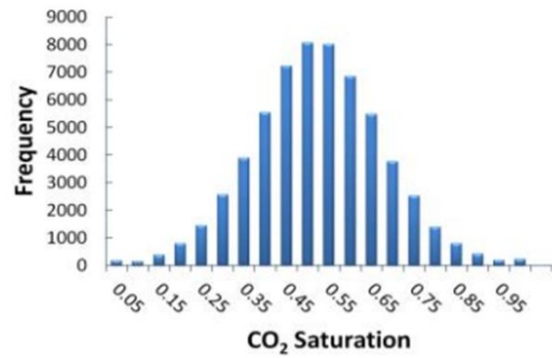


Figure 4.40 Experimental histogram of CO₂ saturation (Krause *et al.*, 2011)

4.4 Summary

In this study, a high resolution CO₂-brine coreflood simulation was conducted on the advanced, in-house reservoir simulator IPARS, using a core model with a fine resolution of 1.27 mm×1.27 mm× 6.35 mm. We developed a new coreflood simulation

model based on geostatistical data and a compositional fluid flow framework. Core permeability and porosity distributions were constructed based on geostatistical data and FFTSIM software package, maintaining correlated trends between permeability and porosity. Capillary pressure was scaled in every grid cell based on the Leverett J-function, coupling the heterogeneous permeability and porosity. Our coreflood simulation result agreed well with published, experimental results. Published laboratory observations were successfully reproduced and history-matched. The similar normal distribution of the CO₂ saturation histogram and the correlated trend between saturation and porosity were observed. A sensitivity study of the residual water saturation modeling revealed the uncertainty in coreflood typical curves modeling, which indicated a constant non-zero residual saturation might not be necessary for coreflood simulations. Simulation results demonstrated that the accurate representation of capillary pressure at small scales was critical in order for simulations to capture coreflood characteristics. The core model and the simulation study both revealed the significance of subcore scale heterogeneity on final CO₂ saturation distribution. A numerical coreflood model was successfully validated against experiments. This coreflood modeling and simulation study will be valuable for future study of the many complex processes involved in this topic.

Some highlights and findings are listed, as follows:

- Krause *et al.* (2011) made an attempt to history match their coreflood using the CT scan images of porosity and generating permeability distributions using several Leverett J-function models and an extension of Calhoun permeability equation. Although they obtained a good history match for average saturation, the images of final saturation map and calculated saturation histogram were still different from the measured data. We decided to use a different approach to

history match the same coreflood using log normal permeability and normal porosity distributions. The arithmetic mean for porosity and geometric mean for permeability gave comparable results to the experiment including pressure drop across the core.

- We used Brooks-Corey model to fit measured relative permeability and capillary pressure curves and then scaled the capillary pressure using the J-function based on geostatistically generated porosity and permeability distributions.
- Scaling of capillary pressure using J-function and heterogeneity was critical to capture sub-core flow characteristics. Simulated results gave large local variations in CO₂ saturation similar to measured CT images.
- The measured final CO₂ saturation gave saturations greater than 0.8, indicating that the residual water saturation was lower than the measured value of 0.2 obtained from the relative permeability and capillary pressure experiments. Therefore, we considered residual brine saturation in addition to permeability and porosity distributions as history match parameters. We used constant residual brine saturation in these simulations where the value of zero gave the best match of the measured saturation histogram. We demonstrated the sensitivity of simulation results to residual brine saturation. We believe that the residual brine saturation needs to be correlated to porosity distributions in order to capture subcore heterogeneity and fluid displacement.

CHAPTER 5: CO₂ Sequestration Simulation with IPARS

Many different CO₂ sequestration scenarios are set up and simulated with IPARS. The impacts of different petrophysical models on CO₂ sequestration are studied.

5.1 Stacked Geological Model

A stacked reservoir model with multiple geological layers is configured in IPARS, with approximately 4 million grid cells. The goal of this test case is to study the migration of CO₂ in multiple aquifers and seals. The capability of IPARS is tested with a 4 million grid model running in parallel using as many 128 processors.

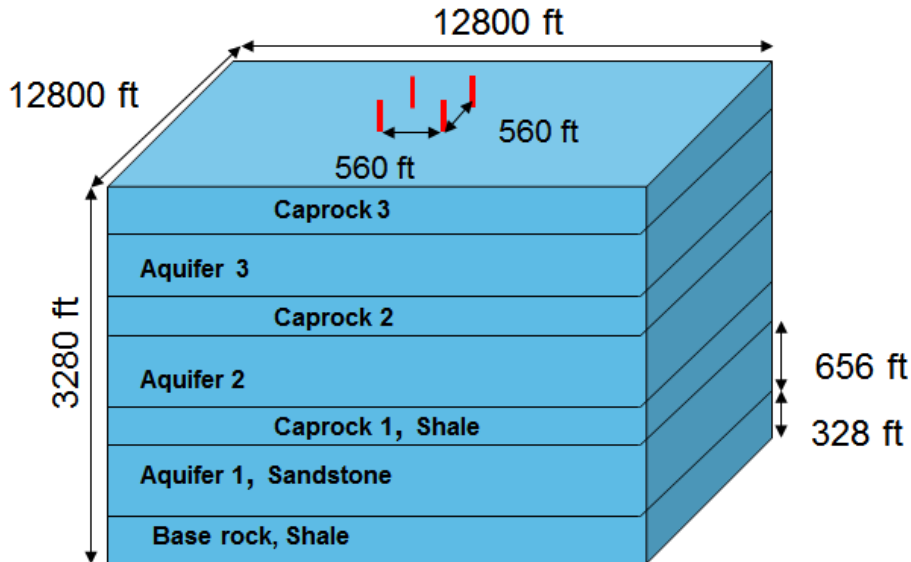


Figure 5.1 Reservoir model configured for the stack aquifer CO₂ sequestration simulation, the four injection wells are completed only in aquifer layer 1

In this stacked geological model, there are four shale layers and three aquifer layers stacked in such a way that one seal i.e. impermeable shale rock lies above each aquifer (Figure 5.1). The three aquifers have the same thickness of 656 ft, and the seal

layers thickness are 328 ft. The total thickness of the model is 3280 ft, with the topmost aquifer corner at 2624 ft. Four injection wells are located in the center of the reservoir, and wells are separated by 560 ft from each other. The four injection wells are completed in the aquifer layer 1, with a perforation length of 100 ft in the lower part. The model parameters are given in Table 5.1.

Table 5.1 Model parameters for the stacked aquifer simulation

Aquifer size, L, W, H (ft)	12800 × 12800 × 3280
Mesh (X,Y,Z)	128× 256×128
Grid size (ft)	100 × 100 × 20
Reservoir dip (degree)	0
Top corner depth (ft)	2624
Aquifer temperature °F	110
Initial pressure (psi)	2300 at 5248 ft
Horizontal permeability (md)	Aquifer: 96, Shale: 0.18
K _v /K _h ratio	0.1
Porosity	Aquifer: 0.20; Cap rock: 0.05
Well position	Four wells in the center of aquifer 1; depth 5248~5348 ft, spacing 560 ft
Vertical well completion length (ft)	100
Initial water saturation	1
Injection rate for each well (MSCFD)	6000
Injection period	5 years injection, 5 years shut-in

The relative permeability and capillary pressure curves are from acquired literature (Bennion and Bachu, 2006a,b).

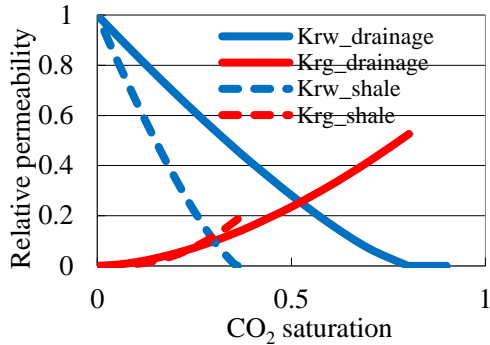


Figure 5.2 Relative permeability curves for shale and sandstone aquifer (Bennion and Bachu, 2006a,b)

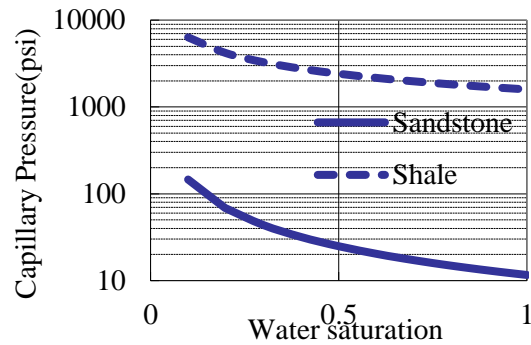


Figure 5.3 Capillary pressure curves for shale and sandstone aquifer (Bennion and Bachu, 2006a,b)

Table 5.2 Rock properties for aquifer and seal are from (Bennion and Bachu, 2006a)

	Aquifer sandstone Cardium #1	Shale cap rock Calmar
Porosity	0.2	0.05
Average permeability (md)	96	0.18
Residual water saturation, S_{wres}	0.197	0.638
Residual CO ₂ saturation, S_{gt}	0.102	0.256
Endpoint water relative permeability, K_{rw}^0	0.905	0.282
Endpoint CO ₂ relative permeability, K_{rg}^0	0.526	0.1875
Exponent for water drainage relative permeability, $\lambda_{w,drainage}$	1.3	1.3
Exponent for CO ₂ drainage relative permeability, $\lambda_{g,drainage}$	1.7	2.5
Exponent for water imbibition relative permeability, $\lambda_{w,imbibe}$	1.2	4
Exponent for CO ₂ imbibition relative permeability, $\lambda_{g,imbibe}$	1.2	2.2
Entry capillary pressure (psi)	10	1200

We can see from Figure 5.2 that shale rock has a very low gas relative permeability (endpoint of 0.1875) and high residual water saturation (0.638). The

capillary pressure in Figure 5.3 shows that shale rock has an entry capillary pressure (1200 psi) that is much higher than the sandstone aquifer rock. This could prevent CO₂ entry to the seal.

The permeability field for shale layers and aquifer sandstone layers are generated using geostatistical tool FFTSIM (Jennings *et al.*, 2000), using the average permeability for shale and sandstone listed in Table 5.2. Each of the four shale layers has $8 \times 128 \times 256$ grids. Each of the sandstone aquifer layers has $32 \times 128 \times 256$ grids. We used the same permeability distribution for all three shale layers. We used same permeability distribution for the upper aquifer sandstone layers 2 and 3. The permeability field in lowest aquifer layer 1 is scaled as 5 times to permeability in aquifer layers 2 and 3, for each of the $32 \times 128 \times 256$ grids. The permeability for the whole model, including the shale and aquifer sandstone, is shown in Figure 5.4. Aquifer rock has higher permeability than seal rock.

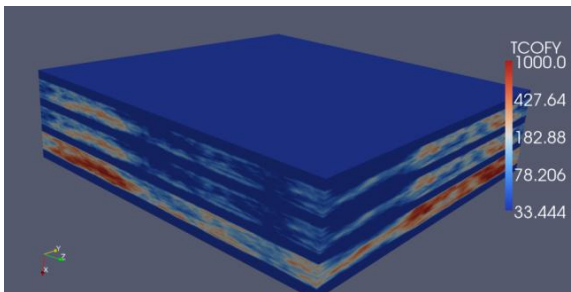


Figure 5.4 Horizontal permeability (md) for the stacked model

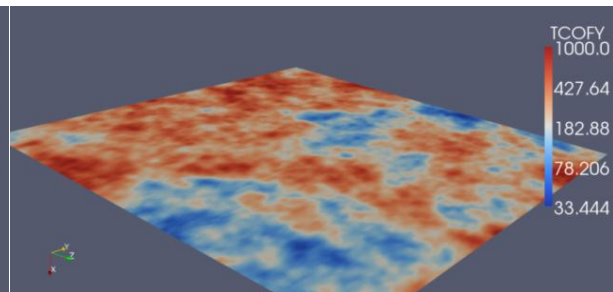


Figure 5.5 Permeability (md) distribution in the injection layer

The permeability field in the horizontal plane at injection depth is shown in Figure 5.5. Permeability in cross-section of the whole model is shown in Figure 5.6. We can clearly see the change of rock type and permeability distribution from aquifer to seal.

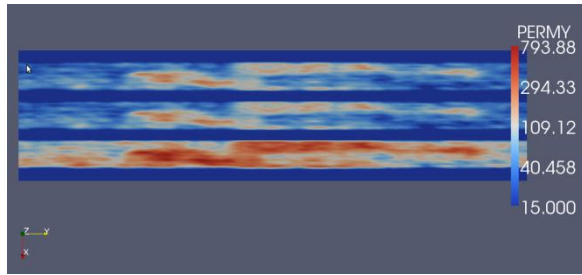


Figure 5.6 Reservoir permeability (md) at vertical slice for all layers

A base case simulation of 5 years of CO₂ injection followed by 5 years shut in for redistribution was conducted. The CO₂ saturation profile is plotted in the cross-section of the injection well.

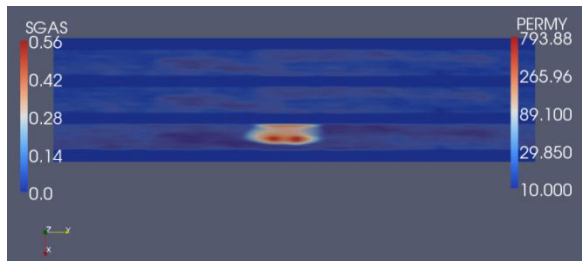


Figure 5.7 CO₂ saturation at the end of 5 years injection for the stacked reservoir case.

The gas saturation distribution after 10 years (5 years after shut in) is given in Figure 5.8. We can see from Figure 5.7 that at the end of 5 years injection period, most of the CO₂ is in near well region and very little CO₂ would have reached the cap rock shale layer 1. At 10 years, more and more CO₂ would have migrated upwards and accumulated under the first shale layer (Figure 5.8). We can also notice that there is no sign of CO₂ migration/leakage beyond the first cap rock. This shows that the shale cap rock would act as an effective stopping barrier for CO₂ migration due to its high entry capillary pressure on the order of 1000 psi and its low permeability.

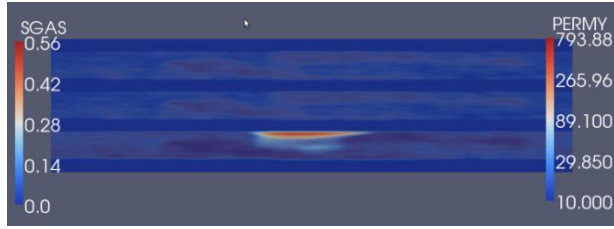


Figure 5.8 CO₂ saturation at the end of 10 years for a stacked reservoir case

5.2 Effect of Interfacial Tension and Capillary Pressure

It is widely observed that IFT, contact angle, and heterogeneous permeability and porosity will affect both the capillary pressure and the residual saturations. A dimensionless function, the Leverett J-function, was developed to couple all these factors for the capillary pressure calculation, by defining a dimensionless Leverett J-function curve for the rock type with similar structure. Given a typical Leverett J-function curve, the capillary pressure curve for a rock of similar pore structure can be calculated for a given condition of wettability, fluid pair properties, and heterogeneity.

The Leverett J-function is implemented to model capillary pressure for different rock and fluid properties in IPARS as

$$J(S_w) = \frac{P_c(S_w)}{\sigma \cos \theta} \sqrt{\frac{k}{\phi}}, \quad (5.1)$$

where θ is the contact angle.

The capillary pressure for each grid block is calculated based on the *in situ* conditions of k , ϕ , σ , θ , and the reference capillary pressure curve from the J-function.

5.2.1 IMPACT OF CAPILLARY PRESSURE SCALING BASED ON J-FUNCTION

The simulation model is configured with an inverted five-spot injection scenario, with one constant-rate CO₂ injector at the center and four constant-pressure producers in the four corners of the aquifer. The reservoir is 940 ft × 880 ft × 100 ft, with a grid size

of 20 ft × 20 ft × 5 ft. The injection well is open through the entire thickness of the aquifer. CO₂ injection continues for 365 days at a constant rate of 500 MSCFD, and then the well is shut-in for another 730 days as a redistribution phase.

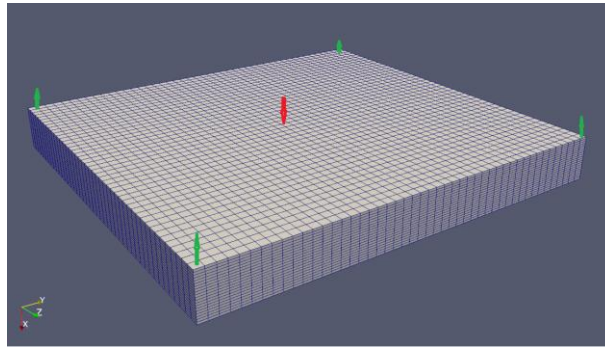


Figure 5.9 Reservoir model for the Leverett J-function test case (red: injector; green: boundary well)

The reservoir model exhibits both heterogeneous porosity and permeability. The permeability and porosity are generated using FFTSIM program with average permeability of about 300 md and average porosity of about 0.2.

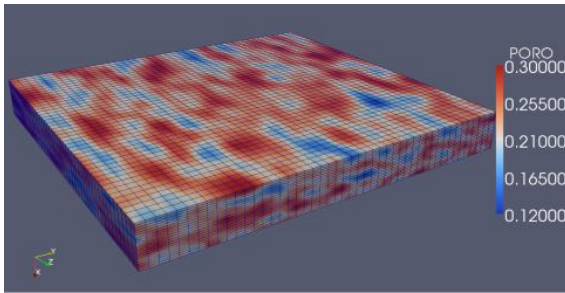


Figure 5.10 Heterogeneous porosity for J-function test case

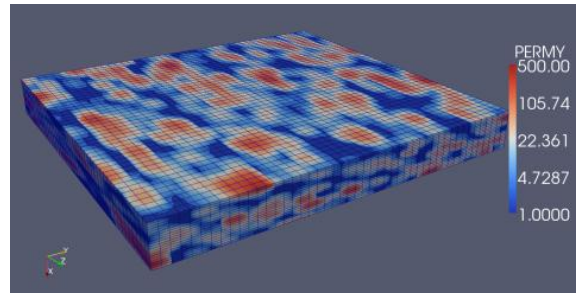


Figure 5.11 Heterogeneous permeability for J-function test case

A set of drainage relative permeability and capillary pressure curves for water wet rock is used for the J-function test case. For the drainage process, the residual gas

saturation is zero. The model parameters for the rock-fluid k_r and P_c curves are listed in Table 5.3.

Table 5.3 Input parameters for the J-function test case

Entry capillary pressure, $P_{c,entry}$ (psi)	3.2
Capillary pressure curve exponent, λ_{Pc}	0.7
Water relative permeability curve exponent, λ_w	7.5
CO ₂ relative permeability curve exponent, λ_g	2.7
Endpoint water relative permeability, K_{rw}^0	1
Endpoint CO ₂ relative permeability, K_{rg}^0	0.1
Residual water saturation, S_{wr}	0.2
Residual CO ₂ saturation, S_{gr}	0.0

CO₂ saturation profiles are shown both at the end of 1 year of injection and at the end of 3 years of injection. We can see from the gas saturation at 1 year and at 3 years that modeling capillary pressure based on the Leverett J-function makes a large difference in CO₂ migration and saturation. The saturation profile is more uniform for the case without the impact of heterogeneity on capillary pressure (Figure 5.12-Figure 5.15).

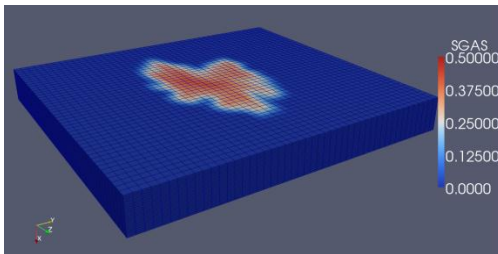


Figure 5.12 CO₂ saturation at 1 year without the Leverett J-function

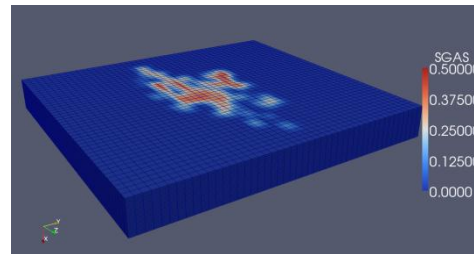


Figure 5.13 CO₂ saturation at 1 year with the Leverett J-function

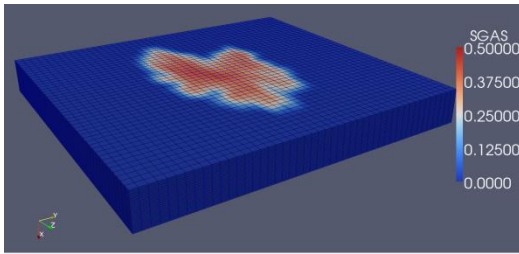


Figure 5.14 CO₂ saturation at 3 years without Leverett J-function

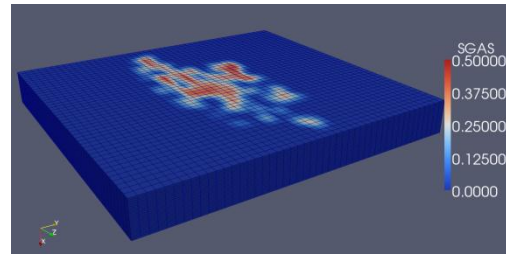


Figure 5.15 CO₂ saturation at 3 years with the Leverett J-function

We can see from gas saturations in cross-section at 1 year and 3 years that heterogeneity plays a much greater role for CO₂ migration when the Leverett J-function model is included (Figure 5.16 and Figure 5.17). CO₂ migration preference to a high permeability channel is more significant than the case without the J-function.

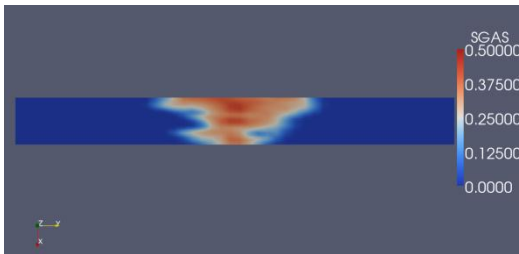


Figure 5.16 Gas saturation in cross-section after 1 year of injection with J-function.

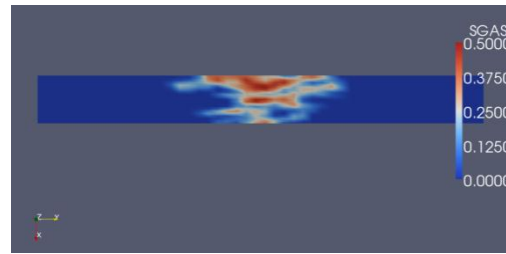


Figure 5.17 Gas saturation in cross-section after 3 years of injection with J-function

5.2.2 IMPACT OF CONTACT ANGLE, IFT, AND WETTABILITY ON CO₂ MIGRATION

Wettability refers to the preference of solid surface to be in contact with one fluid rather than another. The balance of forces in the solid and fluid phases with results in a contact angle θ , between the fluids and solid surface. Wettability will affect the displacement characteristics of CO₂ and water. When the wettability is altered, the contact angle will change (Figure 5.18) as much as ± 20 degrees. The capillary pressure curve will also be affected by the change in the contact angle (Figure 5.19). Hence

modeling contact angle is very important for accurate modeling of capillary pressure and CO₂-water flow

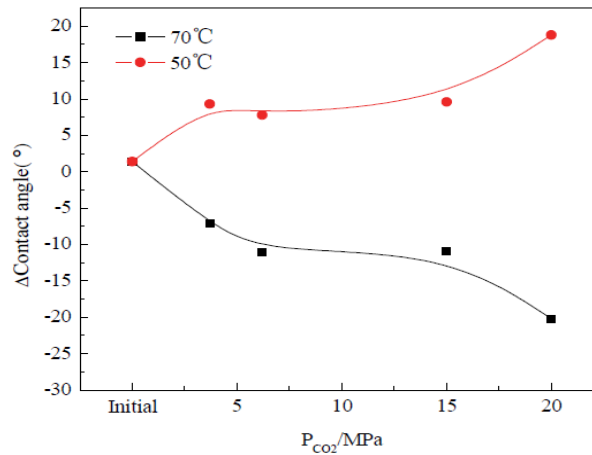


Figure 5.18 Variation in contact angle change at different pressure and temperature (Zhu *et al.*, 2011)

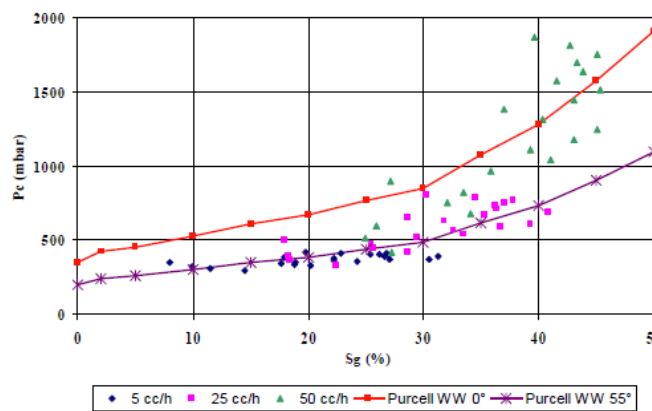


Figure 5.19 Impact of contact angle (Red: $\theta = 0^\circ$, Purple: $\theta = 55^\circ$) on capillary pressure curve (Chalbaud *et al.*, 2007)

The basic relationship between capillary pressure, interfacial tension, and pore throat radius is given by Young-Laplace equation (Young, 1805) as follows:

$$P_c = \frac{2\sigma\cos\theta}{r}, \quad (5.2)$$

where r is the pore throat radius, σ is the interfacial tension, θ is the contact angle.

The Leverett J-function is implemented for capillary pressure, as follows:

$$J(S_w) = \frac{P_c(S_w)}{\sigma \cos \theta} \sqrt{\frac{k}{\phi}}. \quad (5.3)$$

The simulation model is constructed with an inverted five-spot injection pattern, with one constant-rate CO₂ injector at the center and four constant-pressure producers in the four corners of the aquifer in order to maintain constant boundary pressure (Figure 5.20). The reservoir is homogeneous to avoid the impact of heterogeneity on CO₂ plume distribution. We also assume that the interfacial tension is constant throughout the reservoir. The injection well is open in the lower half of the aquifer. CO₂ injection continues for 50 days with a constant rate of 200 MSCFD, and then it stops for 50 days (Table 5.4).

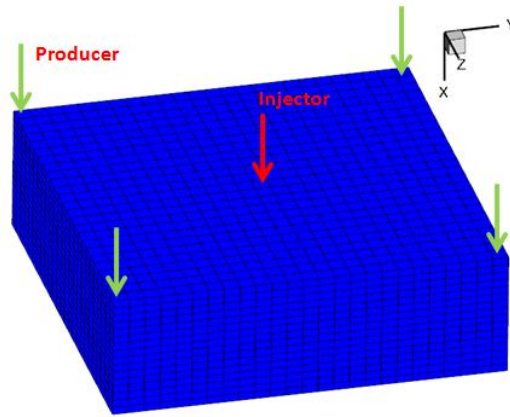


Figure 5.20 Model grid for contact angle tests

Table 5.4 Reservoir model for wettability test case simulation

Number of grid blocks	25 × 25 × 16
Grid size (ft)	10 × 10 × 5
Porosity	0.2
Permeability (md)	100
Injection well rate (MSCFD)	200
Well pattern	Inverted five spot
Injection scheme	Inject 50 days, shut-in 50 days

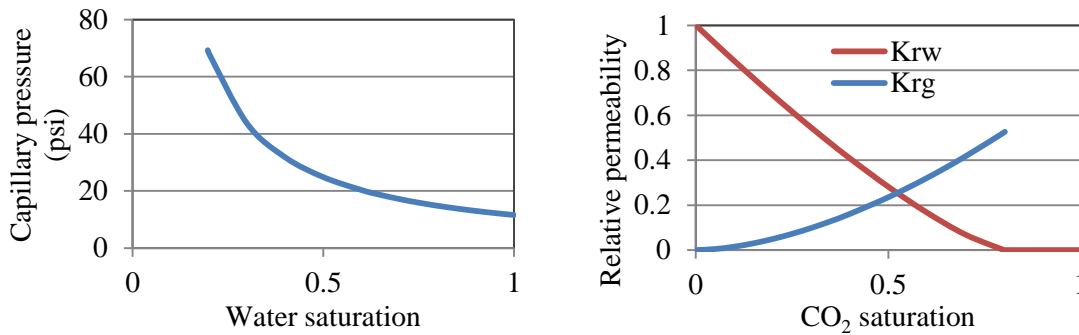


Figure 5.21 Drainage capillary pressure and relative permeability for wettability simulation case

5.2.2.1 Water Wet Case

Four sensitivity tests are used to study the impact of contact angle on CO₂ injection and migration (Table 5.5). We assume that contact angle only impacts capillary pressure. We assumed a constant initial contact angle and also assumed that the injection of CO₂ does not impact the wettability/contact angle in these simulation test cases. Another simplifying assumption is that we used the same relative permeability curves regardless of the rock wettability. This simplification is not true in most conditions, but it is used for simple test for the impact of the contact angle on the capillary pressure. The first case is the base case with no modification of the capillary pressure by contact angle. For the base case, water is the wetting phase, CO₂ is the non-wetting phase, and the

contact angle is 0 degrees. For Case 2, the contact angle is 30 degrees, which means that the reservoir is strongly water wet. For Case 3, the contact angle 60 degrees, which means that the reservoir rock is mixed wet. For Case 4, the contact angle is 90 degree, the rock is neutrally wet, and the capillary pressure is zero.

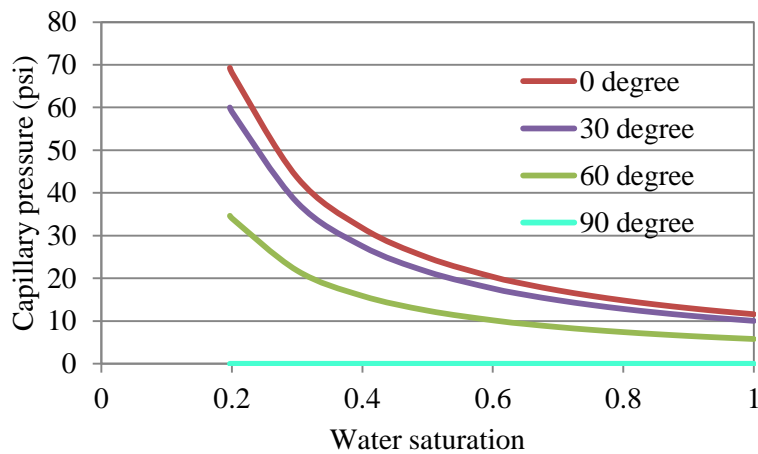


Figure 5.22 Capillary pressure with different contact angles

Table 5.5 Sensitivity test cases for contact angle

Case	Contact angle (degree)	Wettability
1	-	Base case/Water wet
2	30	Water wet
3	60	Mixed wet
4	90	Neural wet

Gas saturation simulation results at 50 days for rock with contact angles from 0 to 90 degrees are shown in Figure 5.23. From the plots in Figure 5.23, we can see that at the end of injection, for the water wet rock, CO₂ saturation near the injection location is lower than the saturation with mixed wet rock. CO₂ plume front is more diffused when the contact angle is small.

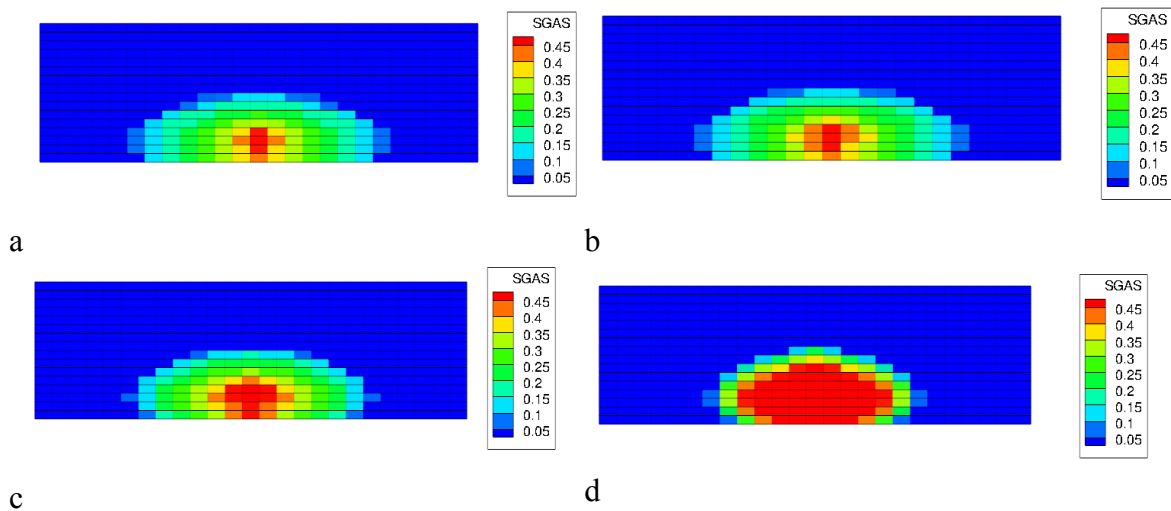


Figure 5.23 CO₂ saturation at 50 days in cross-section of injection well, contact angle a) 0 b) 30 c) 60 d) 90 degrees

From the gas saturation profiles in Figure 5.24, we can see the impact of contact angle on CO₂ migration after injection stops. As contact angle increases from 0 to 90 degrees, the rock becomes increasingly mixed wet. When the rock is strongly water wet, the injected CO₂ migrates upward due to buoyancy force. As the rock becomes more mixed wet, CO₂ saturation near the injection well remains high after 50 days, implying that CO₂ stays closer to the injection zone.

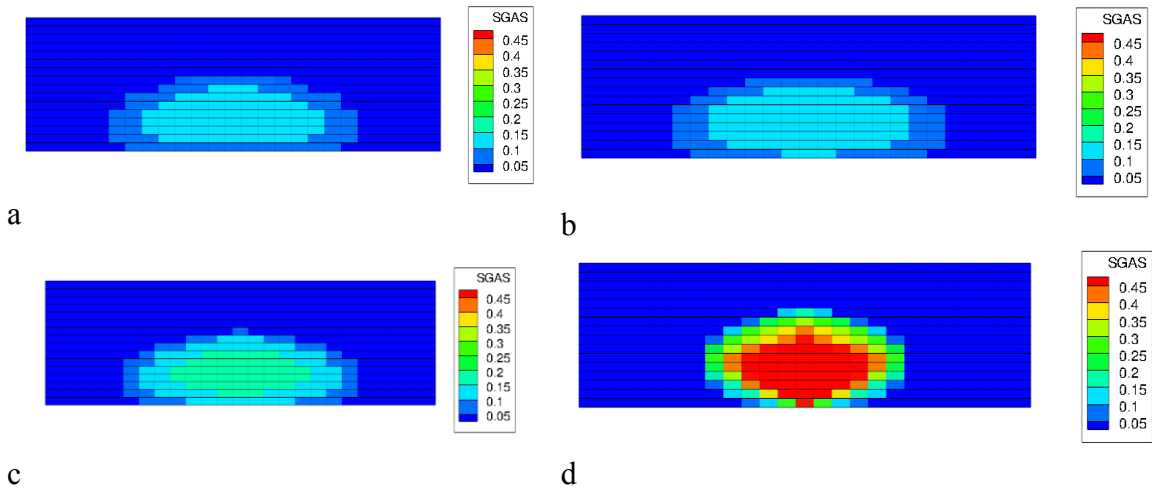


Figure 5.24 CO₂ saturation at 100 days in cross-section of injection well, contact angle a) 0 b) 30 c) 60 d) 90 degrees

5.2.2.2 Test Case with CO₂ Water Contact Angle Greater than 90 Degree

For testing of numerical model, we set up a case with a contact angle greater than 90° for CO₂-water system. Capillary pressure curves using different contact angles of 0, 90, 120, and 180 degrees are shown in Figures 5.25 and 5.26.

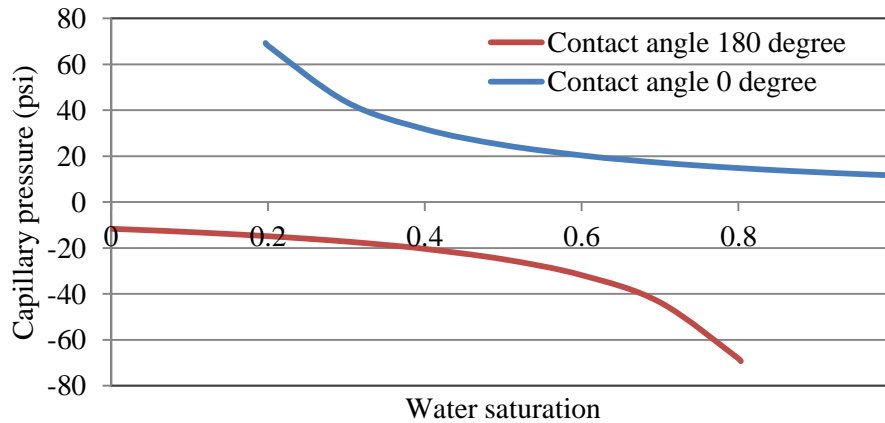


Figure 5.25 Capillary pressure for water and CO₂ system with contact angle of 0 and 180 degree

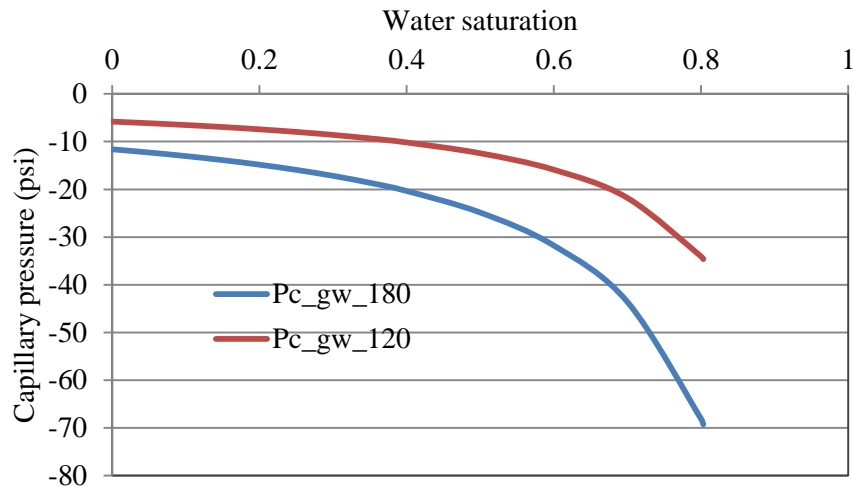


Figure 5.26 Capillary pressure for contact angle of 120 and 180 degrees

Simulation cases are set up to compare the effect of using contact angles of 120 and 180 degrees on CO₂ distribution. Gas saturations at 50 days and 100 days are plotted. Capillary pressure in the reservoir is also compared. We can see from Figure 5.27 and Figure 5.28 the CO₂ saturation near the injection location is high at the injection period for the case with contact angle of 120°.

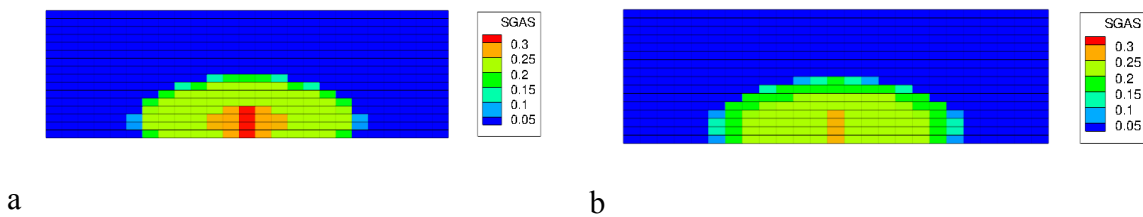


Figure 5.27 CO₂ saturation at 50 days for contact angle a) 120° b) 180°

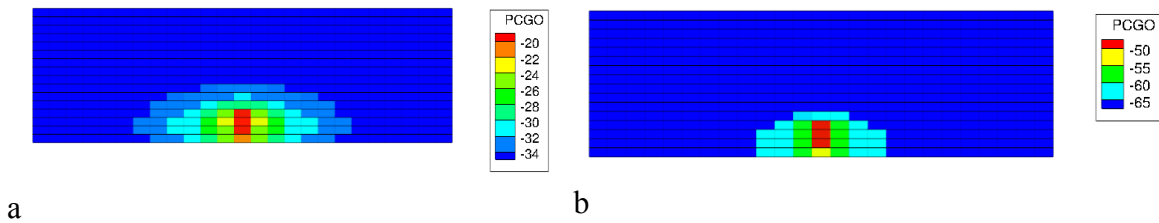


Figure 5.28 Capillary pressure (in psi) for contact angle a) 120° ; b) 180° at the end of injection period

We can see that the capillary pressure is lower for a contact angle of 120° than it is for a contact angle of 180° . The absolute value of capillary pressure around the well is low, where the CO_2 saturation is high. We can see from Figure 5.29 that, after 50 days redistribution, there are minimal differences in CO_2 saturation for different contact angles for this numerical case with homogeneous permeability.

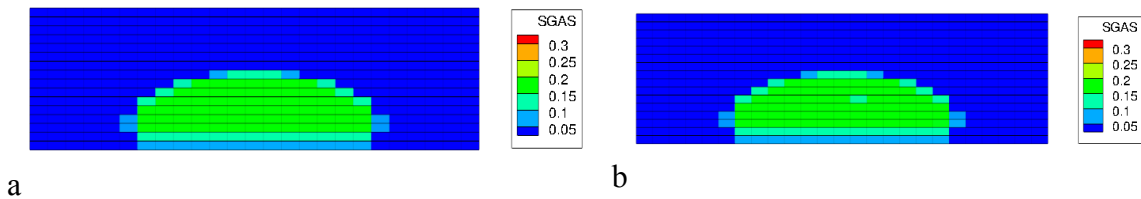


Figure 5.29 CO_2 saturation at 100 days contact angle a) 120° ; b) 180°

Based on this sensitivity test, we can make the following comments:

- The capillary pressure will decrease as the contact angle decreases from 0 to 90° . This reduction in capillary pressure will help CO_2 to displace water and the CO_2 saturation will be high near the injection well.
- For contact angles of 120° and 180° , CO_2 saturation near the well (Figure 5.27) will be low compared to that for the water wet case (Figure 5.23)

- When the contact angle varies from 90 to 180⁰, the CO₂ saturation near the well will decrease. The capillary pressure will help with a higher spatial distribution of CO₂ away from the wells during shut-in period.

5.3 Simulations with the Trapping Model

CO₂ injection and trapping processes are largely dominated by the interplay of viscous, capillary, and gravitational forces. The residual trapping of CO₂ by capillary forces is critical for CO₂ trapping, which can trap gas as residual and disconnected fluid phase in the pore spaces. However, due to heterogeneity and the injection schedule, the residual saturation could vary in both space and time. An accurate model for the variation of CO₂/water residual saturation is needed to account for the interplay of these three forces. Hence a trapping model is developed to model the change of residual saturation with *in situ* conditions. We set up two simulation studies to validate the trapping model. The first study is to show the range of trapping numbers encountered in the aquifer in a typical CO₂ storage operation. The second case is a sensitivity test with and without the trapping models in a 3D reservoir model.

5.3.1 CASE 1 TO STUDY RELATIVE PERMEABILITY AS A FUNCTION OF TRAPPING NUMBER

A homogeneous reservoir model with closed boundary was used to study the trapping number in a reservoir. The initial reservoir pressure is 2700 psi. The reservoir model size is 3500 ft × 3500 ft × 100 ft. One CO₂ injection well is located at the center of the aquifer, injecting CO₂ from the bottom of the aquifer with a constant pressure of 2900 psi. The grid number is 24 × 24 × 3 in three directions. The grid size near the well location is 50 ft × 50 ft × 20 ft, and the grid size in the outer region is

500 ft × 500 ft × 20 ft. The CO₂ saturation during the injection period is shown below in Figure 5.30 and in a vertical cross section through the center well in Figure 5.31.

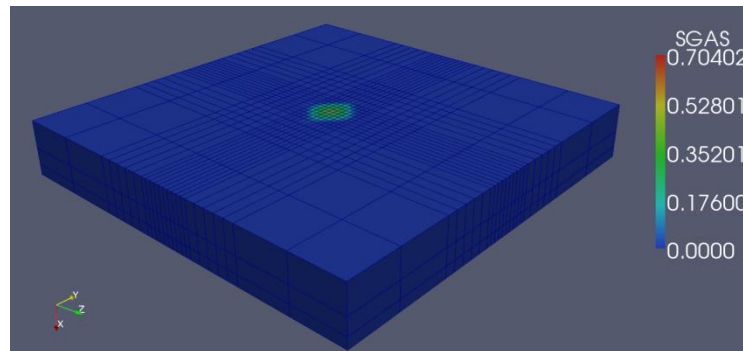


Figure 5.30 Reservoir model for one-year CO₂ injection test

The CO₂ plume moves radially in this homogeneous reservoir model with injection from the center. The gas saturation and pressure are high near the injection well at the bottom of the aquifer (Figure 5.31 and Figure 5.32).

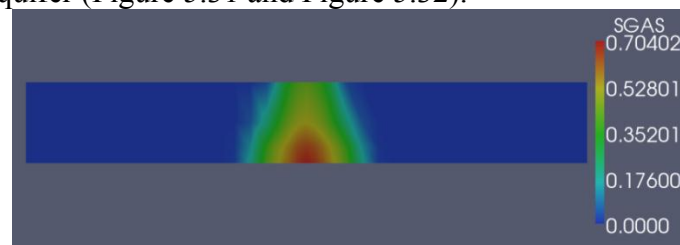


Figure 5.31 Gas saturation in well cross-section during the injection period at 1 year

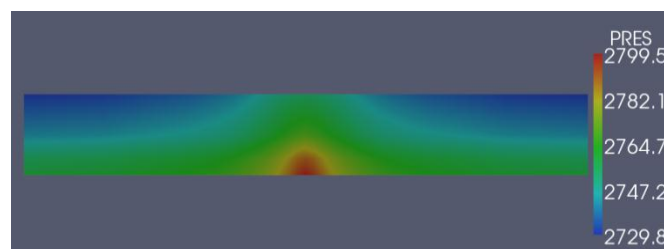


Figure 5.32 Pressure profile (in psi) at 1 year in well cross-section

The interfacial tension and trapping number are shown in Figure 5.33 and Figure 5.34. The IFT is reduced with increasing pressure and CO₂ injection. Figure 5.34 shows trapping number changing with distance to the injection well, ranging from 1×10^{-8} to 1×10^{-6} . The highest trapping number of about 2.8×10^{-7} is observed near the injection well as shown in Figure 5.34.

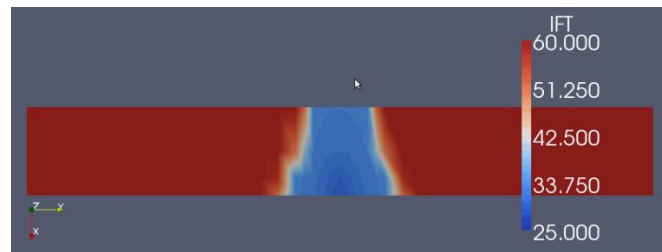


Figure 5.33 Calculated IFT (in mN/m) distribution at 1 year in well cross-section

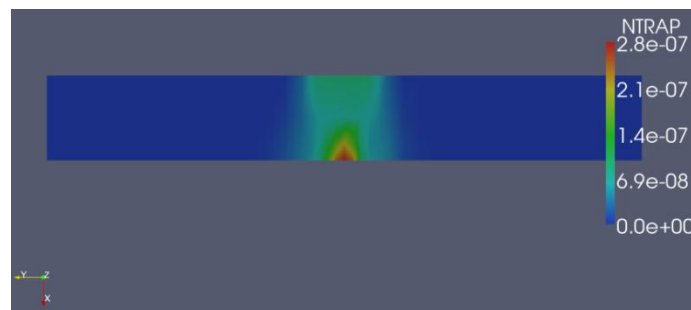


Figure 5.34 Calculated trapping number at 1 year

5.3.2 COMPARISON OF CASES WITH AND WITHOUT TRAPPING MODEL

A comparison case study was conducted to study the effect of a trapping model on relative permeability during CO₂ injection and redistribution. The grid size is $10 \text{ ft} \times 10 \text{ ft} \times 5 \text{ ft}$, and the number of grids is $25 \times 25 \times 4$ in X, Y, and Z directions. There are two wells in the model including one constant-rate CO₂ injection well in the center

and a constant pressure producer in the corner of the box model to maintain the reservoir pressure. The CO₂ injection continues to 50 days with a rate of 200 MSCFD, and injection is followed by 450 days of shut-in to allow CO₂ to redistribute. The producer on boundary is at constant pressure for the purpose of pressure maintenance.

The model grid is shown in the following figure:

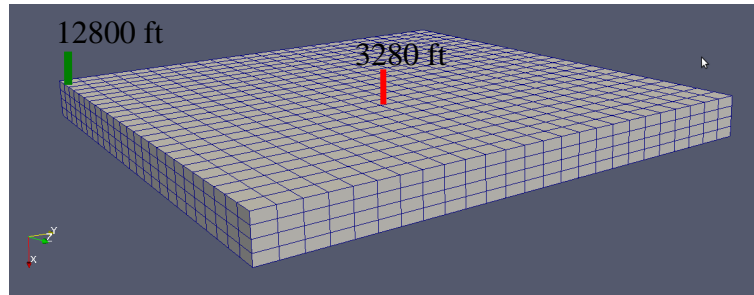


Figure 5.35 Reservoir model (red: injector, green: producer)

When the trapping model is included in the study, the relative permeability for water and gas phases is calculated using Equation 5.1 and Equation 5.2. Relative permeability model parameters are listed in Table 5.6. For high trapping numbers the phase residual saturations are low and the relative permeability exponents are also low. The endpoint relative permeabilities are high at high trapping number, because the residual saturations are reduced.

$$k_{rw} = k_{rw}^0 \bar{S}_w^{\lambda_w} \quad (5.4)$$

$$k_{rg} = k_{rg}^0 (1 - \bar{S}_w)^{\lambda_g} \quad (5.5)$$

in which $\bar{S}_w = \frac{S_w - S_{wr}}{1 - S_{wr} - S_{gr}}$, is the normalized water saturation.

The S_{wr} and S_{gr} are calculated as a function of trapping number and are used for calculating the relative permeability.

Table 5.6 Relative permeability model parameters as a function of trapping number

Trapping number	S_{gr}	S_{wr}	k_{rg}^0	k_{rw}^0	λ_g	λ_w
1×10^{-7}	0	0	1	1	1.2	1.1
1×10^{-9}	0.102	0.197	0.526	1	1.7	1.3

The relative permeabilities at high and low trapping numbers of i.e. 1×10^{-9} and 1×10^{-7} are shown in Figure 5.36.

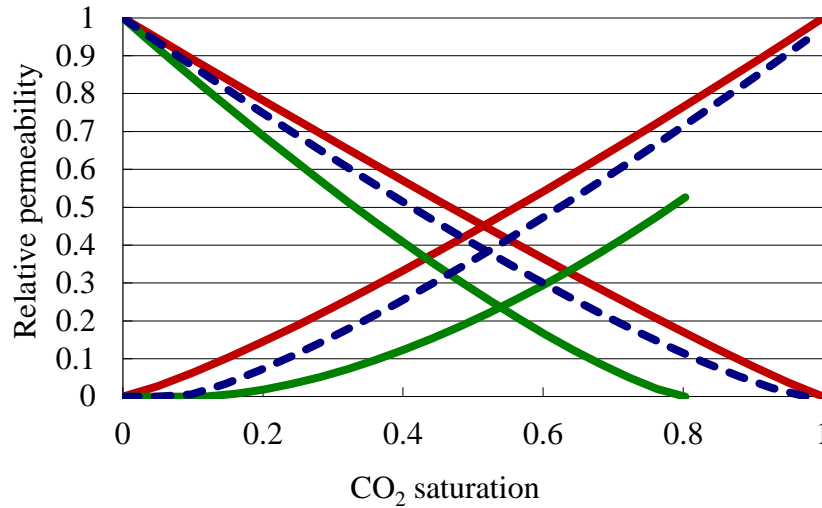


Figure 5.36 Relative permeability curves for trapping numbers of (red: 1×10^{-7} , blue: 1×10^{-8} , green: 1×10^{-9})

Three cases were set up to study the effect of the trapping model on CO₂ migration and trapping. For these cases we didn't include hysteresis.

- Case 1: without trapping model with $S_{gr} = 0$.
- Case 2: Without trapping model with $S_{gr} = 0.102$.
- Case 3: With trapping model and maximum $S_{gr} = 0.102$.

The gas saturations after 50 days of injection and end of the 500 day simulation are compared to study the impact of trapping model on CO₂ migration and trapping.

Figure 5.37, Figure 5.38, and Figure 5.39 indicate that the gas saturation profiles are very similar with and the change in relative permeability as a function of trapping number has very minimal effect for this numerical example during the injection period.

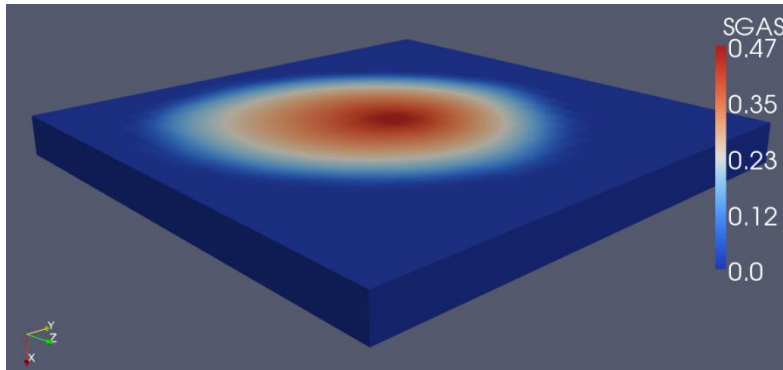


Figure 5.37 Gas saturation at the end of 50 day injection without trapping model and $S_{gr} = 0$ (Case 1)

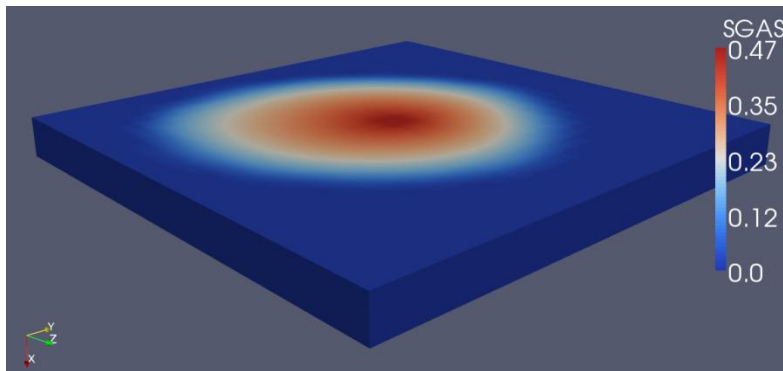


Figure 5.38 Gas saturation at the end of 50 day injection without trapping model and $S_{gr} = 0.102$ (Case 2)

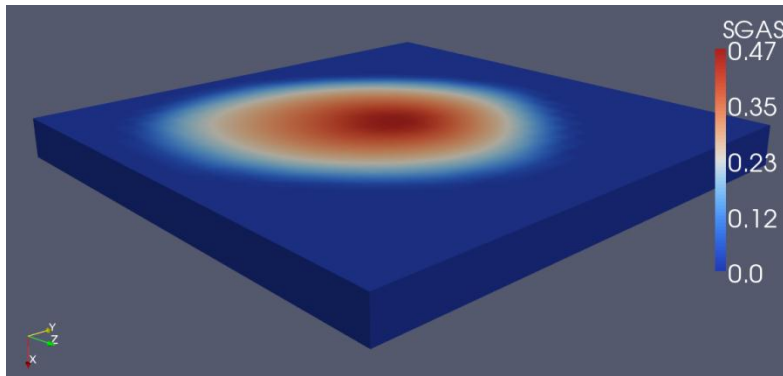


Figure 5.39 Gas saturation at the end of 50 day injection with trapping model and maximum $S_{gr} = 0.102$ (Case 3)

Gas saturation profiles in a vertical cross-section through the injection well also show similar distributions in Figure 5.40, Figure 5.41, and Figure 5.42. During the injection period, the trapping number is high. There is almost no residual trapping of CO_2 , and the relative permeability curves for the case with and without trapping model are similar. Therefore CO_2 saturation profiles are similar during high trapping number injection period.

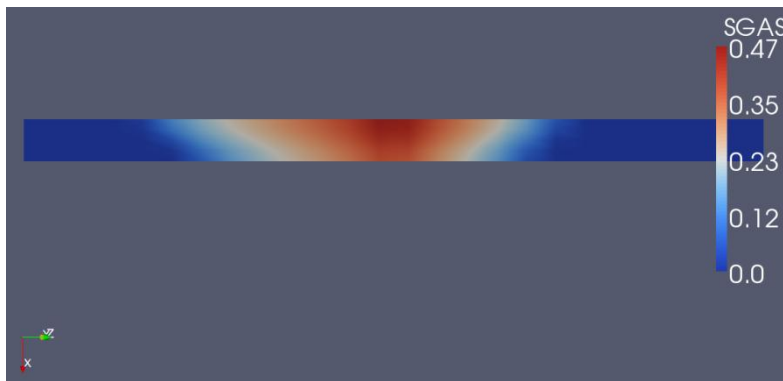


Figure 5.40 Gas saturation at the end of 50 day injection without trapping model and $S_{gr} = 0$ (Case 1)

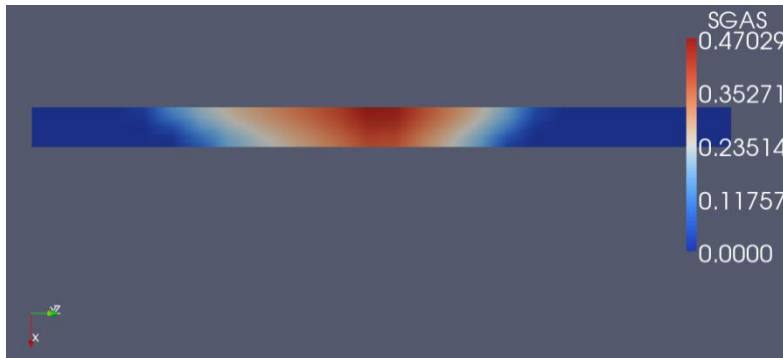


Figure 5.41 Gas saturation at the end of 50 days injection without trapping model and $S_{gr} = 0.102$ (Case 2)

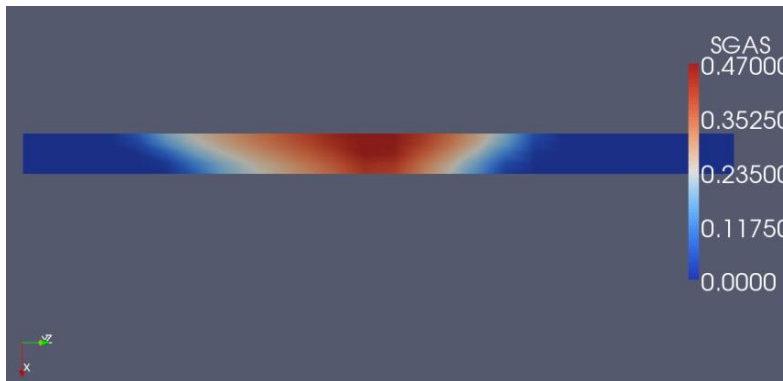


Figure 5.42 Gas saturation at the end of 50 days injection with trapping model and maximum $S_{gr} = 0.102$ (Case 3)

For the case with zero residual gas saturation and without modeling the trapping model, there is no trapping of CO_2 phase throughout the injection and shut-in periods. Most of the injected CO_2 migrates upward after injection stops. We can see from Figure 5.43 that if we set zero residual gas saturation there will be no trapping of CO_2 . If we set constant residual gas saturation (Figure 5.44), a large amount of CO_2 will be trapped near its injected location. Neither case accurately reflects *in situ* conditions.

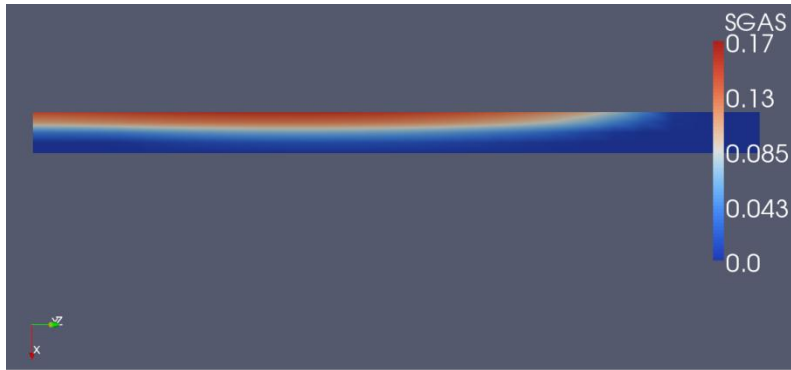


Figure 5.43 Gas saturation at 500 days without a trapping model and with $S_{gr} = 0.0$ (Case 1)

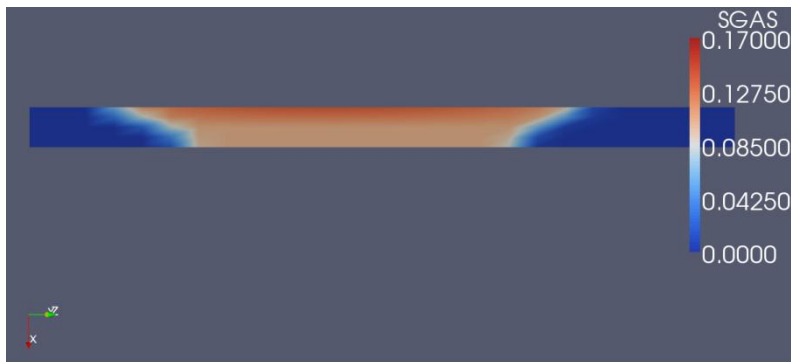


Figure 5.44 Gas saturation at 500 days without a trapping model and with $S_{gr} = 0.102$ (Case 2)

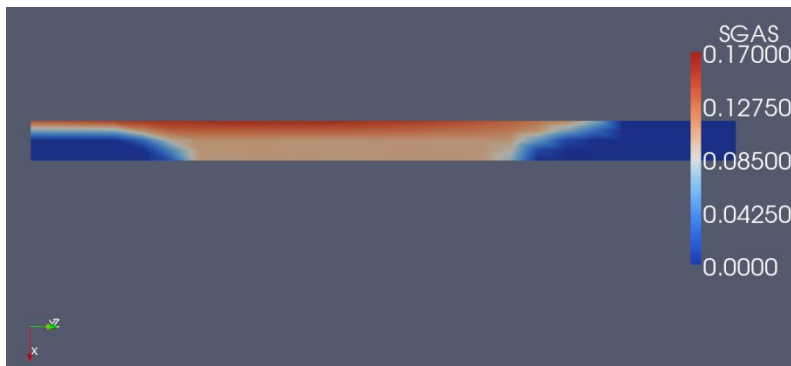


Figure 5.45 Gas saturation at 500 days with a trapping model and with maximum $S_{gr} = 0.102$ (Case 3)

For the case with the trapping model based on trapping number, the CO₂ could be trapped under low trapping number and low viscous gradient flow conditions. During the injection period, the viscous gradient is high, so the trapping number is also high. A high trapping number will reduce the residual saturation of both phases, resulting in less CO₂ trapping. We can see from the gas saturation profile in Figure 5.45 that when the trapping model is included some part of CO₂ will be trapped in the location where it was originally injected, though not as much as in Case 2 with constant residual saturation (Figure 5.44).

When the trapping model is included, the relative permeability curve will be shifted upward for high trapping numbers. The CO₂ could migrate to a larger region due to its higher relative permeability and less CO₂ could be trapped than in the case with a constant residual saturation. We can see that the CO₂ plume migrates further in Case 3 (Figure 5.45) than in Case 2 (Figure 5.44), which also suggests less trapped CO₂.

5.4 Test Study for Hysteresis Model in IPARS

5.4.1 1D HYSTERESIS MODEL

1D test case with a total of 10 grid cells was set up to validate the hysteresis model implementation in IPARS.

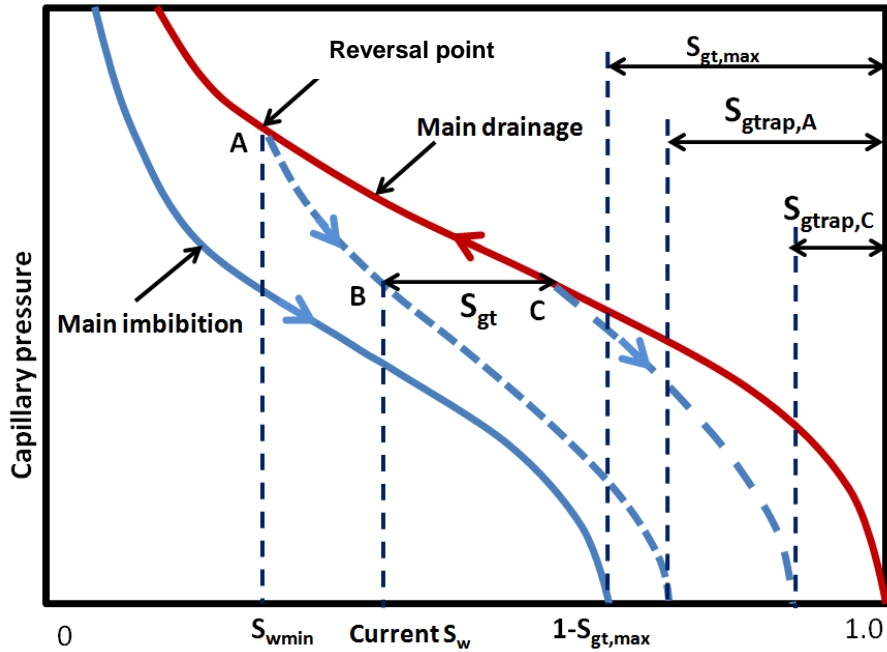


Figure 5.46 Schematic of hysteresis behavior in capillary pressure curve.

As shown in in Figure 5.46, the capillary pressure has different paths from drainage to imbibition as a function of water saturation. During the CO₂ injection period, water saturation decreases and capillary pressure follows the primary/main drainage path. Subsequent to injection and during the redistribution period, water can redistribute along the imbibition path. The water saturation, S_w , increases, while the reversal point, S_{wmin} , and maximum trapped gas saturation, S_{gtrap} , remain the same during the imbibition.

The water saturation in one grid block was tracked as injection began on day 1 and then stopped after 50 days, with a total simulation time of 100 days (Figure 5.47). For the CO₂/water system, we assumed that water was the wetting phase and CO₂ was the non-wetting phase. The gridblock underwent a drainage process during the initial 50 days, with S_{wmin} and S_{wnorm} equal to each other (Figure 5.48). On day 50, the injection well was shut-in, water began to displace CO₂ during the imbibition process,

S_{wnorm} began to increase, while S_{wmin} remained at the lowest normalized water saturation that the grid had reached (Figure 5.48). Finally, the water displaced CO_2 until the residual saturation of CO_2 was reached or capillary pressure prevented one phase from displacing the other (Figure 5.48).

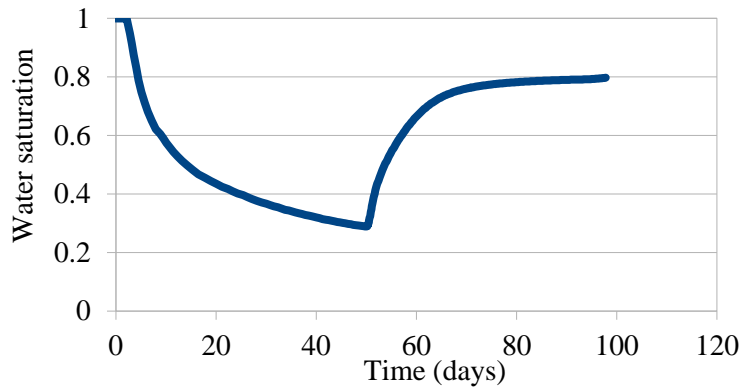


Figure 5.47 Water saturation in grid cell #10 during drainage and imbibition process

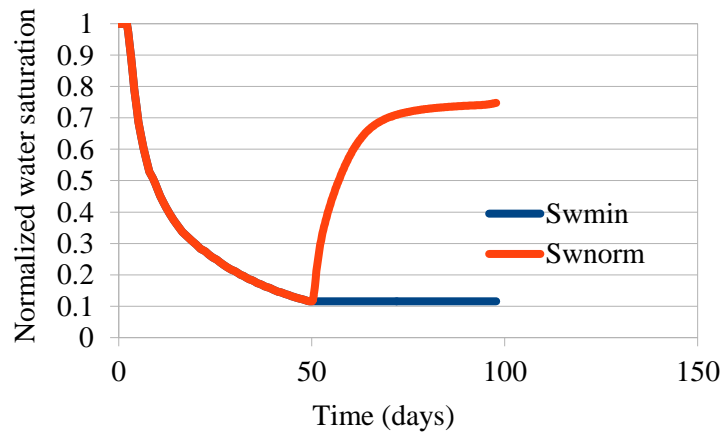


Figure 5.48 Normalized water saturation in gridblock #10 and minimum water saturation at the reversal point.

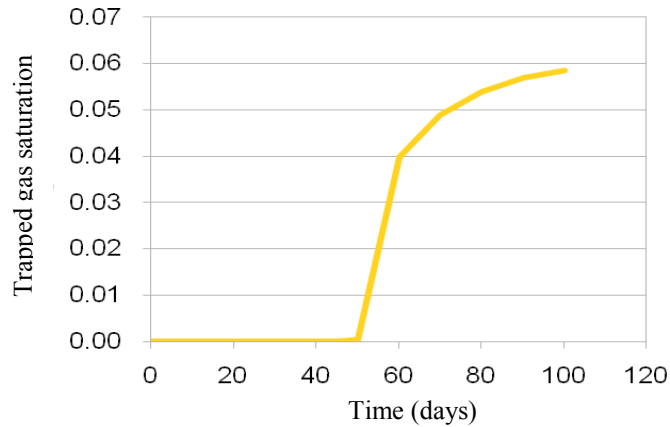


Figure 5.49 Trapped CO₂ saturation in injection well gridblock #10 with the hysteresis model vs. time.

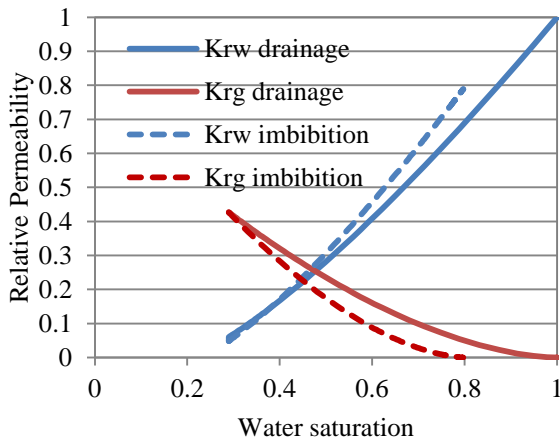


Figure 5.50 Hysteretic relative permeability for wetting phase (K_{rw}) and non-wetting phase (K_{rg}) in grid #10.

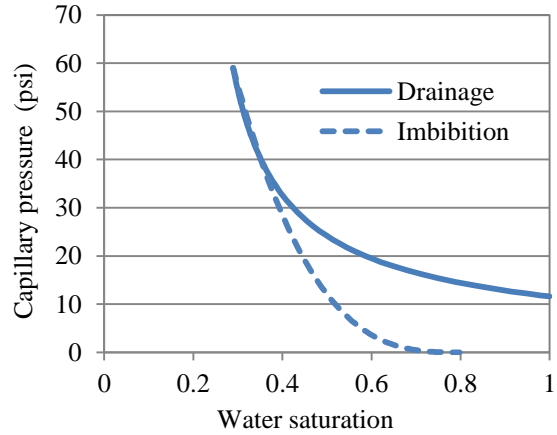


Figure 5.51 Hysteretic capillary pressure during drainage and imbibition in injection well grid #10.

Results clearly show the effect of hysteresis within one gridblock. During the CO₂ injection period and on the main drainage path, there is no trapping of non-wetting phase where water saturation monotonically decreases (Figure 5.49). After injection, imbibition of wetting phase water causes the trapping of CO₂ phase (Figure 5.49). As more water

enters a given pore in the rock, more non-wetting phase is trapped. During this process, the relative permeability and capillary pressure both follow a path that is different from the drainage cycle (Figure 5.50, Figure 5.51).

5.4.2 3D HYSTERESIS TEST

A test case of CO₂ injection into a saline aquifer is set up to study the impact of hysteresis on flow and retention of CO₂. The grid size is 10 ft × 10 ft × 5 ft, with number of gridblocks of 25 × 25 × 4 in X, Y, and Z directions respectively. There are two wells in the model, including one constant-rate CO₂ injection well in the center of the model and a constant pressure producer in the corner of the model to maintain the pressure. CO₂ injection continues for 50 days with a rate of 200 MSCFD, and it is followed by 450 days of shut-in to allow the CO₂ to redistribute.

Table 5.7 Model parameters for hysteresis model test case

Grid number	25 × 25 × 4
Grid size (ft)	10 × 10 × 5
Permeability (md)	100
Porosity	0.2
Injection well rate (MSCFD)	200
Production well bottomhole pressure (psi)	1800
Well perforation	entire thickness
Time (days)	50 days injection, 450 days shut-in

The model grid and well locations are shown in Figure 5.52:

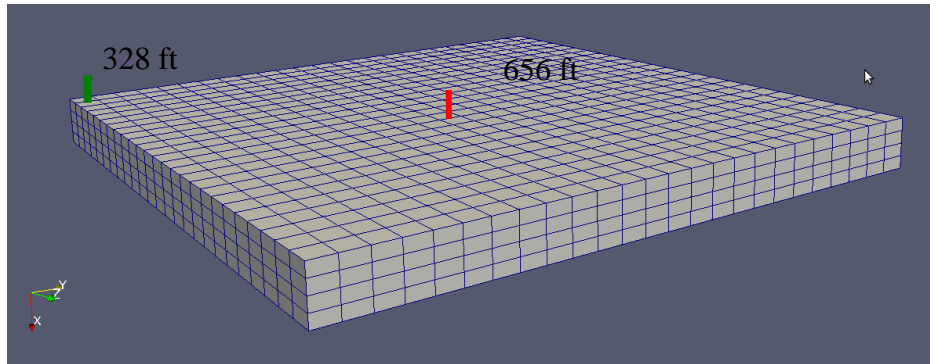


Figure 5.52 Reservoir model for the hysteresis model test case

The properties of Cardium sandstone was used for rock-fluid properties of the aquifer (Bennion and Bachu, 2006), including relative permeability and capillary pressure (Figure 5.53 and Figure 5.54). The Corey-type relative permeability equation is used to curve-fit the measured data of Cardium sandstone (Table 5.8).

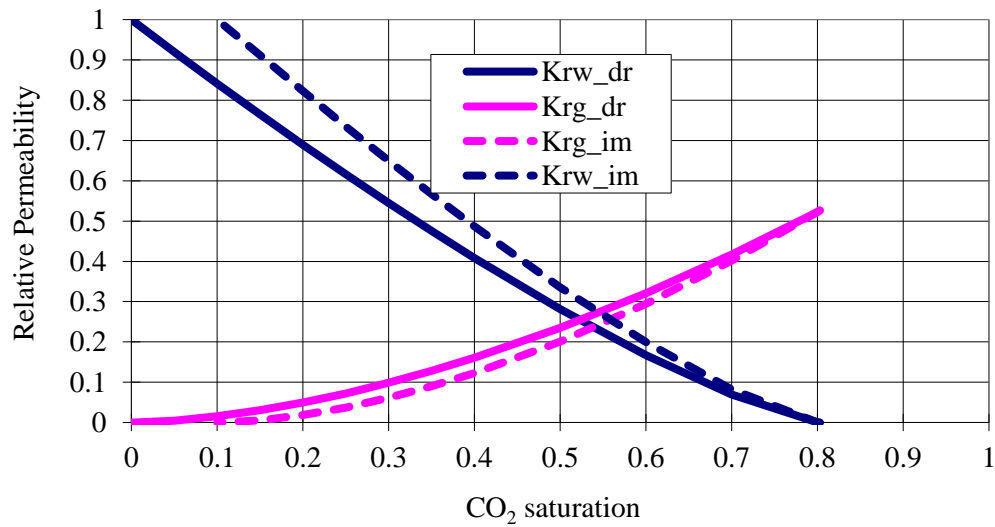


Figure 5.53 Drainage and imbibition relative permeability curves for the hysteresis test model.

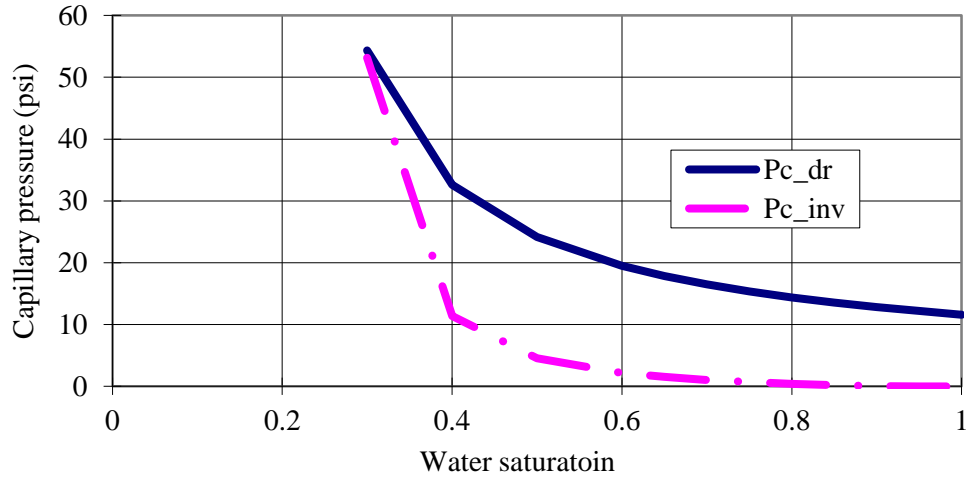


Figure 5.54 Drainage and imbibition capillary pressure curves for the test of hysteresis model.

Table 5.8 Model-fitting parameters for drainage relative permeability of Cardium sandstone (Bennion and Bachu, 2006)

Drainage		Imbibition	
Entry capillary pressure, $P_{c,entry}$ (psi)	11.6	Entry capillary pressure, $P_{c,entry}$ (psi)	NA
P_c curve exponent, $\lambda_{Pc,drainage}$	1.33	P_c curve exponent, $\lambda_{pc,imb}$	5.32
Endpoint water relative permeability, k_{rw}^0	1.0	Endpoint water relative permeability, k_{rw}^0	1.0
Endpoint CO ₂ relative permeability, k_{rg}^0	0.526	Endpoint CO ₂ relative permeability, k_{rg}^0	0.526
CO ₂ relative permeability exponent, λ_g	1.7	CO ₂ relative permeability exponent, λ_g	1.7
Water relative permeability exponent, λ_w	1.3	Water relative permeability exponent, λ_w	1.3
Residual water saturation, S_{wr}	0.197	Residual water saturation, S_{wr}	0.197
Residual CO ₂ saturation, S_{gt}	0	Residual CO ₂ saturation, S_{gt}	0.102

Several reservoir simulation tests are performed to investigate the impact of capillary pressure and relative permeability hysteresis on the distribution of CO₂ plume (Table 5.9).

Table 5.9 Test cases for hysteresis study.

	Relative permeability model	Capillary pressure model
Case 1	No hysteresis	Zero P_c
Case 2	With hysteresis	Zero P_c
Case 3	No hysteresis	No hysteresis: $P_{c,entry} = 11.6 \text{ psi}$, $\lambda_{pc} = 1.33$
Case 4	With hysteresis	With hysteresis: $P_{c,entry} = 11.6 \text{ psi}$, $\lambda_{pc,drainage} = 1.33$, $\lambda_{pc,imbibe} = 4.0$

Case 1 is the base case without hysteresis for relative permeability and without capillary pressure effects. Case 2 is similar to Case 1 but includes the hysteresis for relative permeability. Case 3 is similar to Case 1 but includes capillary pressure. The drainage relative permeability and capillary pressure curves are used for the injection and shut-in period. Case 4 uses hysteresis for both relative permeability and capillary pressure.

5.4.2.1 Cases 1 and 2

Gas saturation profiles at 50 days and 500 days are compared to study the impact of relative permeability hysteresis on the fate and transport of injected CO₂. During the CO₂ injection drainage cycle, we use the drainage relative permeability curves. After CO₂ injection well shut-in, the imbibition process occurs, and hysteresis has a measurable effect.

CO₂ saturation in a cross-section through the injection well is plotted and compared for Case 1 and Case 2 with zero capillary pressure. We can see from both Figure 5.55 and Figure 5.56 that the saturation profile at the injection end is the same for the two cases since drainage relative permeability is used in both cases during the injection period

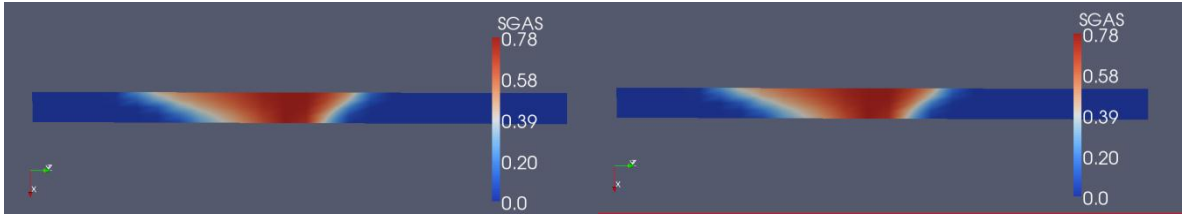


Figure 5.55 Case 1 without hysteresis: gas saturation in a vertical cross-section at 50 days, end of injection.

Figure 5.56 Case 2 with hysteresis: gas saturation in a vertical cross-section at 50 days, end of injection.

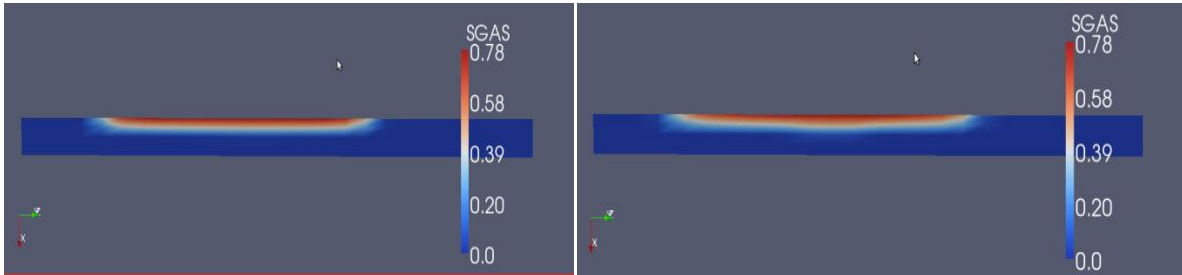


Figure 5.57 Case 1 without hysteresis: gas saturation in a vertical cross-section at 500 days (zero P_c).

Figure 5.58 Case 2 with hysteresis: gas saturation in a vertical cross-section at 500 days (zero P_c).

The CO_2 saturation after a 450 day period of redistribution for Case 1 and Case 2 is shown in Figure 5.57 and Figure 5.58, which shows a similar distribution. Note that we used hysteresis for the relative permeability in Case 2. This similarity between Case 1 and Case 2 demonstrated that hysteresis behavior for relative permeability but excluding capillary pressure fail to capture the flow characteristics. One observation we can make is that the saturation profiles in both cases show sharp front between the gas plume and the water phase, which is due to the zero capillary pressure we assumed here. For both cases without capillary pressure, we observe that there is no trapping of injected CO_2 near the injection well and most CO_2 is accumulated below the first layer with high gas saturation.

This indicates the importance of modeling capillary pressure when simulating CO₂ sequestration.

5.4.2.2 Case 3

Case 3 uses the table lookup for capillary pressure and relative permeability without hysteresis. Everything else is identical to Case 1. CO₂ saturation profiles at 50 days and at 500 days are plotted.

We can see from Figure 5.59 that at the end of injection, CO₂ spans a wide area, and the CO₂ plume front is continuous from high gas saturation to water zone. The gas saturation at 500 days with capillary pressure is shown in Figure 5.60, which shows a much wider area of distribution of CO₂ when compared to the zero capillary pressure case in Figure 5.57. This is because, when CO₂ is migrating upward due to buoyancy forces, more and more CO₂ enters the grid cell in the top layer and the capillary pressure increases. Eventually, the high capillary pressure prevents more CO₂ from entering the pore. This keeps a relatively low saturation of CO₂ and CO₂ is forced to migrate horizontally. Figure 5.60 shows that CO₂ migrates upward to the top layer of aquifer and towards the boundary producer because there is no hysteresis to trap it near the injection well. CO₂ is forced to distribute horizontally when the plume accumulates below the top seal.

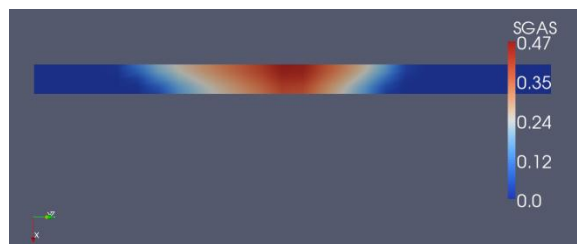


Figure 5.59 Case 3 CO₂ saturation in cross section at the end of 50 days of injection

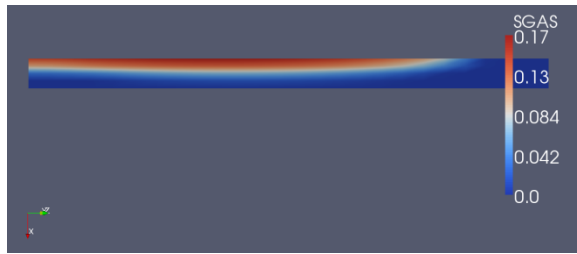


Figure 5.60 Case 3 CO₂ saturation in cross section at the end of 500 days

The calculated capillary pressures at the end of injection and redistribution are shown in Figure 5.61 and Figure 5.62, with a high capillary pressure of about 22.9 psi near the injection well and a low capillary pressure of about 11 psi away from the well. This is consistent with both the saturation profile and the input capillary pressure table, which indicates that higher gas saturation corresponds to higher capillary pressure.

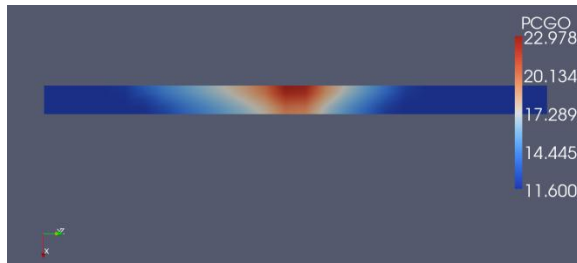


Figure 5.61 Case 3 capillary pressure at the end 50 day injection.

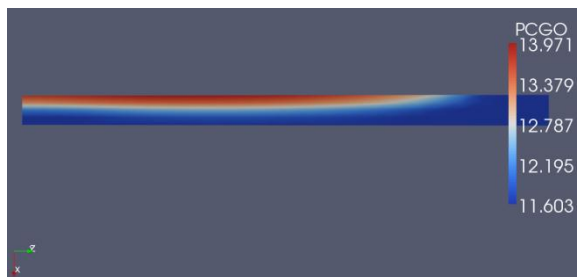


Figure 5.62 Case 3 capillary pressure at the end of 500 day simulation

Trapped CO₂ saturation is zero consistent with the imposed residual CO₂ saturation of zero (Figure 5.63).

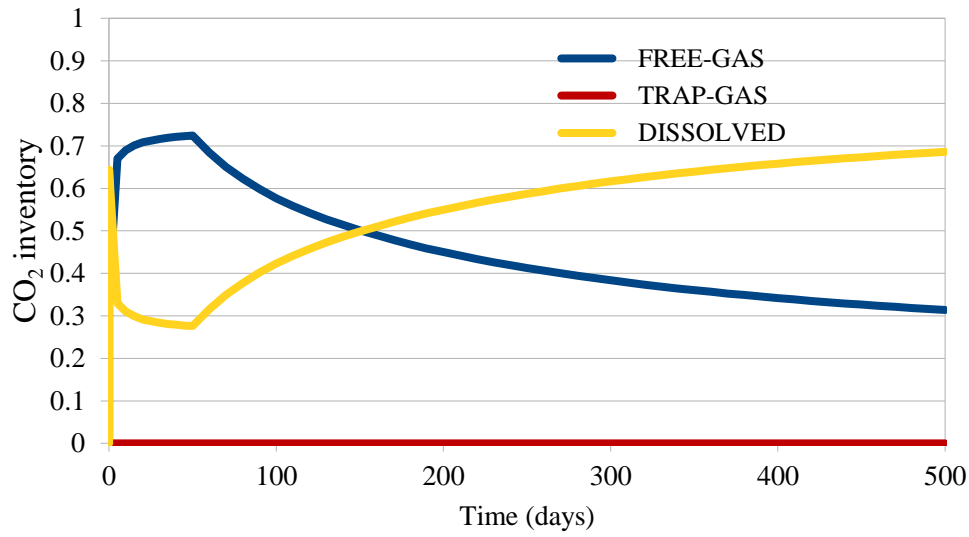


Figure 5.63 CO₂ inventory for free gas, trapped gas, and dissolved gas for Case 3 using $S_{gr} = 0$ without the hysteresis model

5.4.2.3 Case 4

We have seen the effect of including capillary pressure on CO₂ migration. Next we will study the effect of relative permeability and capillary pressure hysteresis on CO₂ distribution. The capillary pressures and relative permeability curves for the drainage and imbibition cycles are different as shown in Figure 5.64.

For the drainage process, Case 4 uses the same drainage capillary pressure and relative permeability curves as Case 3. For the imbibition cycle, Case 4 uses the imbibition capillary pressure and relative permeability curves that are calculated based on trapped CO₂ saturation. The capillary pressure for the imbibition uses the exponent of $\lambda_{pc} = 1.33$. The maximum trapped gas saturation is assumed to be 0.102.

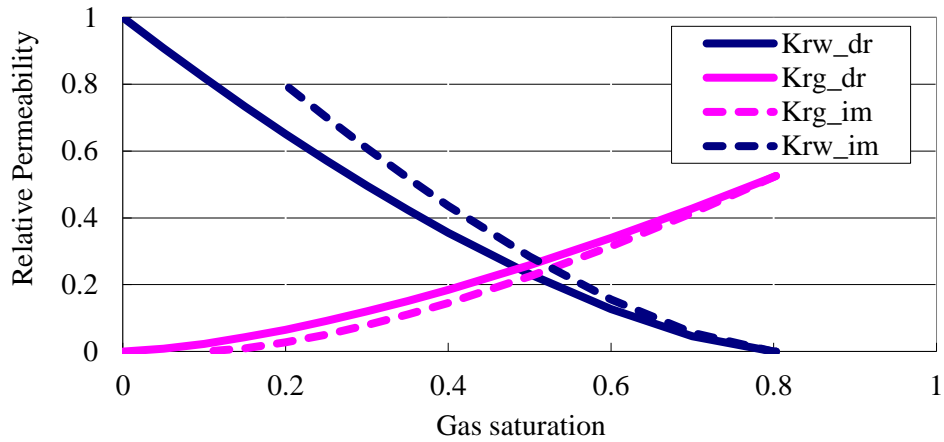


Figure 5.64 Hysteretic relative permeability in Case 4

The CO₂ saturation profiles are plotted at end of 50 day injection and at end of 500 day simulation. Figure 5.65 and Figure 5.66 indicate that case 4 with hysteresis and case 3 without hysteresis give the same CO₂ saturation profile at the end of 50 days of injection. This is because Case 4 used the same drainage relative permeability and capillary pressure as Case 3 in the injection period. However, the final gas saturation at 500 days differs significantly when the hysteresis effect is modeled (Figure 5.67 and Figure 5.68). This difference is because after injection stops, there will be residual CO₂ trapping due to hysteresis in Case 4 with hysteresis model. In Case 4 with hysteresis (Figure 5.67), the saturation profile at 500 days shows that a large amount of CO₂ is trapped in regions near the well, due to hysteresis capillary trapping that occurs in the imbibition process.

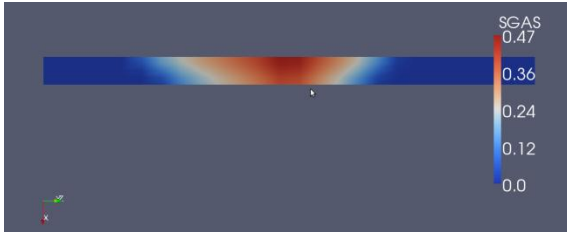


Figure 5.65 Case 4 with hysteresis, CO₂ saturation at the end of 50 day injection

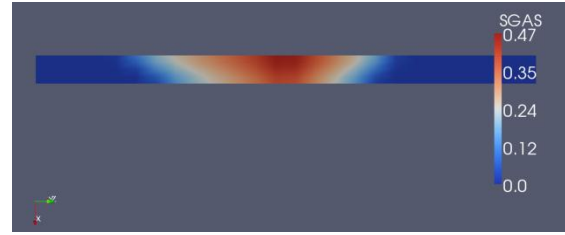


Figure 5.66 Case 3 without hysteresis, CO₂ saturation at the end of 50 day injection

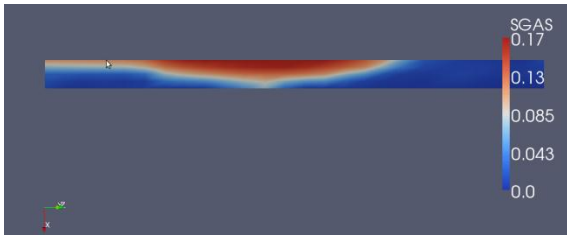


Figure 5.67 Case 4 with hysteresis, CO₂ saturation at the end of 500 days

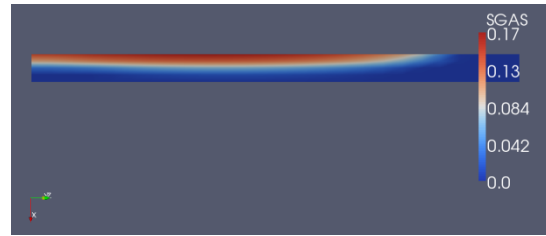


Figure 5.68 Case 3 without hysteresis, CO₂ saturation at the end of 500 days

The CO₂ inventory is shown in Figure 5.69. CO₂ inventory is defined as the amount of CO₂ as mobile, dissolved, and residual trapped during the sequestration process at different time. We observe that during the injection period there is only a small amount of CO₂ that is trapped and that the fractions of free and dissolved amounts are constant. This could be because it is a drainage process, and no significant imbibition is happening. The CO₂ migration is dominated by viscous forces. After shut-in, both trapped and dissolved CO₂ increase greatly as time progresses. This could be due to the gravity-driven upward migration of CO₂ and the water imbibition. As CO₂ migrates upward, it will contact unsaturated water, and some CO₂ will be dissolved. As CO₂ is driven out of the pore space during the imbibition of water, some CO₂ volume will be left behind and trapped by the water. These displaced CO₂ will enter new pore spaces and

leave a portion of CO₂ trapped in the invaded pores. Hence the more poresCO₂ contacts, the more CO₂ will be trapped.

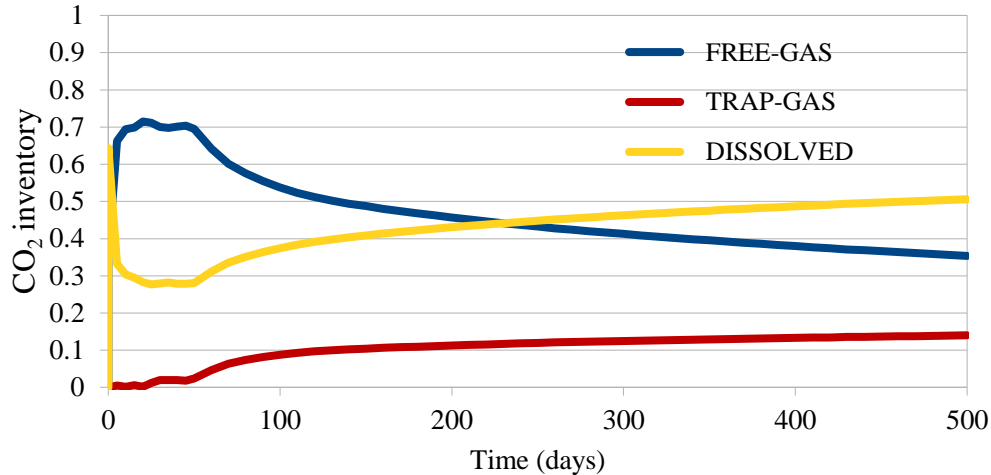


Figure 5.69 CO₂ fractional inventory as free, trapped, and dissolved gas for Case 4 with hysteresis, and with $S_{gt,max} = 0.102$

5.5 Summary

We tested the sensitivity of CO₂ injection and redistribution to different petrophysical models. The new models of interfacial tension, a trapping model, a hysteresis model, and capillary pressure scaling are tested. These models are efficiently coupled in the parallel simulator, which could utilize the high performance computing capability with efficient CPU times. Simulation results indicate the importance of these models when simulating CO₂ sequestration process as highlighted below.

- A stacked sandstone aquifer with shale seals demonstrated that the shale layer could effectively act as a sealing barrier to impede the migration of CO₂ migration upward to shallower zones, because of the high entry capillary pressure of the shale.

- We tested sensitivity of CO₂ migration to rock-fluid properties of interfacial tension and contact angle using capillary pressure model based on Leverett J-function. Results showed that the gas migration was highly sensitive to the heterogeneity, IFT, and wettability. The contact angle close to 90 degrees will help CO₂ displacing water from the rock pores. The CO₂ saturation is also high for contact angle of 90⁰.
- We studied the impact of interfacial tension, viscous force, and gravity force on CO₂ trapping and migration using a trapping model. The trapping number is the highest near the injection well where CO₂ is trapped near injection well.
- We tested the impact of hysteresis on CO₂ trapping and migration, using the newly developed hysteresis model in IPARS. During drainage there is zero trapping of non-wetting phase and during imbibition process, more and more CO₂ saturation is trapped. 3D test results also show indicated increasing residual trapping and decreasing mobile CO₂ as a function of time when hysteresis model is used.
- The application and validation of these models in field cases are presented in Chapter 6 using Cranfield pilot CO₂ sequestration field demonstration.

CHAPTER 6: Cranfield CO₂ Sequestration Pilot Test

6.1 Cranfield Pilot CO₂ Sequestration Project

The Cranfield formation is a depleted oil reservoir in Natchez, Mississippi, that was recently chosen as the site of the field-scale CO₂ sequestration demonstration project. The project is supported by SECARB, with primary sponsorship provided by DOE/NETL & SSEB and secondary sponsorship provided by the Texas Bureau of Economic Geology, Denbury Resources, Advanced Resources International (ARI), Electric Power Research Institute (EPRI), and the University of Alabama. The project aims to develop the technical background necessary for validating and deploying carbon sequestration technologies in the field, as well as building confidence in the capacity of underground formations for holding large volumes of CO₂. A total of 2.5 MT CO₂ injected through DOE Project Phase 2 (1 MT/Yr) and Phase 3 (1.5 MT/Yr), started in December 1st 2009. Observations and monitoring data are available, including pressure and temperature through injection and observation wells.

The Cranfield oil field was discovered in 1943, and production continued to 1966 (Mississippi Oil and Gas Board, 1966). An enhanced oil recovery CO₂ flood was initiated in 2008 in upper part of the field. After many years of shut-in and no activities after depletion, the reservoir condition has reverted to its initial condition due to strong bottom water influx. The initial conditions are a reservoir pressure of 4560 psi and a temperature of 257 °F. The geological setting of the Cranfield reservoir is a dome with a sealing fault on the north-east side (Figure 6.1). The pilot injection site of CO₂ sequestration is located at a depth of approximately 9,950 ft, with a sandstone reservoir thickness of about 80 ft.

The reservoir has a 110 ft top seal and a 90 ft base seal of impermeable shale rocks. The formation brine has a salinity of ~150,000 ppm total dissolved solids (TDS).

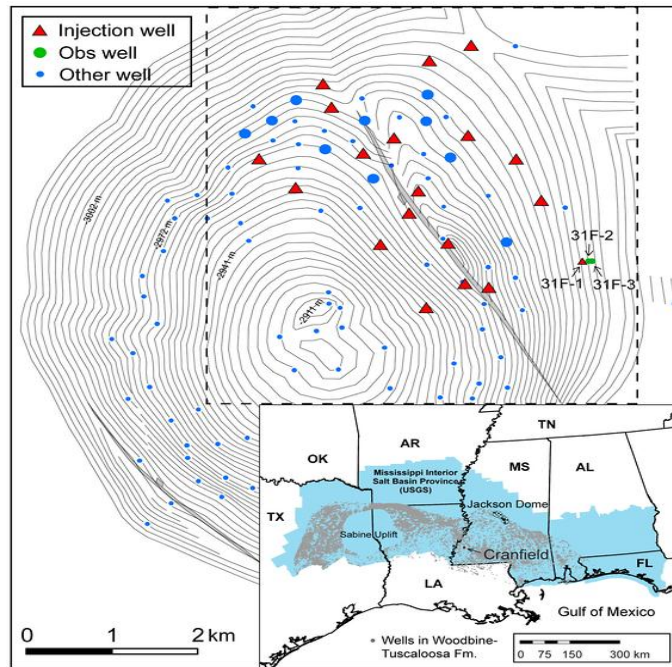


Figure 6.1 Contour map (10 ft elevation interval) of the top of the Lower Tuscaloosa formation (Lu *et al.* 2012a).

CO₂ is injected in the downward dip of the water leg in the detailed area of study (DAS). The DAS has three wells, one injection well (CFU 31-F1) and two observation wells (CFU 31-F2 and CFU 31-F3) (Figure 6.2). The two observation wells (CFU 31-F2 and CFU 31-F3) are to the east of the injection well. The spacing from F1 to F2 is ~227 feet (69 m) and from F1 to F3 it is ~367 ft (111 m). The three wells are completed in the lower Tuscaloosa water leg.

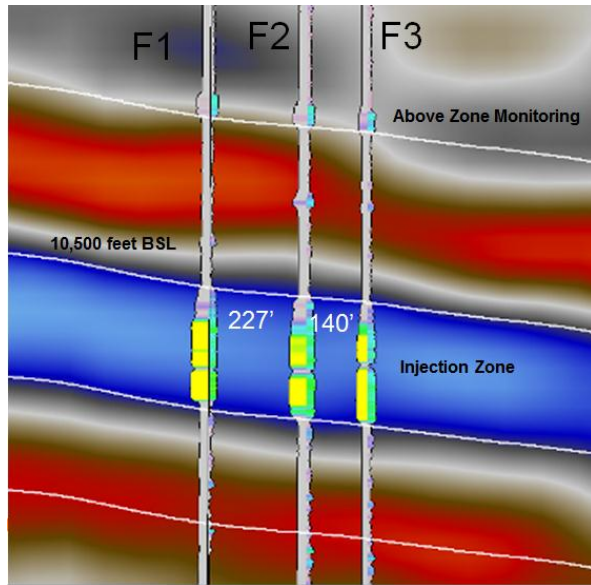


Figure 6.2 Three wells in vertical cross-section of the DAS area (Bryant, 2010)

The injected CO₂ was supplied from Jackson Dome natural CO₂ reservoir by Denbury Resources, Inc. CO₂ is injected through a BEG injection well (CFU 31-F1). The CO₂ injection rate was initially approximately 4500 MSCFD (1 MSCFD = std ft³/d), but it was ramped up to about 9000 MSCFD (Figure 6.3). A total of approximately 2.5 million tons of CO₂ was injected in the period beginning on December 1st 2009 and continuing through the present. However, for the purpose of this work, injection is assumed to have ended on January 7th, 2011.

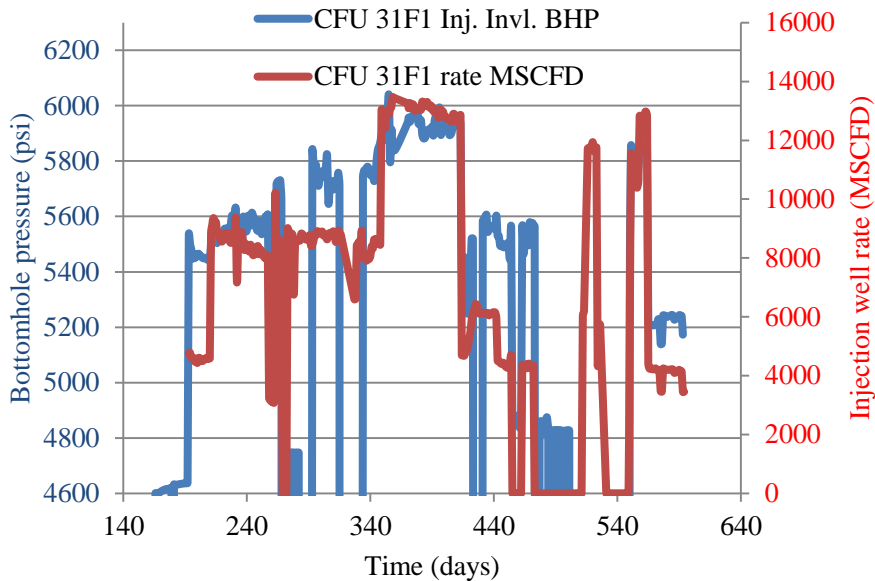


Figure 6.3 Injection well CFU 31-F1 BHP and injection rate with time (start at day 193, Dec. 1, 2009).

An initial rate was approximately 4500 MSCFD, followed by a period with a doubled injection rate of 9000 MSCFD and ending with a period marked by high injection rate of 13000 MSCFD (Figure 6.3). After the high injection rate period, the rate was quite fluctuating.

6.2 Cranfield Simulation Model

Here we discuss the modeling approach in IPARS, taking into consideration some advanced physical and numerical features and their impact both on injection pressure and on the fate of CO₂ several years after the injection has stopped. Table 6.1 gives the details of the numerical model in IPARS. Several geological models with different numbers of cells have been constructed to model the Cranfield demonstration test. The simulation

results were compared with field measured CO₂ breakthrough time, bottomhole injection pressure, and temperature.

Table 6.1 Reservoir properties for the Cranfield test

Reservoir size (ft)	9400 × 8800 × 300
Number of gridblocks	188 × 176 × 20
Aquifer thickness (ft)	80
Top seal thickness (ft)	110
Bottom seal thickness (ft)	90
Aquifer depth (ft)	9950
Aquifer temperature (°F)	257
Rock compressibility (psi ⁻¹)	5.0 × 10 ⁻⁶
Initial saturation	100% water saturation
Initial pressure (psi)	4650
Salinity (TDS) (ppm)	150,000
Boundary conditions	Open boundary on 3 sides

The fluid PVT phase behavior parameters are in Table 6.2. The Peng-Robinson equation of state is used for calculating phase equilibrium for CO₂/brine at the reservoir pressure of 4650 psi and temperature of 257 °F. Geochemical reactions and subsequent CO₂ mineral trapping are not included due to minimal reactivity of Cranfield sandstone rock (Lu *et al.* 2012a,b).

Table 6.2 PVT data for compositional simulation of the Cranfield case.

P = 32 MPa, T =398.15 K (125 °C)	CO₂	Brine
Critical temperature (K)	304.13	647.09
Critical pressure (MPa)	7.38	22.06
Compressibility factor	0.2550	0.200
Acentric factor	0.2240	0.2440
Molecular weight (g/g-mol)	44.01	18.01
Volume-shift parameter	-0.2000	0.2960
Binary interaction coefficient	0.0900	0.0900
Density (kg/m ³)	576.72	1033.29
Viscosity (cp)	0.044	0.44
CO ₂ mole fraction in brine	0.013	--

The reservoir consists of a sandstone aquifer, with a top seal and base rock shale. The relative permeability and capillary pressure curves for sandstone and shale are given in Figure 6.4 and Figure 6.5. The shale rock has a very high capillary pressure (>200 psi) and aquifer sandstone has a low capillary pressure (0.2~1 psi). Simulation shows there is very little penetration of CO₂ into the top seal and the base layer, therefore, we removed the top and bottom shale layers from the reservoir model, keeping only the sandstone aquifer layers.

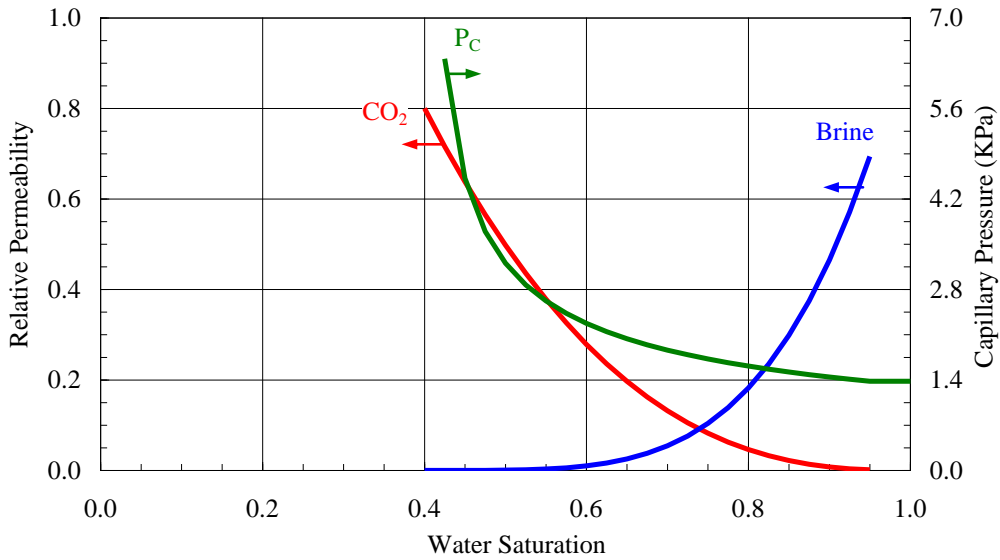


Figure 6.4 CO₂-brine relative permeability and capillary-pressure curves for sandstone aquifer (Hosseini *et al.*, 2012). Blue curve: brine relative permeability; red curve: CO₂ relative permeability; green curve: capillary pressure.

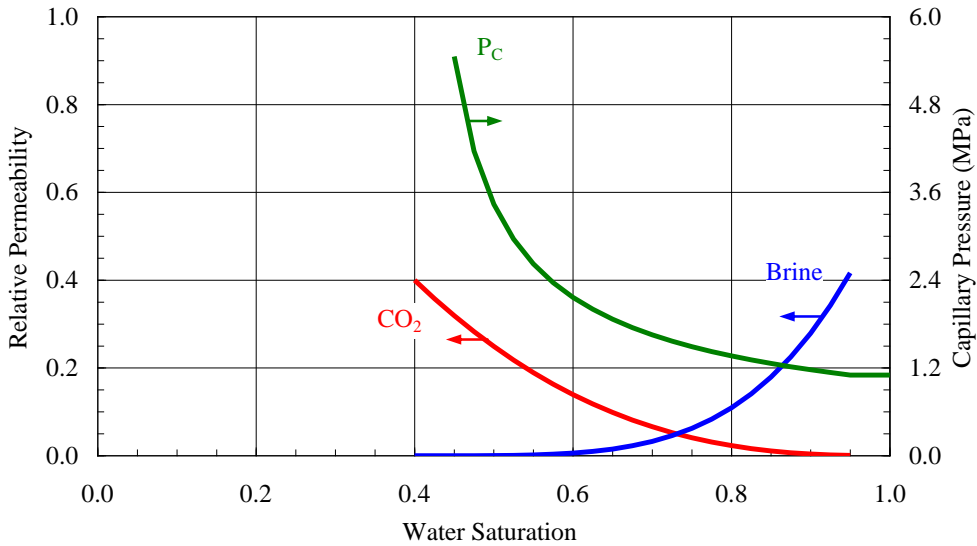


Figure 6.5 CO₂-brine relative permeability and capillary-pressure curves for over- and underlying shale rocks (Hosseini *et al.*, 2012). Very low relative permeabilities (blue: CO₂; red: brine) used for shale. Capillary pressure (green curve) is high for shale rock.

There are a total of five injection wells in the field (Figure 6.6), with one CO₂ injection well in the DAS area studied by BEG, and four CO₂ EOR injection wells in the region far from the DAS. In the the simulation model, the four EOR injection wells only inject CO₂ assuming no oil is present (i.e. 100% water saturated aquifer). Seven constant-pressure boundary wells are located in the three sides of the model to mimic the open boundary condition for pressure maintenance. Four boundary wells on the right-hand side are completed in the bottom layer only (Figure 6.6). The numerical model includes one 110 ft thick layer on the top and one 90 ft layer at the bottom to represent the shale base and cap rocks. The aquifer is sandwiched in the middle with 20 layers. The depth contour is also shown in the top view in Figure 6.7.

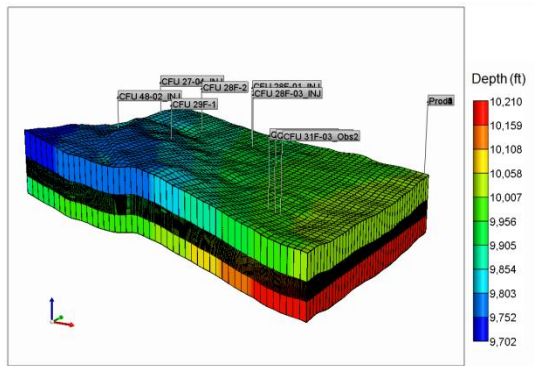


Figure 6.6 Aquifer depth and well locations .

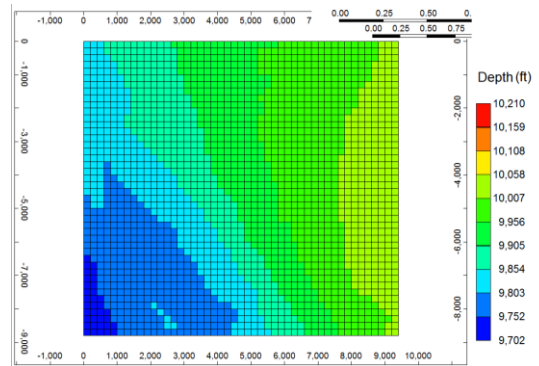


Figure 6.7 Depth from top view.

The well rate in IPARS is converted from field data (Figure 6.8).

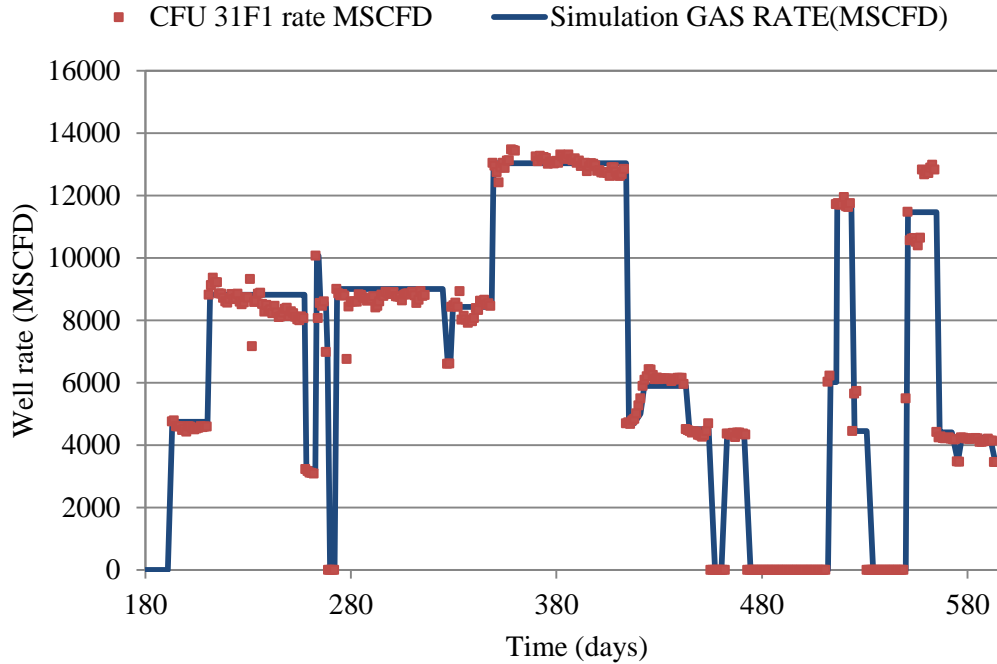


Figure 6.8 CO₂ injection rate schedule for well CFU 31F1.

6.2.1 GRID UPSCALING

The original geological model has 18 million grid cells ($940 \times 880 \times 22$). Grid cells have a size of $10 \text{ ft} \times 10 \text{ ft} \times 4 \text{ ft}$ in length, width, and thickness. The top and bottom layers are impermeable shale rocks. We upscaled the grid using 25 ft, 50 ft, 100 ft, and 200 ft in the x and y directions while keeping the vertical grid resolution of 4 ft (Table 6.3). Simulation models are set up based on upscaled grid resolutions and field injection schedule. The simulation included CO₂ injection for 3 years and is followed by shut-in for 7 years to allow CO₂ to redistribute. Final saturation profiles at 3 and 10 years are compared to study the impact of grid size on simulation results.

Table 6.3 Number of grid cells and grid sizes for upscaled cases

Grid number	Grid number in X-Y-Z direction	Grid size (ft)
41,360	47 × 44 × 20	200 ft × 200 ft × 4 ft
165,440	94 × 88 × 20	100 ft × 100 ft × 4 ft
661,760	188 × 176 × 20	50 ft × 50 ft × 4 ft
2,647,040	376 × 352 × 20	25 ft × 25 ft × 4 ft

The upscaled permeability and porosity fields are shown in Figure 6.9 and Figure 6.10.

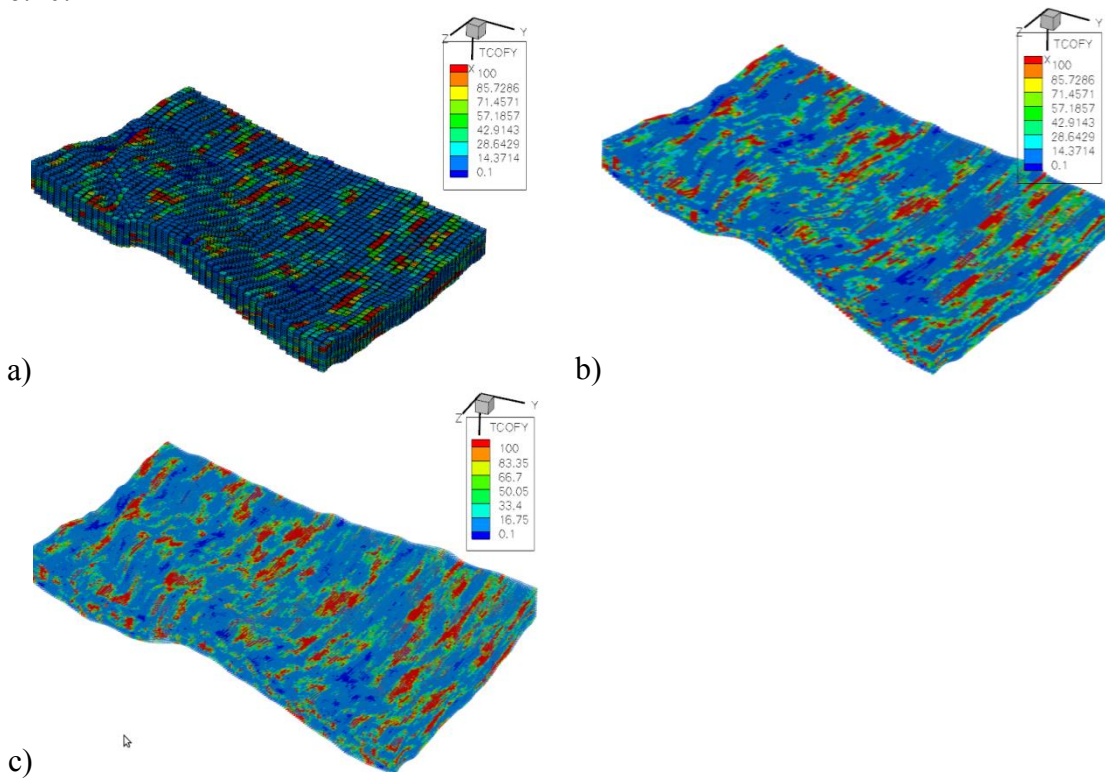


Figure 6.9 Upscaled Cranfield permeability field in Y direction, a) 200 ft; b) 100 ft; c) 50 ft.

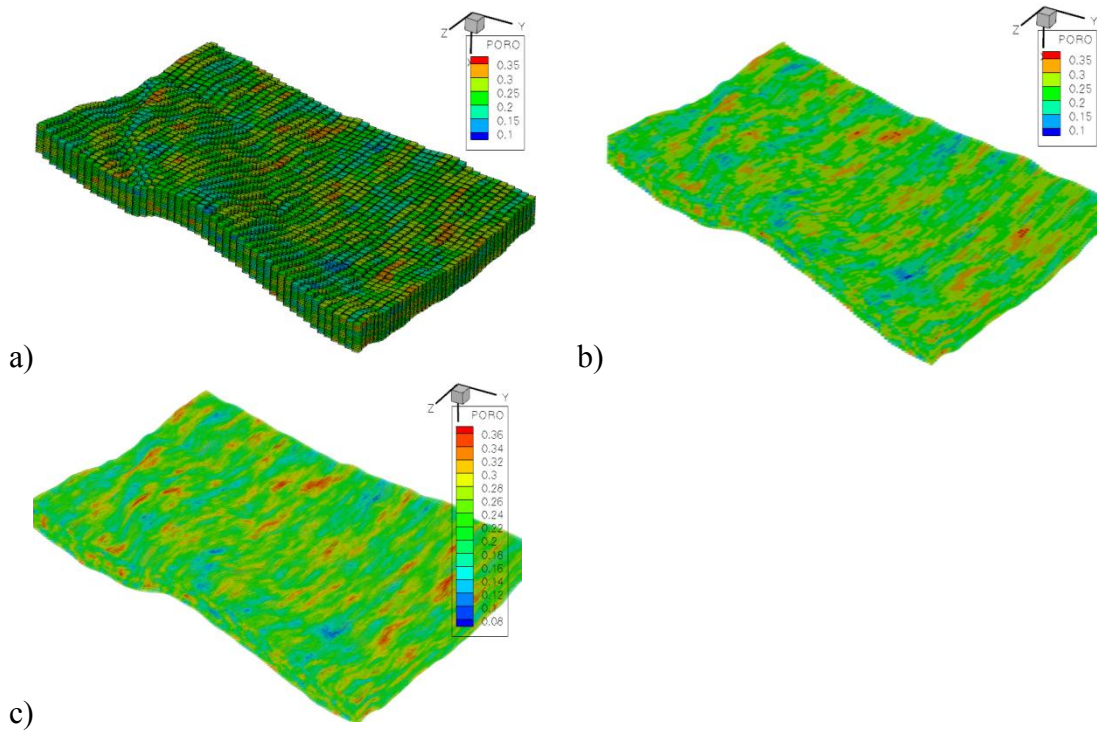


Figure 6.10 Upscaled Cranfield porosity field in Y direction, a) 200 ft; b) 100 ft; c) 50 ft.

We observe that the upscaled permeability and porosity of the 100 ft and 50 ft grid cases give quite similar distributions while the coarse grid of 200 ft gives poorest representation of the field.

Simulation results are provided in the following figures.

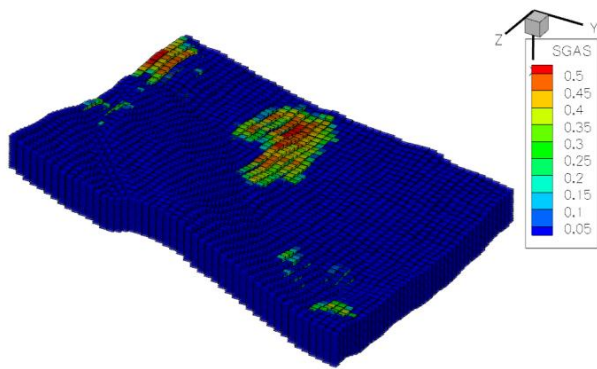


Figure 6.11 CO₂ saturation at the end of 3 years of injection with a grid size of 200 ft.

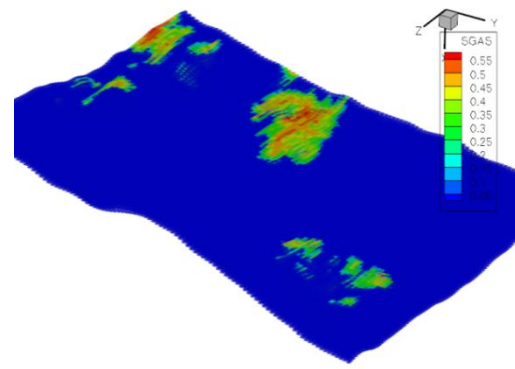


Figure 6.12 CO₂ saturation at the end of 3 years of injection with a grid size of 100 ft.

We observe that the coarse grid of 200 ft in Figure 6.11 gives a poor prediction of the CO₂ plume when compared with the finer grid cases.

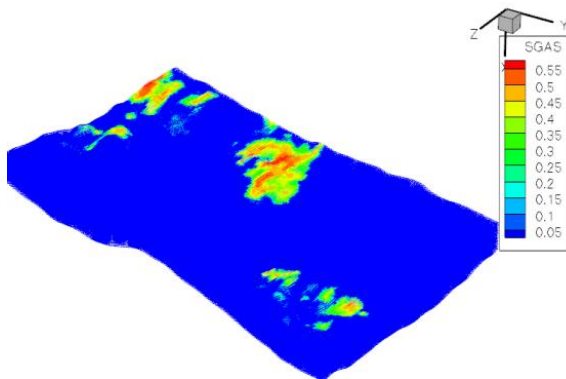


Figure 6.13 CO₂ saturation at the end of 3 years of injection with a grid size of 50 ft.

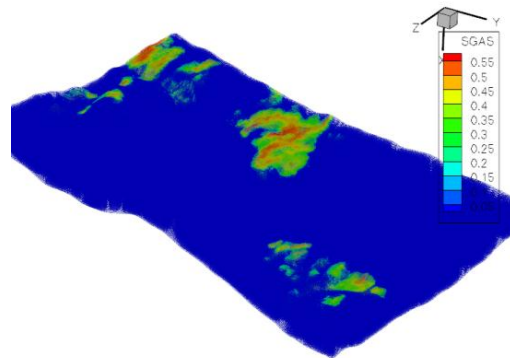


Figure 6.14 CO₂ saturation at the end of 3 years of injection with a grid size of 25 ft.

There is an improvement in the saturation results between grid sizes 100 ft and 50 ft. Further refinement of the grid to 25 ft does not provide significant improvement in saturation results. Therefore, we selected the grid size of 50 ft × 50 ft × 4 ft for history match and sensitivity simulations.

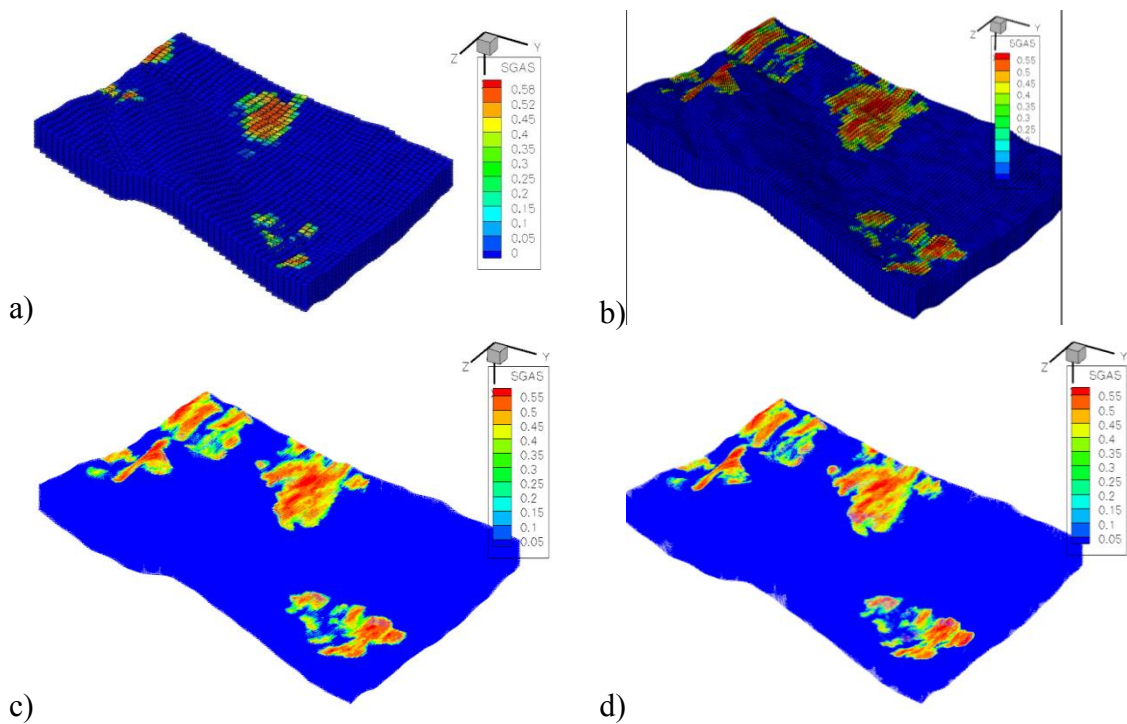


Figure 6.15 CO₂ saturation after 10 years with grid size, a) 200 ft; b) 100 ft; c) 50 ft; d) 25 ft.

We observe that the injected CO₂ spreads laterally and vertically over a large area, due to upward migration and formation dip. We next studied the sensitivity to petrophysical properties and the impact on CO₂ migration.

6.2.2 ISOTHERMAL SENSITIVITY SIMULATIONS

Multiple Cranfield simulations were conducted considering sensitivity to petrophysical properties including interfacial tension, the trapping model, and hysteresis in capillary pressure.

These simulations use the grid size of 50 ft × 50 ft × 4 ft,

Four simulation cases are

- 1) No hysteresis and no capillary pressure scaling

- 2) Hysteresis with capillary pressure scaling
- 3) Relative permeability as a function of trapping number and capillary pressure scaling
- 4) Different rock types

6.2.2.1 Base Case with 50 ft × 50 ft × 4 ft Grid

Base case results are shown in Figure 6.16 and Figure 6.17. We observe the migration of CO₂ at the end of injection and after shut-in the well.

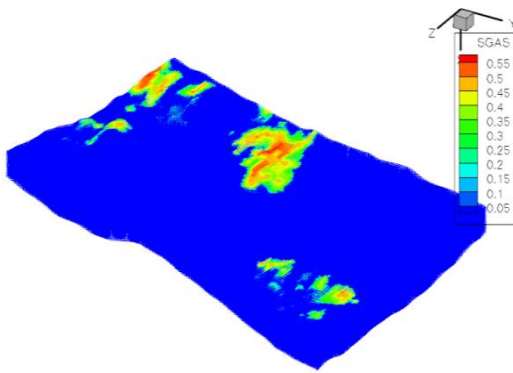


Figure 6.16 Base case CO₂ saturation at 3 years.

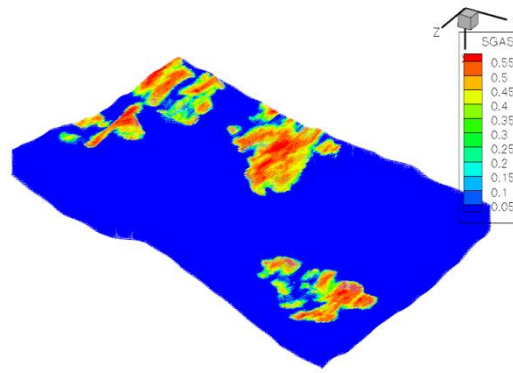


Figure 6.17 Base case CO₂ saturation at 10 years.

The gas saturation in the cross-section of injection well is shown in the following figures. The 2D X-Z views of gas saturation across the injection well at 3 and 10 years show gas migration upward after shut-in (Figure 6.18 and Figure 6.19).

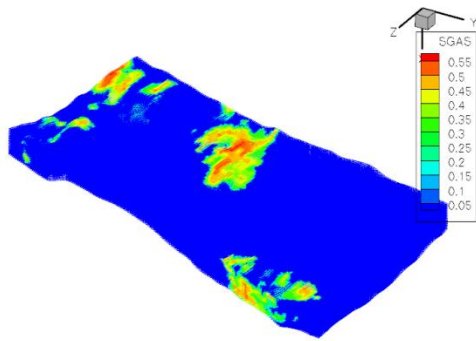


Figure 6.18 Base case CO₂ saturation in injection well cross-section at 3 years.

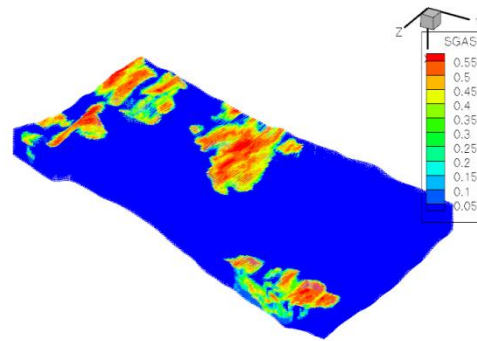


Figure 6.19 Base case CO₂ saturation in injection well cross-section at 10 years.

The CO₂ inventory is shown in Figure 6.20. There is trapping of CO₂ from the beginning of injection (we assumed a constant residual CO₂ saturation). The dissolved CO₂ volume increases after shut-in, which means that CO₂ is contacting more and more unsaturated water.

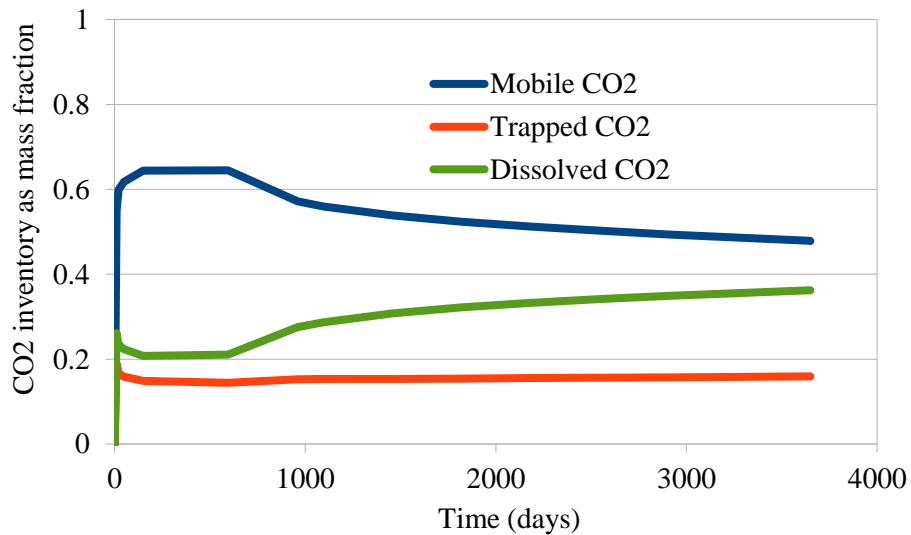


Figure 6.20 CO₂ inventory as fraction of total injection, without hysteresis model

6.2.2.2 Effect of Hysteresis on CO₂ Saturation with P_c Scaling, Case 2

Case 2 includes the hysteresis effect where during the injection period there is no gas trapping, and in the shut-in period, CO₂ trapping occurs. The maximum trapped gas saturation is as assumed to be 0.2, while the trapped gas saturation is calculated in each grid cell based on historical maximum gas saturation.

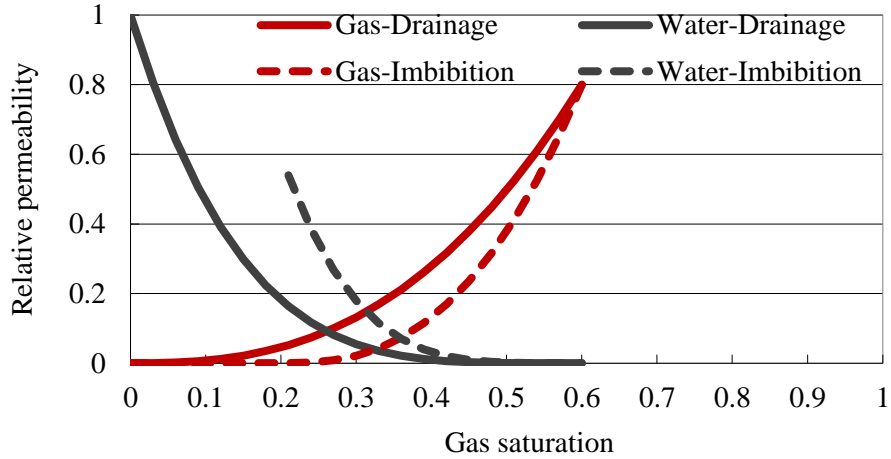


Figure 6.21 Drainage and imbibition relative permeability curves for CO₂-brine.

CO₂ saturation profiles at 3 years and at 10 years with hysteresis are shown in Figure 6.22 and Figure 6.23. We can see CO₂ migrates upward to aquifer top surface after 7 years' shut-in. The CO₂ saturation on cross section of well shows, when hysteresis modeling is included, part of CO₂ is trapped near the bottom during shut-in period (Figure 6.24 and Figure 6.25). After CO₂ redistribution for 7 years, CO₂ is trapped as the residual phase in rock pores during imbibition cycle.

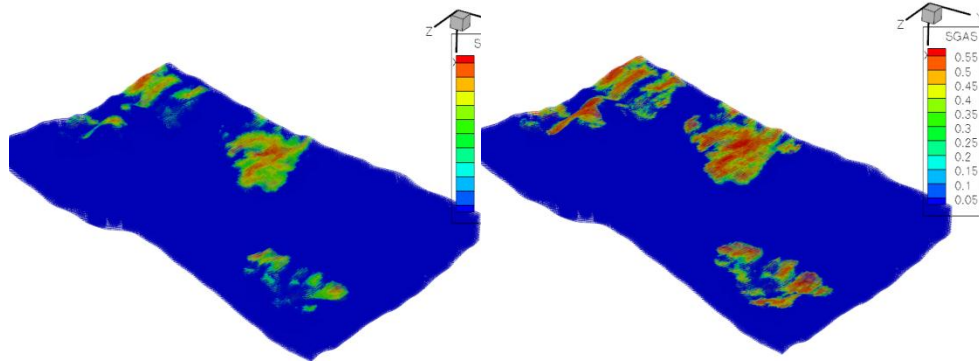


Figure 6.22 CO₂ saturation at 3 years, with hysteresis.

Figure 6.23 CO₂ saturation at 10 years, with hysteresis.

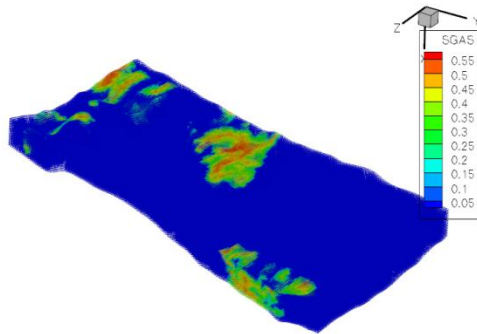


Figure 6.24 A cross section of CO₂ saturation at 3 years, with hysteresis.

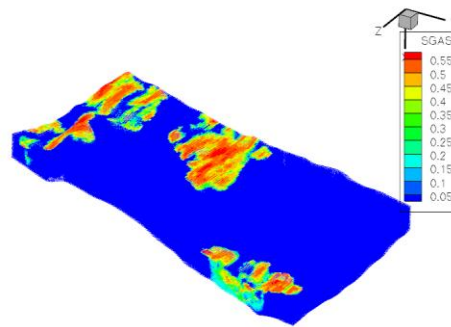


Figure 6.25 A cross section of CO₂ saturation slice at 10 years, with hysteresis.

The CO₂ inventory as fraction of total injection is given in Figure 6.276 for the simulation with the hysteresis model. There is almost no residual trapping of CO₂ during the injection period, and after injection stopped at 595 days, the residual trapping of CO₂ increases with time.

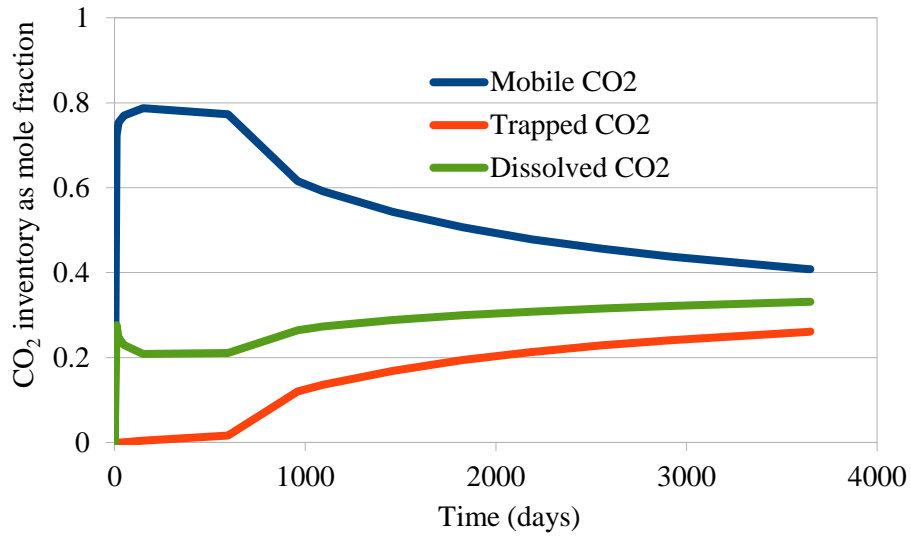


Figure 6.26 CO₂ inventory as fraction of total injection with hysteresis model ($S_{gr, mx} = 0.2$)

The mobile CO₂ fraction with different residual saturation models is shown in Figure 6.27, which shows the mobile CO₂ fraction decreases after injection stops. We can see hysteresis model with different maximum residual saturation has a great impact on the prediction of the mobile CO₂ fraction over time.

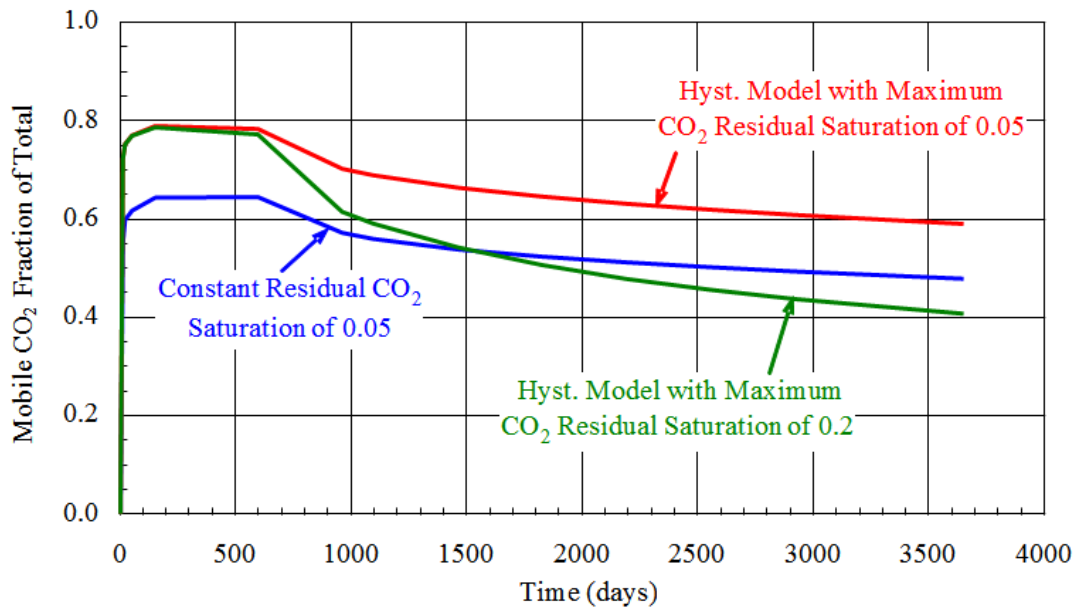


Figure 6.27 Simulated mobile CO₂ as a fraction of total injection for different residual CO₂ saturations

6.2.2.3 Effect of Relative Permeability Model and Trapping Number on CO₂ Saturation, Case 3

Case 3 includes the relative permeability model as a function of interfacial tension and trapping number where residual gas saturation is calculated as a function of trapping number. The maximum residual gas saturation at a low trapping number is 0.05, which is equal to that of the base case.

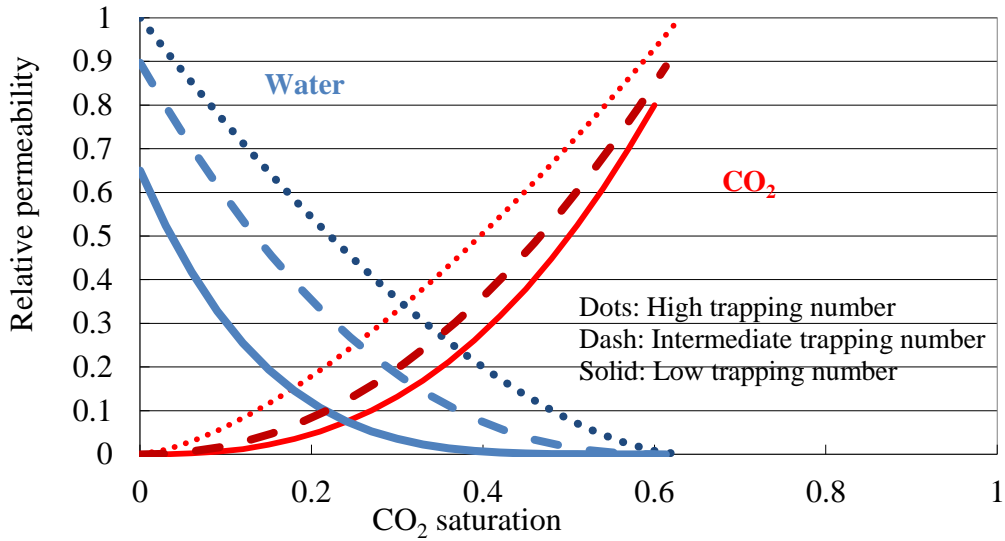


Figure 6.28 Brine/CO₂ drainage relative permeability curves for low (1×10^{-8}), intermediate (1×10^{-7}), and high (1×10^{-6}) trapping numbers.

Simulation results of gas saturation with trapping model are shown in Figure 6.29 and Figure 6.30.

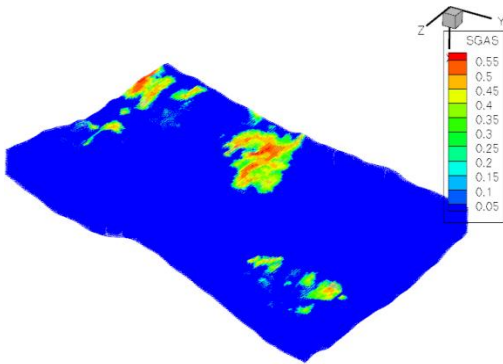


Figure 6.29 CO₂ saturation at 3 years, with the trapping model.

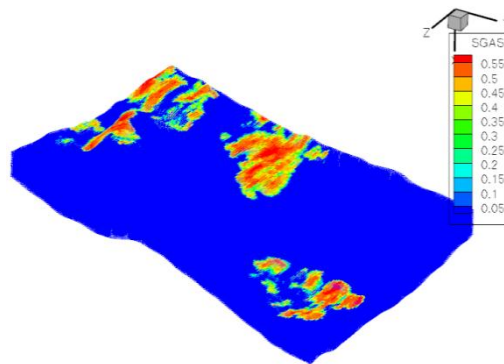


Figure 6.30 CO₂ saturation at 10 years, with the trapping model.

The saturation profile is similar to the base case at the end of 3 years compared in Figure 6.31 and Figure 6.32. While the final distribution shows that much less gas is trapped (Figure 6.32), due to the reduction in residual saturation and consequent change in relative permeabilities. When the residual saturation is reduced due to the high the trapping number, the relative permeability will increase accordingly (Figure 6.28). The high relative permeability will give a high mobility for gas to migrate upward and to further distances from the well.

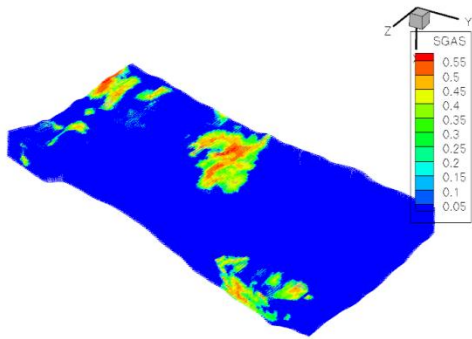


Figure 6.31 CO₂ saturation in the injection well cross-section at 3 years with the trapping model.

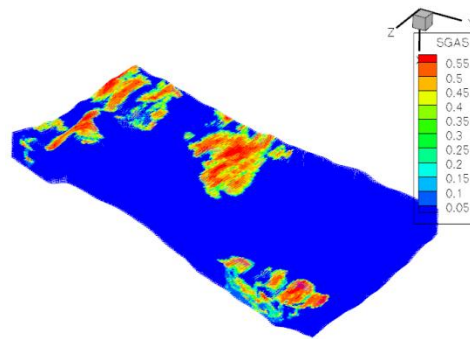


Figure 6.32 CO₂ saturation in the injection well cross-section at 10 years, with the trapping model.

The trapped amount of CO₂ is compared to hysteresis model in Figure 6.33, which shows less CO₂ is trapped after injection.

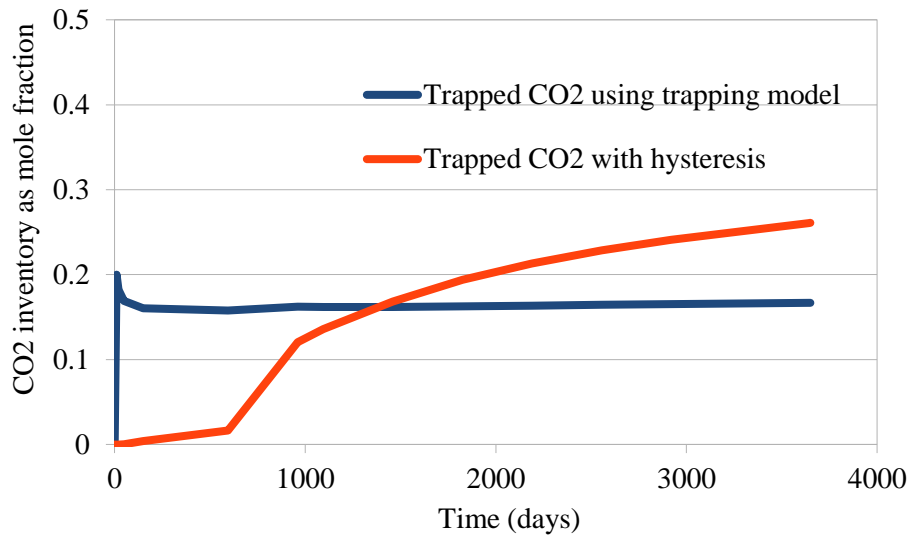


Figure 6.33 Trapped amount of CO₂ with trapping model and hysteresis model.

6.2.2.4 Effect of Rock Type on CO₂ Migration

We tested the impact of different rock relative permeabilities and capillary pressures on sequestration in the Cranfield formation. The laboratory results using Cardium sandstone from Bennion and Bachu (2006a) is used (Figure 6.34 and Figure 6.35). Simulation is conducted without hysteresis and without the trapping model. The injection well is rate controlled well with same injection schedule as the base case.

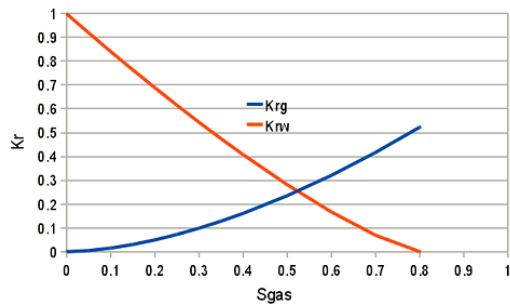


Figure 6.34 Relative permeability of Cardium #1 sandstone from Bennion and Bachu (2006a).

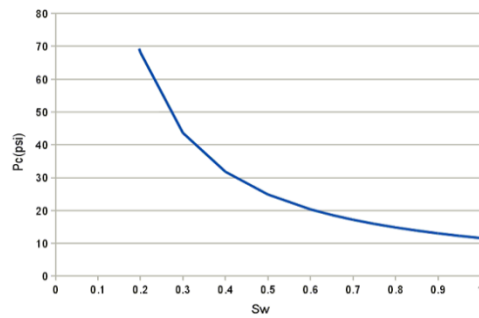


Figure 6.35 Capillary pressure of Cardium #1 sandstone from Bennion and Bachu (2006a).

Simulation results show that the gas saturation is much higher in the reservoir with a new rock type compared to the base case. Gas saturations at 3 and 10 years are shown in Figure 6.36 and Figure 6.37, which shows the significant difference from the base case (Figure 6.16 and Figure 6.17). The saturation distributions in Figure 6.36 and Figure 6.37 show sharp front with high CO₂ saturations compared to Figures 6.31 and 6.32. This difference in saturation profiles shows the significance of rock type and relative permeability on CO₂ migration.

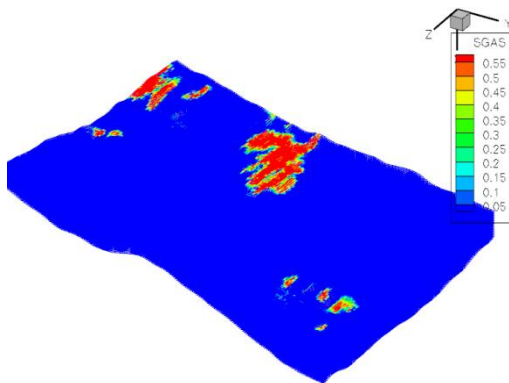


Figure 6.36 CO₂ saturation at 3 years with no hysteresis.

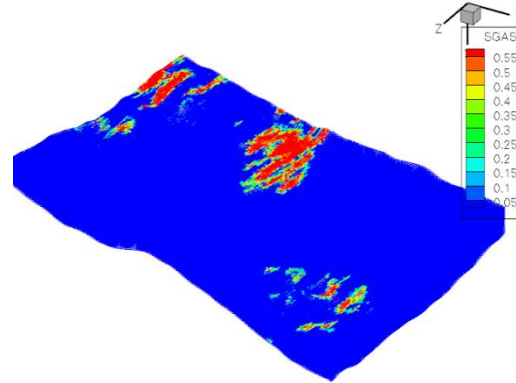


Figure 6.37 CO₂ saturation at 10 years with no hysteresis.

Gas saturation in the cross-section of the injection well is shown in the following figures.

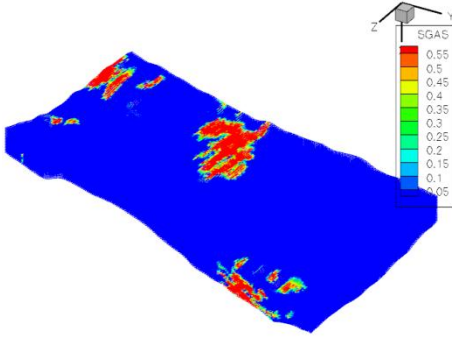


Figure 6.38 A cross section of CO₂ saturation at 3 years with no hysteresis.

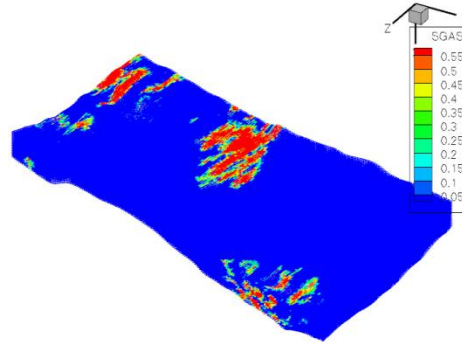


Figure 6.39 A cross section of CO₂ saturation at 10 years without hysteresis.

Simulation results show that CO₂ displacing water is greatly enhanced and resulted in very high gas saturation near the rate controlled injection well. The high gas saturation near the well could be due to increase of gas and water mobility ratio by the high gas relative permeability. Less CO₂ is migrated upward to the top layer below the caprock with the new rock type, thus it is critical to have an accurate characterization for the site and with appropriate relative permeability and capillary pressure curves.

6.2.3 HISTORY MATCHING WITH NEAR WELLBORE FRACTURE MODELING

We conducted a detailed simulation study of Cranfield test in order to history-match the field observation data that includes injection well BHP and CO₂ breakthrough time in the observation wells. The Cranfield base case with a grid size of 50 ft × 50 ft × 4 ft is used for the history-match simulations. The same well array and injection schedule as the field test is used. The injection started on day 193 (Dec. 1st, 2009) of the simulation.

The BHP of the BEG injection well CFU 31-F1 is compared to field data (Figure 6.40). The simulation results match field data reasonably well in early period from day 193 to day 350.

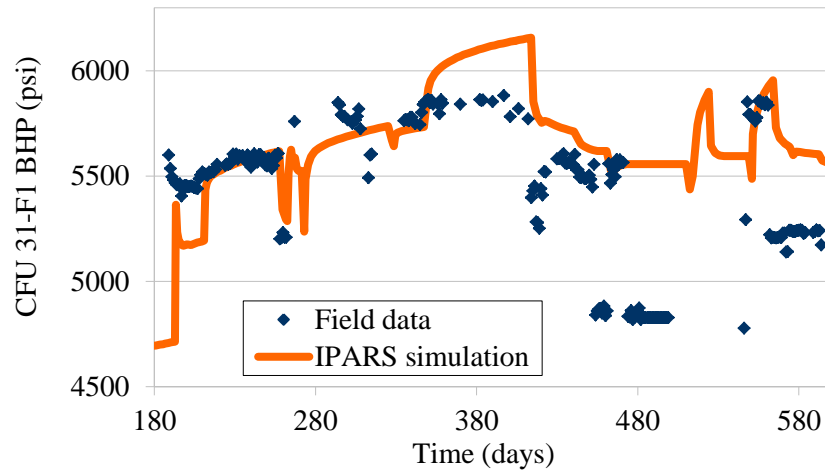


Figure 6.40 IPARS simulation results of CFU 31-F1 well BHP and field data.

From the results of injection well BHP in Figure 6.40, we observe that there is a mismatch after day 350, when the BHP exceeds 5900 psi. There are several possible reasons for this mismatch. One reason for this could be fracturing of the formation rock and well due to the high pressure. Another reason could be the increase in relative permeability due to high injection rate and increase in trapping number. There are also geological uncertainties.

We made an attempt to explore the possibility that injectivity induced fracture explain the pressure insensitivity to the injection rate observed in the field. The vertical fracture is represented using grids with high permeability and porosity. Several simulations were conducted to test the sensitivity of BHP to the fracture length and permeability. The effect of a fracture on the injection well BHP is studied, with a fracture

existing from the beginning and with a fracture occurring when the pressure exceeds the fracture pressure.

We compared simulations including the fracture from the beginning to the base case simulation results and to the field data (Figure 6.41). The fracture has a length of 250 ft, with permeability of 10 Darcy. We observe that fracture will reduce injection well BHP, by about 200 psi beyond 350 d injection.

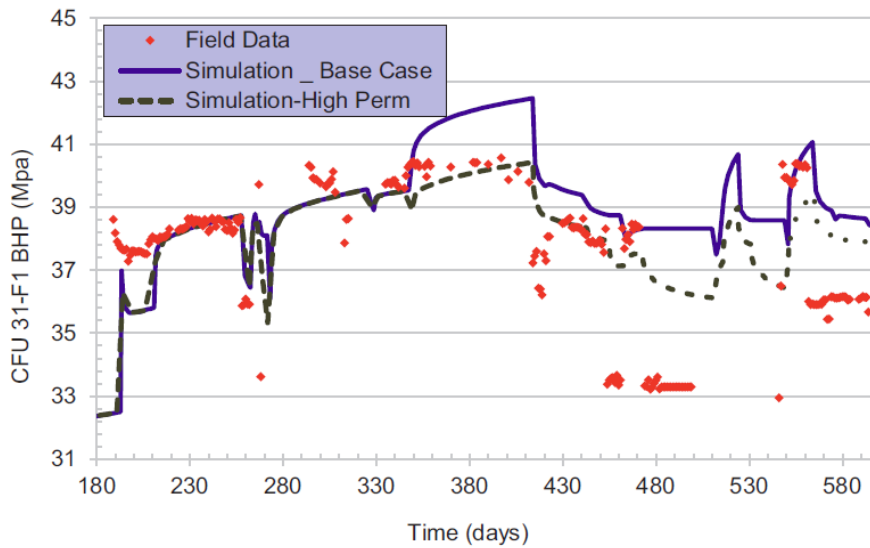


Figure 6.41 Simulation results with and without fracture throughout the whole simulation period compared to the field data.

We modified the way a fracture is represented by introducing high permeability gridblocks only when the injection well pressure exceeds the assumed fracturing pressure of 5900 psi. The injection pressure will continue to increase during the three injection rate increases until 350 days. After day 350, the BHP will increase sharply and the fracture is introduced when BHP exceeds 5900 psi. The value (5900 psi) is chosen to be the fracturing gradient criteria because the field data shows a maximum bottomhole pressure of about 5900 psi.

The simulation and the field bottom-hole pressure data were similar when high permeability cells near well are introduced to mimic the fracture. A vertical fracture with a length of 250 ft from the well and permeability of 10 Darcy was introduced in the model only after the high injection rate period, beginning at 350 days. The simulation results match the field data reasonably well (Figure 6.41). However, the simulation still cannot match the field data after day 480, and this requires further investigation.

The simulated CO₂ breakthrough time in the first observation well is at day 207, which is about 14 days after injection starts (Figure 6.42). This is very close to the field observation of 15 days (Hosseini *et al.*, 2012).

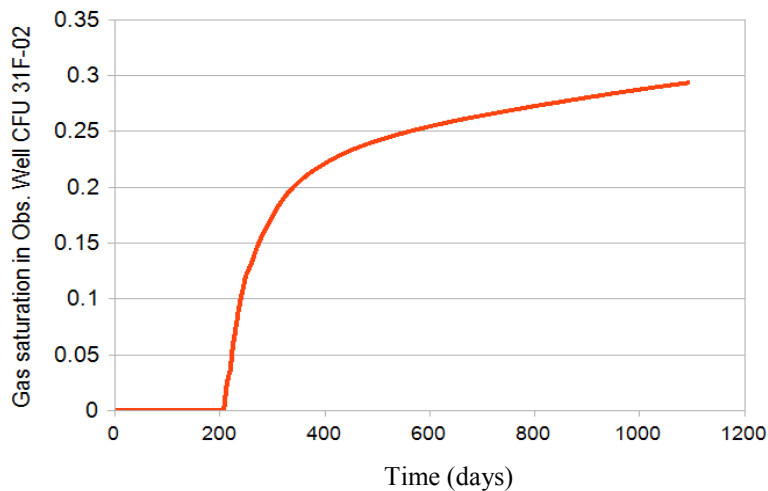


Figure 6.42 CO₂ saturation in the first observation well, CFU 31-F2.

6.2.4 THERMAL SIMULATION

IPARS has a thermal module that is coupled with the compositional transport flow module. The temperature in the reservoir is coupled using a time-split scheme where the temperature is solved in each flow time step. Temperature equation model includes

convection, conduction of heat through each phase, and injector or producer heat sources.

The governing equation is

$$\frac{\partial(U_T T)}{\partial t} + \nabla \cdot (\sum_{\alpha} \rho_{\alpha} u_{\alpha} C_{p\alpha} T) - \nabla \cdot (\lambda \nabla T) = qH, \quad (6.1)$$

where U_T is the internal energy, T is the temperature, ρ_{α} is the density of phase α , u_{α} is the phase velocity, $C_{p\alpha}$ is isobaric phase heat capacity, and qH is the heat source.

Note that phase α also includes the solid rock phase.

The Cranfield pilot CO₂ sequestration project injects cool CO₂ into a hot formation. For the injection well, the recorded bottom-hole temperature difference before and after CO₂ injection is about 44 °C (Hosseini *et al.*, 2012). At the time of simulation, the temperature gauges in observation wells F2 and F3 were malfunctioning (Doughty and Freifeld, 2012). As a result, direct comparison to field observation is not possible.

We constructed non-isothermal Cranfield simulations to study the impact and significance of thermal effects on the CO₂ sequestration under typical, deep saline aquifer conditions. Initial formation temperature of 257 F (125 °C) was assumed and supercritical CO₂ with a temperature of 100 F (37.8 °C) was injected in well CFU31-F1. The temperature in the well and the temperature profile in near well region are monitored as injection continues. The model grid size is 200 ft × 200 ft × 4 ft. The thermal properties are as follows:

Table 6.4 Rock-fluid thermal properties

Rock isochoric specific heat capacity (Btu/lb-F)	0.17913
Brine phase heat capacity (Btu/lb-F)	17.8176
CO ₂ heat capacity (Btu/lb-F)	14.8915
Rock heat conductivity (Btu/ft-Day-F)	48.5343
Brine phase heat conductivity (Btu/ft-Day-F)	10.8856
CO ₂ heat conductivity (Btu/ft-Day-F)	0.2203

Simulation results of CO₂ saturation and temperature profiles at the end of injection and at 1200 days are studied (Figure 6.43 Figure 6.46). We observe that CO migration during and after the injection period covers a large area of the reservoir, while the temperature profile shows a much smaller impacted region than the saturation profile.

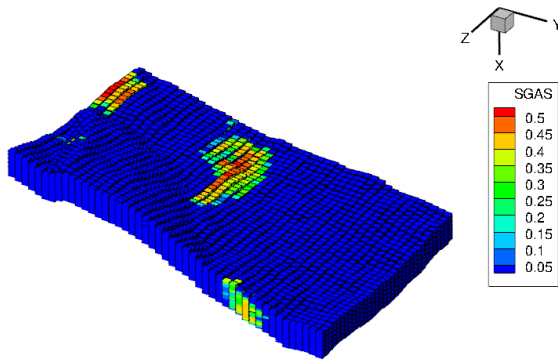


Figure 6.43 CO₂ saturation in the cross-section of injection well F1 at the end of injection at 600 days

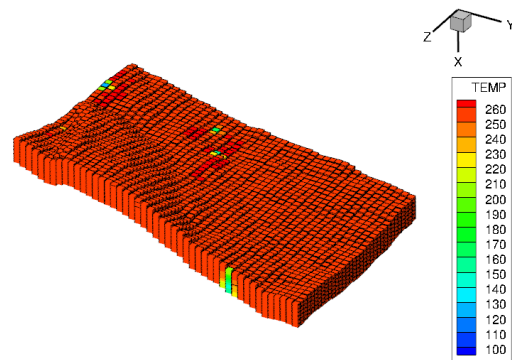


Figure 6.44 Reservoir temperature profile in the cross-section of injection well F1 at the end of injection at 600 days

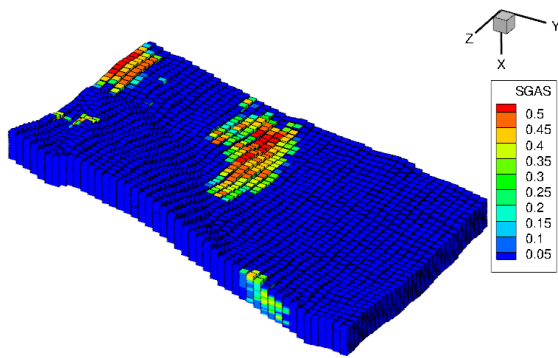


Figure 6.45 CO₂ saturation in the cross-section of injection well F1 at simulation end at 1200 days

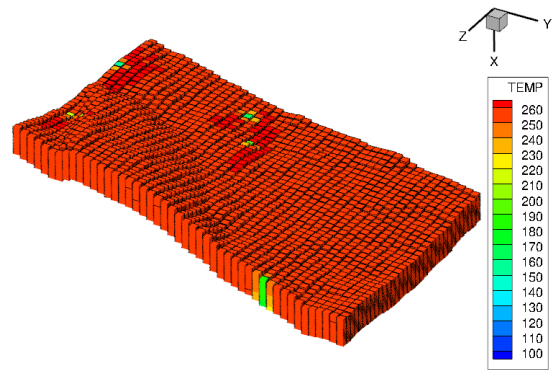


Figure 6.46 Reservoir temperature profile in the cross-section of injection well F1 at simulation end at 1200 days

The temperature history in the wells is also monitored before and after CO₂ injection (Figure 6.47).

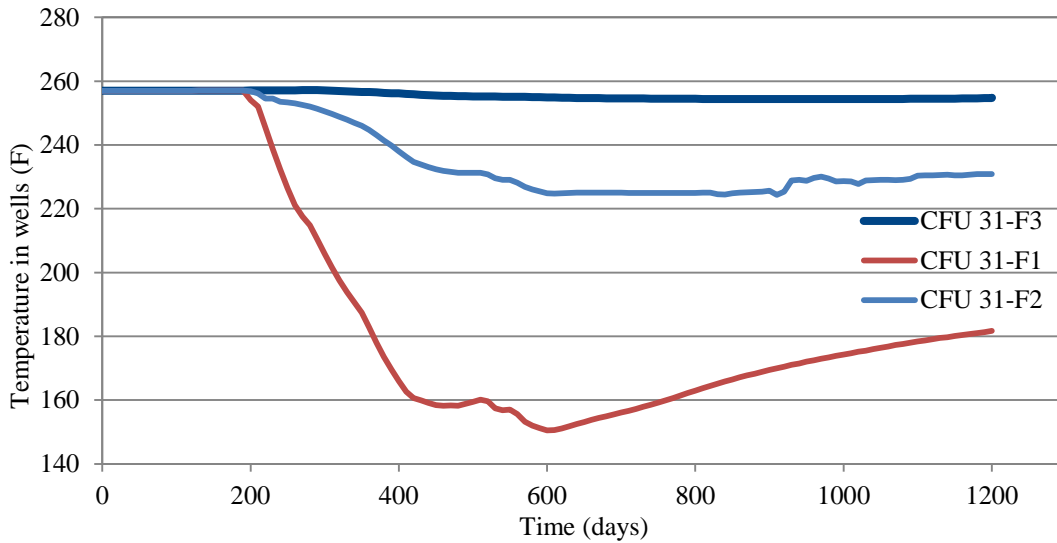


Figure 6.47 Calculated temperature variation in injection and observation wells

The temperature in the injection well CFU 31-F1 drops greatly with the injection of cool supercritical CO₂. The effect of cooler CO₂ was observed in well CFU 31-F2 but

not with very noticeable drop in temperature. The second observation well CFU 31-F3 showed almost no temperature variation.

6.3 Summary

Extensive reservoir modeling and simulation tests were conducted for the Cranfield CO₂ sequestration project, using field data from BEG. The field well rate and bottomhole pressure were imported into the IPARS simulation model. Upscaling and grid resolution tests were first conducted based on the finest field data resolution. The impact of different petrophysical models, such as trapping, IFT, and hysteresis models, were studied. A history matching study was conducted to match the observed injection well BHP and CO₂ breakthrough time in the observation wells. Bottom-hole pressure of injection well 31F1 was closely matched during the early injection period, while the high injection period showed a mismatch. This study indicates the possible geomechanical issues related to high rate injection period. There were also uncertainties in geological data, such as permeability/porosity distribution, measured relative permeability and capillary pressure for its reservoir rocks.

CHAPTER 7: Summary and Future Works

In this chapter, the major findings of this work are summarized and conclusions are presented. Future work is recommended based on current research progress.

7.1 Summary and Conclusions

This study was set out to explore the petrophysical and computational issues related to geological CO₂ sequestration in saline aquifers, and to develop a modeling tool embedded in the existing in-house Integrated Parallel Accurate Reservoir Simulator (IPARS). Geological sequestration is the process of injecting captured CO₂ to underground reservoir and trapping it through many complex geological, chemical, and hydrologic trapping mechanisms. CO₂ sequestration in saline aquifers has proven to have great potential because of wide distribution, large volume, and safety of the storage sites. Successful sequestration requires proper design of the sequestration plan to ensure the large-scale and long-term storage security. However, the geological uncertainties and complex petrophysical phenomena pose a great challenge in this research area. Numerical simulators are essential tools to develop a better understanding of the geologic characteristics of saline aquifers and to build support for future CO₂ storage projects. In this study, we developed the research reservoir simulator (IPARS) to study the CO₂ sequestration in saline aquifers. We developed new petrophysical models related to the process of CO₂ storage in saline aquifers, validated the results against laboratory coreflood, and history matched the observed results of field CO₂ injection demonstration.

The accomplishments and results of research are summarized.

- **Adapted IPARS to CO₂ storage:**

- Used compositional simulation framework for CO₂ sequestration in aquifers.
- Modified the Peng-Robinson equation of state (PR-EOS) to calculate CO₂ solubility in water and phase densities.
- Implemented correlations to model equation of state fluid parameters as a function of brine salinity.
- Enhanced input/output modules to compute and post-process CO₂ sequestration simulation results (listed in Appendix B).
- **Enhancement in Petrophysical Properties:** Geological sequestered CO₂ is trapped in underground reservoirs through four main mechanisms, including structural trapping, residual trapping, dissolution, and mineral trapping. The effectiveness of CO₂ storage in saline aquifers is governed by the interplay of capillary, viscous, and gravitational forces. Petrophysical properties, such as wettability, residual saturation, relative permeability and capillary pressure, etc., are critical for CO₂ migration and trapping under these forces. Variation of these properties under different *in situ* condition is also clearly evident in published experimental results. A key issue is to develop the integrated petrophysical models to characterize the sequestration processes, such as the variation of residual saturation vs IFT, the dependence of CO₂-brine relative permeability on trapping number, and variation of capillary pressure with heterogeneity and contact angle. A trapping model based on trapping number was developed to characterize the dependence of residual saturation and relative permeability on the three forces. A hysteresis model of relative permeability and capillary pressure was developed and implemented in

IPARS. Capillary pressure varies for different reservoir rock permeability and porosity, wettability, and interfacial tension.

- **Interfacial tension**

Interfacial tension model has to be consistent with the published laboratory data for supercritical CO₂/brine. Three published IFT correlations were implemented to calculate CO₂/brine interfacial tension accounting for pressure, temperature, dissolution, density, and salinity.

- **Trapping number**

Capillary number is the ratio of viscous force to capillary force, while Bond number is the ratio of gravity force to capillary force. Trapping number (sum of capillary and Bond numbers) quantifies the interplay of capillary, viscous, and gravity forces. The trapping number model was implemented in IPARS where CO₂ residual trapping is calculated based on the trapping number.

- **Trapping number dependent relative permeability**

We have developed and implemented a relative permeability model coupled with trapping model. This model captures the change in residual saturations and subsequent shift in relative permeabilities.

- **Trapped CO₂ due to hysteresis**

A hysteresis model based on Land's correlation is implemented to account for history-dependent trapped CO₂ saturation. .

- **Saturation path dependent relative permeability and capillary pressure**

Hysteretic relative permeability and capillary pressure models were developed and implemented in IPARS.

- **Capillary pressure model based on Leverett J-function**

The capillary pressure model is developed to couple the variation of IFT, contact angle, and reservoir heterogeneity.

- **Wettability model**

Wettability can be quantified by contact angle between water, CO₂, and rock surface. We coupled the variation of contact angle in capillary pressure function.

- **Sensitivity Tests using Enhanced Petrophysical Models:** Extensive sensitivity tests were conducted in this study, which validated the models and showed the significance of petrophysical modeling on CO₂ sequestration and deepened our understanding to CO₂ sequestration process.

- Stacked aquifer simulation shows the capability of shale cap rock as a sealing barrier for CO₂ migration upward.
- Sensitivity simulation using capillary pressure model shows impact of wettability, IFT, and heterogeneity on CO₂ migration.
- Sensitivity simulation using relative permeability based on trapping number shows the impact of interplay of capillary, viscous, and gravity forces on CO₂ trapping and migration.
- The saturation path dependent relative permeability and capillary pressure are tested using 1D and 3D test case incorporating Land's trapping model, which shows the complexity of hysteresis during drainage and imbibition processes.

- **Validation using Coreflood Results:** The motivation of the coreflood simulation study was to gain confidence in the results of the numerical simulator by validating the models and the numerical accuracies using laboratory results. Published steady state, core-scale supercritical CO₂/brine displacement results were selected as a reference basis for our numerical study. This study provided insights into the role of heterogeneity in the final CO₂ distribution in reservoir rocks, where a slight variation in porosity gives rise to a large variation in the CO₂ saturation distribution. A summary of results is as follow,
 - Geostatistically generated log normal permeability and normal porosity distributions gave a reasonable history match of the steady-state CO₂/brine coreflood results published by Krause *et al.* (2011).
 - Scaling of capillary pressure using Leverett J-function was critical to capture sub-core scale flow characteristics. Simulated results showed significant contrast locally in CO₂ saturation, similar to what was observed in the CT-scan laboratory results.
 - We incorporated the measured drainage relative permeability and capillary pressure provided by Krause *et al.* (2011). However, there are still uncertainties in *in situ* capillary pressure and relative permeability for this coreflood. We demonstrated the sensitivity to residual water saturation. The measured final CO₂ saturation gave saturations greater than 0.8, indicating that residual water saturation was lower than the measured and reported value of 0.2.
 - Several techniques were considered for generating the porosity and permeability distributions in order to match measured average

permeability and porosity. The results indicated that the arithmetic mean for porosity and the geometric mean for permeability matched the experimental results better than other averaging methods. Specifically, the pressure drop was very sensitive to the choice of permeability averaging method (arithmetic/geometric/harmonic).

- **History Match Cranfield Field Demonstration:** Cranfield CO₂ sequestration project is a pilot test conducted by the Bureau of Economic Geology (BEG) at The University of Texas at Austin. A total of approximately 2.5 million tons supercritical CO₂ was injected into a saline aquifer about ~10000 ft deep at a rate of 1 million tons per year for over 2 years. Reservoir simulation model was set up in IPARS by importing field geology data, rock-fluid property data, and well data, aiming to test and demonstrate the capability of IPARS simulator in field scale study. Extensive sensitivity studies were conducted for grid upscaling, fluid phase behavior, trapping, relative permeability, wettability, gravity and buoyancy, and thermal effects on sequestration. Results also illustrated the importance of using accurate trapping models to predict CO₂ immobilization behavior. The impact of CO₂/brine relative permeability curves and trapping model on bottom-hole injection pressure was also demonstrated. A few additional observations and conclusions are outlined as follows.
 - This work successfully demonstrated the capability of IPARS to model the field scale Cranfield CO₂ injection test in a complex geological setting.
 - We upscaled interfacial tension using a dimensionless trapping number. The effects of contact angle, interfacial tension, and reservoir heterogeneity were included in both the relative permeability and the capillary pressure functions.

The simulated bottomhole injection pressure results exhibit a strong sensitivity to the trapping model and relative permeability curves.

- Hysteresis model provided an accurate calculation of CO₂ inventory as residual trapped, dissolved, and structural trapped amount over time. The impact of hysteresis on CO₂ trapping and migration is clearly shown through the saturation profile near injection well.
- Numerical results are consistent with bottomhole injection flowing pressure for the first 350 days prior to the rate increase to 13,000 MSCFD, and injection well pressure after 350 days were successfully history matched by introducing a high permeability vertical plane across the whole thickness of injection well perforation to mimic injection induced fracture.
- Simulation study indicated that CO₂ breakthrough time at the first observation well was about 14 days, which was consistent with the observed data.
- Future CO₂ field demonstrations require additional laboratory measurements of relative permeability and capillary pressure under different pressures and several saturation paths in reservoir cores at reservoir temperature and formation brine salinity.

Finally, this study presents an integrated modeling and comprehensive study of complex petrophysical phenomena involved in geological CO₂ sequestration using compositional framework in the parallel simulator IPARS. Petrophysical model, numerical scheme, and parallel computation worked together provide a scientific tool for future applications in this field. Some conclusions of this work are as follows:

- Small scale heterogeneities have great impact on CO₂ saturation distribution

- Leverett J-function scaling of capillary pressure was needed in order to history match coreflood results
- Our simulation results identified local variations of residual water saturation consistent with measured saturation histogram
- Relative permeability and capillary pressure relationships greatly impact near well pressure response and need to be measured for CO₂ and brine under reservoir conditions to reduce uncertainties
- Cranfield simulations and the sensitivity studies indicated near well geomechanical effects are involved to explain the observed BHP behavior

7.2 Future Works

Future works can include the following:

1. Due to the large scale and long period of sequestration, an efficient and powerful reservoir simulator that is capable of running parallel simulations is needed. New solvers, such as HYPRE, can be implemented in IPARS to speed up the simulations.
2. Continued enhancements to the CO₂ property module in IPARS are necessary for more accurate modeling of field conditions, such as contact angle and residual saturation variation due to CO₂ injection.
3. Geochemical modeling of reactions and mineralization induced by CO₂ injection in the saline aquifer is one topic that could warrant future research.

4. CO₂ sequestration in saline aquifer involves thermodynamic process and cooling effects of injecting cool CO₂ into hot reservoirs. Thermal simulation study is one area for future studies.
5. Geomechanical issues such as fracturing and pressure build up induced by CO₂ injection need to be further studied.
6. The potential for foam assisted CO₂ storage to mitigate gas leakage and buoyancy driven flow through reducing CO₂ mobility with foam needs further investigation.

APPENDIX A: COMPOSITIONAL MODEL

In IPARS compositional simulation of CO₂ sequestration, CO₂ is dissolved into the water phase. In order to simulate this process, compositional modeling is needed. In practical application, the water phase is treated as a "hydrocarbon" component that gas could exist in it. The PVT properties of the brine and CO₂ are given by flash calculation using equation of state (EOS). The most common equations of state are the cubic equation of state similar to van der Waals equation (van der Waals, 1910), with different modeling parameters, such as Peng-Robinson EOS, etc. For a two phase mixture system, the composition of each phase could be determined by flash calculation based on phase equilibrium.

A.1 Phase Equilibrium

The ratio between mole fractions of component i in the vapor and liquid phases is called the equilibrium ratio or the K-factor,

$$K_i = \frac{y_i}{x_i} \quad \text{A-1}$$

In which, y_i is mole fraction of component i in vapor phase, x_i is mole fraction of component i in liquid phase.

Phase equilibrium requires

$$f_i^l = f_i^v \quad \text{A-2}$$

Note that $f_i^l = x_i \varphi_i^l P$, $f_i^v = y_i \varphi_i^v P$, we have

$$K_i = \frac{\varphi_i^l}{\varphi_i^v} \quad \text{A-3}$$

Hence the equilibrium criteria would be,

$$\ln(\varphi_i^l) - \ln(\varphi_i^v) - \ln(K_i) = 0 \quad \text{A-4}$$

In which φ_i^l, φ_i^v are fugacity coefficients that can be calculated from EOS.

A.2 Rachford-Rice Equations for Vapor Fraction

For two phase mixture system with over all mole fraction z_i for component i , we have

$$n_L + n_V = 1 \quad \text{A-5}$$

$$\sum_1^{N_c} x_i = 1 \quad \text{A-6}$$

$$\sum_1^{N_c} y_i = 1 \quad \text{A-7}$$

$$K_i = \frac{y_i}{x_i} \quad \text{A-8}$$

Assume vapor phase molar fraction n_V , then we have

$$z_i = n_V y_i + (1 - n_V) x_i \quad \text{A-9}$$

Substituting y_i and transforming the equation, we will have

$$x_i = \frac{z_i}{1 + (K_i - 1)n_V} \quad \text{A-10}$$

$$y_i = \frac{z_i K_i}{1 + (K_i - 1)n_V} \quad \text{A-11}$$

For the phase composition,

$$\sum_1^{N_c} (y_i - x_i) = 0 \quad \text{A-12}$$

The Rachford-Rice equation for determining vapor fraction n_V would be

$$\sum_i \frac{z_i(K_i-1)}{1+(K_i-1)n_V} = 0 \quad \text{A-13}$$

The flash calculation will be performed in a trial and error way to calculate the vapor fraction n_V . Rachford-Rice equation is used because it is easier to converge than phase compositional equations.

Let F equals residual of Rachford-Rice equation,

$$(n_V)^{k+1} = (n_V)^k + 0.01 \frac{F}{\partial F / \partial n_V} \quad \text{A-14}$$

Iteration continues until convergence criteria is met or n_V no longer changes.

A.3 Peng-Robinson Equation of State

The Peng-Robinson equation of state (PR-EOS) used in IPARS can be described as follow:

$$P = \frac{RT}{v-b} - \frac{a(T)}{v(v+b)+b(v-b)} \quad \text{A-15}$$

It could also be written as

$$Z^3 - (1-B)Z^2 + (A-3B^2-2B)Z - (AB-B^2-B^3) = 0 \quad \text{A-16}$$

In which

$$A = \frac{aP}{R^2T^2}, \quad B = \frac{bP}{RT}, \quad Z = \frac{vP}{RT} \quad \text{A-17}$$

And for pure component,

$$a(T) = a_c \alpha(T) \quad \text{A-18}$$

$$\alpha(T) = \left(1 + m \left(1 - \sqrt{\frac{T}{T_c}}\right)\right)^2 \quad \text{A-19}$$

$$m = 0.37464 + 1.5422\omega - 0.26922\omega^2 \quad \text{A-20}$$

At the critical point we have,

$$a_c = \frac{0.45724R^2T_c^2}{P_c} \quad \text{A-21}$$

$$b_c = \frac{0.07780RT_c}{P_c} \quad \text{A-22}$$

At temperatures other than critical the two parameters are treated differently, which has been clearly indicated by Dingyu-Peng and Robinson's paper *A New Two-Constant Equation of State* (1968).

For liquid/vapor mixture phase α , there are mixing rules,

$$a_\alpha = \sum_i \sum_{j \neq i} z_i z_j a_{ij} \quad \text{A-23}$$

$$b_\alpha = \sum_i z_i b_i \quad \text{A-24}$$

$$a_{ij} = \sqrt{a_i a_j} (1 - BIP_{ij}) \quad \text{A-25}$$

$$a_i(T) = a_{c,i} \alpha_i(T) \quad \text{A-26}$$

$$\alpha_i(T) = \left(1 + m_i \left(1 - \sqrt{\frac{T}{T_c}}\right)\right)^2 \quad \text{A-27}$$

$$m_i = 0.37464 + 1.5422\omega_i - 0.26922\omega_i^2 \quad \text{A-28}$$

In which ω_i is the acentric parameter for each component from user input.

The binary interaction parameter (*BIP*) plays the critical role for fitting the experimental data using the cubic equation of state. BIP should be input between each pair of components that attend the flash calculation.

The cubic equation can be solved for three roots of Z_α , which will be used for next calculation of component fugacity in each phase. If all three roots are real, then the maximum and minimum values are used for vapor and liquid phases. Otherwise, single real root will be used.

The fugacity coefficients for liquid and vapor phases are calculated as,

$$\ln(\varphi_i^\alpha) = \frac{b_i}{b}(Z_\alpha - 1) - \ln(Z_\alpha - B_\alpha) - \frac{A_\alpha}{2\sqrt{2}B_\alpha} \left(\frac{2\sum_j x_j^\alpha a_{ij}}{a} - \frac{b_i}{b} \right) \ln \left(\frac{Z_\alpha + (1 + \sqrt{2})B_\alpha}{Z_\alpha + (1 - \sqrt{2})B_\alpha} \right)$$

A-29

where $B_\alpha = Pb_\alpha/RT$, $A_{icj} = P(1 - \delta_{icj})\sqrt{a_{ic}(T)a_{jc}(T)}/R^2T^2$, $A_\alpha = a_\alpha P/R^2T^2$.

Then convergence criteria is checked with

$$\ln(\varphi_i^l) - \ln(\varphi_i^v) - \ln(K_i) = 0$$

A-30

If not converged, K_i will be updated for next iteration,

$$K_i^{k+1} = K_i^k \frac{f_i^l}{f_i^v}$$

A-31

APPENDIX B: IPARS COMPOSITIONAL INPUT

B.1 IPARS Compositional Input

CO₂ Sequestration in aquifer case input (Chapter 5.3.2 - 3D test with trapping model).

```
TITLE(1)=" TEST CASE "  
TITLE(2)="Scenario 1blk"  
  
DESCRIPTION(=)  
"GRID BLOCKS : 4x25x25 (down, lateral, lateral) = 2500 GRID ELEMENTS"  
  
BLOCKMODEL(1 )="COMPOSITIONAL_MODEL"  
  
TIMEEND = 200.1  
  
$-----$  
$ I/O AND SOLVER OPTIONS  
$-----$  
$ DEBUGS  
$ DEBUGM  
$ OUTLEVEL = 2  
$ BUGKEY(6)  
$ BUGKEY(10)  
  
$ NEWTON OPTIONS  
MAXNEWT = 100  
MAXFLITS = 100  
  
$ BCGS LINEAR SOLVER OPTIONS  
$PRECOND = 3  
$MGLEV = 0  
$MAXMGIT = 1  
$LINTOL = 1.0E-05  
$MISCLINTOL = 1.0E-16  
  
$ GMRES LINEAR SOLVER OPTIONS  
$LSOL_TOL = 1.0E-06  
$LSOL_ITMAX = 5000  
$GMRES_PREC = 16 $ AMG with LSOR.  
$N_GS_STEP = 5  
  
$-----$  
$ PRINTOUTS  
$-----$  
$OUT_MOLDW = TRUE  
$OUT_MOLD = TRUE  
$OUT_VISCW = TRUE  
$OUT_VISC = TRUE  
$OUT_CO2MOL = TRUE  
OUT_CO2DIST = TRUE  
OUT_TEMPR= TRUE  
XDARCYFLUX = TRUE
```

```

OUT_MASSD = TRUE
OUT_OMOLF = TRUE
OUT_VISC = TRUE

OUT_CO2LEAK = TRUE
ICO2OUT = 1
JCO2OUT = 1
KCO2OUT = 10
NCO2OUT = 1
$XTSEOSBIN = TRUE

$-----$
$ FAULT BLOCK AND MESH DATA
$-----$
$FACEBLOCKS(,1) = 1 2
$FACEXYZ(,1) = 0. 0. 0., 0. 0. 0.

BLOCKNAME(1) = "BLOCK1"
DOWN(,1) = 1.0 0 0.00
NX(1) = 1  NY(1) = 1  NZ(1) = 64
DX(,1) = 40.
DY(,1) = 20  DZ(,1) = 5

$ Set the top corner of the reservoir
XYZ111(,1) = 4091. 0. 0.

$DEPTHMOD Block
$ EXTERNAL NBLK,X,Y,Z,DEP
$ DEP=DEP+0.002*(Z-125.0)*(Z-125.0)
$EndBlock
$DEPTHG1(1,1,1 TO 10 )= 4010 4021 4032 4043 4054 4065 4076 4087 4098 4099

$-----$
$ RESERVOIR DATA
$-----$
$ POROSITY
CR1() = 5.E-6
POROSITY1(,,) = .20

$ PERMEABILITIES
XPERM1(,,) = 100.
YPERM1(,,) = 100.
ZPERM1(,,) = 100.

PERMOUT
VIS_SCL = 4
VIS_FNAME = "TEST2D_K"
VISFLAG = 2
VIS_SCL_NAMES(1) = "TCOFX"
VIS_SCL_NAMES(2) = "TCOFY"
VIS_SCL_NAMES(3) = "DEPTHG"
VIS_SCL_NAMES(4) = "PORO"

$-----$
$ COMPONENT PROPERTIES
$-----$
$ WATER PROPERTIES
WATERP = 0.0
WATFVF = 1.0

```

```

WATVIS = .7
WATCMP = 3.3E-6
STDENW = 62.4

$ COMP NAMES
NHCOMP = 2
COMP(1) = "CO2" COMP(2) = "BRINE"
LTCOMP = 1
ICINPH(,1) = 1 0 0
ICINPH(,2) = 0 1 1
ICINPH(,3) = 0 1 0
XMOL_DIFF(,,) = 0.0
XMOL_DIFF(,2,2 TO 3) = 0.5580

$$ COMPNT. CRIT. PROPERTIES

$ CRITICAL TEMPERATURES
TCRIT(1 TO 2) = 547.5600 1120.2300

$ CRITICAL PRESSURES
PCRIT(1 TO 2) = 1070.3785 3540.8836

$ CRITICAL VOLUMES
ZCRIT(1 TO 2) = 0.30234 0.22983

$ ACENTRIC FACTORS
ACENT(1 TO 2) = 0.2240 0.2440

$ MOL WEIGHTS
MOLWT(1 TO 2) = 44.0100 18.0125

$ PARACHOR
PARACHOR(1 TO 2) = 49.00 52.00

$ VOLUMETRIC SHIFT
VSHIFT(1 TO 2) = -0.19 0.0650
VSHIFT(1 TO 2) = 0.0247 0.0950

$ ISOBARIC SPECIFIC HEATS
HCCP(1 TO 2) = 14.8915 17.8176 $ for CO2, take mean of liq. & gas sp. Heats.

$ BINARY INTERACTION COEFFICIENTS
BINACT(1,2) = -0.0852
BINACT(2,1) = -0.0852

$-----$
$THERMAL OPIONS
$-----$
$XTHERMAL = TRUE
$N_THERM_STEPS = 4
$XNOTHERMCOND = TRUE
$XTHERMSOLVE = TRUE
$XTHLINSOL = 2
$$$XTHLINSOL = 1
$$XNOFLXMTR = TRUE
$XFLXMTRTYPE = 3
$$XFLXMTR = 1.0
$XFLXMTR = 0.75

```

```

$=== PHASE THERMAL CONDUCTIVITIES
$PHTCOND(1,1 TO 3) = 48.5343
$PHTCOND(2,1 TO 3) = 8.1714
$PHTCOND(3,1 TO 3) = 10.8856
$PHTCOND(4,1 TO 3) = 0.2203

$ ROCK ISOCHORIC SPECIFIC HEAT CAPACITY
ROCKCV = 0.17913

$-----$
$ ROCK FLUID PROP
$-----$
NXROCKS = 1
ROCK1(,,) = 1
$ == MODEL ROCK TYPE 3-PHASE RELATIVE PERM
MODREL(1) = 1

$== SGRES BASED ON IFT EFFECT
$IFTSATRES = TRUE

$===== IFT RELATIVE PERMEABILITY
$ IFTRLPRM = TRUE
$AQPHSWTCH = TRUE
SGLOW = 0.225
SGHIGH = 0.1
SWLOW=.379
SWHIGH=0.15
KGLow=.298
KGHIGH = 0.6
KWLOW=0.405
KWHIGH=1.0
EGLOW = 1.9
EGHIGH =1.0
EWLOW = 3.8
EWHIGH =1.5
TGL=97000000
TWL=4400000
TAUG=1.05
TAUW=1.05
IFT0 = 30.0
SALIN= 0.0

$XJLFUNPC = TRUE $ J-LEVERETT FUNCTION CAPILLARY PRESSURE

$== HYSTERESIS OPTIONS
$HYSTERESIS = TRUE
$AQPHSWTCH = TRUE

$== HYSTERESIS PARAMETERS
$ ENTRYPRES(1) = .000
ENTRYPRES(1) = 1.1607
SWRES(1) = 0.0
SORES(1) = 0.197
SGRES(1) = 0.203
LAMBDA(1) = 1.33
LAMBDAW(1) = 1.3
LAMB DANW(1) = 1.7
KRWO(1) = 0.5260
KRWO(1) = 0.8

```

REFPERM(1) =100.0
REFPORO(1) =00.2

\$ ENTRYPRES(2) = 1200.0
\$ SWRES(2) = 0.2
\$ SORES(2) = 0.638
\$ SGRES(2) = 0.256
\$ LAMBDA(2) = 4.2
\$ LAMBDAW(2) = 2.2
\$ LAMBDANW(2) = 2.3
\$ KRNO(2) = 0.1875
\$ KRWO(2) = 0.1875
\$ REFPERM(2) =100.0
\$ REFPORO(2) =00.2

KWSW(1) Block \$ WATER RELATIVE PERMEABILITY VS Sw – ROCK TYPES 1
Interpolation Linear
Extrapolation Constant

Data

0.4	0.0
0.425	7.84E-006
0.45	0.00012461
0.475	0.000628309
0.5	0.001980118
0.525	0.004823603
0.55	0.009984184
0.575	0.018468725
0.6	0.031465201
0.625	0.050342427
0.65	0.076649807
0.675	0.112117131
0.7	0.158654383
0.725	0.218351571
0.75	0.29347857
0.775	0.386484981
0.8	0.5

EndBlock

KOSW(1) Block \$ OIL RELATIVE PERMEABILITY VS Sw – ROCK TYPES 1
Interpolation Linear
Extrapolation Constant

Data

0.4	0.65
0.425	0.568995356
0.45	0.489718618
0.475	0.413763848
0.5	0.342457622
0.525	0.276876451
0.55	0.217852251
0.575	0.16597515
0.6	0.121595238
0.625	0.084823784
0.65	0.05553414
0.675	0.033362457
0.7	0.017708256
0.725	0.007734915

```

0.75 0.002370084
0.775 0.000306038
0.8 0
EndBlock

KOSG(1) Block  $ OIL RELATIVE PERMEABILITY VS Sg – ROCK TYPES 1
Interpolation Linear
Extrapolation Constant

Data
0.000 1.0000
0.05 0.9198208722
0.1 0.8412241145
0.15 0.7642877993
0.2 0.6891000746
0.25 0.6157614012
0.3 0.544387534
0.35 0.4751135908
0.4 0.408099771
0.5 0.2816729928
0.6 0.167345732
0.7 0.0692720728
0.8 0.0006984373
0.803 0
0.9 0
1.000 0.000
EndBlock

KSGG(1) Block  $ GAS RELATIVE PERMEABILITY VS Sg – ROCK TYPES 1
Interpolation Linear
Extrapolation Constant

Data
0.000 0.0000
0.203 0.0
0.25 0.0723547974
0.3 0.0986450847
0.35 0.1281991048
0.4 0.1608686075
0.5 0.2350814304
0.6 0.3204988259
0.7 0.4165201203
0.8 0.5226636477
0.803 0.526
0.9 0.526
1.000 0.526
EndBlock

PCOW(1) Block  $ WATER-OIL CAPILLARY PRESSURE – ROCK TYPE 1
Interpolation Linear
Extrapolation Constant

Data
0.4000 10.07
0.4667 4.90
0.5556 1.80
0.6444 0.50
0.7000 0.05
0.7333 0.01

```

```

0.8222 0.0
0.9111 0.0
1.0 0.0
EndBlock

PCGO(1) Block    $ GAS-OIL CAPILLARY PRESSURE – ROCK TYPE 1
Interpolation Linear
Extrapolation Constant

Data
0.197 9.2880208251
0.2 6.8145629807
0.3 4.36252194585
0.4 3.17910604195
0.5 2.48716157848
0.6 2.03518845089
0.65 1.86365840626
0.7 1.71776267142
0.75 1.59222198103
0.8 1.48310541037
0.85 1.38742714309
0.9 1.30287948121
0.95 1.22765133119
1 1.160301904
EndBlock

$-----$
$ WELLS
$-----$

NUMWELL=2

WELLNAME(1) = "INJECTION WELL rate CONST"
$KINDWELL(1) = 0
KINDWELL(1) = 4
WELLBLOCK(,1) = 1
PLIMITC(1) = 4500.
$WDEPTH(1) = 8425.
WELLTOP(1 TO 3,1,1) = 4091. 5. 319.5
WELLBOTTOM(1 TO 3,1,1) = 4130. 5. 319.5
WELLPQ(1) Block
Interpolation Step
Extrapolation Constant
Data 0. 150.0
EndBlock

WELLNAME(2) = "PRODUCTION WELL pres CONST"
KINDWELL(2) = 31
$KINDWELL(2) = 0
WELLBLOCK(,2) = 1
PLIMITC(2) = 4500.
$WDEPTH(2) = 8425.
WELLTOP(1 TO 3,1,2) = 4091. 05. 04.
WELLBOTTOM(1 TO 3,1,2) = 4130. 05. 04.
WELLPQ(2) Block
Interpolation Step
Extrapolation Constant
Data 0. 1800.
EndBlock

```

```

$ WELL OUTPUT

WELLOUTKEY = 3 WELLFILE = "TEST_H_I.WEL" WELLFCUM = "TEST_H_I.CUM"
$WELLOUTKEY = 0 WELLFILE = "TEST_H_I.WEL" WELLFCUM = "TEST_H_I.CUM"

$ WELL OUTPUT FLAGS
$WOUTFLG(1 TO 2) = FALSE

$ NON-AQUEOUS COMPONENT WELL OUTPUT FLAGS
$WELXOUT(1,1 TO 2)
$WXELOUT(1,2) = 7

$ INJECTION COMPOSITION
COMPINJ(,1) = 0.0 1.0 ,0.0
INJCOMP() = 1
TINJ(1 TO 2) = 90.0

$ SEPARATOR ASSIGNMENT FOR WELLS
IWSEP() = 1

$-----$
$ INITIAL CONDITIONS
$-----$
$ SURFACE CONDITIONS
TSURF = 60.0 PSURF = 14.7

$PORPRES1() = 14.7 $ default EQ PRES1
SWINIT1() = 0.00
PRES1(,,) = 1800
CONC1(,,1) = 0.00
CONC1(,,2) = 1.00
REFPRES = 2 $ DEFAULT 2

$ INITIAL TEMPERATURES
TEMPR1(,,) = 110.

$ SEPARATORS
PSEP(,1) = 14.7
TSEP(,1) = 60.

$ SEPARATOR ASSIGNMENT FOR IN-PLACE CALCULATIONS
SEPSURF = 1

EndInitial

$-----$
$ TRANSIENT DATA INPUT BLOCKS
$-----$

BeginTime 0.0
DELTIM = 1.0
DTIMMUL = 1.1
TIMOUT = 0.1
DTIMMIN = .005
DTIMMAX = 10.0
DTIMOUT = 2.
DSMAX = 0.1

```

```

$ testing visualization
VISOUT = .10
DVISOUT = 5.
VIS_SCL = 8
VIS_SCL_NAMES(1) = "PRES"
VIS_SCL_NAMES(2) = "PCOW"
VIS_SCL_NAMES(3) = "PCGO"
VIS_SCL_NAMES(4) = "SWAT"
VIS_SCL_NAMES(5) = "SOIL"
VIS_SCL_NAMES(6) = "SGAS"
VIS_SCL_NAMES(7) = "CO2"
VIS_SCL_NAMES(8) = "TEMP"
VIS_FNAME = "TEST1D_O_Pc"
VISFLAG = 2
EndTime

BeginTime 20.05
DTIMOUT = 5
DVISOUT = 5
EndTime

BeginTime 220.0
DTIMOUT = 20
DVISOUT = 20
DTIMMAX = .20
EndTime

```

B.2 New Keywords for New Models in IPARS

List of keywords and example values of modeling residual saturation as a function of trapping number when IFTSATRES = TRUE.

```

$=== SGRES BASED ON IFT EFFECT
IFTSATRES = TRUE      $ Flag to calculate residual based on IFT and trapping number
TGL=97000000         $ Fitting parameter  $N_{Tl}$  for gas residual with trapping number model
TWL=4400000         $ Fitting parameter  $N_{Tl}$  for water residual with trapping number model
TAUG=1.05           $ Fitting parameter  $\tau_l$  for gas residual
TAUW=1.05           $ Fitting parameter  $\tau_l$  for water residual
IFT0 = 30.0         $ Reference IFT for reference rock (mN/m)
SALIN= 0.0          $ Reservoir fluid salinity for IFT calculation (ppm)

```

List of keywords and example values for relative permeability curves for low and high trapping numbers when IFTRLPRM = TRUE.

```

$===== IFT RELATIVE PERMEABILITY
IFTRLPRM = TRUE      $ flag to calculate Kr based on trapping number
AQPHSWTCH = TRUE     $ flag to use oil phase as "water" property
SGLOW = 0.225        $ gas residual saturation at low trapping number
SGHIGH = 0.1         $ gas residual saturation at high trapping number
SWLOW=.379           $ water residual saturation at low trapping number

```

SWHIGH=0.15	\$ water residual saturation at high trapping number
KGLOW=.298	\$ gas endpoint Krg at low trapping number
KGHIGH = 0.6	\$ gas endpoint Krg at high trapping number
KWLOW=0.405	\$ water endpoint Krw at low trapping number
KWHIGH=1.0	\$ water endpoint Krw at high trapping number
EGLOW = 1.9	\$ gas relative perm Corey exponent at low trapping number
EGHIGH =1.0	\$ gas relative perm Corey exponent at high trapping number
EWLOW = 3.8	\$ water relative perm Corey exponent at low trapping number
EWHIGH =1.5	\$ watre relative perm Corey exponnent at high trapping number

List of keywords and example values for capillary pressure curves scaling using Leverett J-function for permeability, porosity and interfacial tension when XJLFUNPC = TRUE.

XJLFUNPC = TRUE	\$ flag forJ-LEVERRET FUNCTION CAPILLARY PRESSURE
REFPERM() =100.0	\$ reference permeability (md) for reference rock
REFPORO() = 0.2	\$ reference porosity for reference rock
IFT0 = 30	\$ reference fluid IFT (mN/m) for reference rock

List of keywords and example values for hysteresis in relative permeability and capillary pressure curves based on Land's trapping function. Inputs include maximum residual saturation for each phase, endpoint relative permeability, entry capillary pressure, and Brooks-Corey exponents for each rock type.

\$== HYSTERESIS OPTIONS	
HYSTERESIS = TRUE	\$ flag for hysteresis model of Kr Pc and Sgt
AQPHSWTCH = TRUE	\$ flag for treat oil phase as water
\$== HYSTERESIS PARAMETERS	
ENTRYPRES(1) = 1.1607	\$ entry capillary pressure for drainage (psi)
SWRES(1) = 0.0	\$ maximum residual water saturation
SORES(1) = 0.197	\$ maximum residual oil saturation
SGRES(1) = 0.203	\$ maximum residual gas saturation
LAMBDA(1) = 1.33	\$ Corey type drainage Pc exponent
LAMBDAW(1) = 1.3	\$ Corey type drainage water Krw exponent
LAMBDANW(1) = 1.7	\$ Corey type drainage non-wetting phase gas Krg exponent
KRNW0(1) = 0.5260	\$ Corey type imbibition water Krw endpoint
KRW0(1) = 0.8	\$ Corey type imbibition non-wetting gas Krg endpoint
\$ ENTRYPRES(2) = 1200.0	\$ Corey type entry Pc for rock type 2
\$ SWRES(2) = 0.2	
\$ SORES(2) = 0.638	
\$ SGRES(2) = 0.256	
\$ LAMBDA(2) = 4.2	
\$ LAMBDAW(2) = 2.2	
\$ LAMBDANW(2) = 2.3	
\$ KRNW0(2) = 0.1875	
\$ KRW0(2) = 0.1875	

APPENDIX C: SAMG and HYPRE SOLVERS for UTCHEM

C.1 UTCHEM Review

UTCHEM is a 3D, multicomponent, multiphase, and compositional chemical flood reservoir simulator developed at the University of Texas at Austin. This simulator provides a scientific and engineering basis for modeling the enhanced oil recovery through continued development and application of compositional model. The simulator was originally developed by Pope and Nelson in 1978 for simulating the enhanced oil recovery with surfactant and polymer processes. Currently a group of researchers led by Dr. Delshad are actively developing and enhancing this simulator. Here I implemented two new solvers (SAMG and HYPRE) to UTCHEM. The detailed implementation procedure is presented here.

C.1.1 UTCHEM FORMULATIONS

In this simulator, the flow and mass-transport equations are solved for any number of user-specified chemical components (water, organic contaminants, surfactant, alcohols, polymer, chloride, calcium, other electrolytes, microbiological species, electron acceptors, etc.). These components can form up to four fluid phases (gas, water, oil, and microemulsion) and any number of solid minerals depending on the overall composition. The continuity of mass for component k in association with Darcy's law is as follow,

$$\frac{\partial}{\partial t}(\phi C_k \rho_k) + \vec{\nabla} \cdot [\sum_{l=1}^{n_p} \rho_k (C_{kl} \vec{u}_l - \vec{D}_{kl})] = R_k \quad \text{C-1}$$

In which, ϕ is porosity, C_k is the volume of component k per unit pore volume, ρ_k is the component density, u_l is the Darcy velocity for phase l , D_{kl} is the diffusion flux in Fickian form, and R_k is the sum of the reaction and point source/sink rate.

The flow equation is spatially discretized on Cartesian grid using finite volume method to maintain mass conservation. Upstream scheme is used for calculating transport properties between connected grids. The pressure equation is developed by summing up the mass balance equation over all components, as follow.

$$\frac{\phi C_t \partial P_1}{\partial t} + \vec{\nabla} \cdot (\vec{K} \lambda_{rTc} \vec{\nabla} P_1) = -\vec{\nabla} \cdot \sum_{l=1}^{n_p} \vec{K} \lambda_{rlc} \vec{\nabla} h + \vec{\nabla} \cdot \sum_{l=1}^{n_p} \vec{K} \lambda_{rlc} \vec{\nabla} P_{cl1} + \sum_{k=1}^{n_{cy}} Q_k \quad \text{C-2}$$

In which, λ_{rlc} is phase relative mobility with the correction of fluid compressibility, λ_{rTc} is total relative mobility over all phases n_p .

$$\lambda_{rlc} = \frac{k_{rl}}{\mu_l} \sum_{k=1}^{n_{cy}} \rho_k C_{kl} \quad \text{C-3}$$

\vec{K} is the permeability tensor. C_t is the volume weighted sum of rock matrix C_r and component compressibility C_k^o .

$$C_t = C_r + \sum_{k=1}^{n_{cy}} C_k^o C_k \quad \text{C-4}$$

The simulator uses implicit pressure explicit concentration/saturation (IMPEC/IMPES) formulation to solve the flow and transport during time evolution. At each time step, pressure equation is solved using Jacobi conjugate gradient (JCG) method is then followed by a back substitution into the explicit mass conservation equation for each component. The concentration of each component is solved using updated pressure and transport equation in the form of Darcy's Law. Then saturation is solved using concentration and molar density of each component.

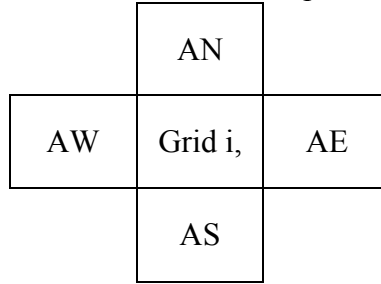
C.1.2 UTCHEM DISCRETIZATION

The pressure equation can be discretized on each grid cell using finite difference method,

$$\sum_{j=A1}^{A6} T_{ij}(P_i - P_j) = q_i \quad \text{C-5}$$

In which T_{ij} is the transmissibility between grid cell i and j .

There are a maximum of 6 adjacent grid cells for each grid cell i in a Cartesian grid system. The transmissibility T_{ij} is denoted AN, AS, AW, AE, AU, AN, and AA for the grid cells around grid cell i and grid cell i itself. These seven coefficients together form the stiffness matrix $[A]$, which is banded and sparse matrix.



The accumulation term is denoted B ,

$$[B] = \left[-\frac{\Delta(\phi C_k \rho_k)}{\Delta t} + Q \right] \quad \text{C-6}$$

Together we can get the matrix equation for pressure solve, as follows

$$[A][P] = [B] \quad \text{C-7}$$

This matrix equation can be solved with different solves, such as JCG solver.

Once pressure is solved for current time step, the saturation/concentration of component c in grid i , C_{ic} , could be evaluated explicitly using,

$$ACCUM_{ic}^{k+1} = [(\phi^{k+1} C_{ic}^{k+1}) - (\phi^n C_{ic}^n)] / \Delta t \quad \text{C-8}$$

$$\phi^{k+1}C_{ic}^{k+1} = \phi^k C_{ic}^k + \Delta(\phi C_{ic})^k = \phi^k C_{ic}^k + \phi^k \delta C_{ic}^k + C_{ic}^k \delta \phi^k \quad \text{C-9}$$

$$ACCUM_{ic}^{k+1} = \frac{1}{\Delta t} [\phi^k C_{ic}^k + \phi^k \delta C_{ic}^k + C_{ic}^k \delta \phi^k - (\phi^n C_{ic}^n)] \quad \text{C-10}$$

$$C_{ic}^{k+1} = \frac{\Delta t(ACCUM_{ic}^{k+1}) + \phi^n C_{ic}^n}{\phi^{k+1}} \quad \text{C-11}$$

For the simulation process, the pressure solve is the most CPU cost part, while saturation/concentration solve is less CPU intensive. Hence it is necessary to use fast and efficient solvers and numerical scheme for matrix equation. I implemented two advanced solvers, SAMG and HYPRE, into the UTCHEM simulator. These solvers with their tuned preconditioners could solve large scale sparse matrix efficiently and robustly. For both of the two solvers, sparse matrix needs to be converted to compressed row storage (CRS) arrays and passed to the solver. I developed the special subroutine to perform the converting and transforming of matrix.

C.2 Implementation of SAMG and HYPRE Solvers

C.2.1 COMPRESSED ROW STORAGE (CRS)

Compressed row storage (CRS) is a technique in computational programming used to store large, sparse matrices using as little memory as possible. The idea of this technique is that rather than saving the whole matrix, we only save the non-zero entries in the sparse matrix to the memory, because only those non-zero entries will be contributing to the matrix equation system. The way for saving the entries is specially engineered to maximize efficiency and minimize memory cost. Finally, the whole matrix equation will be converted to three 1D arrays that each of the arrays contains the information of position of non-zero entry, value of non-zero entry, and accumulation term.

For example, consider a non-symmetry matrix A,

$$A = \begin{pmatrix} 1 & 0 & 5 \\ 0 & 4 & -1 \\ 2 & 1 & 3 \end{pmatrix}$$

After converting to CRS structure, it will be as follow,

The number of non-zero elements in each row is recorded in a 1D array as follows,

Row	1	3	5	8	...
-----	---	---	---	---	-----

The number of non-zero elements is calculated from the 1D array above, as follows

$$number_i = Row_{i+1} - Row_i \quad \text{C-12}$$

The values of non-zero elements and their positions in each row are recorded using two 1D arrays, as follows.

Value	1	5	4	-1	2	1	3	...
Column	1	3	2	3	1	2	3	...

The new arrays created from the original sparse matrix can be passed to the solver and be solved iteratively. The SAMG and HYPRE solver then could be called to execute the solving of the matrix equation.

C.2.2 SAMG

SAMG (Algebraic Multigrid Methods for Systems) is a library of subroutines developed by the Fraunhofer Institute for Algorithms and Scientific Computing (FhG-SCAI) for highly efficient solution of large linear equations with sparse matrix (*by K. Stiben, FhG-SCAI*). It is a library of subroutines based on algebraic multigrid (AMG) approach, used for the highly efficient solution of large linear systems of equations with sparse matrices.

The SAMG solver package is developed in FORTRAN 90, and can be called in different development environment and computation platform. From user's point of view, it is "plug-in" solver, which means it has convenient socket for user to pass the matrix and run the solver. The solver also comes with a bunch of preconditioners which user could choose by specifying different input parameters.

The typical way to call the SAMG solver is as follow,

```
subroutine samg(nnu, nna, nsys, &
  ia, ja, a, f, u, iu, ndiu, ip, ndip, matrix, iscale, &
  res_in, res_out, ncyd_done, ierr, &
  nsolve, ifirst, eps, ncyd, iswtch, &
  a_cmplx, g_cmplx, p_cmplx, w_avrge, &
  chktol, idump, iout).
```

The detailed information for the input parameters is available in SAMG user manual.

In UTCHEM it is coded as follow,

```
CALL SAMG(NNU, NNA1, NSYS, IA(1:NNU+1), JA(1:NNA1), AIJ(1:NNA1), BV(1:NNU
  & ), P(1:NBL, 1), IU, NDIU, IP, NDIP, MATRIX, ISCALE, RES_IN, RES_OUT,
  & NCYC_DONE, IERR, NSOLVE, IFIRSTK, EPS, NCYC, ISWTCH, A_CMPLX,
  & G_CMPLX, P_CMPLX, W_AVRGE, CHKTOL,
  & IDUMP, IOU)
```

The arrays IA, JA, AIJ, BV, P are the Jacobi matrix in compressed row storage format. The solved pressure is storage in array P, and is used for solving saturation.

C.2.3 HYPRE

HYPRE is a library of high performance preconditioners and solvers for solving large, sparse linear systems of equations on massively parallel computers (By [Lawrence Livermore National Laboratory](#)). It was developed at the Center for Applied Scientific Computing (CASC) at Lawrence Livermore National Laboratory. It is developed in C/C++ language, with great flexibility to be used in many developing environments and platforms, such as FORTRAN on LINUX. The main features of the library includes scalable preconditioners, a suit of iterative methods, user defined interfaces, etc.

The HYPRE solver is implemented in UTCHEM, by converting the UTCHEM matrix equation to CRS structure and calling HYPRE subroutines following special procedure. In order to do these, we need to handle calling subroutine between FORTRAN and C/C++. HYPRE objects can usually be declared as in the table because *integer * 8* usually corresponds to the length of a pointer. However, there may be some machines where this is not the case (although we are not aware of any at this time). On such machines, the FORTRAN type for a HYPRE object should be an integer of the appropriate length. Here is an example of defining/calling same subroutine in FORTRAN and C.

This simple example illustrates the above information:

C prototype:

```
int HYPRE_IJMatrixSetValues(HYPRE_IJMatrix matrix, int nrows, int
    *ncols, const int *rows, const int *cols, const double
    *values);
```

The corresponding FORTRAN code for calling this routine is as follows:

```
integer*8 matrix,
integer nrows, ncols(MAX_NCOLS)
integer rows(MAX_ROWS), cols(MAX_COLS)
double precision values(MAX_COLS)
integer ierr
call HYPRE_IJMatrixSetValues(matrix, nrows, ncols, rows,
    & cols, values, ierr)
```

The implementation in UTCHEM is as follow,

```
call HYPRE_IJMatrixCreate(comm, 1, NNU,1, NNU, ij_matrix,ierr)
call HYPRE_IJMatrixSetObjectType(ij_matrix, HYPRE_PARCSR,ierr)
call HYPRE_IJMatrixInitialize(ij_matrix,ierr)
C /* set matrix coefficients */
call HYPRE_IJMatrixSetValues(ij_matrix, NNU,ncols,rows,JA,AIJ,ierr)
call HYPRE_IJMatrixAssemble(ij_matrix,ierr)
C Get parcsr matrix object
call HYPRE_IJMatrixGetObject(ij_matrix, parcsr_A, ierr)

c Create the rhs and solution
call HYPRE_IJVectorCreate(comm, 1, NNU, b, ierr )
call HYPRE_IJVectorSetObjectType(b, HYPRE_PARCSR, ierr)
call HYPRE_IJVectorInitialize(b, ierr)

call HYPRE_IJVectorCreate(comm, 1, NNU, x, ierr )
```

```

call HYPRE_IJVectorSetObjectType(x, HYPRE_PARCSR, ierr)
call HYPRE_IJVectorInitialize(x, ierr)
call HYPRE_IJVectorSetValues(b, NNU, rows, BV(1:NBL), ierr )
call HYPRE_IJVectorSetValues(x, NNU, rows, P(1:NBL,1), ierr)

call HYPRE_IJVectorAssemble( b, ierr)
call HYPRE_IJVectorAssemble( x, ierr)

c get the x and b objects

call HYPRE_IJVectorGetObject( b, par_b, ierr)
call HYPRE_IJVectorGetObject( x, par_x, ierr)

c Choose a solver and solve the system

call HYPRE_BoomerAMGCreate(amg_solver, hypre_ierr)
c print solve info + parameters
call HYPRE_BoomerAMGSetPrintLevel(amg_solver, 0, hypre_ierr)
c Falgout coarsening
call HYPRE_BoomerAMGSetCoarsenType(amg_solver, 6, hypre_ierr)
c G-S/Jacobi hybrid relaxation
call HYPRE_BoomerAMGSetRelaxType(amg_solver, 3, hypre_ierr)
c Sweeps on each level
call HYPRE_BoomerAMGSetNumSweeps(amg_solver, 1, hypre_ierr)
c maximum number of levels
call HYPRE_BoomerAMGSetMaxLevels(amg_solver, 20, hypre_ierr)
c do iteration! The default is 20.
Call HYPRE_BoomerAMGSetMaxIter(amg_solver, 30, ierr)
c conv. Tolerance
call HYPRE_BoomerAMGSetTol(amg_solver, TOL, hypre_ierr)

call HYPRE_BoomerAMGSetup(amg_solver,parcsr_A,par_b,par_x,ierr)
call HYPRE_BoomerAMGSolve(amg_solver,parcsr_A,par_b,par_x,ierr)
call HYPRE_IJVectorGetValues(x, NNU, rows, P(1:NBL,1), ierr)

c Destroy solver
call HYPRE_BoomerAMGDestroy( amg_solver, ierr )
call HYPRE_IJMatrixDestroy( ij_matrix, ierr)
call HYPRE_IJVectorDestroy(b, ierr)
call HYPRE_IJVectorDestroy(x, ierr)

```

C.3 Speed-up Tests

Several waterflood and chemical flood cases with different number of gridblocks were tested to compare the efficiency of the solvers. Results are given in Table 1 and Figure 3. The CPU time for the all solvers has a linear correlation with the number of grid blocks. The SAMG and HYPRE solvers have comparable efficiency and both solvers

reduced the CPU greatly. The CPU time costs are linear to the number of grid numbers for all three solvers.

Table C.1 CPU time for the JCG and SAMG solver

No. of Grid	N_x, N_y, N_z	JCG(s)	SAMG(s)	HYPRE (s)
6050	$55 \times 55 \times 2$	1366	587	612.7
60500	$55 \times 55 \times 20$	11033	4631	4683.6
200000	$100 \times 100 \times 20$	31404	12866	14170

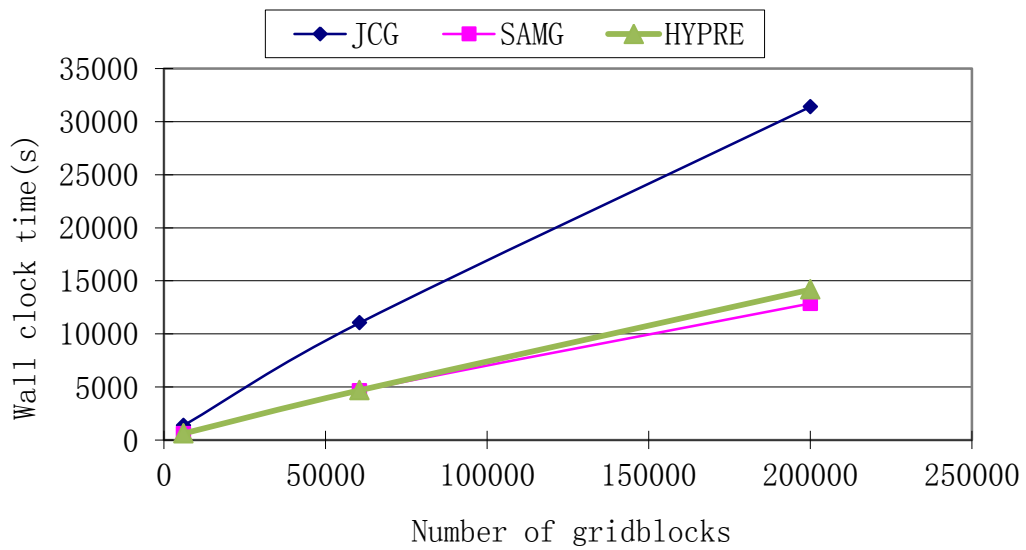


Figure C.1 CPU time for three solvers: JCG, SAMG, and HYPRE

The speed up of each solver is shown below, which shows that the JCG solver takes about 2.3 times CPU time compared to both SAMG and HYPRE solvers.

Table C.2 CPU time cost ratio of JCG solver over SAMG and HYPRE

Grid numbers	N_x, N_y, N_z	JCG(s)	SAMG(s)	HYPRE (s)
6050	$55 \times 55 \times 2$	1	2.32709	2.229476

60500	$55 \times 55 \times 20$	1	2.38242	2.355667
200000	$100 \times 100 \times 20$	1	2.44085	2.216221

The amount of CPU time took by SAMG and HYPRE solvers are compared to JCG solver, which shows both solvers saved about 55% CPU time compared to JCG solver.

Table C.3 CPU time cost ratio of each solver to JCG solver

Grid numbers	N_x, N_y, N_z	JCG(s)	SAMG(s)	HYPRE (s)
6050	$55 \times 55 \times 2$	1	0.42972	0.448536
60500	$55 \times 55 \times 20$	1	0.41974	0.424508
200000	$100 \times 100 \times 20$	1	0.40969	0.451219

Finally, we carried out a chemical flooding test case with $100 \times 100 \times 20$ gridblocks. The simulation time is 1500 days. The CPU time, saturation and pressure at the injection block by the end of simulation are recorded for each solver.

Table C.4 CPU times, S_w , P in injection block

Solver	CPU time (min)	Final Water Saturation	Final Pressure (psi)
JCG	5352	0.998510990832429	2418.54843416218
SAMG	1960	0.998510990832420	2418.54846674235
HYPRE	2030	0.998510990832410	2418.54846674205

From above tests, we can see the JCG solver uses about 2.4 times more CPU time compared to SAMG and HYPRE solvers. By comparing the water saturation and pressure in the injection block at the end of simulation, we can see both solvers give almost identical saturation and pressure results with the same precision.

APPENDIX D: IPARS and CMG Isothermal Benchmark

D.1 Governing Equations for Energy Balance

Geological sequestration of CO₂ in underground reservoir is the process of injecting and trapping CO₂ within aquifers. Due to the thermal gradient and low critical temperature of CO₂, many times, the injected CO₂ will have a lower temperature than the reservoir, in which thermal phenomenon would play a role. The heat in the reservoir can be transmitted through conduction, convection, and radiation. When there is little fluid flow in reservoir, the heat conduction dominates the heat transfer. For high flow rates case, fluid flow driven heat convection could be more significant than conduction.

Thermal governing equations,

$$\frac{\partial(M_T T)}{\partial t} + \nabla \cdot \left(\sum_{\alpha} \rho_{\alpha} C_{p\alpha} u_{\alpha} T - \lambda_T \nabla T \right) = q_H \quad \text{D-1}$$

The total mass for internal energy,

$$M_T = \left[(1 - \phi) \rho_s C_{vs} + \phi \sum_{\alpha} \rho_{\alpha} S_{\alpha} C_{v\alpha} \right] \quad \text{D-2}$$

The heat source/sink,

$$q_H = \sum_{\alpha} C_{p\alpha} q_{\alpha} T_{src} \quad \text{D-3}$$

where $T_{src} = T_{inj}$ at injection well location, otherwise it is reservoir temperature, α is the thermal phase, $C_{v\alpha}$ is isochoric specific heat at a constant volume, $C_{p\alpha}$ is the isobaric specific heat capacity at a constant pressure, λ_T is the overall thermal conductivity of the reservoir.

The mean thermal capacity of rocks was about 2.460 MJ-m⁻³-K⁻¹ (800~1000 J/Kg-K), found by Waples and Waples (2004) (1 MJ/m³-K = 48.31 Btu/ft³-F; 1 BTU/lb-F = 4.184E3 J/Kg-K). Rock heat capacity would be 0.7737 btu/lb-F, assuming

the rock density as 2.4 g/cm^3 . Water has a heat capacity of 4.1813 J/g-K , which is about 1.0 btu/lb-F , and rock has about 0.8350 J/g-K , which is about 0.200 btu/lb-F .

The transport properties of CO_2 are studied by Vescovic *et. al* (1989). The thermal conductivity of CO_2 as a function of density at different temperatures is as follows ($1 \text{ w/m-k} = 0.5778 \text{ Btu/hr-ft-F}$),

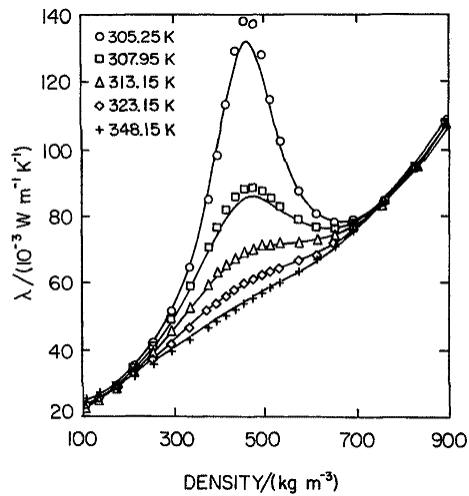


Figure D.1 CO_2 thermal conductivity vs. density at different temperature (Vescovic *et al.*, 1989)

D.2 Analytical Solution for Buckley-Leverett Flow

For 1D CO_2 injection to aquifer initially saturated reservoir, the flow is partially miscible and slightly compressible, which is dominated by convection flow. This process, although not exactly satisfy the assumption of Buckley-Leverett flow problem (Buckley and Leverett, 1942), could still modeled by the B-L flow equation when we assume the dissolution and compressibility are small enough to make no big impact on flow pattern.

One dimension B-L flow equation without gravity effect is as follow,

$$q_w = \frac{KK_{rw}}{\mu_w} \frac{\partial P_w}{\partial x} \quad \text{D-4}$$

$$q_g = \frac{KK_{rg}}{\mu_g} \frac{\partial P_g}{\partial x} \quad \text{D-5}$$

The fraction flow of gas phase displacing water phase would be

$$F_g = \frac{q_g}{q_w + q_g} \quad \text{D-6}$$

If we assume $P_c = P_g - P_w = 0$,

$$F_g = \frac{1}{1 + \frac{1}{M}} \quad \text{D-7}$$

In which $M = \frac{K_{rg}}{\mu_g} \frac{\mu_w}{K_{rw}}$ is the mobility ratio of displacing phase to connate phase.

The continuity equation for gas phase is

$$\phi A \frac{\partial S_g}{\partial t} + \frac{\partial q_g}{\partial x} = 0 \quad \text{D-8}$$

This can be written as

$$\frac{\partial S_g}{\partial t_D} + \frac{\partial F_g}{\partial x_D} = 0 \quad \text{D-9}$$

In which $x_D = x/L$, $t_D = qt/A\phi L$.

The continuity equation could be further transformed to get the final formulation of Buckley-Leverett equation,

$$\frac{\partial S_g}{\partial t_D} + \frac{dF_g}{dS_g} \frac{\partial S_g}{\partial x_D} = 0 \quad \text{D-10}$$

This equation shows a propagation of saturation shock with a shock speed of dF_g/dS_g .

For the test case we assume linear relative permeability ($K_{rg} = S_g$, $K_{rw} = 1 - S_g$) and zero capillary pressure.

The 1D reservoir model parameters are shown in Table D.1.

Table D.1 Reservoir model for benchmark case in IPARS and CMG-GEM

Grid number	64 × 1 × 1
Grid size (ft)	5 × 20 × 40
Porosity	0.2
Permeability (md)	100
Reservoir pressure (psi)	1800
CO ₂ injection well rate (MSCFD)	150
Producer BHP (psi)	1800
Inject fluid temperature (F)	90
Reservoir temperature (F)	110
Water density (<i>lb/ft</i> ³)	62.0
CO ₂ density (<i>lb/ft</i> ³)	40.0
Water viscosity (cp)	0.39
CO ₂ viscosity (cp)	0.052
Simulation time (days)	200

The gas fractional flow vs. saturation plot is as follows,

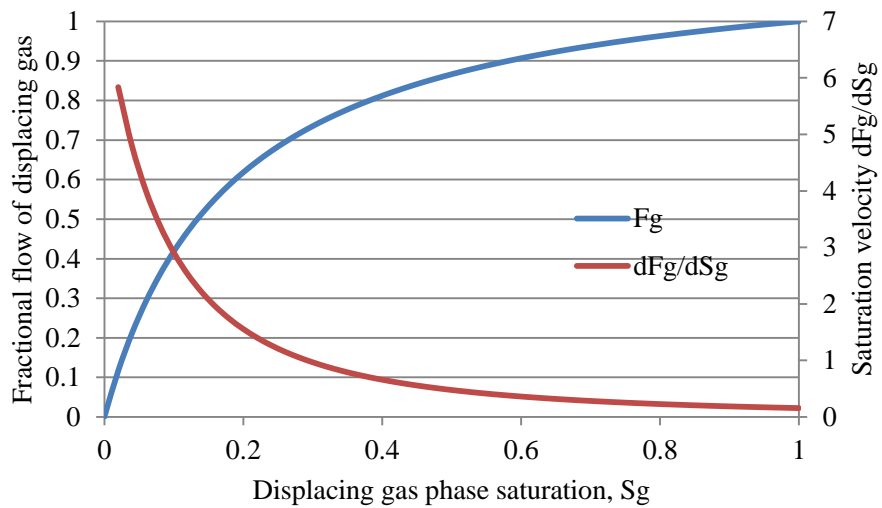


Figure D.2 Fractional flow and saturation speed vs. saturation

We can see this saturation shock is diverging shock that saturation front moves faster than trailing end. We can plot saturation against distance by multiplying dimensionless time t_D by saturation speed.

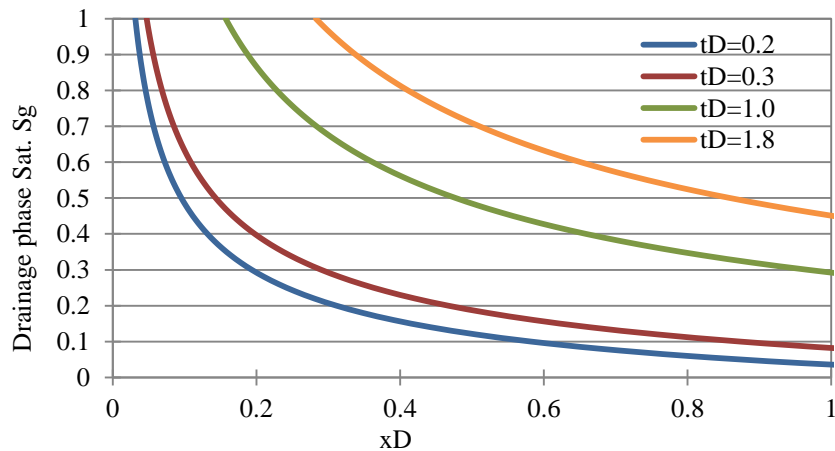


Figure D.3 Saturation profile against dimensionless distance for Buckley-Leverett flow at different injected pore volume

D.3 IPARS and CMG Isothermal Benchmark

We studied the CO₂ migration and temperature propagation in the process of injecting cool supercritical CO₂ into high temperature aquifer. The 1D reservoir has one constant rate CO₂ injector in one end and one constant pressure producer in the other end.

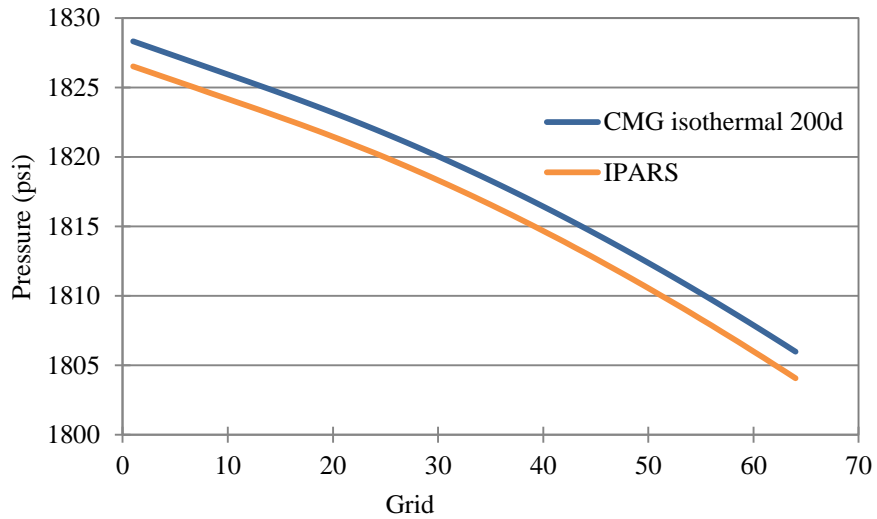


Figure D.4 Simulation pressure drop in IPARS and CMG at 200 days

IPARS simulation results of saturation with different grid refinements are compared with analytical solution,

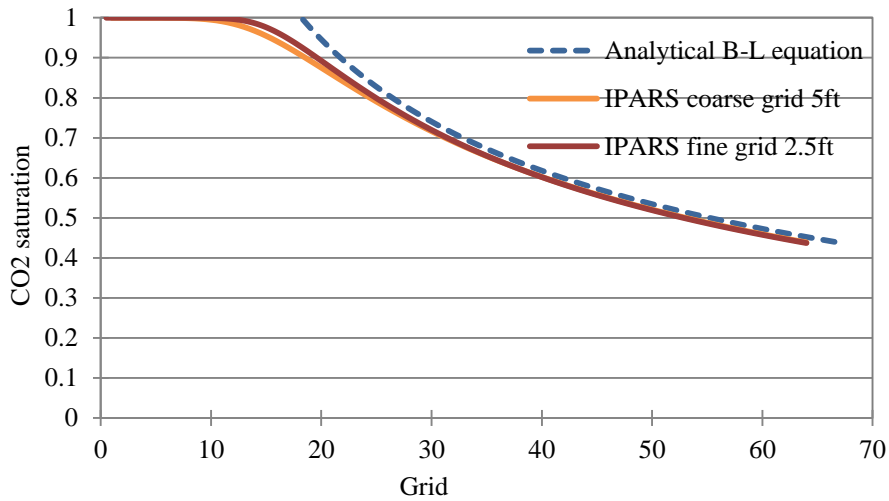


Figure D.5 Comparison of analytical solution and IPARS simulation results of saturation at 200 days with different level of grid refinement

We can see IPARS results of saturation have good match with both CMG and analytical solution based on Buckley-Leverett flow equation. The pressure results in IPARS have a difference of ~2 psi compared to CMG, which is also very small and might be due to different definition of reference depth for the bottom-hole pressure.

D.3.3 NON-ISOTHERMAL TEST WITH IPARS AND CMG

We set up a case with thermal effect due to injection of CO₂ with temperature different from initial reservoir temperature. Supercritical cool CO₂ with temperature 90 °F is injected into the reservoir with initial temperature of 110 °F. Reservoir model parameters are shown in Table D.2.

Table D.2 Non-isothermal benchmark case thermal properties

CO ₂ enthalpy at 110 F (Btu/lb)	98.25
CO ₂ isobaric heat capacity (Btu/lbm-F)	32.00
H ₂ O enthalpy at 110 F (Btu/lb)	251.00
H ₂ O isobaric heat capacity (Btu/lbm-F)	60.00
Rock thermal conductivity (Btu/ft-day-F)	48.5343
Water phase thermal conductivity (Btu/ft-day-F)	8.1714
Oil phase thermal conductivity (Btu/ft-day-F)	10.8856
Gas phase thermal conductivity (Btu/ft-day-F)	0.2203

Simulation results of non-isothermal case show good match for saturation.

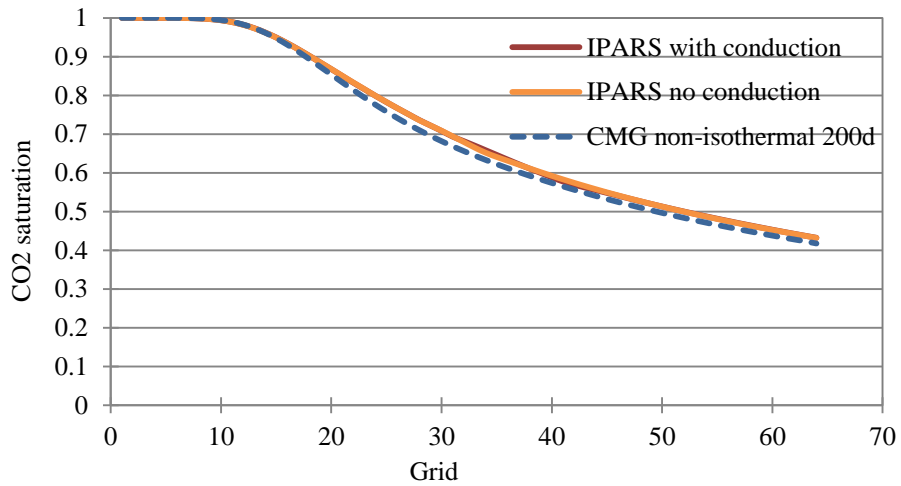


Figure D.6 Non-isothermal simulation results of saturation in IPARS and CMG at 200 days

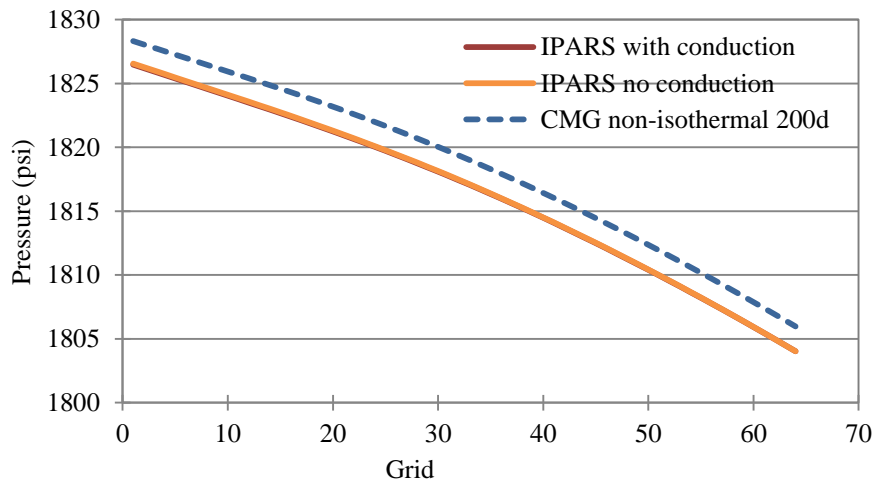


Figure D.7 Non-isothermal simulation results of pressure in IPARS and CMG at 200 days

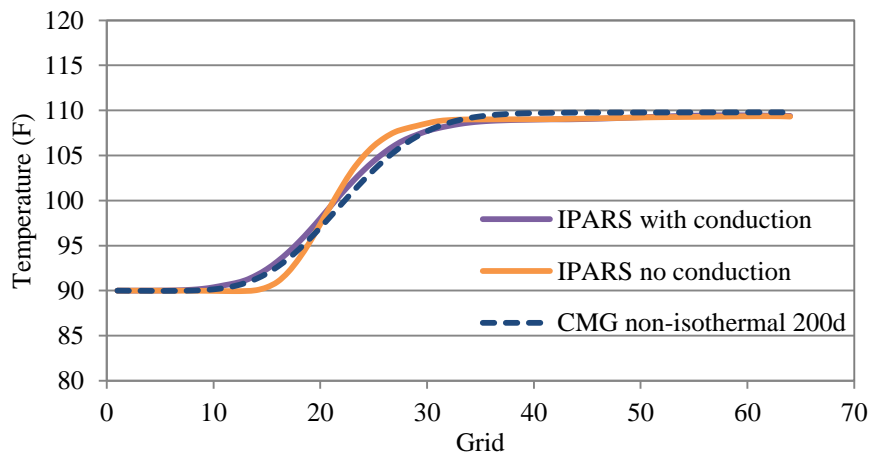


Figure D.8 Non-isothermal simulation results of temperature in IPARS and CMG at 200 days

The saturation and pressure shows good match for non-isothermal case in CMG and IPARS.

The temperature front is less sharp with heat conduction in IPARS (Figure D.8). CMG-GEM by default includes heat conduction. IPARS simulation results of temperature with heat conduction option shows a good comparison with CMG results.

NOMENCLATURE

B_w^0 = Water formation volume factor (RB/STB)

C = Land's coefficient (dimensionless)

$c_{p\alpha}$ = Isobaric phase heat capacity (Btu/lbm-F)

c_r = Rock compressibility (psi^{-1})

c_w = Water compressibility (psi^{-1})

D = Depth (ft)

f_{ic}^α = Fugacity of component ic in phase (v :vapor, l : liquid)

G_i = dimensionless well grid geometric factor

h = Well opening thickness (ft)

$high, low$ superscript = parameter at high and low trapping numbers

$J(S_w)$ = Leverett J-function (dimensionless)

K_i = Permeability of element i normal to the wellbore

K = Permeability (md)

\vec{K} = Permeability tensor (md)

K_{50} = Permeability at >50% of cumulative probability (md)

$K_{84.1}$ = Permeability at >84.1% of cumulative probability (md)

K_{ref} = Permeability for reference rock (md)

K_x, K_y = Permeability in x, y direction (md)

$K_{ic} = x_{ic}^v / x_{ic}^l$ is the K-value for component ic

K_i = the K-value for component i

$k_{f,i}$ = Relative permeability of phase f in element i

k_{rl}^0 = Endpoint relative permeability for phase l

k_{rg}^0 = CO₂ endpoint relative permeability (dimensionless)

- k_{gw} = CO₂ relative permeability (dimensionless)
- k_{rw}^0 = Water endpoint relative permeability (dimensionless)
- k_{rw} = Water relative permeability (dimensionless)
- $k_{r\alpha}$ = Relative permeability for phase α
- L_i = Length of the open wellbore penetrating element i
- M_l = The molecule weight of the liquid phase,
- M_v = The molecule weight of the vapor phase.
- M_w = Molecule weight (g/mol)
- $N_{ic} = \sum_{\alpha} x_{ic}^{\alpha} \rho_{\alpha} S_{\alpha}$ is the concentration of component ic per unit pore volume
- N_c = The capillary number
- N_B = Bond number
- N_p = Number of phases
- N_{Tl} = The trapping number for phase l
- N_w = Water concentration
- P_c = Capillary pressure, kPa
- P^0 = Surface pressure, kPa
- $P_{c\alpha}$ = Phase α capillary pressure kPa
- $P_{c,entry}$ = Entry capillary pressure, kPa
- $P_{c,ref}$ = Capillary pressure for reference rock, kPa
- P_c^{rev} = capillary pressure at reversal point for imbibition process (kPa)
- P_e = Flow pressure at equivalent radius, usually equals well grid element pressure
- P_{α} = Phase α pressure
- $P_{WB,i}$ = Wellbore pressure at the center of the open interval in element i
- P_{BH} = Bottomhole pressure

$P_{f,i}$ = Pressure of phase f at the center of grid element i

$Q_{f,i}$ = The reservoir-volume rate of flow of a phase f from the wellbore to grid element i. Production rate is therefore negative

Q_f = The total reservoir-volume rate of flow of a phase f from the wellbore to the reservoir.

qH = The heat source (Btu/day)

q_{ic} = Molar rate of component ic per unit reservoir volume

R = Universal gas constant, 10.732460 psia-ft³/°R-lbM

r = Pore throat radius (ft)

r_e = Equivalent well radius (ft)

r_w = Well radius (ft)

$r_{e,i}$ = Equivalent radius of the grid element i center

$r_{w,i}$ = Well radius in the grid element i center

S = Salinity in ppm

S_l, S_v = Liquid and vapor phase saturation (dimensionless)

S_{lr} = Residual saturation of phase l (1: water, 2: CO₂) (dimensionless)

S_{wr} = Residual water saturation (dimensionless)

\bar{S}_w = Normalized water saturation (dimensionless)

$\bar{\bar{S}}_w$ = Apparent water saturation (dimensionless)

$S_{g,max}$ = Maximum gas saturation for main drainage (1- S_{wr})

S_{gr} = Residual gas saturation;

S_{gt} = Trapped amount gas at current imbibition \bar{S}_w (not normalized)

$S_{gt,max}$ = Maximum trapping gas saturation in hysteresis, equal to S_{gr} ;

S_{gtrap} = Trapped gas saturation at zero P_c , corresponds to reversal point

$S_{w,inv}$ = Water saturation at reversal point
 S_{wmin} = Normalized water saturation at reversal point A
 S_{wr} = Residual water saturation;
 $S_{lr}^{low}, S_{lr}^{high}$ = Residual saturation for phase l at low and high trapping number
 S_i = Skin factor in element I (dimensionless)
 S_α = Phase α saturation
 T = Temperature
 T_c = Critical temperature of pure phase (Kelvin or Rankin)
 T_l = Trapping model parameter from curve fitting
 T_r = Reduced temperature, ratio to critical T_c in Kelvin or Rankin
 U_α = Flux of phase α
 U_T = Internal energy
 u = Darcy velocity (ft/day)
 V_{DP} = Dykstra–Parsons variation coefficient (dimensionless)
 V_{cj} = Critical molar volume of component j
 WI = Well index (stb/psi-day)
 X_{CO_2} = CO₂ concentration in brine (m^3/m^3)
 x_{ic}^α = Mole fraction of component ic in phase α
 x_j = Mole fraction of component j
 x_{NaCl} = The concentration of salt (mol/L), for Chalbaud 2006 correlation
 $Z_{i,j,k}$ = Normal distribution from FFTSIM software (dimensionless)
 Z_α = Z-factor of phase α
 α_c = Component acentric factor
 γ = Constant parachor number for CO₂ interfacial tension by Chalbaud, 2006

γ_α = Density gradient of phase α
 θ = Contact angle, degree
 $\lambda_{drainage}, \lambda_{imb}$ = Drainage and imbibition capillary pressure exponent
 λ_l = Relative permeability exponent for phase l (dimensionless)
 λ_g = Gas relative permeability exponent (dimensionless)
 λ_w = Water relative permeability exponent (dimensionless)
 λ_{pc} = Capillary pressure exponent (dimensionless)
 μ_α = Viscosity of phase α (cp)
 μ^* = Viscosity of pure phase (cp)
 $\mu_{f,i}$ = Viscosity of phase f in element i (cp)
 μ_{mix}^* = Viscosity of mixture phase (cp)
 $\rho_{c,mix}$ = Pseudo critical density for mixture (mole per volume)
 ρ_r = Reduced molar density of phase (mole per volume)
 ρ_α = Molar density of phase α (mole per volume)
 σ = Interfacial tension (mN/m)
 $\sigma_{plateau}$ = Input interfacial tension for Chalbaud empirical correlation (N/m)
 σ_{std} = Standard deviation of a normal distribution (dimensionless)
 σ_{ref} = Interfacial tension for reference rock (N/m)
 ϕ_{ic}^α = Fugacity coefficient of component ic in phase α , $\phi_{ic}^\alpha = f_{ic}^\alpha / x_{ic}^\alpha P$
 ϕ = Porosity (dimensionless)
 ϕ_0 = Reference porosity at measured condition P_{ref} (dimensionless)
 ϕ_{ref} = Porosity for reference rock (dimensionless)
 ψ_i = parachor of the component i
 ξ, ξ_{mix} = Pure phase and mixture viscosity parameter

τ_l = Trapping model parameters from curve fitting

v = Vapor fraction, the fraction of total non-aqueous moles in the vapor phase.

v_l = Liquid phase molar volume (Volume/mol)

v_v = Vapor phase molar volume (Volume/mol)

v_w = Water molar volume (Volume/mol)

v_w^{ref} = Water molar volume at reference condition (Volume/mol)

ω_i = Component acentric parameter input

Φ = Potential ($P + \rho g D$)

Ψ_i = The parachor of the component i

References

- H. Alkan, Y. Cinar, and E. B. Ülker. Impact of capillary pressure, salinity and *in situ* conditions on CO₂ injection into saline aquifers. *Transport In Porous Media*, Volume 84, Number 3, Page 799-819, 2010
- M. R. Allen, D. J. Frame, C. Huntingford, C. D. Jones, J. A. Lowe, M. Meinshausen, and N. Meinshausen. Warming caused by cumulative carbon emissions towards the trillionth tonne. *Nature*, Volume 458(7242), page 1163-1166, 2009
- Y. B. Altundas, T. S. Ramakrishnan, and N. Chugunov. Retardation of CO₂ caused by capillary pressure hysteresis: a new CO₂ trapping mechanism. SPE 139641-PA, *SPE Journal*, Volume 16, Number 4, Page 784-794, December 2011
- S. Bachu. Sequestration of CO₂ in geological media: Criteria and approach for site selection in response to climate change. *Energy Conversion and Management*, Volume 41, Issue 9, Page 953-970, 2000
- S. Bachu. Sequestration of CO₂ in geological media in response to climate change: road map for site selection using the transform of the geological space into the CO₂ phase space. *Energy Conversion and Management*, Volume 43, Issue 1, Page 87–102, 2002
- S. Bachu. CO₂ storage in geological media: Role, means, status and barriers to deployment. *Progress in Energy and Combustion Science, PROG ENERG COMBUST SCI*, Volume 34, Number 2, Page 254-273, 2008
- S. Bachu and J. J. Adams. Sequestration of CO₂ in geological media in response to climate change: capacity of deep saline aquifers to sequester CO₂ in solution. *Energy Conversion and Management*, Volume 44, Issue 20, Page 3151–3175, 2003
- S. Bachu and D. B. Bennion. Interfacial tension between CO₂, freshwater, and brine in the range of pressure from (2 to 27) MPa, temperature from (20 to 125) °C, and water salinity from (0 to 334 000) mg • L⁻¹. *Journal of Chemical & Engineering Data*, Volume 54, Issue 3, Page 765–775, 2009a
- S. Bachu and D. B. Bennion. Dependence of CO₂-brine interfacial tension on aquifer pressure, temperature and water salinity. *Energy Procedia*, Volume 1, Issue 1, Page 3157–3164, February 2009b
- S. Bachu, W. D. Gunter, and E. H. Perkins. Aquifer disposal of CO₂: hydrodynamic and mineral trapping. *Energy Conversion and Management*, Volume 35, Issue 4, Page 269–279, 1994
- A. Bahadori, H. B. Vuthaluru, and S. Mokhatab. New correlations predict aqueous solubility and density of carbon dioxide. *International Journal of Greenhouse Gas Control*, Volume 3, Issue 4, Page 474-480, 2009

- M. Bickle, A. Chadwick, H. E. Huppert, M. Hallworth, and S. Lyle. Modelling carbon dioxide accumulation at Sleipner: implications for underground carbon storage. *Earth and Planetary Science Letters*, Volume 255, Issue 1-2, Page 164–176, 2007
- D. B. Bennion and S. Bachu. Relative permeability characteristics for supercritical CO₂ displacing water in a variety of potential sequestration zones in the western Canada sedimentary basin. SPE 95547 ATCE conference in Dallas, 2005
- D. B. Bennion and S. Bachu. The impact of interfacial tension and pore size distribution/capillary pressure character on CO₂ relative permeability at reservoir conditions in CO₂-brine systems. SPE 99325-MS, SPE/DOE Symposium on Improved Oil Recovery, Tulsa, Oklahoma, 22-26 April 2006a
- D. B. Bennion and S. Bachu. Dependence on temperature, pressure, and salinity of the IFT and relative permeability displacement characteristics of CO₂ injected in deep saline aquifers. SPE 102138, ATCE in San Antonio, 2006b
- D. B. Bennion and S. Bachu. Permeability and relative permeability measurements at reservoir conditions for CO₂-water systems in ultra low permeability confining caprocks. SPE 106995-MS, EUROPEC/EAGE Conference and Exhibition, London, U.K. 11-14 June 2007
- D. B. Bennion and S. Bachu. A correlation of the interfacial tension between supercritical phase CO₂ and equilibrium brines as a function of salinity, temperature and pressure. SPE 114479-MS, Paper for SPE ATCE Conference in Denver, September 2008a
- D. B. Bennion and S. Bachu. Supercritical CO₂ and H₂S-brine drainage and imbibition relative permeability relationships for intergranular sandstone and carbonate formations. SPE 99326-PA, *SPE Reservoir Evaluation & Engineering*, Volume 11, Number 3, Page 487-496, 2008b
- D. B. Bennion and S. Bachu. Drainage and imbibition CO₂/brine relative permeability curves at reservoir conditions for high-permeability carbonate rocks, SPE 134028-MS, SPE Annual Technical Conference and Exhibition, Florence, Italy, 19-22 September 2010
- S. M. Benson, L. Tomutsa, D. Silin, T. Kneafsey, and L. Miljkovic. Core scale and pore scale studies of carbon dioxide migration in saline formations. Proceedings of 8th International Conference on Greenhouse Gas Control Technologies, IEA Greenhouse Gas Program, Trondheim, Norway, 2006
- S. M. Benson and D. R. Cole. CO₂ Sequestration in Deep Sedimentary Formations. *Elements*, Volume 4, Page 325–331, 2008
- J. T. Birkholzer, Q. Zhou, and C. Tsang. Large-scale impact of CO₂ storage in deep saline aquifers: A sensitivity study on pressure response in stratified systems. *International Journal Greenhouse Gas Control*, Volume 3, Page 181–194, 2009

- M. J. Blunt. Pore level modeling of the effects of wettability. SPE 38435-PA *SPE Journal*, Volume 2, Number 4, Page 494-510, December 1997
- L. E. Brownell and D. L. Katz. Flow of fluids through porous media – Part II, Simultaneous flow of two homogeneous phases. *Chemical Engineering Progress*, Volume 43, Page 601–612, 1947
- S. E. Buckley and M. C. Leverett. Mechanism of fluid displacements in sands. *Transactions of the AIME*, Volume 146, Page 107–116. 1942
- F. M. Carlson. Simulation of relative permeability hysteresis to the non-wetting phase. SPE 10157, SPE Annual Technical Conference and Exhibition, San Antonio, October 5–7, 1981
- C. Chalbaud, J. M. Lombard, M. Robin, H. Bertin, and F. Martin. Two phase flow properties of brine-CO₂ systems in a carbonate core: influence of wettability on P_c and k_r. SPE 111420-MS, SPE/EAGE Reservoir Characterization and Simulation Conference, Abu Dhabi, UAE, 28-31 October 2007
- C. Chalbaud, M. Robin, and P. Egermann. Interfacial tension data and correlations of brine/CO₂ system under reservoir conditions, SPE 102918, SPE Annual Technical Conference and Exhibition, San Antonio, Texas, 24-27 September 2006
- C. Chalbaud, M. Robin, J.M. Lombard, H. Bertin, and P. Egermann. Brine/CO₂ interfacial properties and effects on CO₂ storage in deep saline aquifers, *Oil & Gas Science and Technology – Rev. IFP*, Volume 65, Number 4, Page 541-555, 2010
- M. I. Cabaço, M. Besnard, S. Longelin, and Y. Danten. Evolution with the density of CO₂ clustering studied by Raman spectroscopy. *Journal of Molecular Liquids*, Volume 153, Issue 1, Pages 15-19, 15 April 2010
- P. C. Carman. Fluid flow through granular beds. *Transactions, Institution of Chemical Engineers*, London, Volume 15, Page 150-166, 1937
- P. Chiquet, D. Broseta, and S. Thibeau. Capillary alteration of shaly caprocks by Carbon Dioxide. SPE 94183-MS, SPE Europec/EAGE Annual Conference, Madrid, Spain, 13-16 June 2005
- Y. Cinar, S. Marquez, and F. M. Orr Jr. Effect of IFT variation and wettability on three-phase relative permeability. SPE 90572-PA, *SPE Reservoir Evaluation & Engineering*, Volume 10, Number 3, Page 211-220, June 2007
- Y. Cinar, A. Riaz, and H. Tchelepi. Experimental study of CO₂ injection into saline formations. SPE 110628-PA, *SPE Journal*, Volume 14, Number 4, Page 588-594, December 2009
- H. Class, A. Ebigbo, R. Helmig, H. K. Dahle, J. M. Nordbotten, M. A. Celia, P. Audigane, M. Darcis, J. Ennis-King, Y. Fan, B. Flemisch, S. E. Gasda, M. Jin, S.

- Krug, D. Labregere, A. Naderi Beni, R. J. Pawar, A. Sbai, S. G. Thomas, L. Trenty, and L. Wei: A benchmark study on problems related to CO₂ storage in geologic formations: Summary and discussion of the results. *Computational Geosciences* Volume 13, Number 4, Page 409-434, 2009
- R. E. Collins and J. K. Jordan. Porosity and Permeability Distribution of Sedimentary Rocks. SPE 212-MS. Society of Petroleum Engineers of AIME. 1961
- M. Delshad, R. J. Lenhard, M. Oostrom, and G. A. Pope. A mixed-wet hysteretic relative permeability and capillary pressure model for reservoir simulations. SPE-86916-PA, *SPE Reservoir Evaluation & Engineering*, Volume 6, Issue 5, Page 328-334, 2003
- M. Delshad, S. G. Thomas, and M. F. Wheeler. A benchmark-study on problems related to CO₂ storage in geological formations - Summary and discussion of the results. Special Issue of Computational Geosciences, Springer, July 2009
- M. Delshad, S. G. Thomas, and M. F. Wheeler. Parallel numerical reservoir simulations of nonisothermal compositional flow and chemistry. SPE 118847-PA, *SPE Journal*, Volume 16, Number 2, Page 239-248, 2010
- M. Delshad, M. F. Wheeler, and X. Kong. A critical assessment of CO₂ injection strategies in saline aquifers. SPE 132442, SPE Western Regional Meeting, Anaheim, CA, May 2010
- M. Delshad, X. Kong, and M. F. Wheeler. On interplay of capillary, gravity, and viscous forces on brine/CO₂ relative permeability in a compositional and parallel simulation framework. SPE 142146, SPE Reservoir Simulation Symposium, Woodlands, TX, February 2011
- M. Delshad, X. Kong, R. Tavakoli, S. A. Hosseini, and M. F. Wheeler. Modeling and simulation of carbon sequestration at Cranfield incorporating new physical models. *International Journal of Greenhouse Gas Control*, Volume 18, Page 463–473, May 2013
- L. W. Diamond and N. N. Akinfiev. Solubility of CO₂ in water from –1.5 to 100 °C and from 0.1 to 100MPa: evaluation of literature data and thermodynamic modelling. *Fluid Phase Equilibria*, Volume 208, Issue 1-2, Page 265–290, 2003
- C. Doughty. Modeling geologic storage of carbon dioxide: comparison of nonhysteretic and hysteretic characteristic curves. *Energy Conversion and Management*, Volume 48, Page 1768-1781, 2007
- C. Doughty and K. Pruess. Modeling supercritical CO₂ injection in heterogeneous porous media. Proceedings, TOUGH Symposium 2003
- C. Doughty and K. Pruess. Modeling supercritical carbon dioxide injection in heterogeneous porous media. *Vadose Zone Journal*, Volume 3, Number 3, Page 837–847, 2004

- C. Doughty and B. Freifeld. Modeling CO₂ Injection at Cranfield, Mississippi: investigation of methane and temperature effects, proceedings, TOUGH Symposium 2012, Lawrence Berkeley National Laboratory, Berkeley, California, September 17-19, 2012
- H. Dykstra and R. L. Parsons. The Prediction of Oil recovery by Water flooding, Secondary Recovery of Oil in the United State. 2nd ed., API, Page 160–174, 1950
- Z. Duan and R. Sun. An improved model calculating CO₂ solubility in pure water and aqueous NaCl solutions from 257 to 533 K and from 0 to 2000 bar. *Chemical Geology*. Volume 193, Issue 3-4, Page 257–271, 2003
- Z. Duan, R. Sun, C. Zhu, and I. M. Chou. An improved model for the calculation of CO₂ solubility in aqueous solutions containing Na⁺, K⁺, Ca²⁺, Mg²⁺, Cl⁻, and SO₄²⁻. *Marine Chemistry*, Volume 98, Issues 2–4, Pages 131–139, 1 February 2006
- A. Fenghour, W. A. Wakeham, and V. Vesovic. The viscosity of carbon dioxide. *Journal of Physical and Chemical Reference Data*, Volume 27, Number 1, Page 31-44, 1998
- M. Flett, G. Randal, and I. Taggart. The function of gas-water relative permeability hysteresis in the sequestration of carbon dioxide in saline formations. SPE 88485, SPE Asia Pacific Oil and Gas Conference and Exhibition, Perth, Australia, 18-20 October 2004
- X. Gai, R.H. Dean, M. F. Wheeler, and R. Liu. Coupled geomechanical and reservoir modeling on parallel computers. SPE 79700, SPE Reservoir Simulation Symposium, Houston, TX, February 3-5, 2003
- J. S. Gallagher, R. Crovetto, and J. M. H. Levelt Sengers. The thermodynamic behavior for the CO₂-H₂O system from 400 to 1000 K, up to 100 MPa and .30% mole fraction of CO₂. *Journal of Physical and Chemical Reference Data*, Volume 22 Number 2, Page 431-513, 1993
- M. Godec, V. Kuuskraa, T. V. Leeuwen, L. S. Melzer, and N. Wildgust, CO₂ storage in depleted oil fields: The worldwide potential for carbon dioxide enhanced oil recovery, *Energy Procedia*, Volume 4, Pages 2162-2169, 2011
- A. Hebach, A. Oberhof, N. Dahmen, A. Kögel, H. Ederer, and E. Dinjus. Interfacial tension at elevated pressures – measurements and correlations in the water + carbon dioxide system. *Journal of Chemical & Engineering Data*, Volume 47, Number 6, Page 1540-1546, 2002
- A. A. Heiba, H. T. Davis, and L. E. Scriven. Effect of wettability on two-phase relative permeabilities and capillary pressures. SPE 12172-MS, SPE Annual Technical Conference and Exhibition, San Francisco, California, 5-8 October 1983
- S. A. Hosseini, H. Lashgari, J. W. Choi, J-P Nicot, J. Lu, and S. D. Hovorka, Static and dynamic reservoir modeling for geological CO₂ sequestration at Cranfield,

- Mississippi, USA. *International Journal of Greenhouse Gas Control*, Volume 18, 2012
- N. J. House, D. D. Faulder, G. L. Olson, and J. R. Fanchi. Simulation study of CO₂ sequestration in a North Sea formation. SPE 81202, presented at the SPE/EPA/DOE Exploration and Production Environmental Conferences, San Antonio, Texas, 2003
- S. D. Hovorka, C. Doughty, P. R. Knox, C. T. Green, K. Pruess, and S. M. Benson. Evaluation of brine-bearing sands of the Frio formation, upper Texas gulf coast for geological sequestration of CO₂. First National Conference on Carbon Sequestration, National Energy Technology Laboratory, Pittsburgh, PA, USA, 14–17, May, 2001
- HYPRE, Lawrence Livermore National Laboratory.
http://computation.llnl.gov/casc/linear_solvers/sls_hypre.html
- S. T. Ide, K. Jessen, and F. M. Jr. Orr. Storage of CO₂ in saline aquifers: effects of gravity, viscous, and capillary forces on amount and timing of trapping. *International Journal Greenhouse Gas Control*, Volume 1, Issue 4, Page 481-491, 2007
- IPCC Fourth Assessment Report: Climate Change 2007. A contribution of working groups I, II, and III to the fourth assessment report of the intergovernmental panel on climate change (IPCC). Geneva, Switzerland: IPCC.
- J. L. Jensen, D. V. Hinkley, and L. W. Lake. A statistical study of reservoir permeability: distributions, correlations, and averages. SPE 14270-PA, *SPE Formation Evaluation*, Volume 2, Number 4, Pages 461-468, December 1987.
- G. R. Jerauld and S. J. Salter. The effect of pore-structure on hysteresis in relative permeability and capillary pressure: pore-level modeling. *Transport in Porous Media*, Volume 5, Issue 2, Page 103-151, April 1990
- G. R. Jerauld. General three-phase relative permeability model for Prudhoe Bay. SPE 36178-PA, *SPE Reservoir Engineering*, Volume 12, Number 4, Page 255-263, November 1997
- M. Jin. A study of non-aqueous phase liquid characterization and surfactant remediation. PhD dissertation, The University of Texas, Austin, Texas, 1995
- J. A. A. Jones. Climate change and sustainable water resources: placing the threat of global warming in perspective. *Hydrological Sciences Journal*, Volume 44. Number 4, Page 541-557, 1999
- J. A. Jossi, L. I. Stiel, and G. Thodos. The viscosity of pure substances in the dense gaseous and liquid phases. *AICHE Journal - AICHE J*, Volume 8, Number 1, Page 59-63, 1962

- R. Juanes, E. J. Spiteri, F. M. Jr. Orr, and M.J. Blunt. Impact of relative permeability hysteresis on geological CO₂ storage. *Water Resources Research*, Volume 42, Issue 12, 2006
- J. Kestin, J. V. Sengers, B. Kamgar-Parsi, J. M. H. Levelt Senge. Thermophysical properties of fluid H₂O. *Journal of Physical and Chemical Reference Data*, Volume 13, Number 1, Page 175-183, 1984
- J. E. Killough. Reservoir simulation with history-dependent saturation functions, *SPE Journal*, SPE-5106-PA, Volume 16, Number 1, Page 37–48, 1976
- X. Kong, M. Delshad, and M. F. Wheeler. High resolution simulations with a compositional parallel simulator for history matching laboratory CO₂/brine core flood experiment. SPE 163625-MS, SPE Reservoir Simulation Symposium, Woodlands, TX, February 2013a
- X. Kong, M. Delshad, and M. F. Wheeler. An integrated capillary, buoyancy, and viscous driven model for brine/CO₂ relative permeability in a compositional and parallel reservoir simulator. *Modeling and Simulation in Fluid Dynamics in Porous Media*, Springer Proceedings in Mathematics & Statistics, Volume 28, Page 125-142, 2013b
- J. Kozeny. Ueberkapillare Leitung des Wassersim Boden. *Sitzungsber Akad. Wiss., Wien*, Volume 136(2a), Page 271-306, 1927.
- M. Krause, J. C. Perrin, and S. M. Benson. Modeling permeability distributions in a sandstone core to history match coreflood experiments. SPE 126340-PA, *SPE Journal*, Volume 16, Number 4, pp. 768-777, December, 2011.
- A. Kumar, R. Ozah, , M. H. Noh, G. A. Pope, S. L. Bryant, K. Sepehrnoori, and L. W. Lake. Reservoir simulation of CO₂ storage in deep saline aquifers. *SPE Journal*, Volume 10, Issue 3, Page 336-348, September 2005.
- A. Kumar. A simulation study of carbon sequestration in deep saline aquifers. M.S. Thesis, The University of Texas at Austin, August 2004.
- L. W. Lake. Enhanced oil recovery. Prentice Hall, Inc., Englewood Cliffs, NJ, 1989
- C. S. Land. Calculation of imbibition relative permeability for two- and three-phase flow from rock properties. *SPE Journal*, Volume 8, Number 2, Page 149-156, June 1968
- C. S. Land. Comparison of calculated with experimental imbibition relative permeability. *SPE Journal*, Volume 11, Number 4, Pages 419-425, December 1971
- R. M. Lansangan, M. Taylor, J. L. Smith, and F. S. Kovarik. An improved viscosity correlation for CO₂/reservoir oil systems. SPE 20209-PA, *SPE Advanced Technology Series*, Volume 1, Number 2, Pages 134-141, July 1993

- R. J. Lenhard and J. C. Parker. A model for hysteretic constitutive relations governing multiphase flow: 2. Permeability-saturation relations, *Water Resources Research*, Volume 23, Issue 12, Page 2197–2206, December 1987
- R. J. Lenhard and M. Oostrom. A parametric model for predicting relative permeability saturation-capillary pressure relationships of oil-water systems in porous media with mixed wettability. *Transport in Porous Media*, Volume 31, Issue 1, Page 109-131, 1998
- M. C. Leverett. Capillary behavior in porous solids. Transactions of the AIME, Volume 142, Number 1, Page 159–172, 1941.
- J. Lohrenz, B. G. Bray, and C. R. Clark. Calculating viscosities of reservoir fluids from their compositions, *Journal of Petroleum Technology*, Volume 16, Number 10, Page 1171-1176, 1964
- B. Lu, T. Alshaalan, and, M. F. Wheeler. Iteratively coupled reservoir simulation for multiphase flow in porous media. SPE 110114, SPE Annual Technical Conference and Exhibition, Anaheim, California, November 2007
- J. Lu, P. J. Cook, S. A. Hosseini, C. Yang, K. D. Romanak, T. Zhang, B. M. Freifeld, R. C. Smyth, H. Zeng, and S. D. Hovorka. Complex fluid flow revealed by monitoring CO₂ injection in a fluvial formation. *Journal of Geophysical Research*, 117, B03208, doi:10.1029/2011JB008939. 2012a
- J. Lu, Y. K. Kharaka, J. J. Thordsen, J. Horita, A. Karamalidis, C. Griffith, J. A. Hakala, G. Ambats, D. R. Cole, T. J. Phelps, M. A. Manning, P. J. Cook, and S. D. Hovorka. CO₂-rock-brine interactions in Lower Tuscaloosa Formation at Cranfield CO₂ sequestration site, Mississippi, U.S.A. *Chemical Geology*, Volume 291, Page 269-277. 2012b.
- Q. Lu, M. Peszynska, and M. F. Wheeler. A parallel multi-block black-oil model in multi-model implementation. SPE 79535, SPE Journal, Volume 7, Number 3, Page 278-287, 2002
- G. Løvoll, Y. Me´heust, K. J. Ma˚løy, E. Aker, and J. Schmittbuhl. Competition of gravity, capillary and viscous forces during drainage in a two-dimensional porous medium, a pore scale study. *Energy*, Issue 30, Page 861-872, 2005
- D. B. Macleod. On a relation between surface tension and density. *Trans. Faraday Soc.*, Issue 19, Page 38-41, 1923
- G. Marland, T.A. Boden, and R. J. Andres. Global, regional, and national CO₂ emissions. In Trends: A compendium of data on global change. Carbon Dioxide Information Analysis Center, Oak Ridge National Laboratory, U.S. Department of Energy, Oak Ridge, Tenn., U.S.A, 2003

- F. G. Oakes and J. T. White. Measurement of CO₂ flow in its supercritical and gaseous phase. SPE 14289, *SPE Production Engineering*, Volume 2, Number 3, Pages 209-217, 1987
- J. G. J. Olivier, J. A. Van Aardenne, F. Dentener, V. Pagliari, L.N. Ganzeveld, and J. A. H. W. Peters. Recent trends in global greenhouse gas emissions: regional trends 1970-2000 and spatial distribution of key sources in 2000. *Environmental Science*, Volume 2, Issue 2-3, pages 81-99, 2005
- L. Ouyang. New correlations for predicting the density and viscosity. *The Open Petroleum Engineering Journal*, Issue 4, pages 13-21, 2011
- R. C. Ozah, S. Lakshminarasimhan, G. A. Pope, K. Sepehrnoori, and S. L. Bryant. Numerical simulation of the storage of pure CO₂ and CO₂-H₂S gas mixtures in deep saline aquifers, SPE 97255-MS, SPE Annual Technical Conference and Exhibition, Dallas, 9-12 October 2005
- D. W. Peaceman. Interpretation of well-block pressures in numerical reservoir simulation with non-square grid blocks and anisotropic permeability. *SPE Journal*, Volume 23, Number 3, Page 531-543, 1983
- G. Pencheva, S. G. Thomas, and M. F. Wheeler. Mortar coupling of discontinuous Galerkin and mixed finite element methods. Bergen, Norway, 11th European Conference on the Mathematics of Oil Recovery, ECMOR XI. September 8-11 2008
- G. Pencheva and I. Yotov. Balancing domain decomposition for mortar mixed finite element methods on non-matching grids. *Numerical Linear Algebra with Applications*, Volume 10, Issues 1-2, Page 159-180, 2003
- D. Y. Peng and D. B. Robinson. A new two-constant equation of state. *Industrial & Engineering Chemistry Fundamentals*, Volume 15, Number 1, Page 59-64, 1976
- K. Pruess, ECO2N: A TOUGH2 fluid property module for mixtures of water, NaCl, and CO₂. Report LBNL-57952, Lawrence Berkeley National Laboratory, Berkeley, CA, USA. 2005
- K. Pruess and J. Garcia, Multiphase flow dynamics during CO₂ disposal into saline aquifers. *Environmental Geology*, Volume 42, Issue 2-3, page 282-295, 2002
- K. Pruess, C.M. Oldenburg, and G. Moridis. TOUGH2 user's guide, version 2.0. Report LBNL-43134, Lawrence Berkeley National Laboratory, Berkeley, CA, USA. 1999
- K. Pruess, J. Garcia, T. Kavscek, C.M. Oldenburg, J. Rutqvist, C. Steefel, and T. Xu, Code intercomparison builds confidence in numerical simulation models for geologic disposal of CO₂. *Energy*, Volume 29, Issues 9-10, Pages 1431-1444, 2004

- K. Pruess. Leakage of CO₂ from geologic storage: Role of secondary accumulation at shallow depth. *International Journal of Greenhouse Gas Control*, Volume 2, Issue 1, Page 37-46, 2008
- J. M. Pearce, S. Holloway, H. Wacker, M. K. Nelis, C. Rochelle, and K. Bateman. Natural occurrence as analogues for the geological disposal of carbon dioxide. *Energy Conversion and Management*. Volume 37, Issues 6-8, Page 1123-1128, 1996
- G. A. Pope, W. Wu, G. Narayanaswamy, M. Delshad, M. M. Sharma, and P. Wang. Modeling relative permeability effects in gas-condensate reservoirs with a new trapping model. SPE 62497-PA, *SPE Reservoir Evaluation & Engineering*, Volume 3, Number 2, Page 171-178, April 2000
- S. Portier and C. Rochelle. Modelling CO₂ solubility in pure water and NaCl-type waters from 0 to 300 °C and from 1 to 300 bar: Application to the Utsira Formation at Sleipner. *Chemical Geology*, Volume 217, Issue 3-4, Page 187-199, 2005
- G. Schnaar and D. C. Digiulio. Computational modeling of the geologic sequestration of carbon dioxide. *Vadose Zone Journal*, Volume 8, Number 2, Page 389-403, 2009
- P. Saripalli and P. McGrail. Semi-analytical approaches to modeling deep well injection of CO₂ for geologic sequestration. *Energy Conversion Management*, Volume 43, Issue 2, Page 185-198, 2002
- J. Shi, Z. Xue, and S. Durucan. History matching of CO₂ core flooding CT scan saturation profiles with porosity dependent capillary pressure. *Energy Procedia*, Volume 1, Issue 1, Page 3205-3211, 2009
- R. Span and W. Wagner. A new equation of state for carbon dioxide covering the fluid region from the triple-point temperature to 1100 K at pressures up to 800 MPa. *Journal of Physical and Chemical Reference Data*, Volume 25, Issue 6, Page 1509-1596, November 1996
- Speipner CO₂ capture and storage project, <http://www.bgs.ac.uk/science/CO2/home.html>
- E. J. Spiteri, R. Juanes, M. J. Blunt, and F. M. Jr. Orr. A new model of trapping and relative permeability hysteresis for all wettability characteristics. SPE-96448-PA, *SPE Journal*, Volume 13 Number 3, Page 277-288, 2008
- N. Spycher and K. Pruess. CO₂-H₂O mixtures in the geological sequestration of CO₂. I. Assessment and calculation of mutual solubilities from 12 to 100°C and up to 600 bar, *Geochimica Cosmochim. Acta*, Volume 67, Number 16, Page 3015-3031, 2003
- N. Spycher and K. Pruess. CO₂-H₂O mixtures in the geological sequestration of CO₂. II. Partitioning in chloride brines at 12-100°C and up to 600 bar, *Geochimica Cosmochim. Acta*, Volume 69, Number 13, Page 3309-3320, 2005

- L. I. Stiel and G. Thodos. The viscosity of nonpolar gases at normal pressures. *AIChE Journal*, Volume 7, Issue 4, Page 611–615, 1961
- K. Stüben. SAMG, <http://www.scai.fraunhofer.de/en/business-research-areas/numerical-software/products/samg.html>
- K. Stueben, T. Clees, H. Klie, B. Lu, and M. F. Wheeler. Algebraic Multigrid Methods (AMG) for the efficient solution of fully implicit formulations in reservoir simulation, SPE 105832, SPE Reservoir Simulation Symposium, Houston, Texas, February 26–28, 2007
- T. Suekane, T. Nobuso, S. Hirai, and M. Kiyota. Geological storage of carbon dioxide by residual gas and solubility trapping. *International Journal of Greenhouse Gas Control*, Volume 2, Issue 1, Pages 58–64, January 2008
- S. Sugden. A relation between surface tension, density, and chemical composition. *Journal of the Chemical Society, Transactions*, Volume 125, Page 1177–1189, 1924
- S. Takenouchi and G.C. Kennedy. The solubility of carbon dioxide in NaCl solutions at high temperatures and pressures. *American Journal of Science*, Volume 263, Page 445 – 454, 1965
- S. G. Thomas, M. Balhoff, M. F. Wheeler. Mortar coupling and upscaling of porescale models, *Computational Geosciences*, Springer Neth., Volume 12, Number 1, Page 15–27, 2008
- S. G. Thomas and M. F. Wheeler. Enhanced-velocity-multiblock method for coupled flow and reactive-species transport through porous media: applications to bioremediation and carbon sequestration. *SPE Journal*. SPE-141824-PA, Volume 17, Issue 3, Page 794–804, 2012
- D.Q. Tuan, J.A. Zollweg, P. Harriott, and S. S. H. Rizvi. Measurement and modeling of viscosity of supercritical carbon dioxide/biomaterial(s) mixtures. *Industrial and Engineering Chemistry Research*, Volume 38, Issue 5, Page 2129–2136, 2009
- A. Valtz, A. Chapoy, C. Coquelet, P. Paricaud, and D. Richon. Vapour–liquid equilibria in the carbon dioxide–water system, measurement and modelling from 278.2 to 318.2 K. *Fluid Phase Equilibria*, Volume 226, Pages 333–344, 10 December 2004
- V. Vesovic, W. A. Wakeham, G. A. Olchowy, J. V. Sengers, J. T. R. Watson, and J. Millat. The transport properties of carbon dioxide. *Journal of Physical and Chemical Reference Data*, Volume 19, Issue 3, Page 763–808, 1990
- J. D. Van Der Waals, The equation of state for gases and liquids. Nobel Lectures in Physics, Page 254–265, 1910
- D. W. Waples, J. S. Waples. A review and evaluation of specific heat capacities of rocks, minerals, and subsurface fluids. Part 1: Minerals and Nonporous rocks. *Natural Resource Research*, Volume 13, Issue 2, Page 97–122, 2004

- J. Wheeler, I. Yotov, and M. F. Wheeler. Enhanced velocity mixed finite element methods for flow in multiblock domains. *Computational Geosciences*, Volume 6, Issue 3-4, Page 315-332, 2002
- M. F. Wheeler, M. Delshad, X. Kong, S. Thomas, T. Wildey, and G. Xue. Role of computational science in protecting the environment: geological storage of CO₂. Proceedings of the International Congress of Mathematics, Hyderabad, India, June 2010
- M. F. Wheeler, T. Wildey, and G. Xue. Efficient algorithms for multiscale modeling in porous media. *Numerical Linear Algebra with Applications*, Volume 17, Issue 5, Page 771-785, October 2010
- M. F. Wheeler, T. Arbogast, S. Bryant, J. Eaton, Q. Lu, M. Peszynska, and I. Yotov. A parallel multiblock/multidomain approach for reservoir simulation. SPE 51884, presented at the SPE Reservoir Simulation Symposium, Houston, TX, 1999
- M, Wilson, M, Monea, S, Whittaker, D, White, D. Law, and R. Chalaturnyk. IEA GHG Weyburn CO₂ monitoring & storage project summary report 2000–2004. PTRC
- D. Yang and Y. Gu. Interfacial tensions of crude oil-brine-CO₂ systems under reservoir conditions. SPE 90198, Presented at the 2004 SPE Annual Technical Conference and Exhibition, Houston, September 26-29, 2004
- M.E. Yener, P. Kashulines, S.S.H. Rizvi, and P. Harriott. Viscosity measurement and modeling of lipid-supercritical carbon dioxide mixtures. *The Journal of Supercritical Fluids*, Volume 11, Number 3, Page 151-162(12), 31 January 1998
- C. Yuan, M. Delshad, and M. F. Wheeler, Modeling multiphase non-Newtonian polymer flow in IPARS parallel framework. *American Institute of Mathematical Sciences, Networks and Heterogeneous Media*, Volume 5, Number 3, Page 583-602, September 2010
- Z. Ziabakhsh-Ganji and H. Kooi, An Equation of State for thermodynamic equilibrium of gas mixtures and brines to allow simulation of the effects of impurities in subsurface CO₂ storage. *International Journal of Greenhouse Gas Control*, Volume 11, Supplement, Page S21–S34, November 2012
- Q. Zhou, J.T. Birkholzer, C. Tsang, and J. Rutqvist. A method for quick assessment of CO₂ storage capacity in closed and semi-closed saline formations, *International Journal of Greenhouse Gas Control*, Volume 2, Issue 4, Page 626–639, October 2008
- Z. Zhu, M. Li, M. Lin, B. Peng, L. Sun, and L. Chen. Investigation on variations in wettability of reservoir rock induced by CO₂-brine-rock interactions. SPE 142979-MS, SPE Annual Technical Conference and Exhibition conference in Vienna, Austria, 2011

VITA

The author, Xianhui Kong, was born in Pingyao (ancient city dates back to 2700 years), Shanxi Province, China. He is the youngest son of Zhaoliang Kong and Tianxiang Hao. He completed his middle school education in Pingyao Middle School, Pingyao, Shanxi Province China in 2001. In 2001, he entered the University of Science and Technological of China (USTC), Hefei, Anhui Province, China. He received the Bachelor of Science degree (B.S.) in Mechanical Engineering in 2005 and the Master of Engineering (M.E.) degree in Mechanical Engineering in 2008. In August 2008, he joined the Graduate program of Petroleum and Geosystems Engineering of The University of Texas at Austin, Austin, TX. At the time of writing of this document, 2014, he was pursuing a Ph.D. degree in Petroleum Engineering at The University of Texas at Austin.

Email: xianhui.kong@gmail.com